

Measurements of Direct Photon Higher Order
Azimuthal Anisotropy
in $\sqrt{s_{\text{NN}}} = 200 \text{ GeV}$ Au + Au Collisions
at RHIC-PHENIX

Sanshiro MIZUNO

March 2015

Measurements of Direct Photon Higher Order
Azimuthal Anisotropy
in $\sqrt{s_{\text{NN}}} = 200 \text{ GeV}$ Au + Au Collisions
at RHIC-PHENIX

Sanshiro MIZUNO
Doctoral Program in Physics

Submitted to the Graduate School of
Pure and Applied Sciences
in Partial Fulfillment of the Requirements
for the Degree of Doctor of Philosophy in
Science

at the
University of Tsukuba

Abstract

The universe is started from the Big-Bang. It is expected that the state which quarks and gluons move freely has existed about $10 \mu s$ after Big-Bang, and it is called as “Quark Gluon Plasma (QGP)”. Studying QGP is expected to be very helpful to understand the development of universe. The unique method to create QGP experimentally is high energy heavy ion collision (HIC). Studying the property of QGP has been carried out by the PHENIX experiment at Relativistic Heavy Ion Collider (RHIC) in Brookhaven National Laboratory (BNL) since 2000.

The collision in HIC is called Little-Bang. It is expected that the QGP expands as soon as it is created with cooling, phase transition occurs, then hadrons are emitted. On the other hand, photons are created during all stages of the collisions. Additionally, they do not interact strongly due to their properties of charge-less and color-less. It is expected that photon analysis is more sensitive to the time evolution of the QGP than that of hadron analysis.

Direct photons which are all photons except those originating from hadron decays have been studied actively. It is a challenge to identify their sources when we analyze them. The photon p_T spectra and elliptic flow (v_2) have been measured at PHENIX experiment. From the p_T spectra measurements, it is found that the p_T spectra in Au + Au collisions are enhanced less than 4 GeV/ c compared to that in p + p collisions after scaling by the number of binary collisions. Effective temperature is obtained at about 240 MeV and it is found that photons are emitted from very hot medium in early time of the collisions. In contrast, it is observed that photon has large elliptic flow and the magnitude is comparable to hadron v_2 in low p_T region. Because it is expected that an enough expansion time is required in order to get a large v_2 , it is naively suggested that the observed low p_T photons are emitted at later stages of the collisions. These two observations of photon p_T spectra and v_2 are in contradiction between two scenarios, whether these photons are really from the early stage or in fact from the later stage. It is called as a photon puzzle and it has not yet been well understood. It is introduced that several model calculations that can explain one of these two observations, however, there is no model which can explain simultaneously the both of excess of p_T spectra and large v_2 . Direct photon higher order azimuthal anisotropy (v_3 and v_4) is studied in order to disentangle various different model assumptions, scenarios and to get an additional constraint on photon production mechanisms.

The v_2 , v_3 , and v_4 of neutral pion are measured up to 15 GeV/ c with event plane determined by several forward detectors. In high p_T region, it is found that neutral pion v_2 and v_4 are positive in all centrality while v_3 varies from positive to negative at high p_T especially in peripheral event. Since hadrons in high p_T region are mainly originated from jet fragmentation, high p_T single particles v_n are useful to study jet properties in HIC. It is studied that the jet contribution to measured v_n by AMPT simulation. The jet path length dependence of energy deposit has been studied by measuring v_2 of high p_T hadron. Because di-jet makes v_3 small and third order of initial geometrical anisotropy is smaller than second order, v_3 of high p_T hadron needs to be investigated more precisely in order to understand their detailed dependencies. The behavior of v_3 of high p_T hadron could be understood qualitatively by superposition of path length dependence of jet energy-loss, di-jet effect, and jet-bias effect in determination of event plane. The v_4 of high p_T particles is similar to the behavior of v_2 , and it could be understood that it is given by the geometrical asymmetry of the QGP and energy loss of parton inside the QGP.

The v_2 , v_3 , and v_4 of direct photon are measured up to 15 GeV/ c . It is observed that the

strength of photon v_3 at around 2 GeV/ c is comparable to that of hadron, which is similar to the case of v_2 . These results prefer the scenario of that the photon in low p_T region are mostly emitted from late stage after the sizable azimuthally anisotropic and collective expansion. In high p_T region, it is found that v_2 , v_3 , and v_4 of direct photon are close to zero and it could be consistent with the expectation that the dominant fraction of photons is originated from the prompt photons in high p_T regions.

The ratio of v_2 to v_3 is compared with hydrodynamical model calculations. It is found that the model calculation with MCGlb+ $\eta/s(0.08)$ describes the ratio of photon well while that of charged pion is better described by another set of parameters with MCKLM+ $\eta/s(0.20)$.

Photon p_T spectra and v_n are predicted as massless particle by the parameters determined by blast wave model fitting to hadron observables, if those photons are really emitted during the freeze-out stage. It is found that p_T spectra is well described with the combination of low temperature and large radial flow as well as that of high temperature and no radial flow. It is naturally expected in the collective expansion scenario that there would be no azimuthal anisotropy (zero v_n) if radial flow does not exist. Blast wave model suggests that radial flow is needed to be taken into account in order to understand photon puzzle.

The thermal photon p_T spectra and v_n are calculated with blue shift correction. It is assumed that the temperature, acceleration, and azimuthal anisotropy of medium vary with expansion time. The photon observables are calculated by integrating over the expansion time. The time dependence of these variables are constrained so that the effective temperature and v_n are well described. This calculation indicates that the high effective temperature and large v_n are reproduced with the blue shift correction given by the large expansion velocity during the freeze-out. It is obtained that the true temperature during the photon emission is within 120 to 160 MeV and photons from close to the end of hadronic freeze-out are dominant. Additionally, photon v_n is calculated from thermal photons and pQCD based photons. However it is observed that there is difference between experimental measurement and this calculation from 2 to 5 GeV/ c . It also suggests that the photons originated from the other sources coming from jet energy loss inside of QGP and/or possible modification of jet fragmentation are dominant within 2 to 5 GeV/ c .

In this thesis, neutral pion and direct photon v_2 , v_3 , and v_4 are measured in Au+Au $\sqrt{s_{NN}} = 200$ GeV collisions at RHIC-PHENIX experiment. In the case of neutral pion v_n , it is found that the behavior of v_n in high p_T could be understood by the jet effect; path length dependence of energy loss and jet bias on event plane determination. It is found that the direct photon v_n is close to zero in high p_T region, and it is consistent with the expectation that the prompt photons are dominant and they have small interaction in QGP as also observed as $R_{AA} \sim 1$ for direct photon. In low p_T region, it is observed that photons have non zero and positive v_3 which is similar to the case of v_2 . Blast wave model suggests that a possible explanation of photon puzzle could be the radial flow effect. The high effective temperature and large v_n could be achieved as a consequence of Doppler (blue) shift caused by a large radial flow. The extracted temperature of photon emission source is as low as 120 \sim 160 MeV and photons at close to the end of hadronic freeze-out are dominant. It also indicates that the photons originated from the other additional sources such as modification of jet fragmentations and redistribution of the lost energy coming from the energy loss inside QGP could be existing around 2 to 5 GeV/ c .

Contents

Acknowledgement	XVI
1 Introduction	1
1.1 Quantum Chromodynamics and Quark Gluon Plasma	1
1.2 High Energy Heavy Ion Collider	2
1.2.1 Time Space Evolution of Heavy Ion Collision	4
Pre-equilibrium: $0 < \tau < \tau_0$	4
QGP phase and hydrodynamical evolution: $\tau_0 < \tau < \tau_f$	4
Freeze-out and Hadron Gas phase: $\tau_f < \tau$	5
1.2.2 Geometry of Heavy Ion Collision	5
1.3 Experimental Observables	6
1.3.1 Initial Energy Density and Bjorken Picture	6
1.3.2 Particle Ratio and Chemical Temperature	7
1.3.3 Transverse Mass Distribution and Radial Flow	7
1.3.4 Azimuthal Anisotropy	8
1.4 Direct Photon	10
1.4.1 Photon Production Process	12
Prompt Photons	13
Thermalized Photons from QGP and Hadron Gas	13
Photons originated from the interaction between hard parton and the medium	13
1.4.2 Excess of the direct photon	15
1.4.3 p_T spectra	16
1.4.4 Elliptic flow	16
1.4.5 Direct photon puzzle	17
Radial flow effect to effective temperature	18
Strong magnetic field effect	18
1.4.6 Direct photon measurement in LHC	18
1.4.7 Model prediction of direct photon azimuthal anisotropy	19
1.5 Thesis Motivation	20
2 Experiment	21
2.1 Relativistic Heavy Ion Collider	21
2.2 PHENIX Experiment	22
2.3 PHENIX magnet system	22

2.4	Characterization Detectors	23
2.4.1	Zero Degree Calorimeter	23
2.4.2	Beam Beam Counter	25
2.4.3	Muon Piston Calorimeter	25
2.4.4	Reaction Plane Detector	26
2.5	Central Arm Detectors	27
2.5.1	Pad Chamber	27
2.5.2	Electromagnetic Calorimeter	27
	Lead-scintillator calorimeter	28
	Lead-glass calorimeter	30
2.5.3	Data Acquisition System	32
	Front End Electronics	32
	Data Collection Modules	33
	Event Builder	33
	Event Trigger	33
3	Analysis	34
3.1	Event Selection	34
3.1.1	Centrality Determination	34
3.2	Event Plane Determination	36
3.2.1	Azimuthal Distribution of Emitted Particles	36
3.2.2	Event Plane Determination	37
3.2.3	Event Plane Calibration	38
3.2.4	Event Plane Resolution	38
3.3	Photon Selection	39
3.3.1	EMCal Clustering	39
	Cluster energy measurement	40
	Correction for E_{core}	41
	Cluster position measurement	42
3.3.2	Photon identification	43
	Bad tower rejection	43
3.3.3	Shower shape cut	44
3.3.4	Charged Particle Rejection	45
3.4	Inclusive photon v_n measurement	45
3.4.1	Inclusive photon v_n measurement	45
3.4.2	Systematic uncertainties	46
	Photon PID selections	47
	Difference between different measurement methods	47
	Event Plane definition	48
3.5	π^0 v_n measurement	49
3.5.1	π^0 selection	49
3.5.2	π^0 v_n measurement	51
3.5.3	Systematic uncertainties	52
	Photon selection dependence	52

	π^0 extraction dependence	52
3.6	Decay photon v_n	56
3.6.1	The p_T spectra of meson and decay photon	57
3.6.2	The v_n of meson and decay photon	59
3.6.3	Systematic uncertainties	61
	p_T spectra dependence	62
	Propagated from systematic uncertainty of pion v_n	62
	Propagated from input v_n	63
	Systematic uncertainty	65
3.7	Direct Photon v_n Measurement	65
4	Results	67
4.1	The results of inclusive photon v_n with RxN(I+O) event plane	67
4.1.1	Comparison with conversion photon method	67
4.2	The results of neutral pion v_n with RxN(I+O) event plane	70
4.3	The results of direct photon v_n with RxN(I+O) event plane	72
4.3.1	Comparison with conversion photon method	72
5	Discussion	74
5.1	Neutral pion azimuthal anisotropy	74
5.1.1	Comparison of neutral pion v_n in high p_T with different event planes . . .	74
5.1.2	AMPT model calculation of pion v_n in high p_T region	77
5.2	Direct photon azimuthal anisotropy	79
5.2.1	Comparison of direct photon and neutral pion v_n	82
5.2.2	The ratio of v_2 to v_3	84
5.2.3	Comparison to model calculations	85
5.2.4	Possible solution of photon puzzle	85
	Photon observables prediction with Blast Wave Model	87
	A toy model calculation for thermal photon p_T spectra and v_n with blue shift effect	89
	The adiabatic expansion assumption	96
	Photon v_n calculations with pQCD calculations	98
	Summary for calculations	101
6	Conclusion	102
A	The results of inclusive photon v_n	104
B	The results of neutral pion v_n	110
C	The results of direct photon v_n	116

List of Figures

1.1	The summary of α_s as a function of the energy scale Q [1]. Solid lines are the pQCD calculation. The respective degree of QCD perturbation theory used in the extraction of α_s is indicated in round brackets.	2
1.2	Energy density (ε) and 3 times the pressure as a function of temperature calculated in Lattice QCD. [2]. The Stefan-Boltzmann limits is shown in the right side. . .	3
1.3	(Left) Geometry for the initial state of centrally produced plasma in nucleus-nucleus collisions [3]. (Right) $\epsilon_{Bj}\tau$ deduced from the PHENIX data at three RHIC energies [4].	6
1.4	The comparison of fit results and the particle ratio data in $\sqrt{s_{NN}}=200\text{GeV}$ Au+Au central collisions ($\langle N_{part} \rangle=322$). (Top) Horizontal lines show statistical model fit on the particle ratio. (Bottom) The difference of data to the model, $(R_{exp} - R_{model})/\Delta R_{exp}$, where R_{exp} is ratio from data, R_{model} is ratio by model calculation, and ΔR_{exp} is error of R_{exp} [5].	8
1.5	(Left) Transverse mass distributions for π^\pm , K^\pm , protons, and anti-protons for central 0-5% (top), mid-central 40-50% (middle), and peripheral 60-92% (bottom) in Au+Au collisions at $\sqrt{s_{NN}}=200\text{GeV}$ [6]. The lines on each spectra are the fitted results using exponential equation. (Right) Mass and centrality dependence of inverse slope parameters T in m_T spectra for positive (left) and negative (right) particles in Au+Au collisions at $\sqrt{s_{NN}}=200\text{ GeV}$. The dotted lines represent a linear fit of the results from each centrality bin as a function of mass using Eq. (1.21).	9
1.6	(Left) The image of the ideal nucleus and nucleus collisions. (Right) The image of the realistic nucleus and nucleus collisions.	11
1.7	The results of azimuthal anisotropy v_n of charged particle measured in PHENIX experiment [7]. Black is $v_2(\Psi_2)$, red is $v_3(\Psi_3)$, and blue is $v_4(\Psi_4)$	11
1.8	(Left) The results of particle identified (π^\pm , K^\pm and p/\bar{p}) azimuthal anisotropy v_n [8]. (Right) The results of the number of constituent quark scaling for v_n as a function of KE_T . Red are charged pion, blue is charged kaon, and black are proton.	12
1.9	Feynman diagrams of prompt photon production mechanisms. (a) : Quark-gluon Compton scattering, (b) : Annihilation between quark and anti-quark, (c) : Bremsstrahlung, (d) : Gluon fusion.	13

1.10	(a) Direct photon p_T spectra with NLO pQCD calculation for three theory scales, μ [9]. (b) Comparison to NLO pQCD calculation for $\mu=p_T$, with upper and lower curves for $\mu=p_T/2$ and $2p_T$	14
1.11	Comparison of direct photon p_T spectra from different photon sources [10]. Blue line shows photon radiated from hadron gas, red line is photons emitted from QGP, green line is primordial photon, violet line is total of photons, and black points are PHENIX data.	14
1.12	Feynman diagrams of photon production mechanisms in hadron gas. (a) : $\pi + \pi \rightarrow \rho + \gamma$ (b) : Hadron interaction (c) : meson-meson Bremsstrahlung.	15
1.13	The excess of direct photon R_γ as a function of p_T measured by calorimeter (blue), virtual photon (red), and external conversion photon method (green).	15
1.14	(Left) Direct photon p_T spectra measured in Au+Au and p+p 200 GeV collisions [11, 12]. (Right) Direct photon R_{AA} measured in PHENIX experiment. Blue is R_{AA} measured in calorimeter method, red (black) is R_{AA} measured by virtual photon method in Au+Au (d+Au) collisions, respectively.	16
1.15	The v_2 of π^0 (a), inclusive photon (b), direct photon (c) as a function of p_T [13]. Red (Black) points are measured with respect to event plane reconstructed by Reaction Plane detector (BBC).	17
1.16	Inverse slope temperature as a function of a function of temperature in Au+Au collisions at RHIC 0-20% centrality (left) and in Pb+Pb collisions at LHC 0-40% centrality (right) [14]. Vertical axis is the inverse slope of exponential, and horizontal axis is true temperature. Red (white) points are simulated from equilibrium thermal emission rates (hydrodynamic simulation), respectively. Horizontal blue line shows the experimental results.	18
1.17	(Left) The coupling of the conformal anomaly to the external magnetic field resulting in photon production. Photon is produced by the trace of the energy-momentum tensor (θ_μ^μ) and magnetic field makes photon. (Right) The azimuthal anisotropy v_2 of the direct photons for different values of bulk viscosity corresponding to C_ξ in the range of $2.5 \div 5$ calculated for minimum bias Au+Au collisions.	19
1.18	Direct photon p_T spectra (left) and second order azimuthal anisotropy (right) as a function of p_T in $\sqrt{s_{NN}}=2.76$ TeV Pb+Pb collisions at LHC-ALICE experiment [15, 12]. Non zero positive v_2 is found and it is similar trend with it is seen in RHIC-PHENIX experiment.	19
1.19	(Left) p_T -differential v_2 and v_3 calculated with event-by-event viscous hydrodynamic simulations from MCGlb or MCKLM [16]. (Right) The ratio of v_2 to v_3 of thermal photon and thermal charged pion. Both calculations are carried out for 0-40% centrality in $\sqrt{s_{NN}}=2.76$ TeV Pb+Pb collisions.	20
2.1	The PHENIX detectors operated in 2007 RHIC run period. (Left) The central arm detector with several types of spectrometers from beam view. (Right) The side view of the PHENIX detectors.	22

2.2	(Left) Line drawings of the PHENIX magnets, shown in perspective and cut away to show the interior structures. Arrows indicate the beam line of the colliding beams in RHIC. (Right) Vertical cutaway drawing of central and north muon magnets showing the coil positions for both magnets [17].	24
2.3	Mechanical design of the production tungsten modules [18].	24
2.4	(a) Single BBC consisting of 1 in mesh dynode photomultiplier tubes mounted on a 3 cm quartz radiator, (b) A BBC array comprising 64 BBC elements, (c) The picture of BBC mounted on the PHENIX detector [19].	25
2.5	(Left) The design of the MPC. (Right) The picture of MPC South [20].	26
2.6	(Left) Schematic diagram illustrating the arrangement of the inner (red) and outer (blue) scintillator rings. The length of each scintillator side is shown in centimeters. (Right) The picture of the RxN's north half installed on the Cu nosecone of PHENIX's central magnet prior to the installation of the HBD [21].	27
2.7	Interior view of a Pb-scintillator calorimeter module showing a stack of scintillator and lead plates, wavelength shifting fiber readout and leaky fiber inserted in the central hole [22].	28
2.8	Pb-scintillator EMCal energy linearity measured in beam test at AGS (left) and SPS (right). The residual (calorimeter measured energy loss the beam energy, divided by the beam energy) is for the 5×5 tower energy sum. The solid lines show total systematic uncertainties in the analysis [22].	29
2.9	Pb-scintillator EMCal energy resolution obtained by beam tests at AGS and SPS. The blue dashed line shows a fit to the linear formula $\sigma(E)/E=1.2\%+6.2\%/\sqrt{E(\text{GeV})}$. The red dashed-dotted line shows the fit to the quadratic formula $\sigma(E)/E=2.1\%\oplus 8.1\%/\sqrt{E(\text{GeV})}$	30
2.10	Exploded view of a Lead-Glass detector supermodule [22].	31
2.11	PbGl energy resolution as a function of the incident energy. The marker style indicates the difference of incident angle. Energy resolution is $\sigma(E)/E = (0.8 \pm 0.1)\% \oplus (5.9 \pm 0.1)\%/\sqrt{E(\text{GeV})}$ [22].	31
2.12	Schematic diagram of the PHENIX on-line system [23].	32
3.1	(Left) The charge sum distribution in BBC South (blue) and the <i>NBD</i> fitting (red) [24]. (Right) The ratio of data to the <i>NBD</i> equation.	35
3.2	The event plane angle distributions of RxN(I+O) in 10-20% centrality. (Blue) The event plane angle with no correction. (Green) The distribution of event plane after re-centering. (Ref) The distribution of event plane after flattening.	38
3.3	(Top) The event plane angle correlation between North and South subdetectors. (Bottom) The event plane resolution of the detector combining South and North.	40
3.4	The example of predicted shower energy fraction in towers under assuming that a photon hits on the center of tower perpendicularly. The core clusters formed by the towers contained more than 2% of total energy. The cluster is surrounded by dotted line [25].	41

3.5	The resolution distributions of reconstructed photon energy studied by using GEANT simulation. The ratio of core energy E_{core} (dashed line) and total energy E_{tot} (solid line) to the true photon energy (E_{org}) on the simple gaussian distribution with intrinsic EMCal energy resolution for 0.5, 1.0, and 4.0 GeV photons [25].	42
3.6	(Left) Definitions of impact angle and vector of (v_x, v_y, v_z) . (Right) The hit position correction from energy gravity to true position. The amplitude of deposit energy is represented by shaded gray area [25].	43
3.7	Hit distribution per tower in sector 1. Dotted line shows the fitted gaussian equation. The towers out of 5σ denote as bad towers [25].	44
3.8	χ^2 distribution for showers induced by 2 GeV/ c electrons and pions in the Pb-scintillator calorimeter. The arrow marks the χ^2 cut corresponding to 90% electron efficiency [25].	45
3.9	Inclusive photon yield distribution as a function of $ \Delta\phi = \phi - \Psi_n $ with 4 p_T selections. Top figures are distributions with respect to the second order event plane and bottom figures are with respect to the third order of event plane. The solid lines show the fitting results of a Fourier function.	46
3.10	(Top) Inclusive photon v_n measured by method 1, method 2 and averaged v_n . (Bottom) The deviation of v_n between method 1 and method 2.	47
3.11	(Top) : Inclusive photon v_2 , v_3 , and v_4 with several photon selections (open). Black solid points are v_n with nominal selections. (Bottom) : Δv_n of difference between each v_n and mean v_n as a function of p_T . Systematic uncertainty is defined as averaging within $1 < p_T < 1.5$, $1.5 < p_T < 2.5$, $2.5 < p_T < 5.5$, and $5.5 < p_T < 15$ GeV/ c	48
3.12	(Top) The v_2 , v_3 , v_4 , and $v_4(\Psi_2)$ of charged particle with event plane measured by each detector. (Bottom) The ratio of each v_n to the average of v_n and defined systematic uncertainties.	48
3.13	(a): π^0 invariant mass distribution which is combined two photons in same event (blue histogram) and mixed event (red histogram). (b): π^0 invariant mass distribution after subtracting mixed event. Green histogram shows the linear function to estimate residual background. (c): π^0 invariant mass distribution after subtracting residual background.	51
3.14	π^0 yield distribution as a function of $ \Delta\phi = \phi - \Psi_n $ with 4 p_T selections. The solid lines show the fitting results of a Fourier function.	52
3.15	Systematic uncertainty of neutral pion v_n estimated from photon selections. (Top) : (open) π^0 v_2 , v_3 , v_4 with several photon selections. (solid) v_n with nominal photon selection. (Bottom) : Δv_n as a function of p_T and systematic uncertainty are shown. Systematic uncertainty of photon selection is defined as the average of these deviations within 4 p_T region, $1 < p_T < 1.5$, $1.5 < p_T < 2.5$, $2.5 < p_T < 5.5$, and $5.5 < p_T < 15$ GeV/ c	53

3.16	Systematic uncertainty of neutral pion v_n estimated from normalization of background distribution. (Top) : (open) π^0 v_2 , v_3 , and v_4 with several normalized range of background distribution. (solid) v_n with nominal normalization of background distribution. (Bottom) : Δv_n as a function of p_T . Systematic uncertainty of normalization of background distribution is defined as the average of these deviations within 4 p_T region, $1 < p_T < 1.5$, $1.5 < p_T < 2.5$, $2.5 < p_T < 5.5$, and $5.5 < p_T < 15$ GeV/ c	55
3.17	(Top) : π^0 signal range dependence of π^0 v_2 , v_3 , and v_4 . (Bottom) : Δv_n as a function of p_T . Black solid points are estimated systematic uncertainties.	56
3.18	(Top) Pion p_T spectra fitted by the Eq. (3.44), and obtained parameters. (Middle) The comparison of meson p_T spectra between experimental results [6, 26, 27, 28] and meson p_T spectra estimated with m_T scaling. (Bottom) The ratio of meson p_T spectra of experimental results to estimated p_T spectra.	59
3.19	(Left):Simulated decay photon p_T spectra. (Right):Contribution ratio of decay photon from each hadron to all decay photon.	59
3.20	Charged pion and neutral pion v_2 , v_3 , and v_4 are combined with the F(p_T) equation, and F(p_T) equation is shown in right. Charged pion v_n are taken from [8].	60
3.21	v_2 , v_3 , and v_4 of η , ω , ρ , and η' estimated from pion v_n by KE_T scaling.	60
3.22	v_2 , v_3 , and v_4 of all combined decay photon and each hadronic decay photon. . .	61
3.23	(Top) Decay photon v_2 (left), v_3 (middle), and v_4 (right) with event plane measured by RxN(I+O) in 0-20% centrality bin. (Bottom) The systematic uncertainty estimated from decay photon spectra.	62
3.24	(Top) Decay photon v_2 (left), v_3 (middle), and v_4 (right) with event plane measured by RxN(I+O) in 0-20% centrality bin. (Bottom) The systematic uncertainty propagated from systematic uncertainty of neutral pion v_n	63
3.25	The difference of input pion v_n between the parameters in connection equation.	63
3.26	The neutral pion v_2 , v_3 , and v_4 are fitted by the equations. Red lines are utilized as an input for decay photon v_n simulation.	64
3.27	(Top) Decay photon v_2 (left), v_3 (middle), and v_4 (right) with event plane measured by RxN(I+O) in 0-20% centrality bin. (Bottom) The systematic uncertainty estimated from the shape of input of pion v_n dependence.	64
3.28	(Top) Decay photon v_2 , v_3 , and v_4 with statistical error. (Bottom) Systematic uncertainty from each components (blue, green, red, orange) and summed systematic uncertainty (black).	65
3.29	The R_γ as a function of p_T , where green points show that measured by calorimeter [29], and green points show that measured by external conversion photon method [30], red points show that measured via virtual photon [11].	66
4.1	The results of inclusive photon v_2 (RxN(I+O)) with 10% centrality interval. . .	68
4.2	The results of inclusive photon v_3 (RxN(I+O)) with 10% centrality interval. . .	68
4.3	The results of inclusive photon v_4 (RxN(I+O)) with 10% centrality interval. . .	69

4.4	Inclusive photon v_2 (top) and v_3 (bottom) measured by calorimeter (blue) and conversion photon method (green), respectively. The results of conversion photon method are preliminary on PHENIX.	69
4.5	The results of neutral pion v_2 (RxN(I+O)) with 10% centrality interval.	70
4.6	The results of neutral pion v_3 (RxN(I+O)) with 10% centrality interval.	70
4.7	The results of neutral pion v_4 (RxN(I+O)) with 10% centrality interval.	71
4.8	The results of direct photon v_2 (RxN(I+O)) with 20% centrality interval.	72
4.9	The results of direct photon v_3 (RxN(I+O)) with 20% centrality interval.	72
4.10	The results of direct photon v_4 (RxN(I+O)) with 20% centrality interval.	73
4.11	Direct photon v_2 (top) and v_3 (bottom) measured by calorimeter (black) and conversion photon method (green), respectively. The direct photon v_n with external conversion method is extracted decay photon v_n (Section 3.6) from inclusive photon v_n (Figure 4.1.1).	73
5.1	Neutral pion v_2 , v_3 , and v_4 with event plane measured by RxN(In)+MPC (blue) and RxN(Out) (red) with 10% centrality steps from 0 to 60%.	75
5.2	Integrated v_2 (left), v_3 (middle), and v_4 (right) of neutral pions within $6 < p_T < 15$ GeV/ c as a function of $\langle N_{part} \rangle$ with respect to the RxN(In)+MPC (blue) and RxN(Out) (red).	76
5.3	Comparison of experimental π^0 v_2 , v_3 with RxN(In)+MPC (blue) and RxN(Out) (green), and simulated pion v_2 , v_3 with RxN(In)+MPC (red) and RxN(Out) (violet). Comparison of π^0 v_2 , (left) v_3 (middle), and v_4 (right) as a function of p_T in 40-60% centrality.	77
5.4	(a) The p_T distribution in the region of $1 < \eta < 2.8$ corresponding to the acceptance of RxN(I+O) detector. Panel (b), (c), and (d) show the second, third, and forth order event plane resolution. Event plane is estimated by the particles in the region of $p_T < 2$ GeV/ c (blue), $2 < p_T$ GeV/ c (red), and all particles (green).	78
5.5	The pion v_2 (top), v_3 (middle), and v_4 with p_T selected event plane. Black points are experimental measurement, blue points are v_n with event plane defined by particles less than 2 GeV/ c , and red points are v_n with event plane estimated from particles larger than 2 GeV/ c	78
5.6	The integrated v_2 (top) and v_3 (bottom) as a function of $\Delta\eta$. Event plane is estimated by the particles in the region of $p_T < 2$ GeV/ c . $\Delta\eta$ is the difference between the event plane and the region of measuring the pion angle. The v_n within $0 < p_T < 2$ (blue), $2 < p_T < 5$ (green), and $5 < p_T < 10$ GeV/ c (red).	80
5.7	The integrated v_2 (top) and v_3 (bottom) as a function of $\Delta\eta$. Event plane is estimated by the particles in the region of $p_T > 2$ GeV/ c . $\Delta\eta$ is the difference between the event plane and the region of measuring the pion angle. The v_n within $0 < p_T < 2$ (blue), $2 < p_T < 5$ (green), and $5 < p_T < 10$ GeV/ c (red).	81
5.8	The image of the v_n with affected by particles fragmented from jet from side view (a) and beam view (b). Jet biasing on determining event plane (red) and away side jet (blue). Biased 2nd order event plane (orange) and 3rd order event plane (green).	82

5.9	Direct photon and neutral pion v_2 (top), v_3 (middle), and v_4 (bottom) with RxN(I+O) event plane.	83
5.10	Integrated v_2 (left), v_3 (middle), and v_4 (right) within $6 < p_T < 10$ GeV/ c of direct photon and neutral pion with RxN(I+O) event plane.	83
5.11	The ratio of v_2 to v_3 of direct photon (black) and charged pion [8] (red). Theoretical curves are calculated with hydrodynamic model [16, 31].	84
5.12	Comparison of direct photon v_2 with model calculations. Blue (red) lines are photon v_2 calculating with expanding elliptic fireball from thermal and non-thermal photons, and non-thermal photon is estimated by pQCD calculations (fit to the experimental data in PHENIX experiment) [10]. Orange line are calculated by PHSD transport model [32]. Cyan (pink) lines are calculated with initial condition calculated by Monte Carlo Glauber (KLN), and hydrodynamical simulation is started from $\tau_0 = 0.6$ fm/ c to $T = 120$ MeV with $\eta/s=0.08$ (0.20) [16]. Violet line is calculated with initial condition calculated with optical Glauber model and evolved 3+1D hydrodynamical simulations [33].	86
5.13	Comparison of direct photon v_2 and v_3 in 20-40% centrality bin with model calculations. Blue (red) lines are photon v_2 calculating with expanding elliptic fireball from thermal and non-thermal photons, and non-thermal photon is estimated by pQCD calculations (fit to the experimental data in PHENIX experiment) [10]. Orange line are calculated by PHSD transport model [32]. Cyan (pink) lines are calculated with initial condition calculated by Monte Carlo Glauber (KLN), and hydrodynamical simulation is started from $\tau_0 = 0.6$ fm/ c to $T = 120$ MeV with $\eta/s=0.08$ (0.20) [16]. Violet line is calculated with initial condition calculated with optical Glauber model and evolved 3+1D hydrodynamical simulations [33]. Dark violet line is calculated photon v_2 in a magnetic field, and it shows upper bound for photon v_2 [34].	86
5.14	(Top) The p_T spectra (left), v_2 (middle), and v_3 (right) of identified charged particle ($\pi^\pm, K^\pm, p\bar{p}$) [8, 6]. The thick lines are the blast wave functions obtained by fitting, and thin lines are extrapolations. (Bottom) The p_T spectra [30] (left), v_2 (middle), and v_3 (right) of direct photon. Black lines are predicted photon observables. Orange, red, and violet lines are predicted lines with freeze-out temperature $T_f=104, 240, \text{ and } 300$ (MeV) with zero radial expansion $\langle\rho\rangle=0$	88
5.15	The time dependence of temperature (top left), normalized yield (top middle), acceleration (bottom left) velocity (bottom middle), and azimuthal anisotropy (0-20%, $p_T=2.135$ GeV/ c) (bottom right) of the photon sources. Blue line is the time dependence of the apparent temperature.	91
5.16	The photon p_T spectra (left), v_2 (middle), and v_3 (right) in 0-20 % centrality bin. The experimental measurement of p_T spectra is taken from [30]. The calculations of p_T spectra are scaled so that they are consistent with the experimental measurement at 1 GeV/ c . The red (blue) lines are the calculations with (without) blue shift correction. The effective temperature is obtained by exponential equation fitting in the range of $0.6 < p_T < 2$ GeV/ c	91

5.17	The time dependence of temperature (top left), yield (top middle), probability (top right), acceleration (bottom left) velocity (bottom middle), and azimuthal anisotropy (0-20%, $p_T=2.135$ GeV/c) (bottom right) of the photon sources. The color shows the difference of α in Eq. (5.17).	92
5.18	The thermal photon p_T spectra (left), the v_2 (middle), and v_3 (right) depending on acceleration development. The color shows the difference of α in Eq. (5.17). Effective temperature is obtained via fitting by exponential equation in the region of $0.6 < p_T < 2$ GeV/c.	93
5.19	The time dependence of the yield of photon and the probability density. The color shows the difference of b in Eq. (5.18).	93
5.20	The thermal photon p_T spectra (left), v_2 (middle), and v_3 (right) depending on the photon yield. The color shows the difference of b in Eq (5.18). Effective temperature is obtained via fitting by exponential equation in the region of $0.6 < p_T < 2$ GeV/c.	93
5.21	The time dependence of temperature (left), velocity (middle), and azimuthal anisotropy (0-20%, $p_T=2.135$ GeV/c) (right) of the photon sources. The color shows the difference of c in Eq. (5.19).	94
5.22	The thermal photon p_T spectra (left), the v_2 (middle), and v_3 (right) depending on azimuthal anisotropy development. The color shows the difference of c in Eq (5.19). Effective temperature is obtained via fitting by exponential equation in the region of $0.6 < p_T < 2$ GeV/c.	94
5.23	The difference of effective temperature (σT_{eff}) and v_2 (σv_2) between calculations and experimental measurement. (Black) The difference obtained from the basic assumption. (Blue) The α controls the time dependence of acceleration. (Green) The b controls the time dependence of yield. (Red) The c controls the time dependence of v_n	95
5.24	(Left) The b dependence in yield component on the difference of effective temperature between calculations and experiment measurement. (Middle) The c dependence in azimuthal anisotropy component for v_2 on the difference between calculations and experiment measurement. (Right)) The c dependence in azimuthal anisotropy component for v_3 on the difference between calculations and experiment measurement. Blue (green) line is calculated with the limitation of $\alpha \rightarrow 0$ (∞). Solid black line indicates σT_{eff} , $\sigma v_n=0$ and dotted lines indicate the limitation within 1σ	96
5.25	The calculation results of p_T spectra, v_2 , and v_3 . Black points are the results of direct photon v_n in 0-20 % centrality interval.	97
5.26	The time dependence of temperature, normalized yield, acceleration, velocity, and anisotropy. Black line in temperature is the time dependence of true temperature.	97
5.27	The time dependence of velocity (a), radius (b), volume (c), true temperature (d), temperature corrected by blue shift effect (e), and azimuthal anisotropy (f). The difference of line color is defined by b in Eq. (5.32) and (5.33).	99
5.28	The photon p_T spectra (left), v_2 (middle), and v_3 (right). The difference of line color is defined by b in Eq. (5.32) and (5.33). The effective temperature is obtained by fitting via exponential equation in the region of $0.6 < p_T < 2$ GeV/c.	99

5.29	Direct photon p_T spectra in 0-20% centrality taken from [30]. (a) Direct photon p_T spectra in Au+Au collisions. (b) Photon p_T spectra estimated from $p + p$ collisions by the number of binary collisions (pQCD photon). (c) The p_T spectra after subtraction of scaled $p + p$ collisions (Thermal photon). (d) The ratio of the number of thermal photon to that of thermal and pQCD photons.	100
5.30	The direct photon v_2 (left) and v_3 (right). Dotted lines are predicted thermal photon v_n shown in Figure 5.14 (red) and 5.25 (blue). Solid lines are all photons v_n calculated with Eq. (5.37).	101
A.1	The results of inclusive photon v_2 , v_3 , and v_4 (RxN(In)) with 10% centrality interval.	105
A.2	The results of inclusive photon v_2 , v_3 , and v_4 (RxN(Out)) with 10% centrality interval.	106
A.3	The results of inclusive photon v_2 , v_3 , and v_4 MPC with 10% centrality interval.	107
A.4	The results of inclusive photon v_2 , v_3 , and v_4 BBC with 10% centrality interval.	108
A.5	The results of inclusive photon v_2 , v_3 , and v_4 RxN(In)+MPC with 10% centrality interval.	109
B.1	The results of neutral pion v_2 , v_3 , and v_4 (RxN(In)) with 10% centrality interval.	111
B.2	The results of neutral pion v_2 , v_3 , and v_4 (RxN(Out)) with 10% centrality interval.	112
B.3	The results of neutral pion v_2 , v_3 , and v_4 MPC with 10% centrality interval.	113
B.4	The results of neutral pion v_2 , v_3 , and v_4 BBC with 10% centrality interval.	114
B.5	The results of neutral pion v_2 , v_3 , and v_4 RxN(In)+MPC with 10% centrality interval.	115
C.1	The results of direct photon v_2 , v_3 , and v_4 (RxN(In)) with 20% centrality interval.	117
C.2	The results of direct photon v_2 , v_3 , and v_4 (RxN(Out)) with 20% centrality interval.	118
C.3	The results of direct photon v_2 , v_3 , and v_4 (MPC) with 20% centrality interval.	119
C.4	The results of direct photon v_2 , v_3 , and v_4 (BBC) with 20% centrality interval.	120
C.5	The results of direct photon v_2 , v_3 , and v_4 (RxN(In)+MPC) with 20% centrality interval.	121

List of Tables

1.1	The summary of high heavy ion collision experiments.	3
2.1	The summary of PHENIX detectors [35].	23
3.1	The summary of relations between the centrality and the parameters of $\langle N_{part} \rangle$, $\langle N_{coll} \rangle$, impact parameter $\langle b \rangle$ [36].	35
3.2	This is the table of tested photon selection. Boldface is the nominal selection. . .	47
3.3	The summary of systematic uncertainty for inclusive photon $v_n(\text{RxN(I+O)})$ from photon selection. They are absolute value (Δv_n).	49
3.4	The summary of systematic uncertainty for inclusive photon $v_n(\text{RxN(I+O)})$ from measurement method. They are absolute value (Δv_n).	50
3.5	The table of systematic uncertainty of Event Plane definition.	51
3.6	This is the table of tested photon selections. Boldface is the nominal selection. The 6 pattern selections are tested to estimate systematic uncertainty of $\pi^0 v_n$ from “Photon selection dependence”.	53
3.7	The summary of systematic uncertainty for neutral pion $v_n(\text{RxN(I+O)})$ from photon selection. They are absolute value (Δv_n).	54
3.8	Invariant mass range to calculate normalization of mixed event background to foreground distribution. The 4 patterns of normalized range are considered to estimate systematic uncertainty of $\pi^0 v_n$	55
3.9	The 4 pattern of π^0 counting range are performed to evaluate systematic uncertainty of $\pi^0 v_n$	56
3.10	The summary of systematic uncertainty for neutral pion $v_n(\text{RxN(I+O)})$ from π^0 extraction dependence. They are absolute value (Δv_n).	57
3.11	Summary of meson properties, such as invariant mass, branching ratio to photons, from PDG [1].	58
3.12	The table for the spectra ratio of each meson to π^0 [37, 28, 38].	58
5.1	The summary of χ^2 taken from Figure 5.11.	84
5.2	Parameters of blast wave function obtained by fitting to p_T spectra and v_n of identified charged particle [8, 6]. T_f is kinetic freeze-out temperature, $\langle \rho \rangle$ is the average transverse rapidity, ρ_n and s_n are the transverse rapidity and spacial density anisotropy.	88

- 5.3 The summary of true temperature and average emission time. Lower (upper) limit of true temperature is determined by $\alpha = 0$ (∞). Lower (upper) limit of average emission time is determined by $\alpha = \infty$ (0). The time of freeze-out is defined as 1. 97

Acknowledgements

I would like to express my appreciation to Prof. Yasuo Miake for inviting me to the field of high energy heavy ion collision physics and giving sound advices to my analysis. I am also grateful to Prof. ShinIchi Esumi for giving me continuous encouragements and supporting my activities in my college life. I appreciate Prof. Tatsuya Chujo for his advices for the analysis and for the work in BNL. I would like to thank Prof. M. Inaba for his professional advices about the detector. I also would like to thank Prof. H. Masui for his insightful advices and careful reading of my thesis. I received generous supports from Mr. S. Kato for arranging computer system at Tsukuba. I also grateful to Prof. Akira Ozawa for his careful reading my thesis and giving useful comments and suggestions.

I would like to express my thanks to all the member of the high energy nuclear physics group at University of Tsukuba. I would like to thank Dr. M. Shimomura, Dr. Y. Ikeda, Dr. T. Niida, Dr. T. Todoroki, and Mr. H. Nakagomi for their useful discussions and supports at BNL life. I would like to express my great thanks to Dr. T. Horaguchi, Ms. H. Sakai, Mr. K. Watanabe, Dr. D. Sakata, Mr. M. Sano, Mr. H. Yokoyama, Ms. B. Jihyun, Ms. M. Kajigaya, Mr. E. Hamada, Ms. M. Kimura, Mr. Y. Sekine, Mr. S. Takauchi, Mr. Y. Watanabe, Mr. Y. Kondo, Mr. S. Kubota, Mr. H. Nakazato, Mr. R. Funato, Mr. D. Watanabe, Ms. K. Gunji, Mr. M. Horiuchi, Ms. T. Nakajima, Mr. T. Kobayashi, Mr. K. Kihara, Mr. K. Oshima, Ms. H. Ozaki, Mr. T. Nonaka, Mr. K. Yodogawa, Mr. H. Watanabe, Mr. W. Sato, Mr. R. Hosokawa, Mr. R. Aoyama, Mr. J. Lee, Ms. I. Sakatani, Mr. T. Shioya, Mr. M. Hirano, Mr. H. Yamamoto, Mr. T. Sugiura, Mr. K. Ito, Mr. B.C. Kim, Ms. S. Kudo, Ms. M. Chang, and Mr. Y. Fukuda for their friendships and useful discussions. Especially, I would like to thank to Mr. N. Tanaka for his friendships, many discussions, and supports at laboratory.

I would like to express my thanks to the staffs and students of the University of Tokyo and University of Hiroshima, especially thank to Dr. Y. Yamaguchi, Dr. R. Akimoto, Mr. H. Asano, and Mr. M. Nishashi for their helps at BNL life. I also would like to thank to Dr. K. Watanabe, Mr. T. Tsuji, and Mr. S. Hayashi for their friendships and many discussions.

I am grateful to Prof. K. Ozawa for management the PHENIX-J group for his financial support. I would like to express a deep gratitude to Dr. H. En'yo, Dr. Y. Akiba, Dr. I. Nakagawa, Dr. R. Seidl, Dr. T. Hachiya, and the other many staffs and students of the Radiation Laboratory of RHIKEN Nishina Center for their financial support and stimulating experiences as a RIKEN-JRA student.

I would like to express many thanks to the PHENIX Collaboration. I am grateful to the spokespersons, Prof. B. V. jack, Prof. J. Nagle, and Prof. D. Morrison for their arrangement and encouragement to my activity at the PHENIX. I appreciate Dr. G. David and Dr. T. Sakaguchi

for their many kinds of suggestions. I would like to thank many collaborators, Prof. J. C. Hill, Dr. P. Stankus, Dr. R. Seto, Dr. R. Victor, Prof. K. Shigaki, Prof. K. Homma, Dr. S. Huang, Prof. R. Lacey, Dr. J. C. H. Chen, Dr. J. Seele, and Dr. B. Bannier for their advises.

At last, I would like to thank my family, Takuji, Yuko, and Kurumi. I could not finish my work without their helps and understandings.

Chapter 1

Introduction

1.1 Quantum Chromodynamics and Quark Gluon Plasma

Quantum chromodynamics (QCD) is a gauge field theory that describes the strong interaction between quarks and gluons. QCD is analogous to the quantum electrodynamics (QED), which is quantum theory of describing electromagnetic interaction between charged particles. In QCD (QED), the force is mediated by gluon (photon) between quarks (charged particles), respectively. The critical difference between QCD and QED is that the photons do not carry charge due to electrically neutral, while gluons exchange color charge since they have color charge. In addition, gluons can interact among themselves due to their color charge. In QCD, a quark can take one of three color charges and an anti-quark can take one of three anti-color charges. To make it possible for quarks with different colors to interact, it is required that there are eight gluons, which are mixtures of a color and an anti-color.

The classical Lagrangian density \mathcal{L}_{cl} is given by

$$\mathcal{L}_{cl} = \bar{q}^a (i \not{D}_{\alpha\beta} - m \delta_{\alpha\beta}) q^\beta - \frac{1}{4} F_{\mu\nu}^a F_a^{\mu\nu}, \quad (1.1)$$

where m is a quark mass, q^α is the quark field with color index α which belongs to the $SU_c(3)$ triplet. The $F_{\mu\nu}^a$ is the field strength tensor of the gluon. The \not{D} is defined as $\not{D} \equiv \gamma^\mu D_\mu$ where D_μ is a covariant derivative acting on the color-triplet quark field. They are written as

$$F_{\mu\nu}^a = \partial_\mu A_\nu^a - \partial_\nu A_\mu^a - g f_{abc} A_\mu^b A_\nu^c, \quad (1.2)$$

$$D_\mu \equiv \partial_\mu + i g t^a A_\mu^a, \quad (1.3)$$

where f_{abc} is the structure constants, A_μ^a is the gluon field which belongs to the $SU_c(3)$ octet, and t^a is the fundamental representation of $SU_c(3)$ Lie algebra. The g is the dimensionless coupling constant in QCD and defined as $g \equiv \sqrt{4\pi\alpha_s}$ where α_s is the fine structure constant in strong interaction. The α_s can be defined with momentum transfer Q as

$$\alpha_s(Q^2) = \frac{1}{\beta_0 \ln(Q^2/\Lambda_{QCD}^2)}, \quad (1.4)$$

where Λ_{QCD} is called the QCD scale parameter and β_0 is defined with n_q which is the number of flavor with $2m_q < Q$ as

$$\beta_0 = \frac{33 - 2n_q}{12\pi}. \quad (1.5)$$

Figure 1.1 shows the results α_s measured by several experiments [1].

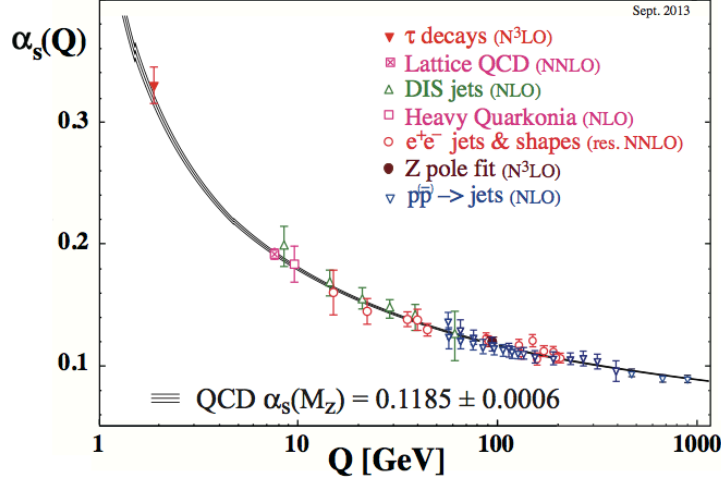


Figure 1.1: The summary of α_s as a function of the energy scale Q [1]. Solid lines are the pQCD calculation. The respective degree of QCD perturbation theory used in the extraction of α_s is indicated in round brackets.

QCD has two important characteristics of quark-gluon dynamics which are “color confinement” and “asymptotic freedom”. If momentum transfer is small (distance among partons is large), partons are strongly coupled due to large α_s . Therefore, partons are confined in hadron and it is called “color confinement”. On the other hand, when large momentum transfer Q corresponding to small distance, partons approximately move freely due to small α_s . This property is called “asymptotic freedom”.

The behavior of QCD with large momentum transfer ($Q > 1$ GeV) or short distance can be calculated with perturbative calculation method which is perturbative QCD (pQCD). It is observed that pQCD calculation (solid line) is in good agreement with experimental data shown in Figure 1.1.

When we consider small Q or large α_s , Lattice-QCD calculation can be utilized. Figure 1.2 shows the Lattice-QCD calculations of ε/T^4 and $3p/T^4$ as a function of T where ε and p are the energy density and pressure [2]. It is observed that the both of ε/T^4 and $3p/T^4$ change significantly at around 180 MeV. It indicates the existence of the phase transition at around $T = 180$ MeV corresponding to the critical energy density $\varepsilon = 1$ GeV/fm³. The rapid evolution of ε/T^4 indicates the de-confinement of quarks and gluons from a hadron. This unclear state is called quark-gluon plasma (QGP).

1.2 High Energy Heavy Ion Collider

Experimentally high energy heavy ion collision is unique method to create QGP in laboratory. Various experiments have been carried out at Brookhaven National Laboratory (BNL) and European organization for Nuclear Research (CERN). They are summarized in Table 1.1. In this section, the overview of the heavy ion collision is described in terms of the time history and the geometry of the collisions.

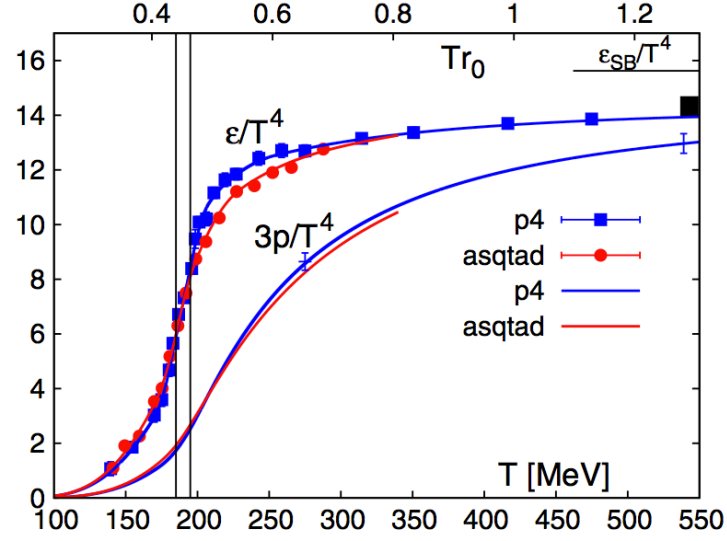


Figure 1.2: Energy density (ε) and 3 times the pressure as a function of temperature calculated in Lattice QCD. [2]. The Stefan-Boltzmann limits is shown in the right side.

Accelerator	Laboratory	Species	Particle energy $\sqrt{s_{NN}}$ (GeV)	Year
SPS	CERN	$^{16}\text{O}, ^{32}\text{S}$	19.4	1986
		^{208}Pb	17.4	1994
AGS	BNL	$^{16}\text{O}, ^{28}\text{Si}$	5.4	1986
		^{197}Au	4.8	1992
RHIC	BNL	^{197}Au	130	2000
		^{197}Au	200	2001
		$\text{d}+^{197}\text{Au}$	200	2003
		^{197}Au	200, 62.4	2004
		^{63}Cu	200, 62.4	2005
		^{197}Au	200	2007
		$\text{d}+^{197}\text{Au}$	200	2008
		^{197}Au	200, 62.4, 39	2010
		^{197}Au	200, 27, 19.6	2011
		^{238}U	192	2012
		$^{63}\text{Cu}+^{197}\text{Au}$	200	2012
		^{197}Au	200, 14.6	2014
		$^3\text{He}+^{197}\text{Au}$	200	2014
LHC	CERN	^{208}Pb	2760	2010
		$\text{p}+^{208}\text{Pb}$	5020	2012

Table 1.1: The summary of high heavy ion collision experiments.

1.2.1 Time Space Evolution of Heavy Ion Collision

The time space evolution is introduced in this section. When the nuclei are accelerated enough at high energy, their shapes are changed as the pancakes due to Lorentz-contraction. If heavy ions are accelerated up to relativistic energy, it is expected that they go through each other when they collide. It is expected that the extremely high energy density, hot and low baryon density matter is created in the collision area and QGP is created. The time evolution of the collision is classified as following. They are introduced with respect to time scale (τ).

- Pre-equilibrium: $0 < \tau < \tau_0$
- QGP phase and hydrodynamical evolution: $\tau_0 < \tau < \tau_f$
- Freeze-out and Hadron Gas phase: $\tau_f < \tau$

Pre-equilibrium: $0 < \tau < \tau_0$

A large number of partons are created by the parton-parton hard scattering in the initial overlap of two nuclei. Many models such as the pQCD, the color strings model, and the color glass condensate (CGC), try to describe the parton production mechanism. While it has not yet understood perfectly, they indicate that QGP is not created at the same time of the collisions. However local thermalization should take place quite fast at proper time τ_0 and QGP is created. It is predicted that τ_0 of less than 1 fm/ c gives a reasonable description of the RHIC data.

QGP phase and hydrodynamical evolution: $\tau_0 < \tau < \tau_f$

Once the local thermal equilibrium is reached at τ_0 , the many observables can be explained by the expansion of the QGP with the relativistic hydrodynamics (in Section 1.3). It is considered that QGP expands hydrodynamically with cooling until freeze-out (τ_f). The basic hydrodynamic equations are the conservation of the energy-momentum tensor and the baryon number:

$$\partial_\mu \langle T^{\mu\nu} \rangle = 0, \quad (1.6)$$

$$\partial_\mu \langle j_B^\mu \rangle = 0, \quad (1.7)$$

where $T^{\mu\nu}$ is the energy-momentum tensor, and j_B^μ is the baryon number current. They are given with perfect fluid as

$$T^{\mu\nu} = (\varepsilon + P)u^\mu u^\nu - g^{\mu\nu}P, \quad (1.8)$$

$$j_B^\mu = n_B u^\mu, \quad (1.9)$$

where ε is the local energy density, P is the local pressure, u^μ is a fluid four-velocity, and n_B is the baryon number density. The conservation laws: Eq. (1.6) and (1.7) include five independent equations, and there are six unknown valuables: ε , P , n_B , and three components of the flow vector v_x , v_y , v_z . We can solve them with additional equation such as an equation of state.

Freeze-out and Hadron Gas phase: $\tau_f < \tau$

The surface of QGP starts hadronization at τ_f , which is defined as freeze-out. There are two types of freeze-out which are “chemical freeze-out” and “kinetic freeze-out”. After the beginning of hadronization, inelastic scattering among hadrons continues and particle species are changeable. The temperature that the particle species are fixed is called as “chemical freeze-out temperature”. Inelastic scattering has been finished but elastic scattering is still ongoing. The “kinetic freeze-out temperature” is the temperature when elastic scatterings finish and the momentum distributions are fixed. After these freeze-out, hadrons are free streaming and measured by the detectors.

1.2.2 Geometry of Heavy Ion Collision

The overlap region of the colliding nuclei is important to understand collision dynamics in high energy heavy ion collisions. Collision occurs when the impact parameter b which is the distance between the center of nuclei is less than $2R$ where R denotes the radius of nucleus. However the electromagnetic interactions may happen when $b > 2R$. If $b \approx 0$, the shape of overlap region is the same as that of nuclei, it is called “central collision”. The area of overlap region gets small with increasing b and it is mentioned “mid-central collision” or “peripheral collision”. The nucleons are classified into two types that nucleons in the overlapped region is called *participant* and the others are called *spectator*. This geometrical treatment is known as participant-spectator model. The size of overlap region and the number of colliding nucleons are determined by the impact parameter which will be discussed in Section 3.1.1.

The Glauber model has been utilized to describe high energy nuclear reaction. It can evaluate the number of the collisions/participants (N_{coll} , N_{part}) and the participant shape (ε). It is a semi-classical model treating the nucleus collisions as multiple nucleon-nucleon interactions, namely nucleons are assumed to travel in straight lines and are not affected after the collisions. This model does not consider secondary particle production and possible excitation of nucleons.

The nuclear thickness function is defined as

$$T_A(\mathbf{s}) = \int dz \rho_A(z, \mathbf{s}), \quad (1.10)$$

$$A = \int d^2\mathbf{s} T_A(\mathbf{s}), \quad (1.11)$$

where ρ is the nuclear mass number density normalized to mass number A and vector \mathbf{s} is in the transverse plane with respect to the collision axis z . The Woods-Saxon parameterization is utilized to describe the density distribution for heavy nucleus such as Au or Pb, and it is given as

$$\rho_A(r) = \frac{\rho_{nm}}{1 + \exp \{(r - R_A)/a\}}, \quad (1.12)$$

where ρ_{nm} is the density at central, R_A is the nuclear radius, and a is the surface diffuseness.

The number of collisions N_{coll} and participants N_{part} are calculated as

$$N_{coll}(b) = \int d^2s T_A(s) T_B(s - b),$$

$$N_{part}(b) = \int ds T_A(s) [1 - \exp \{-\sigma_{NN}^{in} T_B(s - b)\}] \quad (1.13)$$

$$+ \int ds T_B(s - b) [1 - \exp \{-\sigma_{NN}^{in} T_A(s)\}], \quad (1.14)$$

$$(1.15)$$

where σ_{NN}^{in} is the nucleon-nucleon inelastic cross section.

1.3 Experimental Observables

There are many experimental observables indicating QGP in high energy heavy ion collisions and they are investigated to understand the properties of the QGP. Some results are shown in this section.

1.3.1 Initial Energy Density and Bjorken Picture

The estimation of the initial energy density created by the nucleus collisions was proposed by J. D. Bjorken [3]. It can be estimated by measuring the transverse energy of particles as

$$\varepsilon_{Bj} = \frac{1}{A\tau_0} \frac{dE_T}{dy}, \quad (1.16)$$

where A is the size of overlap region and τ_0 is defined as the proper time when the system reaches local thermal equilibrium. Left figure in Figure 1.3 is the image of Bjorken picture and right figure is the estimated initial energy density at τ [4]. If one assumes $\tau = 1$ fm/c, ε_{Bj} achieves much larger than $1 \text{ GeV c}^{-1} \text{ fm}^{-2}$ of critical energy density predicted by the Lattice QCD.

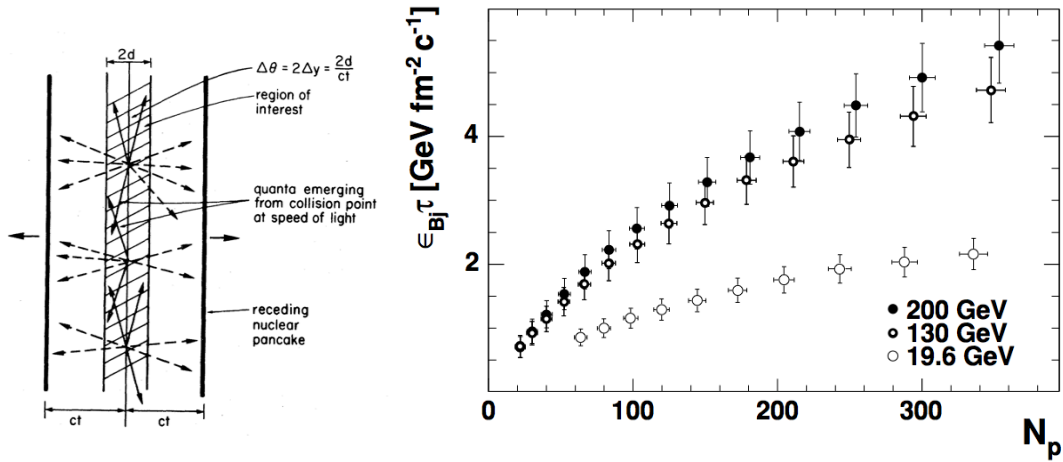


Figure 1.3: (Left) Geometry for the initial state of centrally produced plasma in nucleus-nucleus collisions [3]. (Right) $\varepsilon_{Bj}\tau$ deduced from the PHENIX data at three RHIC energies [4].

1.3.2 Particle Ratio and Chemical Temperature

The ratios of the particle yields of each species are measured and the statistical model is compared to obtain Chemical temperature. The hadron gas is described by a chemical freeze-out temperature (T_{ch}), light quark (u and d) potential (μ_q), strange quark potential (μ_s), and strangeness saturation factor (γ_s) which takes account of the possible incomplete chemical equilibration for strange quarks. The density of a particle i in the hadron gas is given as

$$\rho_i = \gamma_s^{\langle s+\bar{s} \rangle_i} \frac{g_i}{2\pi^2} T_{ch}^3 \left(\frac{m_i}{T_{ch}} \right)^2 K_2(m_i/T_{ch}) \lambda_q^{Q_i} \lambda_s^{s_i}, \quad (1.17)$$

where m_i is the mass of the hadron i , g_i is the number of spin-isospin degree-of-freedom, K_2 is the second-order modified Bessel function and,

$$\lambda_q = \exp(\mu_q/T_{ch}), \quad \lambda_s = \exp(\mu_s/T_{ch}). \quad (1.18)$$

The potential μ_q is for u, d, \bar{u}, \bar{d} quarks, and μ_s is for s, \bar{s} quarks. The μ_q is a third of baryon chemical potential μ_B . Q_i and s_i are the net number of valence u/d quarks ($Q_i = \langle u - \bar{u} + d - \bar{d} \rangle_i$), and s quark ($s_i = \langle s - \bar{s} \rangle_i$) of particle species i , respectively.

Figure 1.4 shows the results of the particle ratio in $\sqrt{s_{NN}}=200\text{GeV}$ Au+Au central collisions ($\langle N_{part} \rangle=322$) and they are fitted by the model calculations [5]. The parameterizations are obtained as chemical freeze-out temperature $T_{ch}=157\pm 3$ MeV, light quark potential $\mu_q=9.4\pm 1.2$ MeV ($\mu_B=28.2\pm 3.6$ MeV), strange quark potential $\mu_s=3.1\pm 2.3$ MeV, and strangeness saturation factor $\gamma_s=1.03\pm 0.04$. From bottom figures, it is found that model calculation is in good agreement with data.

1.3.3 Transverse Mass Distribution and Radial Flow

The emitted hadrons are expected to have important informations of the dynamics of collisions. The spectra of identified particles are usually presented in terms of an Lorentz-invariant differential cross-section ($E \frac{d^3\sigma}{dp^3}$, where E is particle energy and p is particle momentum). It is written by their four momentum (E, p_x, p_y, p_z), rapidity ($y = \tanh^{-1} \beta$), transverse momentum ($p_T = \sqrt{p_x^2 + p_y^2}$), and azimuth angle (ϕ) as

$$\begin{aligned} E \frac{d^3\sigma}{dp^3} &= E \frac{d^3\sigma}{dp_x dp_y dp_z}, \\ &= \frac{d^3\sigma}{p_T dp_T d\phi dy} \quad (dx dy = p_T dp_T d\phi, \quad dp_z = E dy), \\ &= \frac{1}{2\pi p_T} \frac{d^2\sigma}{dp_T dy}. \end{aligned} \quad (1.19)$$

In the case of p+p collisions, it is known that the transverse momentum distribution in low p_T region is well described by an exponential equation in transverse mass ($m_T = \sqrt{m_0^2 + p_T^2}$,

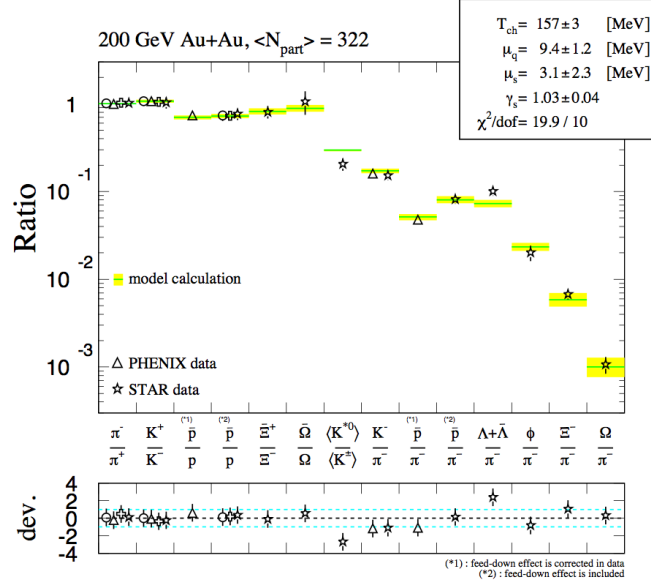


Figure 1.4: The comparison of fit results and the particle ratio data in $\sqrt{s_{NN}}=200\text{GeV}$ Au+Au central collisions ($\langle N_{part} \rangle=322$). (Top) Horizontal lines show statistical model fit on the particle ratio. (Bottom) The difference of data to the model, $(R_{exp} - R_{model})/\Delta R_{exp}$, where R_{exp} is ratio from data, R_{model} is ratio by model calculation, and ΔR_{exp} is error of R_{exp} [5].

where m_0 is the hadron mass).

$$\begin{aligned}
 E \frac{d^3\sigma}{dp^3} &= \frac{1}{2\pi p_T} \frac{d^2\sigma}{dp_T dy} \\
 &= \frac{1}{2\pi m_T} \frac{d^2\sigma}{dm_T dy} \\
 &\approx \exp(-m_T/T).
 \end{aligned} \tag{1.20}$$

This phenomenon is called m_T scaling. The inverse slope T is known as kinetic freeze-out temperature.

Left figure in Figure 1.5 shows the transverse mass distribution for identified hadrons (π^\pm , K^\pm , p/\bar{p}) in heavy-ion collisions with exponential fitting [6]. Right figure shows the obtained inverse slopes. It is found that the inverse slopes has particle mass and centrality dependence. This feature indicates that the expanding source emits hadrons and the apparent temperature is affected by the particle mass. This can be expressed as

$$T \approx T_0 + m_0 \langle v_r \rangle^2, \tag{1.21}$$

where T_0 is the true kinetic freeze-out temperature, m_0 is hadron mass, and $\langle v_r \rangle$ is the strength of the (average radial) transverse flow of the medium at freeze-out temperature. Fitting results show, $T_0=177.0 \pm 1.2$ MeV and $\langle v_r \rangle=0.48 \pm 0.07$, for most central collisions.

1.3.4 Azimuthal Anisotropy

It has been observed that the number of particles emitted from collisions are anisotropic in azimuth angle in event-by-event. This phenomenon is called as an azimuthal anisotropy. The

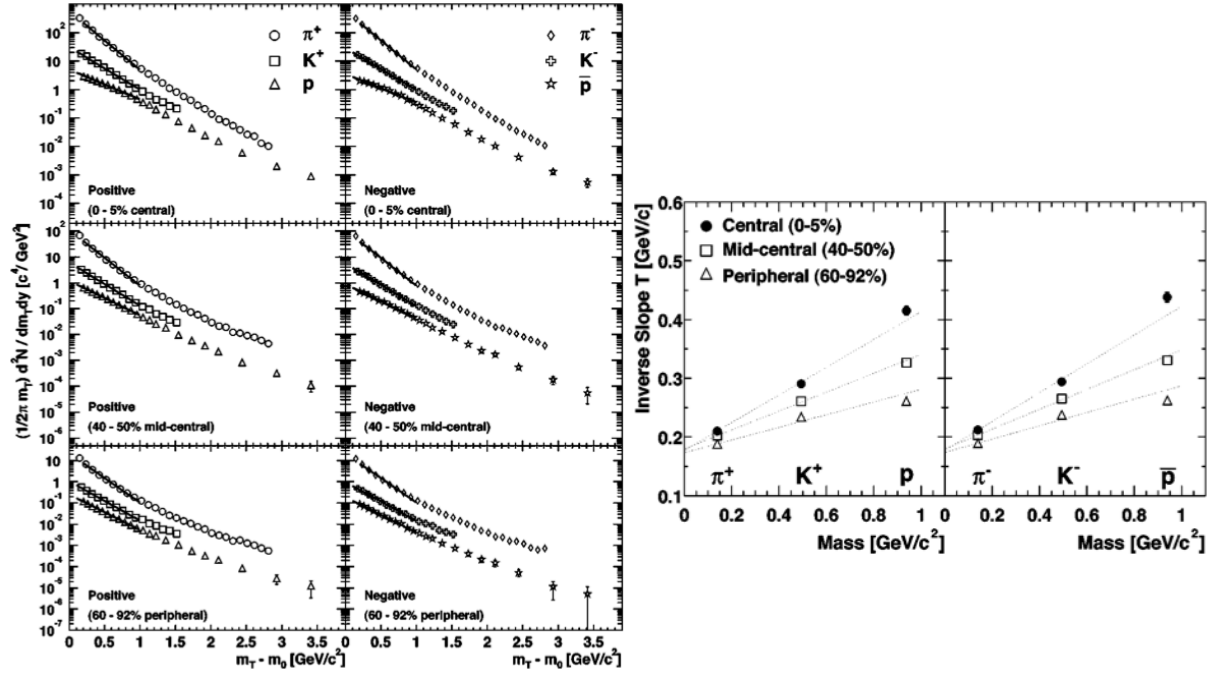


Figure 1.5: (Left) Transverse mass distributions for π^\pm , K^\pm , protons, and anti-protons for central 0-5% (top), mid-central 40-50% (middle), and peripheral 60-92% (bottom) in Au+Au collisions at $\sqrt{s_{NN}}=200\text{GeV}$ [6]. The lines on each spectra are the fitted results using exponential equation. (Right) Mass and centrality dependence of inverse slope parameters T in m_T spectra for positive (left) and negative (right) particles in Au+Au collisions at $\sqrt{s_{NN}}=200\text{ GeV}$. The dotted lines represent a linear fit of the results from each centrality bin as a function of mass using Eq. (1.21).

strength is extracted by Fourier expansion of the emitted particles in azimuthal angle as

$$\begin{aligned} N(\phi) &= N_0 \left[1 + 2 \sum_{n=1}^{\infty} v_n e^{in(\phi - \Psi_n)} \right] \\ &= N_0 \left[1 + 2 \sum_{n=1}^{\infty} v_n \cos \{n(\phi - \Psi_n)\} \right], \end{aligned} \quad (1.22)$$

$$v_n = \langle \cos \{n(\phi - \Psi_n)\} \rangle, \quad (1.23)$$

where v_n is the strength of n^{th} order azimuthal anisotropy, ϕ is the azimuthal angle of the emitted particle, and Ψ_n is the direction of event plane. The sine terms disappear due to the symmetry. The v_2 which is called as “elliptic flow” has been studied for many years. Higher order azimuthal anisotropy $v_n (n > 2)$ has recently been analyzed since about 2010 actively.

If we consider the ideal nuclei collisions, the participant shape is like almond shape as shown in left of Figure 1.6. Because there is a clear geometrical difference of the participant zone in the transverse plane (elliptic shape) between the direction of parallel and perpendicular to reaction plane, which is defined by the impact parameter and beam direction, the anisotropic pressure gradient is created. The QGP expands according to the pressure with cooling and hadrons are emitted. This is the mechanism of azimuthal anisotropy. The initial almond shape has an anisotropy in geometrical source and QGP expansion converts the geometric anisotropy to a momentum anisotropy.

If we consider ideal nuclei collisions, the even order of the azimuthal anisotropy can be observed at the midrapidity in symmetric collisions system. However the profile of realistic nucleus is not smooth because it is composed with finite number of nucleons. Indeed, the initial participant shape can be fluctuated due to the fluctuation of the number of participants as shown in right of Figure 1.6. This geometrical fluctuation is the main source of higher order ($n > 2$) and odd order azimuthal anisotropy. It is expected that measurement of higher order azimuthal anisotropy is very important in order to define the initial geometry and to constrain the shear viscosity to entropy density ratio (η/s) of QGP in the model calculations.

Figure 1.7 shows the charged particle v_n results. It is found that v_3 have weak centrality dependence, whereas v_2 and v_4 show centrality dependence. It has been observed that the centrality dependence of v_n is correlated with the initial geometrical anisotropy.

The one of interesting results is particle identified v_n shown in left of Figure 1.8. It has been observed that heavier hadrons show smaller v_2 than those for light hadrons in $p_T < 2 \text{ GeV}/c$ and meson/baryon splitting in $p_T > 2 \text{ GeV}/c$ [8]. Mass ordering is well described by hydrodynamical model calculation and meson/baryon splitting is understood by quark recombination model. It is found that there is the scaling which scales all particle species and harmonics, and it is called “The number of constituent quark scaling (NCQ)” as shown in bottom Figure 1.8.

1.4 Direct Photon

Photons have been studied in high energy heavy ion collision experiment very actively. That is because photons carry the information when they are created since they do not strongly interact with the medium due to the properties of charge-less and color-less. In addition, we can study the time evolution of the collisions since they are originated from several sources and are emitted

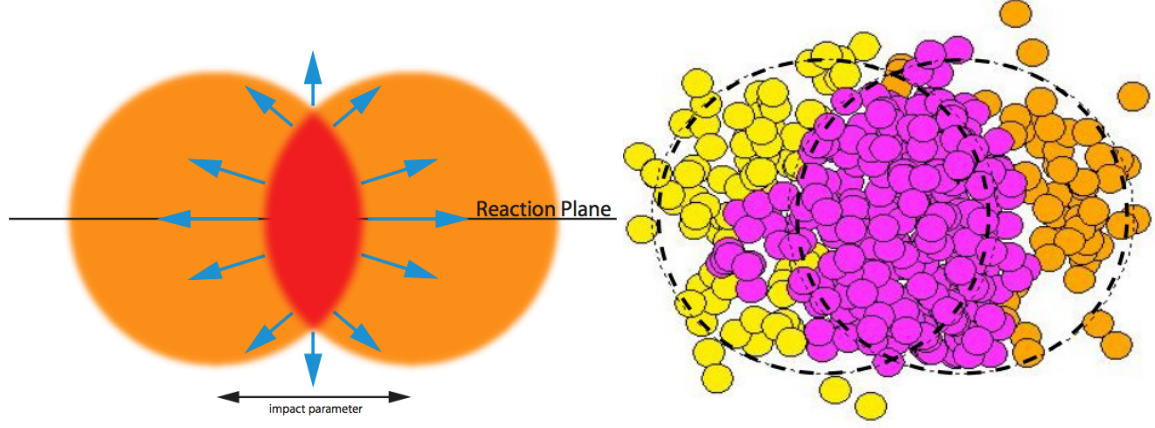


Figure 1.6: (Left) The image of the ideal nucleus and nucleus collisions. (Right) The image of the realistic nucleus and nucleus collisions.

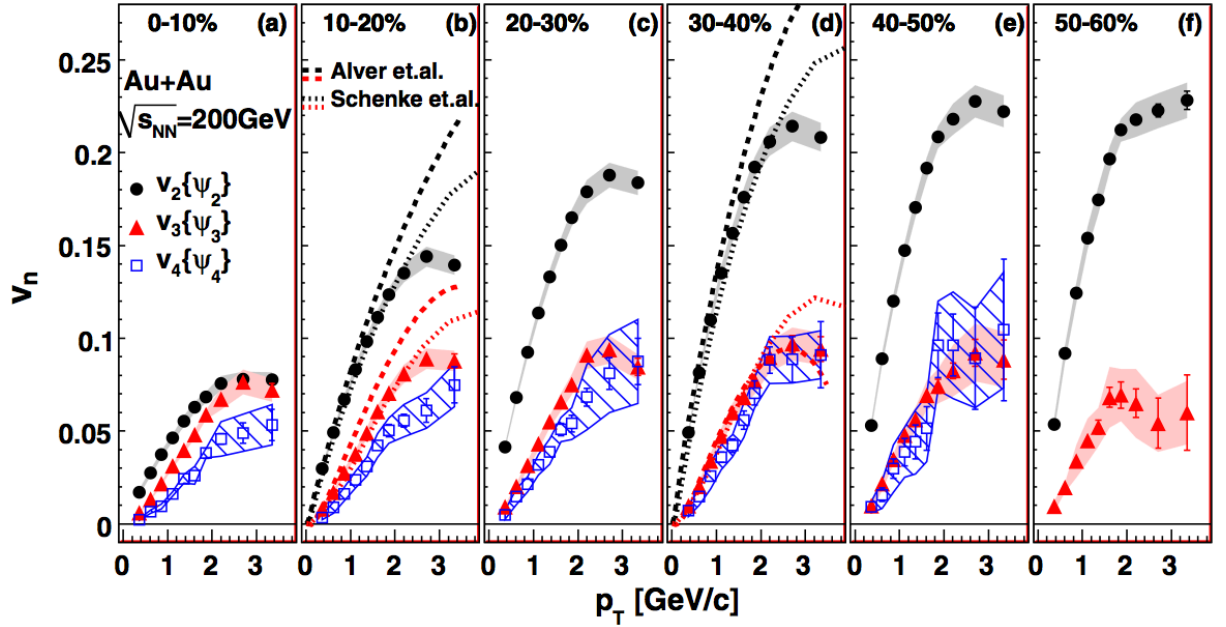


Figure 1.7: The results of azimuthal anisotropy v_n of charged particle measured in PHENIX experiment [7]. Black is $v_2(\Psi_2)$, red is $v_3(\Psi_3)$, and blue is $v_4(\Psi_4)$.

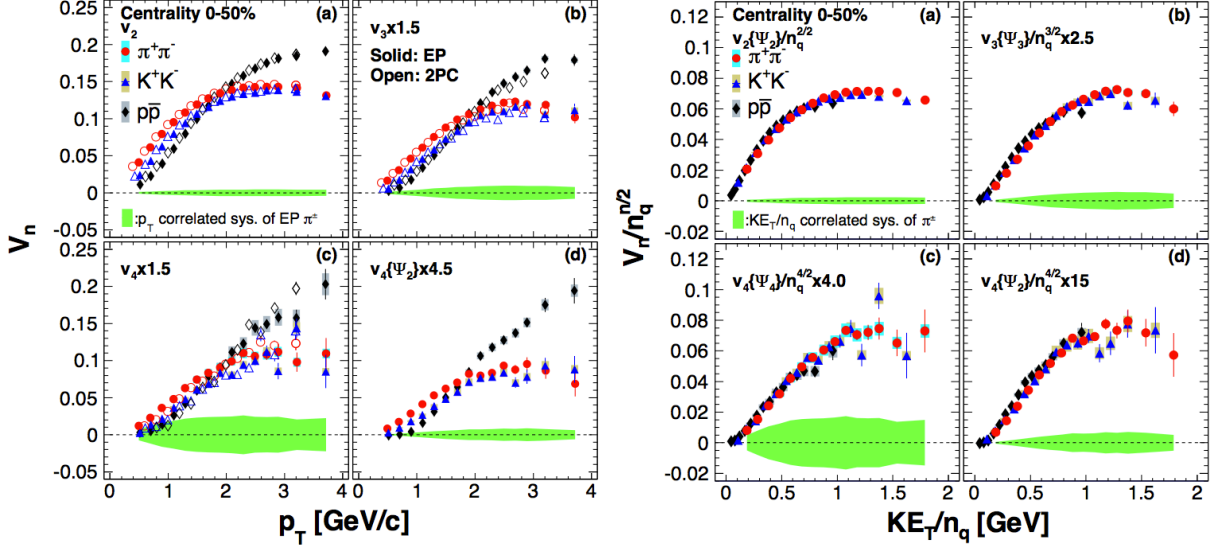


Figure 1.8: (Left) The results of particle identified (π^\pm , K^\pm and p/\bar{p}) azimuthal anisotropy v_n [8]. (Right) The results of the number of constituent quark scaling for v_n as a function of KE_T . Red are charged pion, blue is charged kaon, and black are proton.

during entire duration time of expanding colliding zone. That is the reason why it is expected as a powerful probe. The photon production processes are introduced in Section 1.4.1 and the experimental results are reviewed in Section 1.4.2.

1.4.1 Photon Production Process

There are four main sources of photons; the initial hard scattering between partons, the thermal production in the hot medium, the interaction between hard parton with the medium, and the decay of the produced hadrons (e.g. π^0 , $\eta \rightarrow \gamma\gamma$). Direct photon is defined as all photons except for those coming from hadron decays. Experimentally measured photons are summation of all photons and it is a challenge to identify their sources of photons.

The direct photons produced in nucleus-nucleus collisions can be classified. Prompt photons are originated from primary collision, such as hard interactions of partons, quark-antiquark annihilation ($q + \bar{q} \rightarrow g + \gamma$), Bremsstrahlung emissions from quarks undergoing hard scattering ($q + q \rightarrow q + q + \gamma$), quark-gluon Compton scattering ($q + g \rightarrow q + \gamma$), and gluon fusion ($g + g \rightarrow \gamma$). In high energy heavy ion collisions, since it is expected that the very hot medium is created by the collisions, the thermal photons are radiated from its matter. It is important to study the evolution of the medium. Thermal photons are divided into two types which are radiated from the scattering of partons in QGP phase (e.g. $q + \bar{q} \rightarrow g + \gamma$) and in hadron gas phase (e.g. $\pi^+ + \pi^- \rightarrow \rho + \gamma$ [39]). There is a source of photons created from interaction between the medium and hard parton. It is expected that these photons provide the information of jet energy loss in the medium.

Prompt Photons

Prompt photons are created from parton hard scattering such as quarks and gluons, Compton scattering, annihilation of quarks, Bremsstrahlung, and gluon fusion. Their Feynman diagrams are shown in Figure 1.9. It is predicted that they are dominant in high p_T region. The prompt photon spectra in nuclei collisions are expected to be described by the superposition of p+p collisions scaled by the number of binary collisions. Figure 1.10 shows the photon p_T spectra in p+p collision and it is compared with next-to-leading order (NLO) pQCD calculation. It is found that they are generally in good agreement.

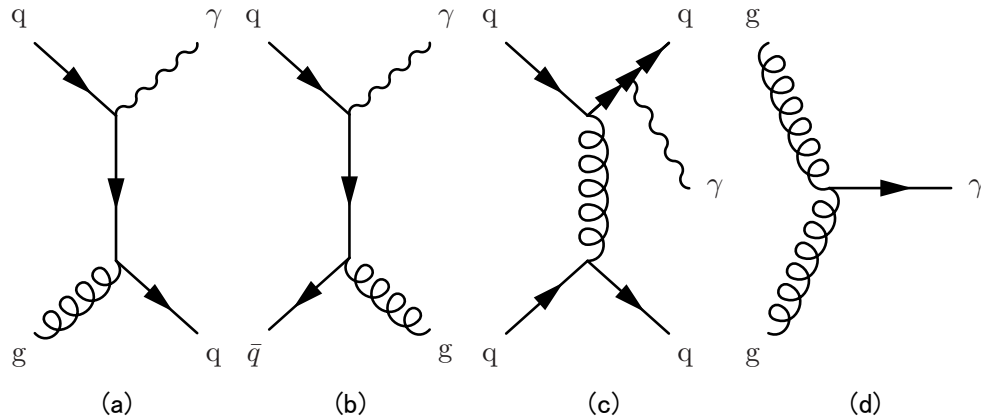


Figure 1.9: Feynman diagrams of prompt photon production mechanisms. (a) : Quark-gluon Compton scattering, (b) : Annihilation between quark and anti-quark, (c) : Bremsstrahlung, (d) : Gluon fusion.

Thermalized Photons from QGP and Hadron Gas

The photons in low p_T are predicted to be dominantly radiated from thermal medium. These photons are mainly created by quark-gluon scattering in QGP phase and π - π scattering in hadron gas phase. Figure 1.11 shows the photon p_T spectra calculated by the thermal models from QGP phase, hadron gas phase, and primordial photon. It is found that thermal photons are dominant less than about 2 GeV/c. It is expected that these photons are very important to study the time evolution of the collisions.

Photons originated from the interaction between hard parton and the medium

When hard parton passes through QGP, photons are produced from Compton scattering and annihilation of a quark by interacting with medium [40]. Because they could not be produced in p+p collisions, it is important to study jet energy loss in the medium. It produces photons by interact between parton with the thermal gluons (Compton scattering) and with the thermal anti-quarks (quark annihilation). It is found that these photons are dominant in the range of $p_T < 6$ GeV/c for Au+Au collisions [40].

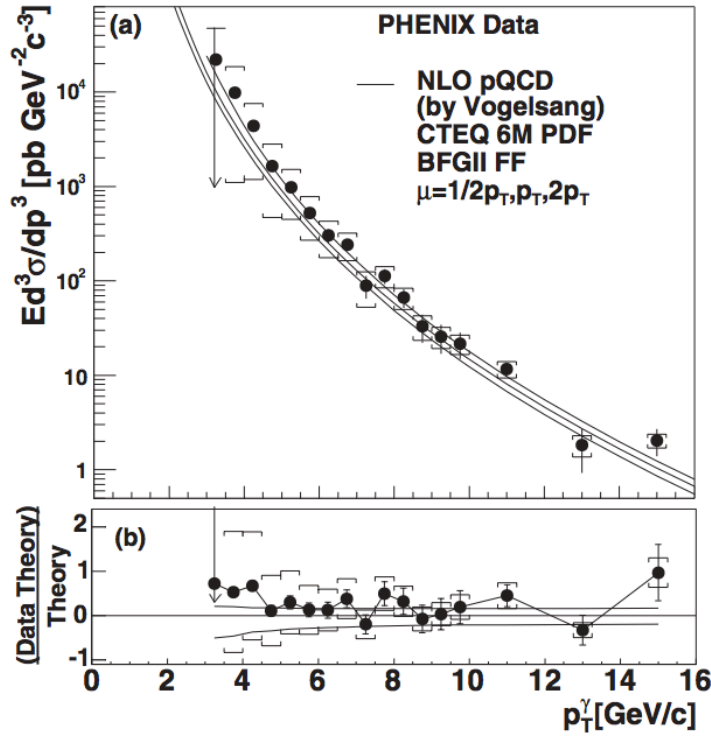


Figure 1.10: (a) Direct photon p_T spectra with NLO pQCD calculation for three theory scales, μ [9]. (b) Comparison to NLO pQCD calculation for $\mu = p_T$, with upper and lower curves for $\mu = p_T/2$ and $2 p_T$.

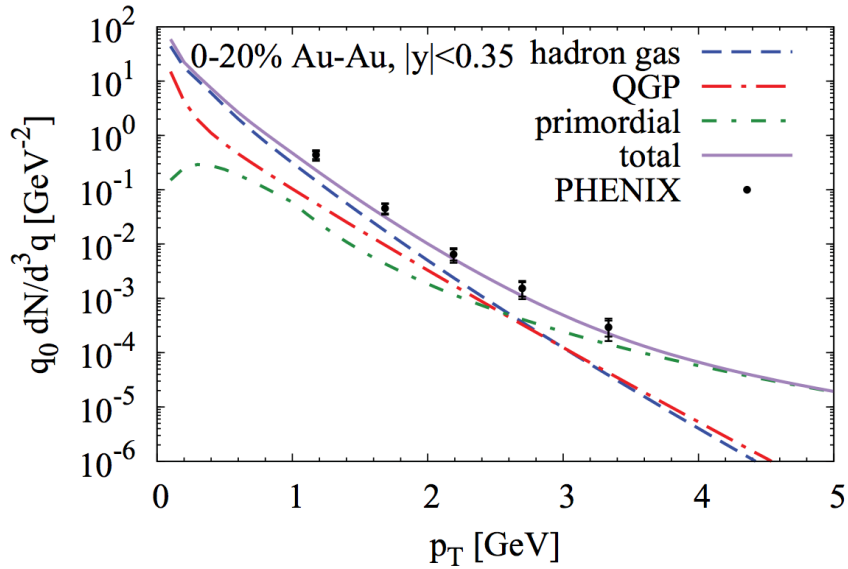


Figure 1.11: Comparison of direct photon p_T spectra from different photon sources [10]. Blue line shows photon radiated from hadron gas, red line is photons emitted from QGP, green line is primordial photon, violet line is total of photons, and black points are PHENIX data.

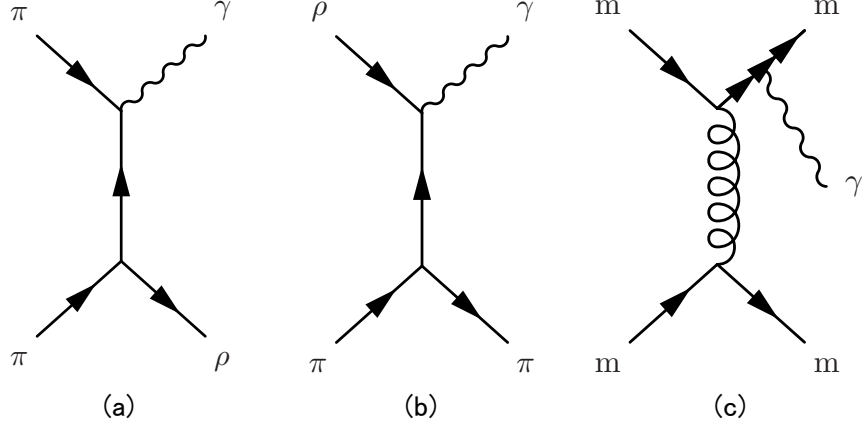


Figure 1.12: Feynman diagrams of photon production mechanisms in hadron gas. (a) : $\pi + \pi \rightarrow \rho + \gamma$ (b) : Hadron interaction (c) : meson-meson Bremsstrahlung.

1.4.2 Excess of the direct photon

The excess of direct photon has been measured by calorimeter [29], virtual photon [11], and external conversion method [30] as shown in Figure 1.13. The excess of direct photon R_γ is defined by

$$R_\gamma = \frac{\frac{dN^{inc}/dp_T}{dN^{\pi^0}/dp_T}}{\left(\frac{dN^{dec.}/dp_T}{dN^{\pi^0}/dp_T}\right)_{MC}} = \frac{N_{inc.}}{N_{dec.}}, \quad (1.24)$$

where, $N_{inc.}$, $N_{dec.}$ are the number of inclusive photon and hadronic decay photon, respectively. R_γ measured by calorimeter covers a wide p_T range, which is significantly above unity especially for high p_T region, while relative systematic uncertainty is large at lower p_T region. The R_γ is measured by virtual photon and external photon method more precisely in the p_T region less than 4 GeV/c, and it is observed that about 20% of direct photon signal is contained in the measured inclusive photon yield.

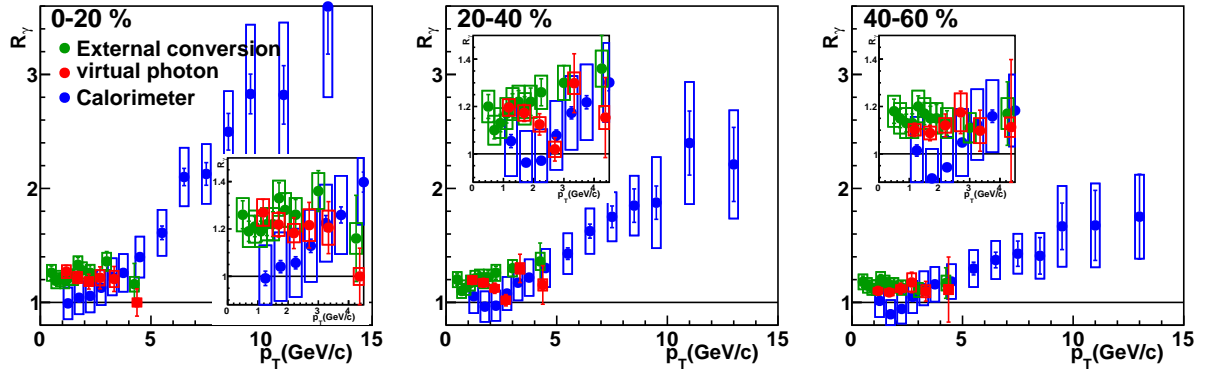


Figure 1.13: The excess of direct photon R_γ as a function of p_T measured by calorimeter (blue), virtual photon (red), and external conversion photon method (green).

1.4.3 p_T spectra

Direct photon p_T spectra in 200 GeV Au+Au collisions are measured via real and virtual photons analysis. They are compared with p+p collisions scaled by the number of binary collisions, and the enhancement in low p_T region has been observed and shown in Figure 1.14. The effective temperature which is the inverse slope of the exponential function is measured by the fitting to the excess of direct photon p_T spectra after subtraction of the scaled p_T spectra in p+p. The obtained effective temperature is about 240 MeV, and it is found that there is no significant centrality dependence within systematic uncertainty [30]. Because the kinetic freeze-out temperature is obtained about 100 MeV [8], obtained effective temperature is much higher than kinetic freeze-out temperature. Additionally hydrodynamical model expects initial temperature is more than or at least 300-600 MeV [11].

The R_{AA} which is the ratio of the p_T spectra in Au+Au to that in p+p collisions scaled by the number of binary collisions are also calculated [41]

$$R_{AA} = \frac{d\sigma_{AA}/dp_T}{\langle N_{coll} \rangle d\sigma_{pp}/dp_T},$$

where σ_{AA} , σ_{pp} are the p_T spectra in Au+Au, p+p collisions, respectively. It is observed that R_{AA} is enhanced in low p_T and consistent with unity in high p_T shown in Figure 1.14. Because it is expected that the photons emitted from initial hard collisions are dominant in high p_T , it is consistent with the expectation introduced in Section 1.14. Conversely the enhancement in low p_T could indicate the existence of the other photon sources which do not exist in p+p collisions, namely thermal photon sources of the hot and dense matter in the nuclei collisions. Therefore, photons in low p_T are considered to be radiated from very hot medium at early time of collisions.

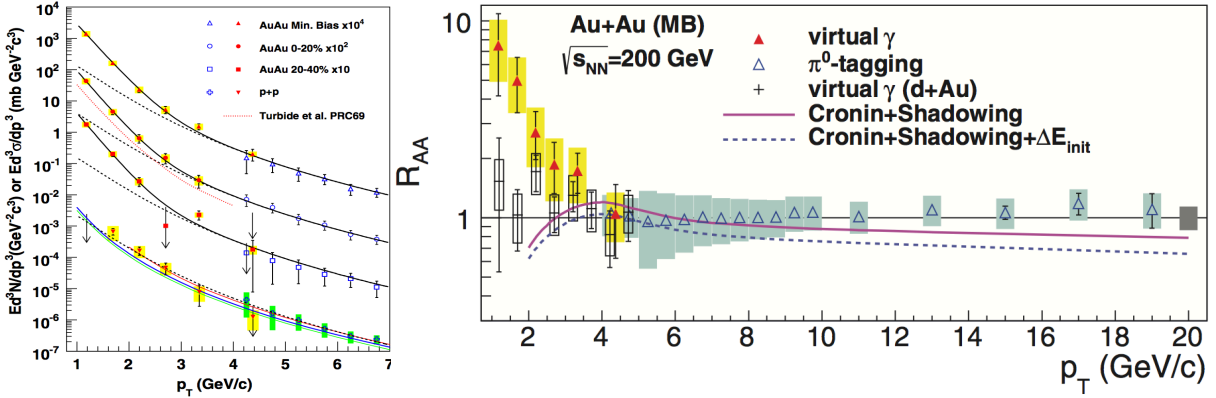


Figure 1.14: (Left) Direct photon p_T spectra measured in Au+Au and p+p 200 GeV collisions [11, 12]. (Right) Direct photon R_{AA} measured in PHENIX experiment. Blue is R_{AA} measured in calorimeter method, red (black) is R_{AA} measured by virtual photon method in Au+Au (d+Au) collisions, respectively.

1.4.4 Elliptic flow

Because one expects that photons have different angular emission patterns depending on their production mechanism, it is investigated to identify the photon sources via the emitting angle

dependence by measuring azimuthal anisotropy. In the following discussions, initial geometry is assumed to be smooth, i.e. there are no fluctuations for positions of participant nucleons.

If the prompt photons do not interact with the matter, they would not depend on initial geometry, therefore it is expected to be $v_2=0$. Jet-fragmentation photons have positive v_2 since jet trends to be emitted to in-plane due to the path length difference between in-plane and out-of-plane. Jet conversion photons and Bremsstrahlung photons have negative v_2 because the energy loss increases with the path length in the medium [42]. Radiated photons from QGP and HG have positive v_2 because they are emitted from expanding medium. The measured direct photon v_2 is superposition of these sources.

It is observed that v_2 at high p_T region are very small, and it is consistent with the expectation that prompt photons are dominant in that region. On the other hand, it is found that the strength of v_2 is as large as those of hadrons in $p_T < 2$ GeV/c. Since photons are emitted during all stages of collision, they should include photons emitted from the medium which is not yet expanded. That is why direct photon v_2 was predicted to be smaller than hadron v_2 . Because photon has large v_2 , the results suggest that photons in low p_T are mainly created from late state of collisions.

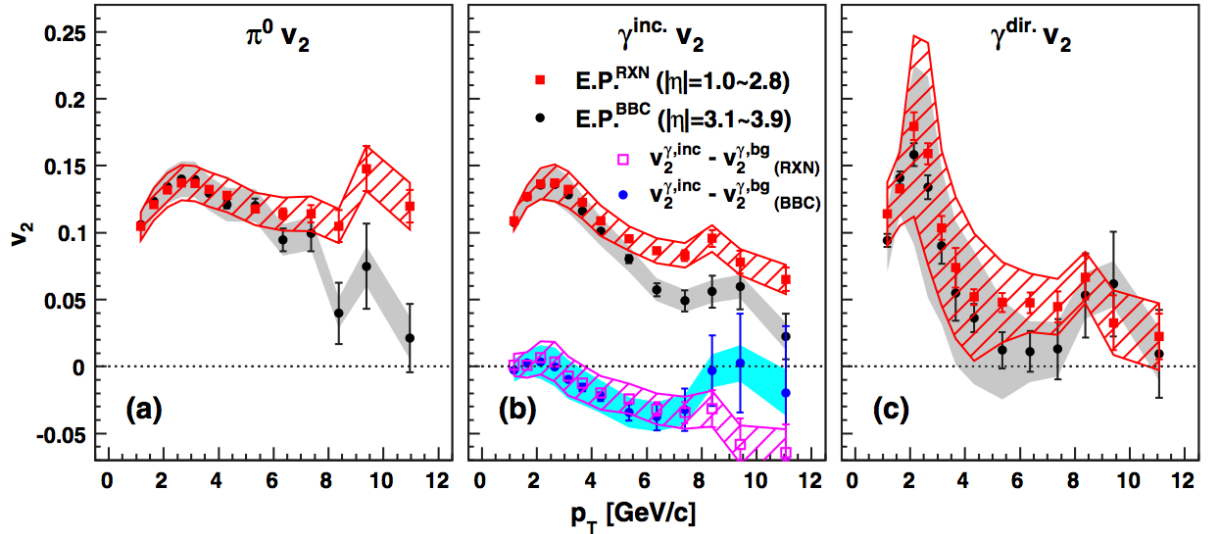


Figure 1.15: The v_2 of π^0 (a), inclusive photon (b), direct photon (c) as a function of p_T [13]. Red (Black) points are measured with respect to event plane reconstructed by Reaction Plane detector (BBC).

1.4.5 Direct photon puzzle

There is the discrepancy between the results obtained from p_T spectra and elliptic flow, whether they are coming from the early or later stage of collisions as it has been discussed in previous section. It is called “direct photon puzzle”, and there are no models to explain the both results simultaneously. There are two models to solve the direct photon puzzles, which will be discussed below in detail.

Radial flow effect to effective temperature

The effective temperature (T_{eff}) measured by photon p_T spectra which is emitted from expanding medium are written as,

$$T_{eff} \approx T_0 \sqrt{\frac{1+\beta}{1-\beta}}, \quad (1.25)$$

where T_0 is the true temperature of the medium, and β is the speed of the medium. It is indicated that strong radial flow makes effective temperature higher than real temperature like as blue shift effect. This model suggests that photons are indeed created at later stage than the expected from the photon p_T spectra.

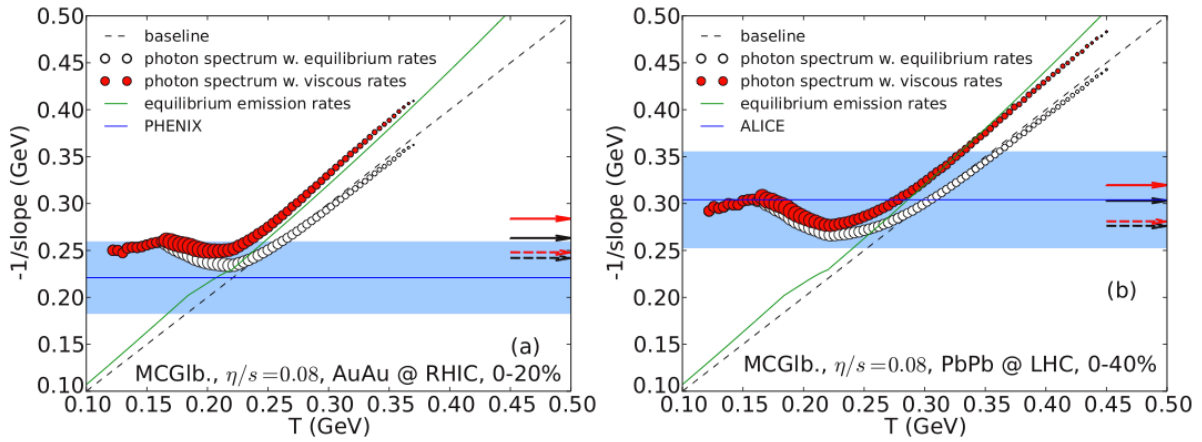


Figure 1.16: Inverse slope temperature as a function of a function of temperature in Au+Au collisions at RHIC 0-20% centrality (left) and in Pb+Pb collisions at LHC 0-40% centrality (right) [14]. Vertical axis is the inverse slope of exponential, and horizontal axis is true temperature. Red (white) points are simulated from equilibrium thermal emission rates (hydrodynamic simulation), respectively. Horizontal blue line shows the experimental results.

Strong magnetic field effect

The theory predicts that the very strong magnetic field is created by the high energy nuclei collisions with respect to the perpendicular direction to the reaction plane [43]. This magnetic field is considered to be the key to understand the photon puzzle in [43] [44]. In [44] study, the coupling of the conformal anomaly in QCD and strong magnetic field created by the collision is introduced to make new photon production mechanism. Although their calculation is schematic and uses many approximations, it is found that their calculated direct photon v_2 is comparable to the experimental results as shown in Figure 1.17.

1.4.6 Direct photon measurement in LHC

Direct photon has been studied in Pb-Pb collisions at $\sqrt{s_{NN}}=2.76$ TeV at LHC-ALICE experiment [15, 12]. Extracted effective temperature is 341 ± 51 MeV from the measured p_T spectra in $p_T < \text{GeV}/c$, which is obtained by the exponential function fit. It is higher than RHIC energy

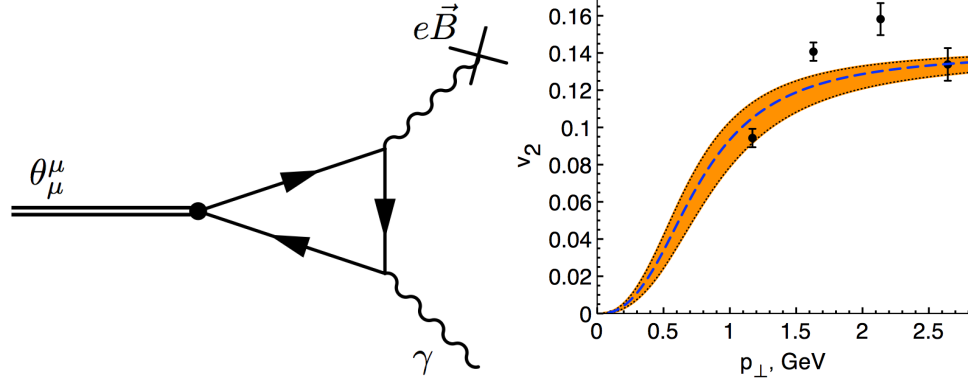


Figure 1.17: (Left) The coupling of the conformal anomaly to the external magnetic field resulting in photon production. Photon is produced by the trace of the energy-momentum tensor (θ_μ^μ) and magnetic field makes photon. (Right) The azimuthal anisotropy v_2 of the direct photons for different values of bulk viscosity corresponding to C_ξ in the range of $2.5 \div 5$ calculated for minimum bias Au+Au collisions.

by 40%. Elliptic flow is also measured and non zero positive v_2 is found for $1 < p_T < 3$ GeV/ c . The trend is similar to the case of v_2 measured in RHIC-PHENIX experiment.

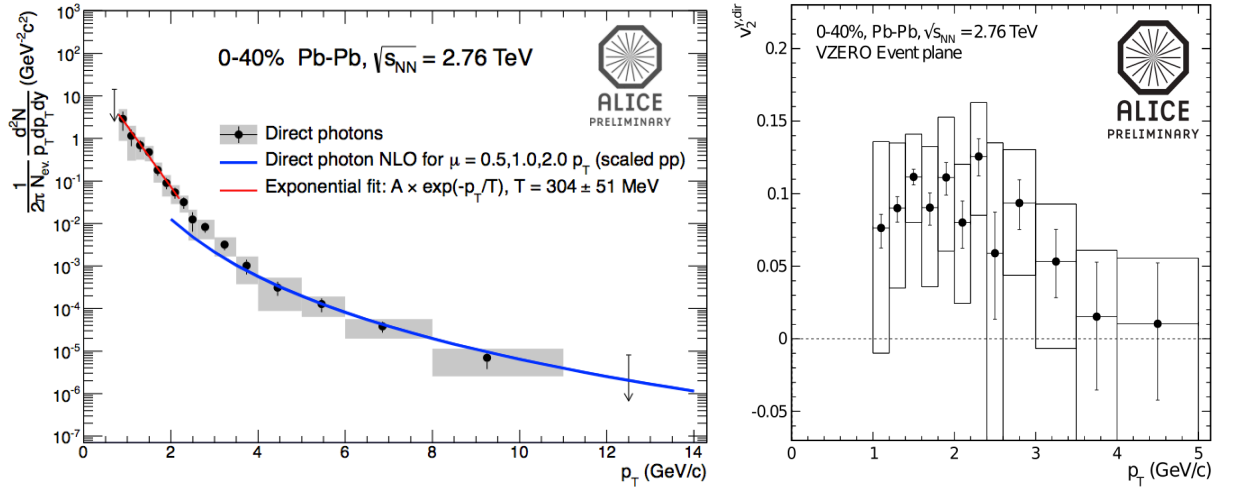


Figure 1.18: Direct photon p_T spectra (left) and second order azimuthal anisotropy (right) as a function of p_T in $\sqrt{s_{NN}}=2.76$ TeV Pb+Pb collisions at LHC-ALICE experiment [15, 12]. Non zero positive v_2 is found and it is similar trend with it is seen in RHIC-PHENIX experiment.

1.4.7 Model prediction of direct photon azimuthal anisotropy

Thermal photon azimuthal anisotropy v_2 and v_3 are calculated from event-by-event viscous hydrodynamic simulations, which has been successful in describing soft hadron observables at RHIC and LHC [16]. Initial conditions are generated by Monte-Carlo Glauber (MCGlb) and Monte-Carlo KLM (MCKLM) models. The results of photon v_2 and v_3 with several initial conditions are

shown in Figure 1.19. Model calculation shows that the ratio v_2/v_3 of photon is more sensitive than that of hadron, though magnitude of v_2 in the model is much smaller than the data [16]. This model calculation suggest that photon v_2/v_3 measurements provide further constraint on η/s of the thermal medium.

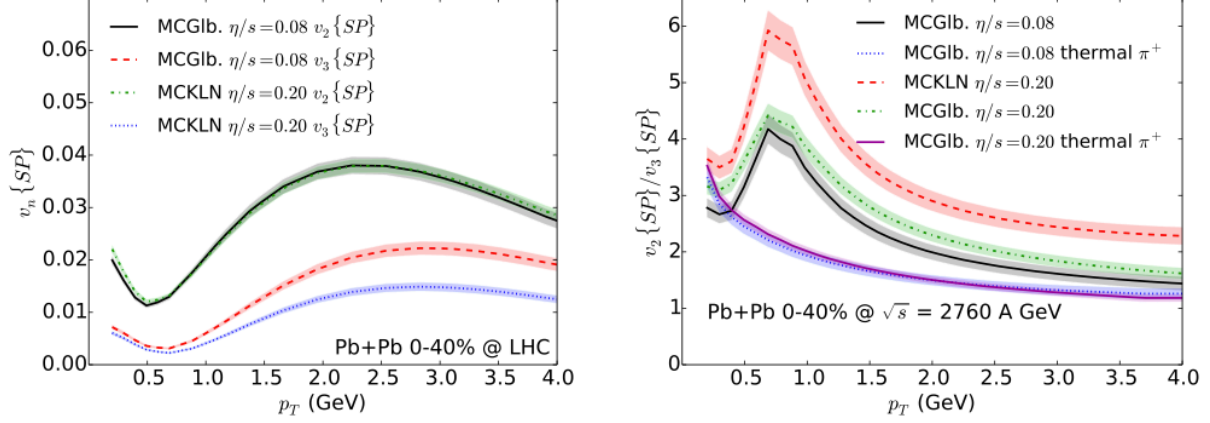


Figure 1.19: (Left) p_T -differential v_2 and v_3 calculated with event-by-event viscous hydrodynamic simulations from MCGlb or MCKLM [16]. (Right) The ratio of v_2 to v_3 of thermal photon and thermal charged pion. Both calculations are carried out for 0-40% centrality in $\sqrt{s_{NN}}=2.76$ TeV Pb+Pb collisions.

1.5 Thesis Motivation

The results of direct photon provide the two opposing and competing physics scenarios. One is the large excess of the p_T spectra in Au+Au collisions compared to that in $p+p$ collisions scaled by the number of the binary collisions, which tells us the photons are from early stage. Another is large elliptic flow v_2 , which tells us the photons are from the later stage. There is no model to explain simultaneously the both of high effective temperature and large v_2 . The additional constraint is necessary to understand the photon production mechanisms in nucleus-nucleus collisions. Measurement of higher order azimuthal anisotropy is expected to be very sensitive to the initial participant geometry, and more precise analysis of photon emitting angle dependence is studied. In this thesis, the results of v_2 , v_3 and v_4 of direct photon as a function of p_T and centrality in $\sqrt{s_{NN}}=200$ GeV Au+Au collisions at RHIC-PHENIX experiments.

Chapter 2

Experiment

2.1 Relativistic Heavy Ion Collider

Relativistic Heavy Ion Collider (RHIC) is a heavy ion collider, which is at Brookhaven National Laboratory in America. RHIC is designed for aiming to collide various nucleus from proton to Uranium in order to study the property of QGP, and polarized protons for understanding the structure of nucleon. The achieved top energy ranges are 100 GeV and 255 GeV per nucleon for gold ion and proton, which depend on the mass of ion.

Because heavy ion beams cannot be accelerated up to relativistic energies by a single accelerator, it can only be achieved step by step with a series of accelerators. At the RHIC facility, the Tandem Van de Graaf, the Booster Synchrotron, and the Alternating Gradient Synchrotron (AGS) are used to pre-accelerate heavy ions before injection into the collider. The manner of accelerating a gold beam is introduced [45]. At the beginning, negative gold ions are created by a pulsed sputter ion source and are accelerated by the first stage of the Tandem Van de Graaf. The atomic electrons of the ion are partially stripped off by a foil located inside the high-voltage terminal. The gold ions, now in a positive charge state, are accelerated during the second stage up to ~ 1 A MeV. These positive ions are transferred through a 540 m transfer line to the Booster Synchrotron. A radio frequency (RF) electric field is applied, the ions are grouped into three bunches, and are accelerated up to 78 A MeV. Another foil at the exit of the Booster strips away all of the atomic electrons of the gold ion. The fully stripped positive gold ions are injected into the AGS, where the three bunches of gold ions are accelerated further up to 10.8 A GeV, which is the required injection energy for the RHIC. The three bunches of gold ions from the AGS are injected into the two 3.834 km long RHIC rings called the blue ring and the yellow ring, where they circulate in opposite directions. By repeating this process, the bunches are increased, and they are accelerated up to 100 A GeV.

There are six sections in RHIC rings and four experiments have been carried out, which are the Pioneering High Energy Nuclear Interaction eXperiment (PHENIX), the Solenoidal Tracker At RHIC (STAR), the Broad RAnge Hadron Magnetic Spectrometer (BRAHMS), and PHOBOS named after one of the two moons of MARS which is the Modular Array for RHIC Spectra. PHOBOS and BRAHMS finished their works, and PHENIX and STAR experiments have been operated now.

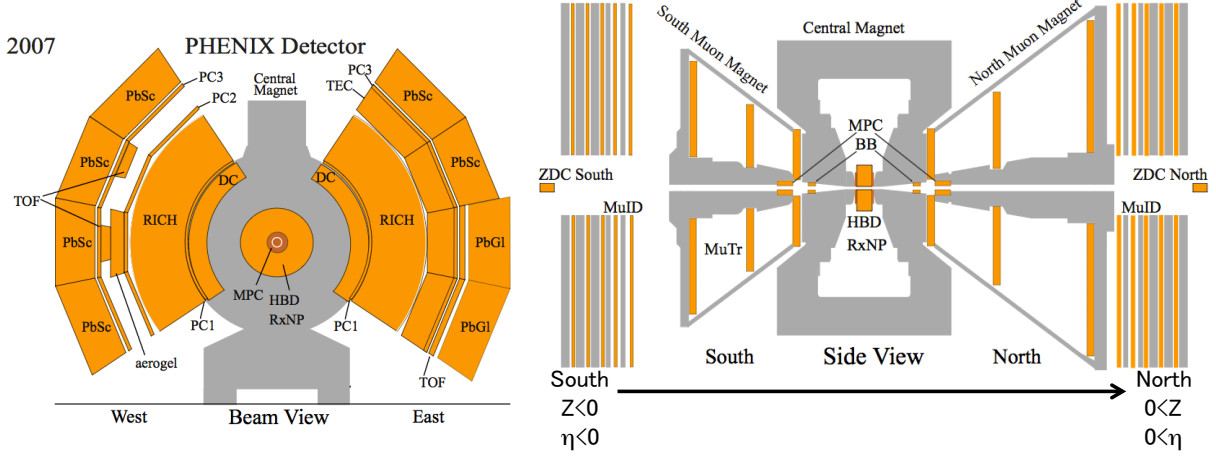


Figure 2.1: The PHENIX detectors operated in 2007 RHIC run period. (Left) The central arm detector with several types of spectrometers from beam view. (Right) The side view of the PHENIX detectors.

2.2 PHENIX Experiment

The PHENIX probes several fundamental features of the strong interaction. A prime goal is to study the property of QGP and it has been continued for more 15 years. Especially, we have studied QGP from the aspect of detecting direct photon and low mass lepton pairs as a penetrating probe, J/Ψ which are $c\bar{c}$ vector meson as a probe of initial state of collisions. In order to study them, PHENIX detectors are composed by the many subsystems.

Figure 2.1 shows the PHENIX detectors in 2007 RHIC run period. PHENIX detectors are able to be divided into three segments, which are characterization detectors, central arm (CNT), and muon detectors. Characterization detectors are utilized to classify the collisions, such as centrality and event plane. CNT is composed by the several types of spectrometers which measure electrons, hadrons and photons at mid-rapidity. Muon spectrometers locate at forward and backward rapidity for studying low- x physics.

2.3 PHENIX magnet system

The PHENIX magnet system [17] is composed of three spectrometer magnets with warm iron yokes and water-cooled copper coils. The Central Magnet (CM) is energized by two pairs of concentric coils and provides a field around the interaction vertex that is parallel to the beam. We can measure momentum of charged particles in the polar angle range from 70° to 110° . The north and south Muon Magnets (MMN and MMS) use solenoid coils for muon analysis at forward/backward rapidity. Each of the three magnets provides a field integral of about 0.8 T-m. The magnetic volumes of the PHENIX magnets are very large and complex, so a new technique was developed to map the fields based on surface measurements of a single field component using single axis Hall probes mounted on a rotating frame.

Summary of PHENIX detector subsystem			
Element	$\Delta\eta$	$\Delta\phi$	Purpose and Special Features
Central magnet (CM)	$ \eta < 0.35$	360°	Up to 1.15 T·m
muon (MMS)	$-1.1 < \eta < -2.2$	360°	0.72 T·m for $\eta=2$
muon (MMN)	$1.1 < \eta < 2.4$	360°	0.72 T·m for $\eta=2$
BBC	$3.1 < \eta < 3.9$	360°	Start timing, first vertex
ZDC	± 2 mrad	360°	Minimum bias trigger
MPC (South)	$-3.7 < \eta < -3.1$	360°	Forward calorimeter
MPC (North)	$3.1 < \eta < 3.9$	360°	Measurement event plane
RxN (Inner)	$1.5 < \eta < 2.8$	360°	Measurement event plane
RxN (Outer)	$1 < \eta < 1.5$	360°	Good event plane resolution
DC	$ \eta < 0.35$	$90^\circ \times 2$	Good momentum and mass resolution $\Delta m/m = 0.4\%$ at $m = 1\text{GeV}$
PC	$ \eta < 0.35$	$90^\circ \times 2$	Parton recognition, tracking for non-bend direction
RICH	$ \eta < 0.35$	$90^\circ \times 2$	Electron identification
TOF	$ \eta < 0.35$	45°	Good hadron identification, $\sigma \sim 120\text{ps}$
PbSc EMCal	$ \eta < 0.35$	$90^\circ + 45^\circ$	Energy and position measurement of photons and electrons
PbGl EMCal	$ \eta < 0.35$	45°	Good e^\pm/π^\pm separation at $p > 1\text{GeV}/c$ EM shower and $p < 0.35\text{GeV}/c$ by TOF K^\pm/π^\pm separation up to $1\text{GeV}/c$ by TOF
μ tracker: (μTS)	$-1.15 < \eta < -2.25$	360°	Tracking for muons
μ tracker: (μTN)	$1.15 < \eta < 2.44$	360°	Muon tracker north installed for Year-3
μ identifier: (μIDS)	$-1.15 < \eta < -2.25$	360°	Steel absorbers and Iarocci tubes for
μ identifier: (μIDN)	$1.15 < \eta < 2.44$	360°	muon/hadron separation

Table 2.1: The summary of PHENIX detectors [35].

2.4 Characterization Detectors

In this section, characterization detectors classifying the collisions, such as centrality and event plane are introduced. The Zero Degree Calorimeter (ZDC) is introduced in Section 2.4.1, the beam beam counter (BBC) is explained in Section 2.4.2, the muon piston calorimeter (MPC) is shown in Section 2.4.3, and the reaction plane detector (RxN) is introduced in Section 2.4.4.

2.4.1 Zero Degree Calorimeter

The Zero Degree Calorimeters (ZDC) [46, 18] is a hadron calorimeter consisting of tungsten plates alternating with layers of undoped optical fibers, sampling the energy deposit through Cherenkov light produced by shower electrons in fiber. Figure 2.3 shows the mechanical design. They are installed about 18 m away from the nominal collision point on upstream/downstream of beam line.

ZDCs are installed for measuring the deposited energy of spectator neutrons. The coincidence of ZDC and Beam-Beam Counter (Section 2.4.2) is used for minimum bias trigger.

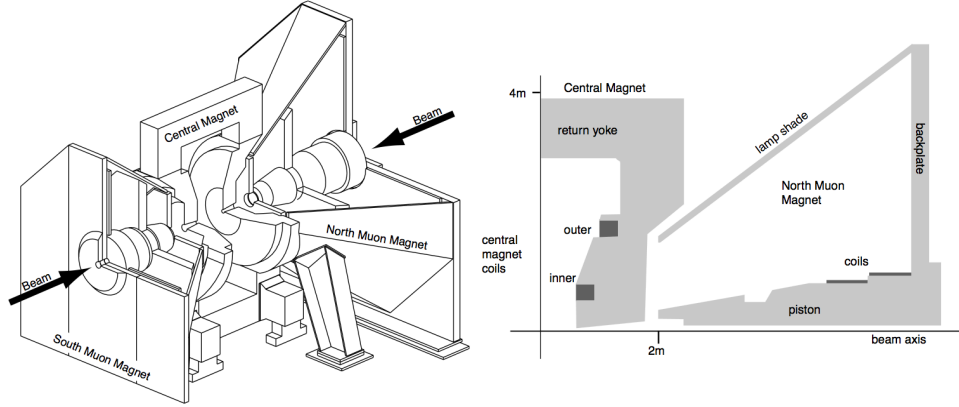


Figure 2.2: (Left) Line drawings of the PHENIX magnets, shown in perspective and cut away to show the interior structures. Arrows indicate the beam line of the colliding beams in RHIC. (Right) Vertical cutaway drawing of central and north muon magnets showing the coil positions for both magnets [17].

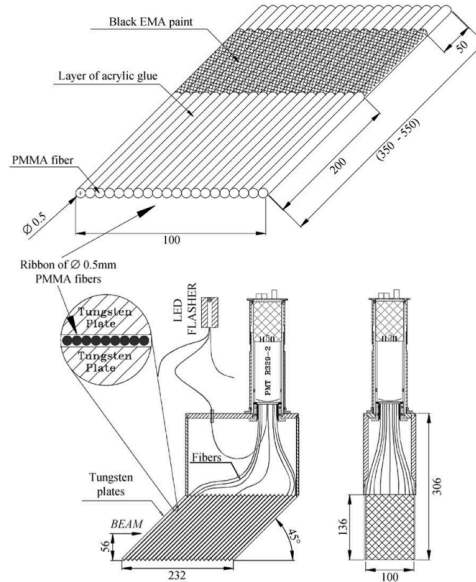


Figure 2.3: Mechanical design of the production tungsten modules [18].

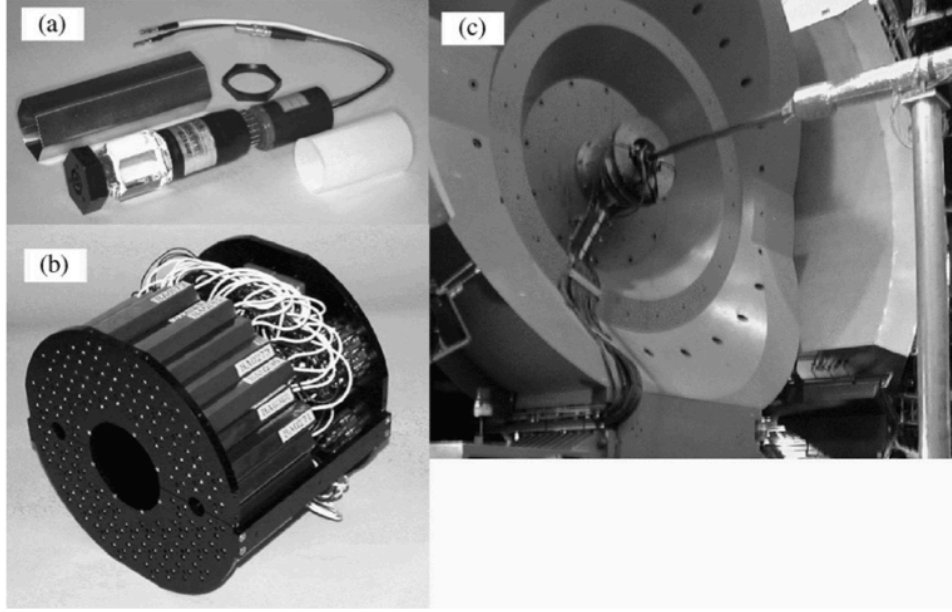


Figure 2.4: (a) Single BBC consisting of 1 in mesh dynode photomultiplier tubes mounted on a 3 cm quartz radiator, (b) A BBC array comprising 64 BBC elements, (c) The picture of BBC mounted on the PHENIX detector [19].

2.4.2 Beam Beam Counter

The Beam-Beam Counters (BBC) [19] are composed of two arrays of 64 Cherenkov counters with quartz radiators and photomultiplier readout. Figure 2.4 shows the pictures of the dynode photomultiplier tubes mounted on quartz radiator, the BBC array, and the BBC mounted on the PHENIX. BBCs are placed 144 cm away from the nominal collision position on north/south sides with surrounding the beam pipe. They are installed for determination the time of interaction T_0 and the position in z direction of a collision Z_{vtx} by measuring the flight time of prompt particles as

$$T_0 = \frac{T_S + T_N - 2L/c}{2}, \quad (2.1)$$

$$L = \frac{c(T_S + T_N)}{2}, \quad (2.2)$$

where T_S, T_N are the detected time at BBC South and North, and L is the distant between the nominal of collision to the Z_{vtx} . The time of interaction is used for as a start time for the time-of-flight (TOF) measurement and signal for the Level-1 (LVL1) trigger. The interaction position is utilized for limiting the vertex region within the PHENIX acceptance. Total charge distribution in BBC is used to determinate centrality in event-by-event.

2.4.3 Muon Piston Calorimeter

The Muon Piston Calorimeter (MPC) locates at forward and backward rapidity for aiming to measure photons and charged particles [20]. They are consisted with a highly segmented Lead-Tungstate (PbWO_4) crystal array with Avalanche Photodiode (APD) readout. Lead-Tungstate

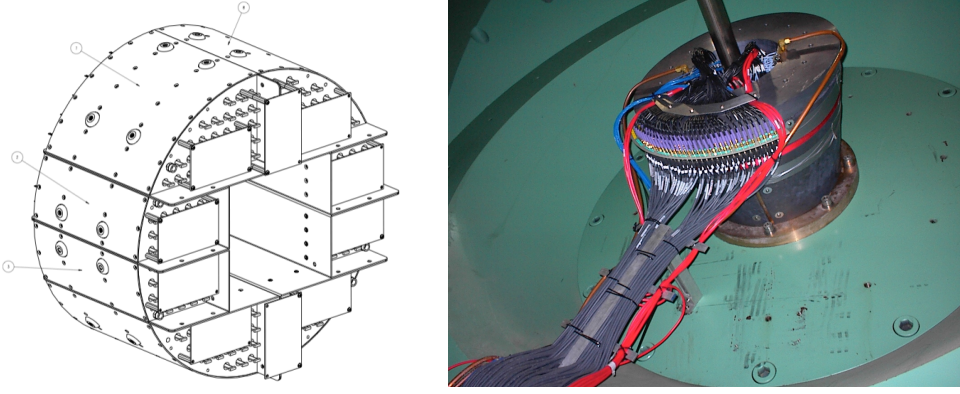


Figure 2.5: (Left) The design of the MPC. (Right) The picture of MPC South [20].

is one of the best candidate materials for a compact calorimeter since it has one of the smallest radiation length (0.89 cm) and moliere radius (2.0 cm) of any known scintillator. Each MPC has 192 (220) crystals of size $2.2 \times 2.2 \times 18 \text{ cm}^3$, sits around the beam-pipe 220 cm from the interaction point, and covers $-3.7 < \eta < -3.1$ ($3.1 < \eta < 3.9$), respectively. Figure 2.5 shows the design of the MPC and the picture of MPC south mounted in PHENIX.

2.4.4 Reaction Plane Detector

The Reaction Plane Detector (RxN) is a scintillator paddle detector embedded with optical fiber light guides connected to photomultiplier tubes [21]. Figure 2.6 shows the schematic diagram and the picture of RxN north mounted in PHENIX. The design purpose is to measure accurately the reaction plane (R.P.) angle of heavy ion collisions. A 2 cm lead (Pb) converter is located directly in front of the scintillators, and it makes photons deposit their energy in the scintillators. Thereby the overall particle flux through the scintillators increases and the accuracy also increases. However due to finite particle statistics and detector granularity, it is impossible to know the angle of Reaction Plane, $\Psi_{R.P.}$, with absolute certainty, thus its experimental measurement is referred to as the event plane angle.

The RxN was designed to optimize the resolution of the 2nd harmonic event plane measurement, while not interfering with the location and particle acceptance of existing PHENIX sub-systems. Because one contributing factor that strongly influences the resolution is the particle multiplicity on the detector, RxN had been installed in the location close to CNT.

The RxN is composed of two sets of 24 scintillators, a north and a south, and located ± 39 cm from the nominal vertex position. The scintillators are arranged perpendicular to and surround a 10 cm diameter beam pipe in 2 concentric rings (inner, outer), with each ring having 2π coverage and 12 equally sized segments in ϕ . All scintillators are trapezoidal in shape, 2 cm thick, made of EJ-200 material from Djent Technology (equivalent to BC408) and individually wrapped with an inner layer of aluminized mylar sheeting for light reflection and an outer layer of black plastic for light tightness. The inner ring covers $1.5 < \eta < 2.8$ and outer ring covers $1.0 < \eta < 1.5$. Because Reaction Plane detector is close to CNT, non-flow effect such as jet and resonance decay should be considered when azimuthal anisotropy study.

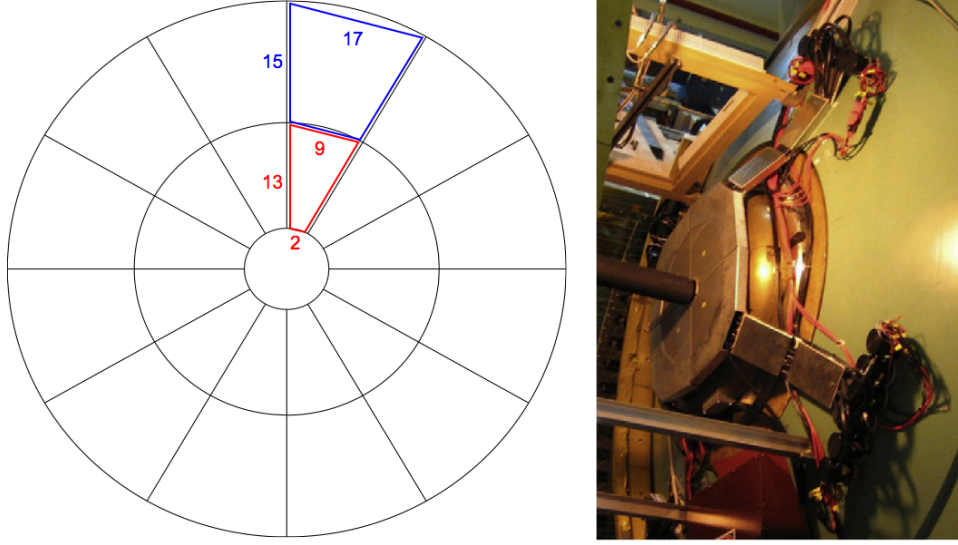


Figure 2.6: (Left) Schematic diagram illustrating the arrangement of the inner (red) and outer (blue) scintillator rings. The length of each scintillator side is shown in centimeters. (Right) The picture of the RxN's north half installed on the Cu nosecone of PHENIX's central magnet prior to the installation of the HBD [21].

2.5 Central Arm Detectors

Central Arm detectors (CNT) are composed by many kinds of spectrometers in order to measure several observables such as momentum, energy, and identify particle species. Pad Chamber is introduced in Section 2.5.1 and Electromagnetic Calorimeter is shown in Section 2.5.2.

2.5.1 Pad Chamber

The PHENIX Pad Chambers (PC) [47] are multi-wire proportional chambers consisted of three separate layers of the PHENIX central tracking system shown in Figure 2.1. Each detector contains a single plane of wires inside a gas volume bounded by two cathode planes. They are installed in order to determine space points along the straight line particle trajectories outside the magnetic field.

The innermost pad chamber plane, called PC1, is located outer of Drift Chamber on both East and West arms. PC2 layer behind the Ring Imaging Cherenkov Detector is present in the West arm. PC3 is mounted just in front of the Electromagnetic Calorimeter. In this analysis, PC3 is used to reject the charged particle signals from photon signal.

2.5.2 Electromagnetic Calorimeter

Electromagnetic Calorimeter (EMCal) [22] is installed in order to measure the energies and spatial positions of photons and electrons. It is also an important part of the PHENIX trigger system. EMCal covers the full central arm with two type of calorimeter, Pb-scintillator (PbSc) sampling calorimeter and Pb-glass Cherenkov calorimeter (PbGl) as shown in Figure 2.1. The four sectors of West arm are PbSc, and two sectors of East arm are PbSc and two of PbGl.

Both calorimeter has different strengths and weaknesses, for example, PbSc has good linearity of energy and timing response to hadrons, PbGl has good granularity and energy resolution.

Lead-scintillator calorimeter

The Pb-scintillator electromagnetic calorimeter is a shashlik type sampling calorimeter made of alternating tiles of Pb and scintillator consisting of 15,552 individual towers. Each Pb-scintillator tower contains 66 sampling cells consisting of alternating tiles of Pb and scintillator. These cells are optically connected by 36 longitudinally penetrating wavelength shifting fibers for light collection. Four towers are mechanically grouped together into a single module as shown in Figure 2.7. Thirty six modules are attached to a backbone and held together by welded stainless-steel skins on the outside to form a rigid structure called a supermodule. Eighteen supermodules make a “sector”, a $2 \times 4 \text{ m}^2$ plane with its own rigid steel frame.

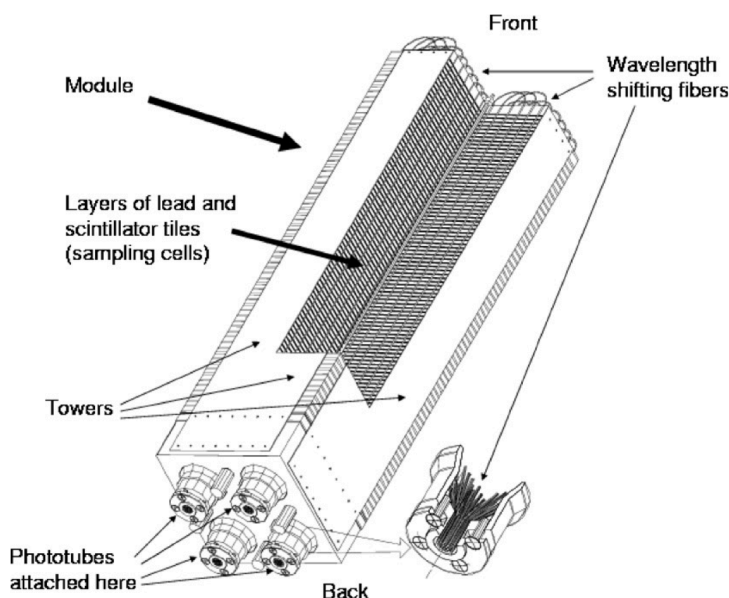


Figure 2.7: Interior view of a Pb-scintillator calorimeter module showing a stack of scintillator and lead plates, wavelength shifting fiber readout and leaky fiber inserted in the central hole [22].

Performance of Detector Response from beam test The energy linearity, resolution and position are measured with the test beam at AGS (BNL) and SPS (CERN). The correlation plot between the incident beam energy and the energy measured in the calorimeter is shown in Figure 2.8. Data are normalized to 1 GeV. The finite light attenuation length (100 cm) in the WS fibers is a major contributor to the response non-uniformities at the low end of the energy scale, although this effect is mitigated by the fact that each fiber is looped back as shown in Figure 2.7, and the light collected always has a short and a long path to the phototube. Other contributors at low energies are coarse sampling and energy leakage at the front face. At high momenta the “positive” effect of the light attenuation in the fibers is overcompensated by the “negative” effect of energy leakage from the back of the calorimeter. The resulting nonlinearity is about a factor of 2 lower than what one would expect from the effect of light attenuation alone.

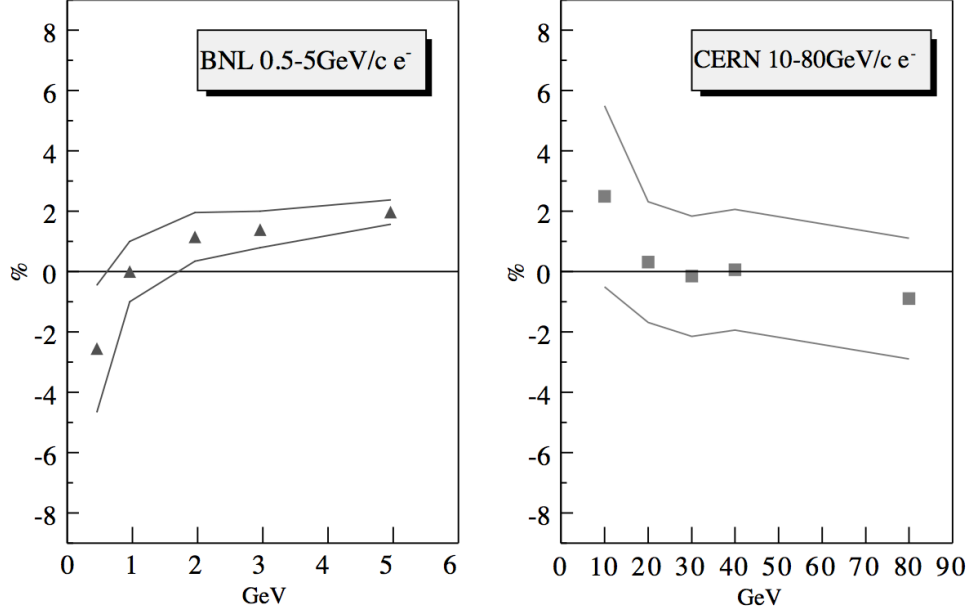


Figure 2.8: Pb-scintillator EMCal energy linearity measured in beam test at AGS (left) and SPS (right). The residual (calorimeter measured energy loss the beam energy, divided by the beam energy) is for the 5×5 tower energy sum. The solid lines show total systematic uncertainties in the analysis [22].

Energy resolution The obtained energy resolution of Lead-Scintillator is shown in Figure 2.9. The resolutions are given by fitting with a liner (A) or quadratic (B) formula as following,

$$\left(\frac{\sigma_E}{E}\right)_A = 1.2\% + \frac{6.2\%}{\sqrt{E(\text{GeV})}}, \quad (2.3)$$

$$\left(\frac{\sigma_E}{E}\right)_B = 2.1\% \oplus \frac{8.1\%}{\sqrt{E(\text{GeV})}}. \quad (2.4)$$

The 8.1% value for the stochastic term is close to the expected resolution from sampling as predicted by GEANT.

Position resolution Both simulation data (GEANT) and experimental data taken at different impact angles show that the measured shower shape (the projection onto the front face of the calorimeter) becomes skewed for non-normal angles of incidence. The data also show a gradual spread of the shower core mainly related to the longitudinal shower fluctuations contributing to the observed width. It depends on impact angle θ as

$$b(\theta) = b_0 \oplus a(E) \times \sin^2(\theta), \quad (2.5)$$

where $b_0=7.3$ mm is the average width of 1 GeV electromagnetic showers for $\theta=0$. At larger angles the contribution from longitudinal fluctuations becomes dominant and the position resolution degrades. All available data on position resolution can be well described by the simple formula as

$$\sigma_x(E, \theta) = \sigma_0(E, 0) \oplus \Delta \times \sin(\theta), \quad (2.6)$$

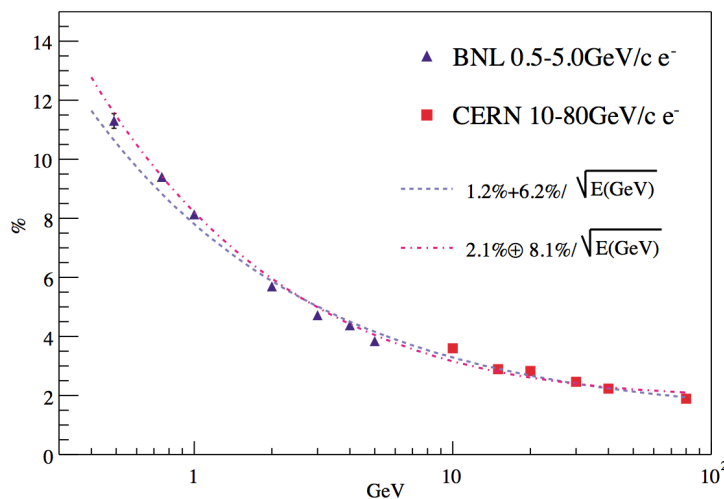


Figure 2.9: Pb-scintillator EMCAL energy resolution obtained by beam tests at AGS and SPS. The blue dashed line shows a fit to the linear formula $\sigma(E)/E = 1.2\% + 6.2\%/\sqrt{E(\text{GeV})}$. The red dashed-dotted line shows the fit to the quadratic formula $\sigma(E)/E = 2.1\% + 8.1\%/\sqrt{E(\text{GeV})}$.

where

$$\sigma_0(E, 0) = 1.55 \oplus \frac{5.7}{\sqrt{E(\text{GeV})}} (\text{mm}), \quad (2.7)$$

is the position resolution for normal incidence.

Lead-glass calorimeter

The Pb-glass calorimeter array comprises 9216 of a system previously used in CERN experiment WA98. The Pb-glass calorimeter locates the two lower sectors of the East Central arm. Each Pb-glass sector comprises 192 supermodules (SM) in an array of 16 Pb-glass SM wide by 12 SM high. Each Pb-glass SM comprises 24 Pb-glass modules in an array of 6 Pb-glass modules wide by 4 modules high. Each Pb-glass module is 40 mm \times 40 mm \times 400 mm in size. Figure 2.10 shows the exploded design of SM.

Energy and position resolution study from beam test The response of the Pb-glass was studied in the beam tests at the AGS (BNL) and SPS (CERN). Figure 2.11 shows the energy resolution of e^+ showers as a function of the incident energy with various angles of incidence on the calorimeter surface. The energy resolution was parameterized as

$$\frac{\sigma(E)}{E} = (0.8 \pm 0.1)\% \oplus \frac{(5.9 \pm 0.1)\%}{\sqrt{E(\text{GeV})}}. \quad (2.8)$$

The position resolution was obtained by

$$\sigma_x(E) = (0.2 \pm 0.1)(\text{mm}) \oplus \frac{(8.4 \pm 0.3)(\text{mm})}{\sqrt{E(\text{GeV})}}. \quad (2.9)$$

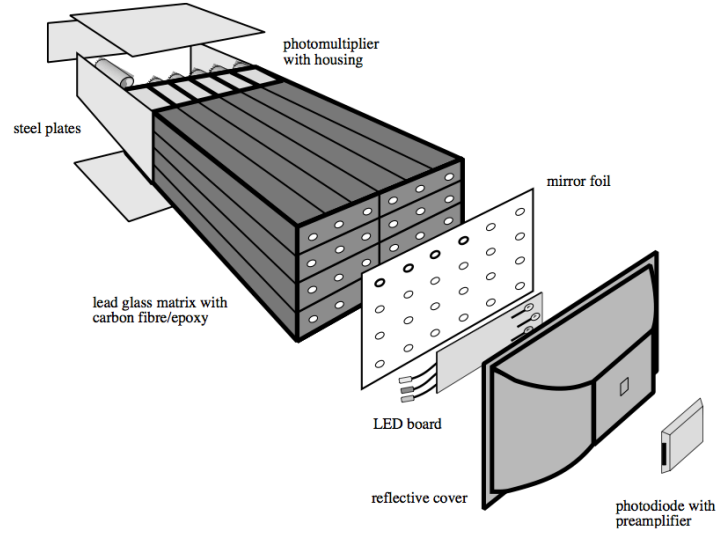


Figure 2.10: Exploded view of a Lead-Glass detector supermodule [22].

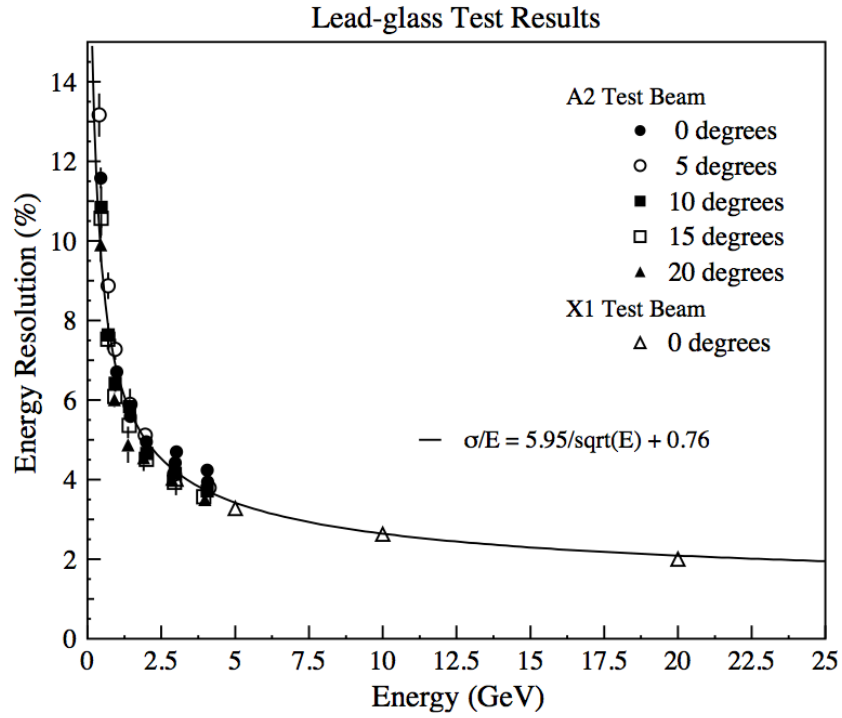


Figure 2.11: PbGl energy resolution as a function of the incident energy. The marker style indicates the difference of incident angle. Energy resolution is $\sigma(E)/E = (0.8 \pm 0.1)\% \oplus (5.9 \pm 0.1)\%/\sqrt{E(\text{GeV})}$ [22].

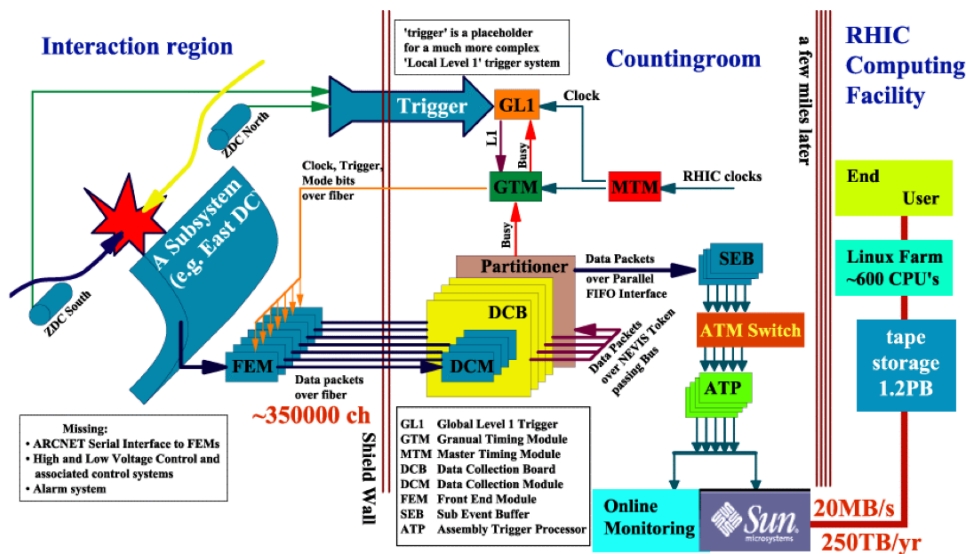


Figure 2.12: Schematic diagram of the PHENIX on-line system [23].

2.5.3 Data Acquisition System

The PHENIX Data Acquisition System (DAQ) is designed to accomplish the data taking in a variety of colliding system from $p+p$ to $U+U$ collisions [23]. The occupancy in the detector varies from a few tracks in $p+p$ collisions to approximately 10% of all detector channels in central Au+Au collision. The interaction rate changes from a few kHz for Au+Au collisions to approximately 500 kHz for $p+p$ collisions. The PHENIX DAQ system was accomplished through the pipelined and deadtimeless features of the detector front ends and the ability to accommodate higher level triggers. Figure 2.12 shows the general schematic for the PHENIX On-Line system.

In PHENIX it is required to measure low-mass lepton pairs and low p_T particles in a high-background environment. It is also needed to detect rare interactions that provide direct probes of the QGP, such as high p_T photon. In order to preserve the high interaction-rate capability of PHENIX, a flexible triggering system that permits tagging of events was constructed.

Front End Electronics

Signals from the various PHENIX subsystems are processed by Front End Electronics (FEE). The detector signals are converted into digital data at FEE. The signals are buffered in order to wait for the Level-1 trigger (LVL1) decisions, which takes about 40 beam crossings. This involves analog signal processing with amplification and shaping to extract the optimum time and/or amplitude information, development of trigger input data. If the LVL1 trigger accepts an event, a signal is transmitted to the Granule Timing Module (GTM) generating an ACCEPT signal sent to the detector FEMs. Then the FEMs process the data from the individual sub-detectors and send it to the Data Collection Modules (DCM) for assembly.

Data Collection Modules

The data of the individual sub-detectors are collected to the Data Collection Modules (DCM). Zero suppression, error checking, and data reformatting are operated in the DCMs. The average LVL1 trigger is 25 kHz and the RHIC beam crossing clock runs at 9.4 MHz. At the maximum LVL1 trigger rate, the FEMs send over 100 Gbytes of data per second. The data are sent to the Event Builder (EvB).

Event Builder

The two primary functions of the Event Builder (EvB) are the final stage of event assembly in the DAQ and to provide an environment in which Level-2 trigger (LVL2) processing is performed. Many parallel data streams from DCMs are sent to the EvB and each data stream is assembled into complete event. The EvB performs LVL2 trigger processing on the events and transmits accepted events to the Online Control System (ONCS) for logging and distribution to monitoring processes.

Event Trigger

The On-Line system has two level of triggering denoted as the Level-1 trigger (LVL1) and the Level-2 trigger (LVL2). The responsibility of the LVL1 is to select potentially interesting events for all colliding species and provide event rejection sufficient to reduce the data rate. The LVL1 consists of two separate subsystems. The Local Level-1 (LL1) system communicates with participating detector systems such as BBC and ZDC. The input data from these detector systems are processed by the LL1 algorithms to produce a set of reduced-bit input data for each event. The Global Level-1 (GL1) system receives, combines this data to provide a trigger decision, and manage the busy signals.

In order to collect the rare events, for example, which includes high p_T photon or electron pair, and reduce dead-time, LVL2 trigger is set additionally. The LVL2 is performed in the EvB.

Chapter 3

Analysis

In this study, about 4.4 billion events in $\sqrt{s_{NN}} = 200$ GeV Au + Au collisions taken at the RHIC-PHENIX experiment in 2007 (Run7) are analyzed. In this chapter, event selection is described in Section 3.1, event plane determination is discussed in Section 3.2, photon selection is explained in Section 3.3, measurement of inclusive photon v_n is shown in Section 3.4, measurement of neutral pion v_n is described in Section 3.5, simulation of decay photon v_n is discussed in Section 3.6, and measurement of direct photon v_n is shown in Section 3.7.

3.1 Event Selection

Minimum Bias (MB) trigger is used to select the data. MB is defined that there is at least two hits in each BBC, at least one hit in each ZDC, and primary vertex position on z direction is within 38 cm from nominal vertex position. In addition to MB, the selection with vertex position within 30 cm is applied in this thesis.

3.1.1 Centrality Determination

The centrality is a part of classifying collision geometry which is given by impact parameter or volume of overlap region between nuclei in event-by-event as shown in Figure 1.6. However it is impossible to measure impact parameter experimentally. Because it is expected that the number of the emitted particles are closely proportional to the volume of overlap region, we define centrality with the multiplicity.

In PHENIX experiment, the centrality is defined from the charge sum in the BBC North and South combined. Because the centrality is expected to relate the number of participants (N_{part}), the relation between centrality and N_{part} is studied. The negative binomial distribution (NBD) is introduced to connect between N_{part} and the multiplicity. The assumptions are (1) each nucleon independently produces particles, (2) underlying probability distribution of particle production as following

$$NBD(x; \mu, \kappa) = \left(1 + \frac{\mu}{\kappa}\right) \frac{(\kappa + x - 1)!}{x! (\kappa - 1)!} \left(\frac{\mu}{\mu + \kappa}\right)^x, \quad (3.1)$$

$$nNBD(x; \mu, \kappa) = NBD(x; n\mu, n\kappa). \quad (3.2)$$

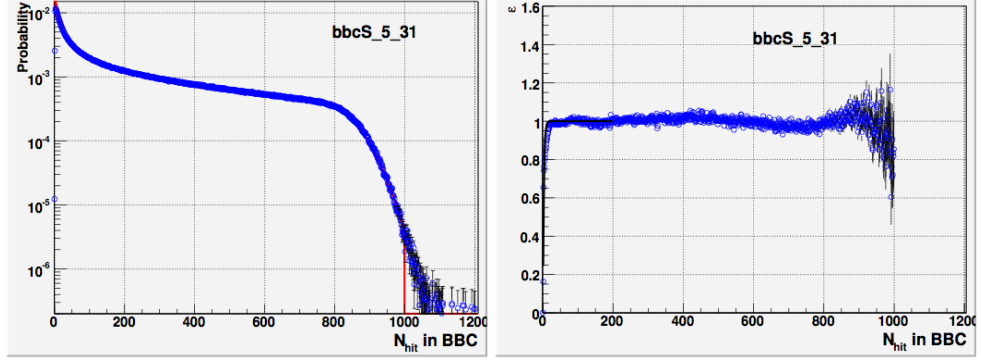


Figure 3.1: (Left) The charge sum distribution in BBC South (blue) and the NBD fitting (red) [24]. (Right) The ratio of data to the NBD equation.

The NBD is parameterized by the average number of emitting particles per one participant (μ) and the fluctuation (κ). Randomly sampling from $nNBD(\mu, \kappa)$ distributions follow $NBD(n\mu, n\kappa)$.

The possibility that BBC has charge x ($P(x)$) with normalized per event is given as

$$P(x) = \sum_{n=1}^{N_{coll}(max)} G(n) \times NBD(x; n\mu, n\kappa), \quad (3.3)$$

where $G(n)$ is the number of binary collisions calculated by the Glauber Monte-Carlo model and two parameters of μ and κ are free parameters. Figure 3.1 shows the charge sum distribution in the BBC (N_{hit}^{BBC}) fitted by $P(x)$ to determine μ and κ in $N_{hit}^{BBC} > 20$ in order to avoid the trigger inefficiency in low BBC charge. The BBC charge distribution fitted by the NBD is shown in Figure 3.1. It is defined that the relation between the charge sum in BBC and the parameter N_{part} , N_{coll} , impact parameter b simulated by the Glauber Monte-Carlo. They are summarized in Table 3.1 [36].

The table of parameters with systematic uncertainty			
Centrality %	$\langle N_{part} \rangle$	$\langle N_{col} \rangle$	$\langle b \rangle$
0-10	325 ± 4	960 ± 96	3.13 ± 0.11
10-20	236 ± 6	609 ± 60	5.65 ± 0.21
20-30	167 ± 6	377 ± 36	7.33 ± 0.28
30-40	115 ± 6	223 ± 23	8.70 ± 0.33
40-50	76 ± 6	124 ± 15	9.88 ± 0.39
50-60	47 ± 5	63 ± 9	10.94 ± 0.43
0-20	280 ± 5	783 ± 78	4.40 ± 0.16
20-40	141 ± 6	300 ± 30	8.02 ± 0.31
40-60	62 ± 5	94 ± 12	10.41 ± 0.41

Table 3.1: The summary of relations between the centrality and the parameters of $\langle N_{part} \rangle$, $\langle N_{col} \rangle$, impact parameter $\langle b \rangle$ [36].

3.2 Event Plane Determination

In this section, we introduce how to determine the event plane. The particle distribution in azimuthal angle is discussed in Section 3.2.1, the method of determination of event plane is described in Section 3.2.2, the manner of event plane calibration is introduced in Section 3.2.3, and the resolution of event plane is shown in Section 3.2.4.

3.2.1 Azimuthal Distribution of Emitted Particles

The azimuthal distribution $r(\phi)$ of emitted particles is written by Fourier expansion of the periodic function with 2π period as below,

$$\begin{aligned} r(\phi) &= \frac{x_0}{2\pi} + \frac{1}{\pi} \sum_{n=1}^{\infty} \{x_n \cos(n\phi) + y_n \sin(n\phi)\}, \\ &= \frac{x_0}{2\pi} \left[1 + 2 \sum_{n=1}^{\infty} \left\{ \frac{x_n}{x_0} \cos(n\phi) + \frac{y_n}{x_0} \sin(n\phi) \right\} \right], \end{aligned} \quad (3.4)$$

where n is the harmonics, x_n and y_n are the integral components of the r for x and y direction. The x_n and y_n are given by the summation of the number of particles due to a finite number of particles in an event as following

$$x_n = \int_0^{2\pi} d\phi r(\phi) \cos(n\phi) = \sum_i r_i(\phi) \cos(n\phi_i), \quad (3.5)$$

$$y_n = \int_0^{2\pi} d\phi r(\phi) \sin(n\phi) = \sum_i r_i(\phi) \sin(n\phi_i), \quad (3.6)$$

where i runs over all particles generated by collisions and ϕ_i is the azimuthal angle of i^{th} particle. When the angle of emitted particles are measured with respect to event plane angle (Ψ_n), then Fourier-expansion is modified as

$$\begin{aligned} r(\phi) &= \frac{x_0}{2\pi} + \frac{1}{\pi} \sum_{n=1}^{\infty} [x'_n \cos\{n(\phi - \Psi_n)\} + y'_n \sin\{n(\phi - \Psi_n)\}], \\ &= \frac{x_0}{2\pi} \left[1 + 2 \sum_{n=1}^{\infty} \frac{x'_n}{x_0} \cos\{n(\phi - \Psi_n)\} \right], \\ &= \frac{x_0}{2\pi} \left[1 + 2 \sum_{n=1}^{\infty} v_n \cos\{n(\phi - \Psi_n)\} \right]. \end{aligned} \quad (3.7)$$

Because the emitted particle distribution in azimuthal angle with respect to event plane angle is assumed to be symmetric, sine term is vanished. The coefficients $v_n = \langle \cos\{n(\phi - \Psi_n)\} \rangle$ is the strength of azimuthal anisotropy, where brackets $\langle \dots \rangle$ means an average over all particles in all events.

From emitted particle distribution in azimuthal angle, v_n and Ψ_n are written as

$$v_n = \frac{\sqrt{x_n^2 + y_n^2}}{x_0}, \quad (3.8)$$

$$\Psi_n = \frac{1}{n} \tan^{-1} \left(\frac{y_n}{x_n} \right) \quad (0 \leq \Psi_n \leq \frac{2\pi}{n}). \quad (3.9)$$

Using Eq.(3.8) and (3.9), the azimuthal distribution Eq. (3.4) is modified as,

$$\begin{aligned}
 r(\phi) &= \frac{x_0}{2\pi} \left[1 + 2 \sum_{n=1}^{\infty} \left\{ \frac{x_n}{x_0} \cos(n\phi) + \frac{y_n}{y_0} \sin(n\phi) \right\} \right], \\
 &= \frac{x_0}{2\pi} \left[1 + 2 \sum_{n=1}^{\infty} \{ v_n \cos(n\phi) \cos(n\Psi_n) + v_n \sin(n\phi) \sin(n\Psi_n) \} \right], \\
 &= \frac{x_0}{2\pi} \left[1 + 2 \sum_{n=1}^{\infty} v_n \cos\{n(\phi - \Psi_n)\} \right].
 \end{aligned} \tag{3.10}$$

However, the v_n measured by experimentally observed Ψ_n is not true v_n . It is needed to estimate true v_n (v_n^{true}) from observed v_n ($v_n^{obs.}$). The $v_n^{obs.}$ can be rewritten as

$$\begin{aligned}
 v_n^{obs.} &= \langle \cos\{n(\phi - \Psi_n^{obs.})\} \rangle, \\
 &= \langle \cos\{n(\phi - \Psi_n^{true} + \Psi_n^{true} - \Psi_n^{obs.})\} \rangle, \\
 &= \langle \cos\{n(\phi - \Psi_n^{true})\} \cos\{n(\Psi_n^{true} - \Psi_n^{obs.})\} \rangle - \langle \sin\{n(\phi - \Psi_n^{true})\} \sin\{n(\Psi_n^{true} - \Psi_n^{obs.})\} \rangle, \\
 &= \langle \cos\{n(\phi - \Psi_n^{true})\} \rangle \langle \cos\{n(\Psi_n^{true} - \Psi_n^{obs.})\} \rangle, \\
 &= v_n^{true} \langle \cos\{n(\Psi_n^{true} - \Psi_n^{obs.})\} \rangle,
 \end{aligned} \tag{3.11}$$

$$v_n^{true} = \frac{v_n^{obs.}}{\langle \cos\{n(\Psi_n^{true} - \Psi_n^{obs.})\} \rangle}, \tag{3.12}$$

where the average of sine terms vanish because the ϕ distributions with respect to Ψ_n^{true} is expected to be symmetry. It is found that the v_n^{true} is estimated from the ratio of $v_n^{obs.}$ and $\langle \cos\{n(\Psi_n^{true} - \Psi_n^{obs.})\} \rangle$. The term of $\langle \cos\{n(\Psi_n^{true} - \Psi_n^{obs.})\} \rangle$ is called the event plane resolution which will be discussed in Section 3.2.4

3.2.2 Event Plane Determination

In this analysis, RxN, MPC and BBC are used for determination of event plane. As shown in Section 2.4, they cover full azimuthal angle and are divided into several segments in azimuthal angle. For example, The RxN(In) have 24 segments (scintillators) combined of North and South. Event plane is obtained by Eq. (3.9), experimentally, it can be estimated as

$$\Psi_n^{obs} = \frac{1}{n} \tan^{-1} \left(\frac{Q_y}{Q_x} \right), \tag{3.13}$$

$$Q_x = \sum_{i=1}^m w_i \cos(n\phi_i), \tag{3.14}$$

$$Q_y = \sum_{i=1}^m w_i \sin(n\phi_i), \tag{3.15}$$

where m is the total number of the segments, Ψ_n^{obs} is the measured n^{th} harmonic of event plane, Q_x and Q_y are the event flow vectors, w_i and ϕ_i are the weight and the azimuthal angle of i^{th} segment, respectively. For example, w_i is the charge output of each PMT which is normalized by the total charge of all segments. The azimuthal angle distribution of event plane should be flat but measured distribution is be flat due to existence of dead PMTs, unequal PMT's gains, finite number of PMTs, and the offset of beam position, shown as blue distribution in Figure 3.2. The calibration method is introduced in Section 3.2.3.

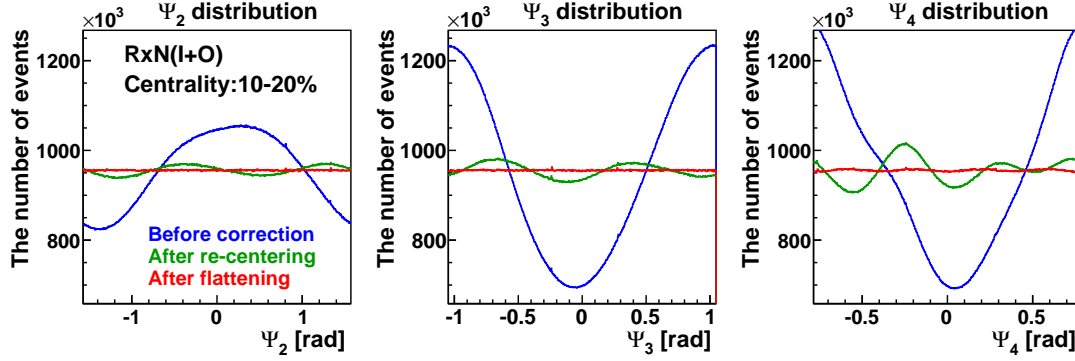


Figure 3.2: The event plane angle distributions of RxN(I+O) in 10-20% centrality. (Blue) The event plane angle with no correction. (Green) The distribution of event plane after re-centering. (Ref) The distribution of event plane after flattening.

3.2.3 Event Plane Calibration

There are several steps of calibrations to correct event plane angle. First, PMT's gains are calibrated to have the same mean charge value. The second step is re-centering calibration which recenters the average of the event flow vector Q_x , Q_y , and normalizing the width of their distribution.

$$\Psi_n^{corr} = \frac{1}{n} \tan^{-1} \left(\frac{Q_y^{corr}}{Q_x^{corr}} \right), \quad (3.16)$$

$$Q_x^{corr} = \frac{Q_x - \langle Q_x \rangle}{\sigma_x}, \quad (3.17)$$

$$Q_y^{corr} = \frac{Q_y - \langle Q_y \rangle}{\sigma_y}, \quad (3.18)$$

where $\langle Q_x \rangle$ ($\langle Q_y \rangle$) are the mean of Q_x (Q_y) over many events, and σ_x , (σ_y) are the standard deviation of Q_x (Q_y) distribution, respectively.

The third step is flattening calibration to remove the remaining non-flatness of event planes [48]. It is written as

$$\Psi_n^{flat} = \Psi_n^{corr} + \sum_i \left[\frac{2}{i} \{ \langle \cos(in\Psi_n^{corr}) \rangle \sin(in\Psi_n^{corr}) - \langle \sin(in\Psi_n^{corr}) \rangle \cos(in\Psi_n^{corr}) \} \right]. \quad (3.19)$$

In this analysis, i runs up to 8. It is found that the event plane distributions is flat after all correction, and it is shown as red distributions in Figure 3.2.

3.2.4 Event Plane Resolution

The method of estimating event plane resolution is introduced in this section. In this analysis, 2-sub method is utilized. Event plane resolution can be expressed as [49],

$$\langle \cos \{ km(\Psi_m^{obs.} - \Psi_l^{true}) \} \rangle = \frac{\sqrt{\pi}}{2\sqrt{2}} \chi_m \exp(-\chi_m^2/4) [I_{(k-1)/2}(\chi_m^2/4) + I_{(k+1)/2}(\chi_m^2/4)] \quad (3.20)$$

$$\chi_m = v_m \sqrt{2N}, \quad (3.21)$$

where I_ν is the modified Bessel function of the first kind of order ν , the constant of m, l are the harmonics, and N is the number of particles used to determine the event plane. When the harmonics of event plane are the same ($m = l$), $k=1$ is used.

The correlation between Ψ_n^a and Ψ_n^b can be expanded as,

$$\langle \cos \{n(\Psi_n^a - \Psi_n^b)\} \rangle = \langle \cos \{n(\Psi_n^a - \Psi_n^{true})\} \rangle \langle \cos \{n(\Psi_n^b - \Psi_n^{true})\} \rangle. \quad (3.22)$$

The sine term is vanished due to symmetry. It is obtained that the correlation between event plane measured by detector a (Ψ_n^a) and b (Ψ_n^b) is represented by multiplying between the resolution of Ψ_n^a and Ψ_n^b . Experimentally the resolution of event plane angle is estimated by the correlation between the measured event plane.

When multiplicity and v_n are the same between the detector a and b , for example, they are RxN South and North, it is expected that the resolutions of Ψ_n^{South} and Ψ_n^{North} are the same. Therefore, the resolution of each detector can be given as

$$\langle \cos \{n(\Psi_n^{South} - \Psi_n^{true})\} \rangle = \langle \cos \{n(\Psi_n^{North} - \Psi_n^{true})\} \rangle = \sqrt{\langle \cos \{n(\Psi_n^{South} - \Psi_n^{North})\} \rangle}. \quad (3.23)$$

Additionally, because χ_n is proportional to \sqrt{N} , χ_n for the combinations of South and North RxN detector is given as

$$\chi_n^{South+North} = \sqrt{2}\chi_n^{South} = \sqrt{2}\chi_n^{North}. \quad (3.24)$$

Because the resolution can be calculated from χ_n , the resolution of the combination of South and North detectors can be estimated from the correlation between the event plane of South and North detector. The correlation between event plane measured by each of South and North detector and the resolution for the combination of South and North detectors are shown in Figure 3.3

3.3 Photon Selection

In this section, experimental photon identifications at Electromagnetic calorimeter are introduced. The manner of clustering is introduced in Section 3.3.1, and photon identification is shown in Section 3.3.2.

3.3.1 EMCal Clustering

In this section, the manner of EMCal clustering is introduced [50, 25]. The Moliere radius (R_M) of the calorimeter is the characteristic radius of the electromagnetic shower where 90% of the energy is contained. The R_M of EMCal is calculated about 3 - 4 cm by using the typical value of a radiation length (X_0) as 2.1 cm for PbSc and 2.8 cm for PbGl. Electromagnetic shower deposits its energy on some towers. It is needed to merge their towers to measure the particle energy and position. In this section, the measurement and correction of cluster energy and hit position are shown.

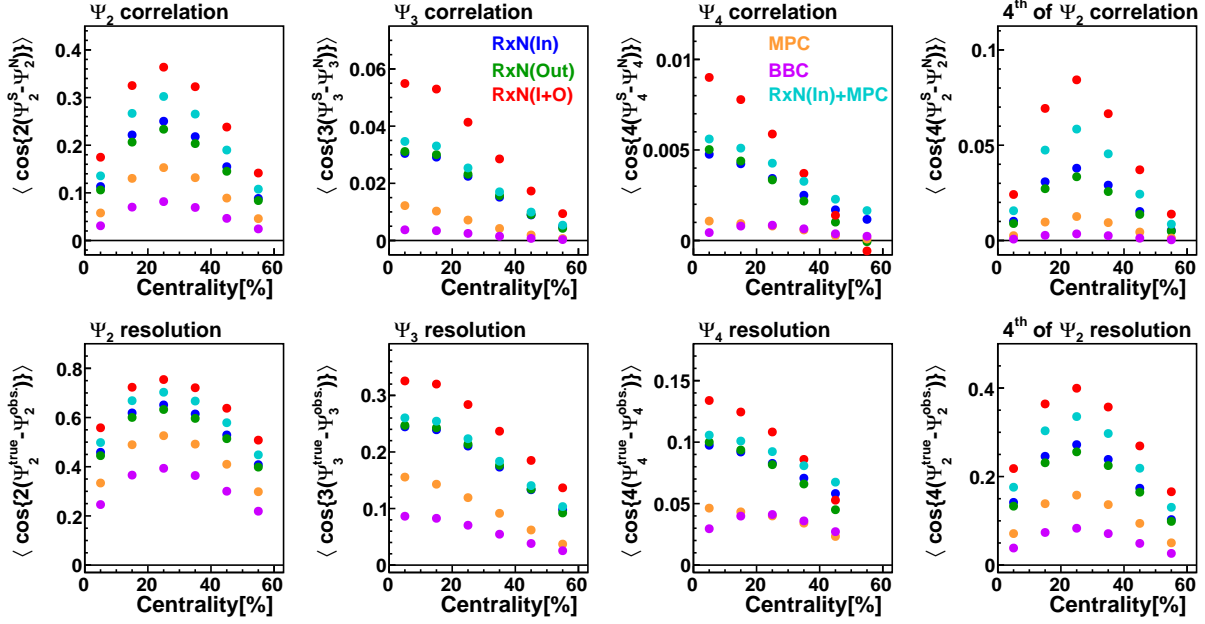


Figure 3.3: (Top) The event plane angle correlation between North and South subdetectors. (Bottom) The event plane resolution of the detector combining South and North.

Cluster energy measurement

The energy deposit from electromagnetic shower in EMCal was studied in the beam test, which was precisely calibrated by electrons and positrons. The predicted shower shape function of i -th tower (F_i) which is 2-D exponential in the tower distance from local maximum tower is parameterized by

$$\begin{aligned}
 F_i &= \frac{E_i^{pred.}}{E_{tot}}, \\
 &= P_1(E_{tot}, \alpha) \exp \left\{ -\frac{(r_i/r_0)^3}{P_2(E_{tot}, \alpha)} \right\} + P_3(E_{tot}, \alpha) \exp \left\{ -\frac{(r_i/r_0)}{P_4(E_{tot}, \alpha)} \right\}, \quad (3.25)
 \end{aligned}$$

where, $E_i^{pred.}$ is the predicted energy of i^{th} tower, r_i is the distance between the center of i^{th} tower and corrected hit position, and r_0 is the surface size of a EMCal cell (5.5 cm). P_n is the parameterized function which depend on the total energy E_{tot} and impact angle α defined as the angle of incidence. The parameters P_n is obtained from the beam test as

$$P_1 = 0.59 - (1.45 + 0.13 \ln E_{tot}) \sin^2(\alpha), \quad (3.26)$$

$$P_2 = 0.27 + (0.80 + 0.32 \ln E_{tot}) \sin^2(\alpha), \quad (3.27)$$

$$P_3 = 0.25 + (0.45 - 0.036 \ln E_{tot}) \sin^2(\alpha), \quad (3.28)$$

$$P_4 = 0.42. \quad (3.29)$$

Figure 3.4 shows the example of the shower shape function in the case of that a photon hits at the center of a tower perpendicularly. It is found that the electromagnetic shower deposits about 84% of own energy in the hit tower, and other towers have less than 4% energy. The

shower core energy E_{core} is defined by the predicted fractions F_i having more than 2% of F_i . The E_{corr} is defined as

$$E_{core} = \sum_{\text{for } F_i > 0.02} E_i, \quad (3.30)$$

where E_i is the measured energy deposit in the i^{th} tower. The example of core clustering is shown as the area surrounded by dotted line.

The variance of the predicted energy function σ_E is parameterized with α and the total of missed energy due to the clustering thresholds $q(E_{tot})$ as

$$\sigma_E^2 = A \cdot E_i^{pred.} \left\{ 1 + B \sqrt{E_{tot}} \sin^4(\alpha) \right\} \left(1 - \frac{E_i^{pred.}}{E_{tot}} \right) + q(E_{tot}), \quad (3.31)$$

$$q(E_{tot}) = 0.005^2 + 0.0014^2 \cdot E_{tot}^2 (\text{GeV}^2), \quad (3.32)$$

where $A=0.03$ (GeV^2) is the scale for energy fluctuations of the shower and $B = 4.0/0.03 - 133$ is the amplitude of correction function for impact angle given by the test beam data. For example, when one 1 GeV photon entered to EMCAL perpendicularly, the predicted energy deposit on the center tower is about 840 MeV and the energy fluctuation variance is 64 MeV.

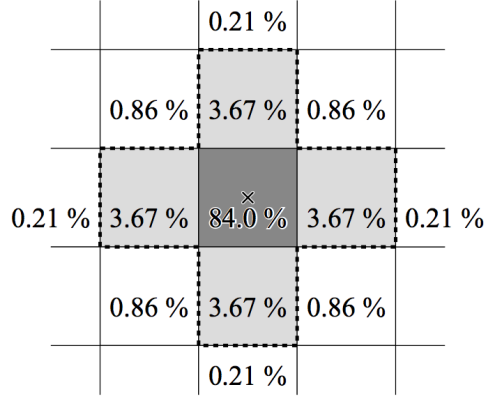


Figure 3.4: The example of predicted shower energy fraction in towers under assuming that a photon hits on the center of tower perpendicularly. The core clusters formed by the towers contained more than 2% of total energy. The cluster is surrounded by dotted line [25].

Correction for E_{core}

The number of towers used for E_{core} depends on the hit position on the tower surface. The contribution from the shower tail is definitely neglected from E_{core} . For example, $0.86 \times 4 + 0.21 \times 4 = 4.28\%$ of shower energy is missed in Figure 3.4. Therefore, it is needed to correct E_{core} with the incident angle α and measured E_{core} . It is estimated by Monte Carlo simulation which uses the parameterization obtained by beam test as

$$E_{core}^{corr} = \frac{1.089}{1.0 - 1.35 \sin^4(\alpha) \{1.0 - 0.003 \ln(E_{core})\}} E_{core}. \quad (3.33)$$

The corrected core energy E_{core}^{corr} denotes E_{core} simply in the following.

The resolution of the E_{core} is studied by a simple convolution of the energy by the fluctuation due to the E_{core} algorithm. Figure 3.5 shows the results with respect to 0.5, 1, and 4 GeV photon energy. Although the E_{core} algorithm causes a bit worth performance in energy resolution, the effect is small.

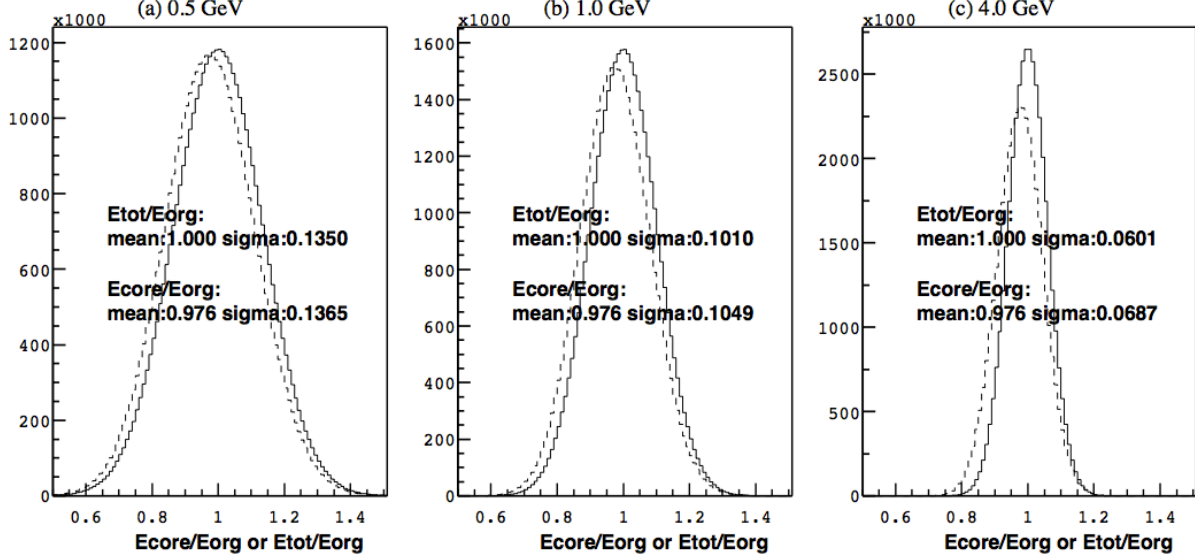


Figure 3.5: The resolution distributions of reconstructed photon energy studied by using GEANT simulation. The ratio of core energy E_{core} (dashed line) and total energy E_{tot} (solid line) to the true photon energy (E_{org}) on the simple gaussian distribution with intrinsic EMCal energy resolution for 0.5, 1.0, and 4.0 GeV photons [25].

Cluster position measurement

In this section, the estimating of the hit position on the surface of EMCal is introduced. The energy gravity $(x, y)_c$ of the cluster can be written as

$$(x, y)_c = \frac{\sum (x_i, y_i) E_i}{\sum E_i}, \quad (3.34)$$

where (x_i, y_i) , E_i are the center of position and deposit energy of i^{th} tower, respectively. However, it is not sufficient that the hit position is estimated by the energy gravity in the experiment, because the shower shape depends on the incidence angle α . The correlation between true hit position $(x, y)_{corr}$ and $(x, y)_c$ was studied by beam test and they are parameterized as

$$\begin{pmatrix} x_{corr} \\ y_{corr} \end{pmatrix} = \begin{pmatrix} x_c - \{1.05 + 0.12 \ln(E_{tot})\} \sin^2(\alpha_x) \\ y_c - \{1.05 + 0.12 \ln(E_{tot})\} \sin^2(\alpha_y) \end{pmatrix}, \quad (3.35)$$

$$\sin \alpha_x = \frac{v_x}{\sqrt{v_x^2 + v_z^2}}, \quad (3.36)$$

$$\sin \alpha_y = \frac{v_y}{\sqrt{v_y^2 + v_z^2}}, \quad (3.37)$$

where (v_x, v_y, v_z) is the vector from collision vertex to the center of gravity. The definition of (v_x, v_y, v_z) , α_x , α_y are shown in Figure 3.6.

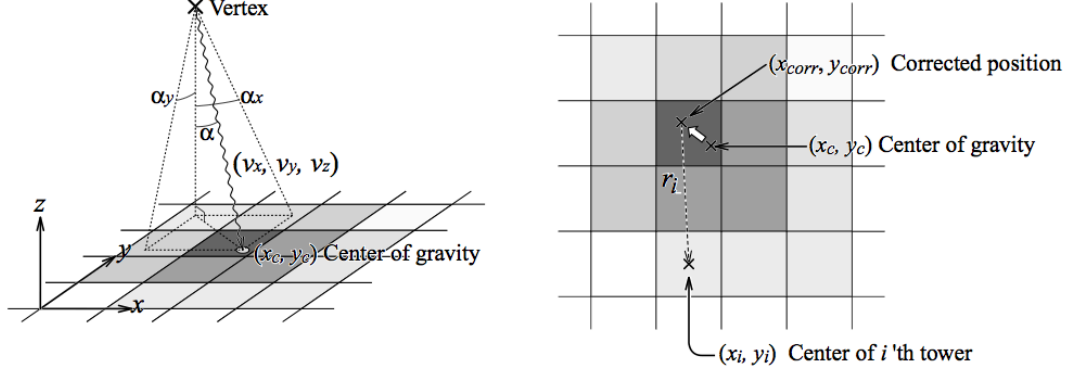


Figure 3.6: (Left) Definitions of impact angle and vector of (v_x, v_y, v_z) . (Right) The hit position correction from energy gravity to true position. The amplitude of deposit energy is represented by shaded gray area [25].

3.3.2 Photon identification

The clustering algorithm to measure the energy and hit position of photon is introduced in Section 3.3.1. Additional selections are utilized to identify photon in this analysis, and they are listed below.

- Energy threshold for E_{core}
- Bad tower rejection
- Shower shape cut χ^2
- Charged particle rejection

Energy threshold cut ($E_{core} > 200$ MeV) is applied to exclude the noise clusters because a lot of small fragment clusters which have energy of about 100 MeV are constructed due to the PHENIX clustering algorithm.

Bad tower rejection

In the PHENIX EMCal, bad condition towers are recognized by the “bad tower map”, which is defined by following rules,

Warn map high frequency of hits in the low energy (< 2 GeV) region

Hot map high frequency of hits in the high energy region

Dead map low frequency or no hits

The “bad tower map” is identified in online analysis before data reconstruction by the total number of hits, the integrated energy, and the average per event energy for each tower. Figure 3.7 shows the hit distribution per a tower in sector 1 and gaussian equation is fitted in order to identify bad towers. The high frequency towers which hit higher than 5σ of the hit frequency per tower are tagged as “Warn tower” (in low energy region), or “Hot tower” (in high energy region). Low frequency towers which hit lower than 5σ of the hit frequency per tower are tagged as “Dead tower”. The towers failed in energy scale calibration are also added to “Dead tower” map. The “bad” towers and their around 3×3 towers are excluded from following analysis because the 3×3 towers are used for core clustering in the clustering algorithm. In addition, the towers on edge of each sector are also removed from analysis because a shower shape can not be reconstructed correctly.

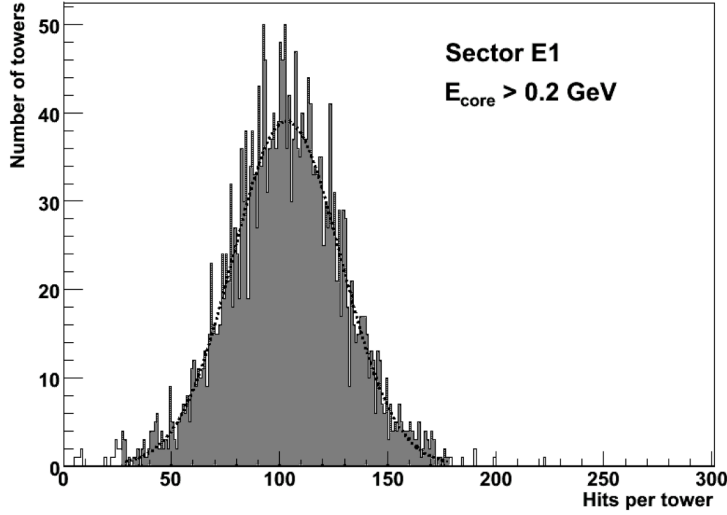


Figure 3.7: Hit distribution per tower in sector 1. Dotted line shows the fitted gaussian equation. The towers out of 5σ denote as bad towers [25].

3.3.3 Shower shape cut

We measure the shower shape at EMCal to identify the signal as a electromagnetic and hadronic particles. Electromagnetic particles drop their entire energy at the calorimeter while almost hadronic particles pass through with losing a part of their energy. That is why the shower shape is expected to distinguish electromagnetic particles and hadrons. Therefore, shower shape is used for differentiating photons.

The shower shape is defined as

$$\chi^2 = \frac{\sum_i (E_i^{pred.} - E_i^{meas.})^2}{\sigma_i}, \quad (3.38)$$

where $E_i^{meas.}$ is the energy measured in i^{th} tower, $E_i^{pred.}$ is the predicted energy estimated by Eq. (3.25), and σ_i is the variance of tower energy estimated by Eq. (3.31). This χ^2 value characterizes how “electromagnetic” a particular shower is, and the χ^2 distributions for 2 GeV/c electrons and pions (with energy deposit above minimum ionization) are shown in Figure 3.8.

The shower shape of photon is known to be the almost same with that of electron excepting the starting point of energy deposit in the EMCal. The $\chi^2 < 3$ is applied for selecting photon signal in this thesis.

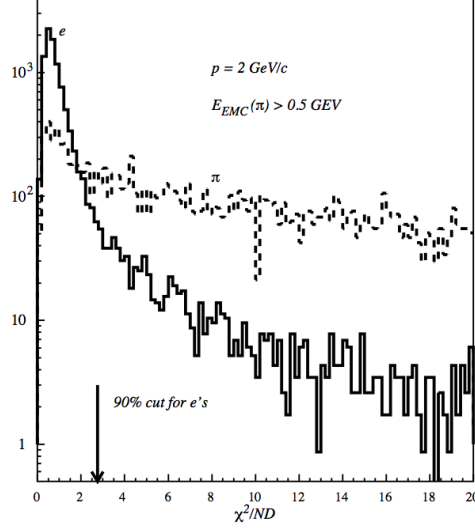


Figure 3.8: χ^2 distribution for showers induced by 2 GeV/c electrons and pions in the Pb-scintillator calorimeter. The arrow marks the χ^2 cut corresponding to 90% electron efficiency [25].

3.3.4 Charged Particle Rejection

The shower created by charged particles can be rejected via using PC3. The PC3 is located in front of the EMCal as shown in Figure 2.1. The distance of the position between the cluster on EMCal and nearest the signal on PC3 ($r_{EMCal-PC3}$) is given as

$$\begin{aligned} r_{EMCal-PC3} &= \sqrt{dx_{EMCal-PC3}^2 + dy_{EMCal-PC3}^2 + dz_{EMCal-PC3}^2} \\ &= \sqrt{(r_T \sin(d\phi_{EMCal-PC3}))^2 + dz_{EMCal-PC3}^2}, \end{aligned} \quad (3.39)$$

$$r_T = \sqrt{x_{EMCal-PC3}^2 + y_{EMCal-PC3}^2}, \quad (3.40)$$

where r_T is the length between EMCal hit position and vertex position in x and y direction. The $r_{EMCal-PC3} > 6.5$ cm (6.5 cm is defined referring to Moliere radius) is applied for rejecting the cluster of charged hadron in this thesis.

3.4 Inclusive photon v_n measurement

3.4.1 Inclusive photon v_n measurement

Inclusive photon v_n is measured by two type of methods, which is related with bin selections.

- method 1 : $\langle \cos \{n(\phi - \Psi_n)\} \rangle$
- method 2 : $N_0(1 + 2v_n \cos \{n(\phi - \Psi_n)\})$ is fitted to $\Delta\phi$ distribution

where brackets indicates average for all photons and events. Fitting function is Fourier expansion and written as

$$N_0[1 + 2v_2 \cos \{2(\phi - \Psi_2)\} + 2v_4(\Psi_2) \cos \{4(\phi - \Psi_2)\}] \quad (\text{for } v_2 \text{ and } v_4(\Psi_2)), \quad (3.41)$$

$$N_0[1 + 2v_n \cos \{n(\phi - \Psi_n)\}] \quad (\text{for } v_3 \text{ and } v_4(\Psi_4)). \quad (3.42)$$

Figure 3.9 shows the example plots of these equations fitting to the inclusive photon distribution with respect to each harmonics event plane. The average value of v_n obtained method 1 and method 2 is utilized for the mean points in this analysis. Figure 3.10 shows the results of inclusive photon v_2 , v_3 , and v_4 with method 1 and method 2. The difference of v_n between these method is defined as systematic uncertainty.

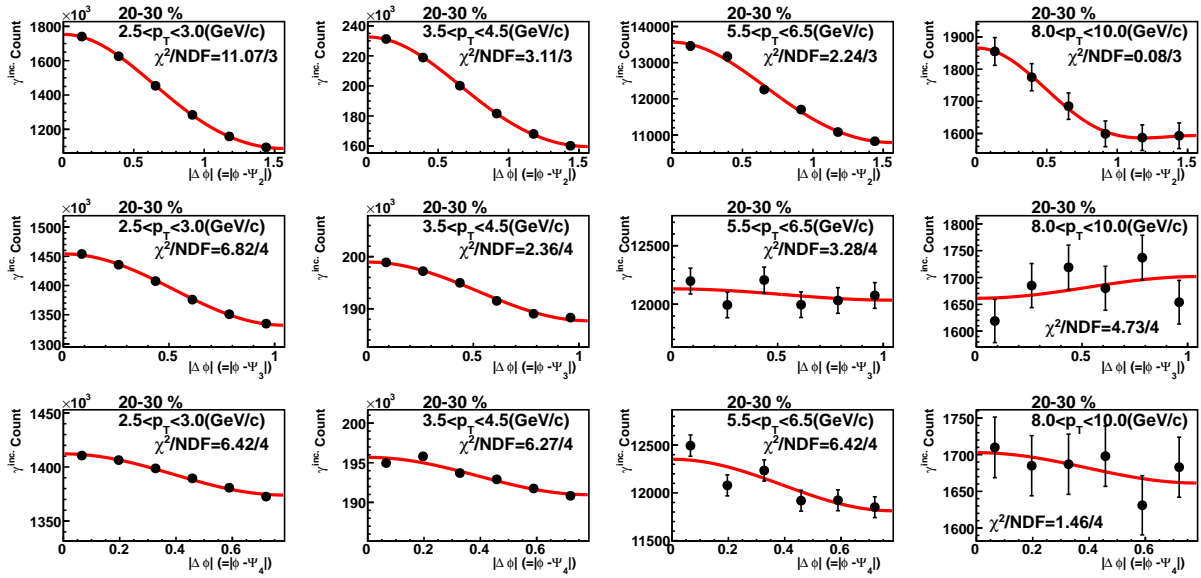


Figure 3.9: Inclusive photon yield distribution as a function of $|\Delta\phi| = |\phi - \Psi_n|$ with 4 p_T selections. Top figures are distributions with respect to the second order event plane and bottom figures are with respect to the third order of event plane. The solid lines show the fitting results of a Fourier function.

3.4.2 Systematic uncertainties

Systematic uncertainty for inclusive photon v_n is estimated by three sources in this analysis.

- Photon PID selections
- Difference between different methods to extract v_n
- Event plane determination

Total systematic uncertainties are evaluated by adding up each source in quadrature by assuming that they are no correlations between systematic uncertainties.

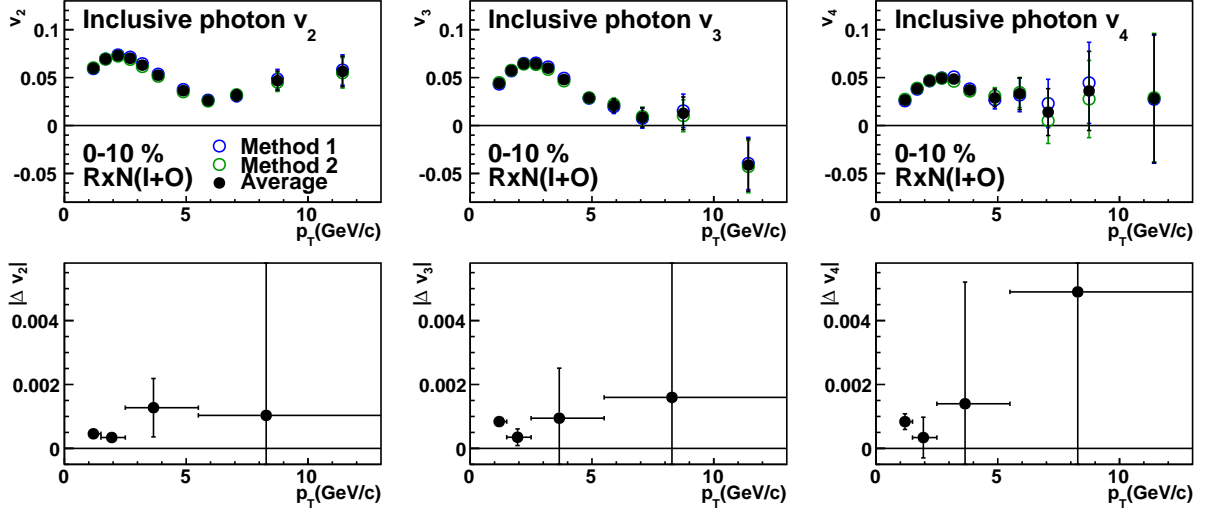


Figure 3.10: (Top) Inclusive photon v_n measured by method 1, method 2 and averaged v_n . (Bottom) The deviation of v_n between method 1 and method 2.

Photon PID selections

Estimation of systematic uncertainty from photon PID is discussed. Inclusive photon v_n is measured with varying photon selection of “Shower shape cut” and removing “PC3 charged particle rejection”, and the deviation between each v_n and v_n with nominal cut are calculated. The average value of each deviations, which is averaged within four p_T ranges without any weight, is defined as a systematic uncertainty. The divided p_T ranges are $1 < p_T < 1.5$, $1.5 < p_T < 2.5$, $2.5 < p_T < 5.5$ and $5.5 < p_T < 15$ GeV/c. Tested photon selections are shown in Table 3.2. Figure 3.11 shows the v_n with several photon PID selections, and mean v_n measured with nominal selection is shown as black solid point. The difference between mean v_n and several v_n are shown in lower figures, and averaged value is defined as systematic uncertainty.

The table of tested photon selection for inclusive photon v_n					
Shower shape cut (χ^2)	2.0	2.5	3.0	3.5	4.0
charged particle rejection	with	without			

Table 3.2: This is the table of tested photon selection. Boldface is the nominal selection.

Difference between different measurement methods

Inclusive photon v_n is measured by two types of method, which are method 1 and method 2 in Section 3.4.1. The difference between each v_n and mean v_n is used for systematic uncertainty. Systematic uncertainty is estimated within four p_T ranges, which are $1 < p_T < 1.5$, $1.5 < p_T < 2.5$, $2.5 < p_T < 5.5$ and $5.5 < p_T < 15$ GeV/c.

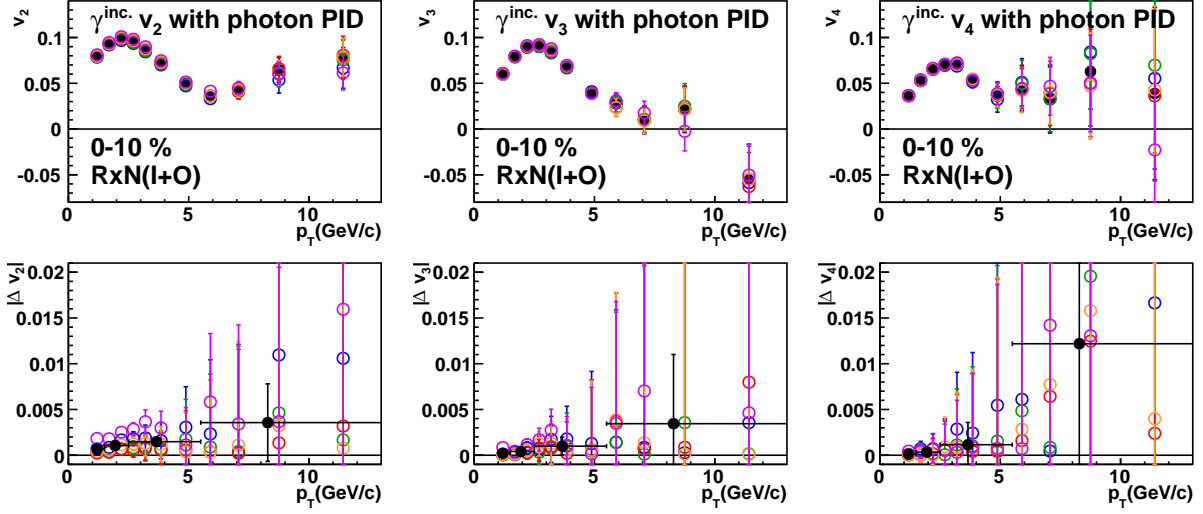


Figure 3.11: (Top) : Inclusive photon v_2 , v_3 , and v_4 with several photon selections (open). Black solid points are v_n with nominal selections. (Bottom) : Δv_n of difference between each v_n and mean v_n as a function of p_T . Systematic uncertainty is defined as averaging within $1 < p_T < 1.5$, $1.5 < p_T < 2.5$, $2.5 < p_T < 5.5$, and $5.5 < p_T < 15$ GeV/c.

Event Plane definition

Systematic uncertainty of event plane determination is not expected to depend on particle species, therefore it is estimated by charged particle due to large statistics. The ratio of v_n with each event plane to averaged v_n is fitted by constant and the largest value is defined as a systematic uncertainty. Figure 3.12 shows the estimation of systematic uncertainty of event plane definition. The systematic uncertainty from event plane definition is summarized in Table 3.5.

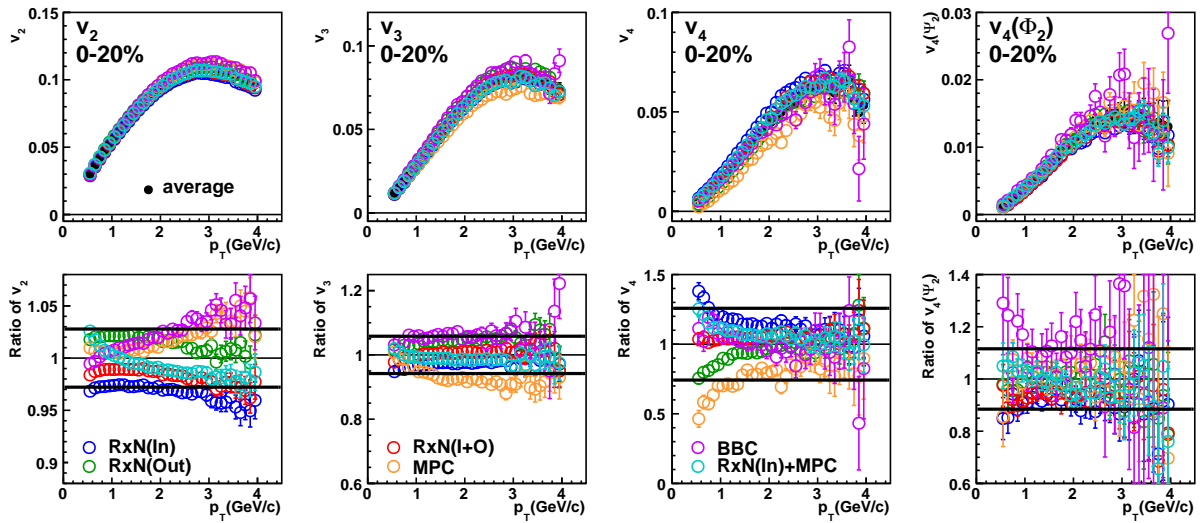


Figure 3.12: (Top) The v_2 , v_3 , v_4 , and $v_4(\Psi_2)$ of charged particle with event plane measured by each detector. (Bottom) The ratio of each v_n to the average of v_n and defined systematic uncertainties.

Systematic uncertainty of inclusive photon $v_n(\text{RxN(I+O)})$ from photon selection					
	centrality(%)	p_T (GeV/c)			
		1 - 1.5	1.5 - 2.5	2.5 - 5.5	5.5 - 15
v_2	0 - 10	0.0007	0.0011	0.0015	0.0036
	10 - 20	0.0008	0.0012	0.0016	0.0023
	20 - 30	0.0006	0.0012	0.0016	0.0018
	30 - 40	0.0003	0.0009	0.0014	0.0043
	40 - 50	0.0003	0.0006	0.0011	0.0025
	50 - 60	0.0004	0.0005	0.0012	0.0047
v_3	0 - 10	0.0002	0.0004	0.0010	0.0034
	10 - 20	0.0002	0.0004	0.0013	0.0047
	20 - 30	0.0002	0.0004	0.0009	0.0059
	30 - 40	0.0003	0.0004	0.0011	0.0108
	40 - 50	0.0003	0.0004	0.0011	0.0187
	50 - 60	0.0006	0.0005	0.0012	0.0256
v_4	0 - 10	0.0001	0.0003	0.0011	0.0122
	10 - 20	0.0003	0.0004	0.0015	0.0099
	20 - 30	0.0002	0.0005	0.0019	0.0143
	30 - 40	0.0004	0.0006	0.0034	0.0159
	40 - 50	0.0003	0.0013	0.0087	0.0469
$v_4(\Psi_2)$	0 - 10	0.0001	0.0002	0.0017	0.0082
	10 - 20	0.0002	0.0003	0.0009	0.0048
	20 - 30	0.0003	0.0005	0.0008	0.0046
	30 - 40	0.0002	0.0005	0.0010	0.0047
	40 - 50	0.0001	0.0004	0.0007	0.0083
	50 - 60	0.0001	0.0003	0.0025	0.0187

Table 3.3: The summary of systematic uncertainty for inclusive photon $v_n(\text{RxN(I+O)})$ from photon selection. They are absolute value (Δv_n).

3.5 π^0 v_n measurement

3.5.1 π^0 selection

Neutral pion is reconstructed by two photons that are detected in the EMCal. The photon selections are shown in Section 3.3, additionally several selections are added for π^0 selections. The additional selections are listed below.

- Asymmetry selection : $|E_1 - E_2|/(E_1 + E_2) < 0.8$
- two photons are captured in the same sector

Asymmetry selection is useful method to reject low p_T photons which make large combinatorial background. Since opening angle of two photons originated from π^0 is very narrow in high p_T region, the selections that two photons captured in the same sector is added in order to reduce

Systematic uncertainty of inclusive photon $v_n(\text{RxN(I+O)})$ from measurement method					
	centrality(%)	p_T (GeV/c)			
		1 - 1.5	1.5 - 2.5	2.5 - 5.5	5.5 - 15
v_2	0 - 10	0.0005	0.0003	0.0013	0.00103
	10 - 20	0.0009	0.0005	0.0018	0.00078
	20 - 30	0.0010	0.0007	0.0025	0.00119
	30 - 40	0.0011	0.0009	0.0024	0.00192
	40 - 50	0.0010	0.0010	0.0022	0.00243
	50 - 60	0.0009	0.0009	0.0020	0.00615
v_3	0 - 10	0.0008	0.0003	0.0009	0.00160
	10 - 20	0.0009	0.0004	0.0010	0.00301
	20 - 30	0.0009	0.0004	0.0020	0.00087
	30 - 40	0.0009	0.0003	0.0017	0.00187
	40 - 50	0.0007	0.0005	0.0030	0.00862
	50 - 60	0.0003	0.0008	0.0051	0.00980
v_4	0 - 10	0.0008	0.0003	0.0014	0.00490
	10 - 20	0.0008	0.0004	0.0005	0.00973
	20 - 30	0.0008	0.0007	0.0020	0.01230
	30 - 40	0.0009	0.0005	0.0031	0.00604
	40 - 50	0.0011	0.0014	0.0037	0.00852
$v_4(\Psi_2)$	0 - 10	0.00005	0.00015	0.00039	0.00390
	10 - 20	0.00005	0.00030	0.00041	0.00224
	20 - 30	0.00003	0.00047	0.00057	0.00283
	30 - 40	0.00005	0.00061	0.00078	0.00384
	40 - 50	0.00009	0.00068	0.00086	0.00475
	50 - 60	0.00002	0.00060	0.00112	0.00982

Table 3.4: The summary of systematic uncertainty for inclusive photon $v_n(\text{RxN(I+O)})$ from measurement method. They are absolute value (Δv_n).

combinatorial background. This reduces some statistics of two close photons in neighboring sectors or some open pairs, too.

The invariant mass of particles that is the amount of Lorentz invariance is powerful tool to identify the particle identification. The invariant mass of two photons ($m_{\gamma\gamma}$) is calculated by following function.

$$\begin{aligned}
Mass &= \sqrt{(E_1 + E_2)^2 - (\mathbf{p}_1 + \mathbf{p}_2)^2} \\
&= \sqrt{2E_1E_2 \left(\frac{x_1x_2 + y_1y_2 + z_1z_2}{l_1l_2} \right)},
\end{aligned} \tag{3.43}$$

where E_i and \mathbf{p}_i is photon energy deposited in EMCal and momentum, x_n, y_n, z_n are positions of each cluster, and l_n is the length from event vertex to cluster. The invariant mass distribution is shown in Figure 3.13(a). One can see the signal peak at around 0.135 GeV/ c^2 in blue distribution but large combinatorial background is also seen. The combinatorial background is estimated by mixed event method that two photons are selected from different event in this analysis. Mixed

Systematic uncertainty of Event Plane				
Centrality(%)	Ψ_2	Ψ_3	Ψ_4	4th of Ψ_2
0-10(%)	4(%)	11(%)	15(%)	17(%)
10-20(%)	2(%)	5(%)	37(%)	12(%)
20-30(%)	2(%)	6(%)	46(%)	8(%)
30-40(%)	3(%)	9(%)	52(%)	6(%)
40-50(%)	3(%)	14(%)	66(%)	8(%)
50-60(%)	4(%)	26(%)	—	12(%)
0-20(%)	3(%)	6(%)	26(%)	12(%)
20-40(%)	2(%)	7(%)	48(%)	6(%)
40-60(%)	3(%)	18(%)	—	9(%)
20-60(%)	3(%)	10(%)	—	6(%)
0-60(%)	3(%)	6(%)	—	7(%)

Table 3.5: The table of systematic uncertainty of Event Plane definition.

event is selected by similar centrality (10bin), z-vertex (10bin) and event plane angle (10bin) class. As one can see in Figure 3.13(b), there is residual background after combinatorial background subtraction especially in low p_T . The remaining background is subtracted by fitting with the linear function.

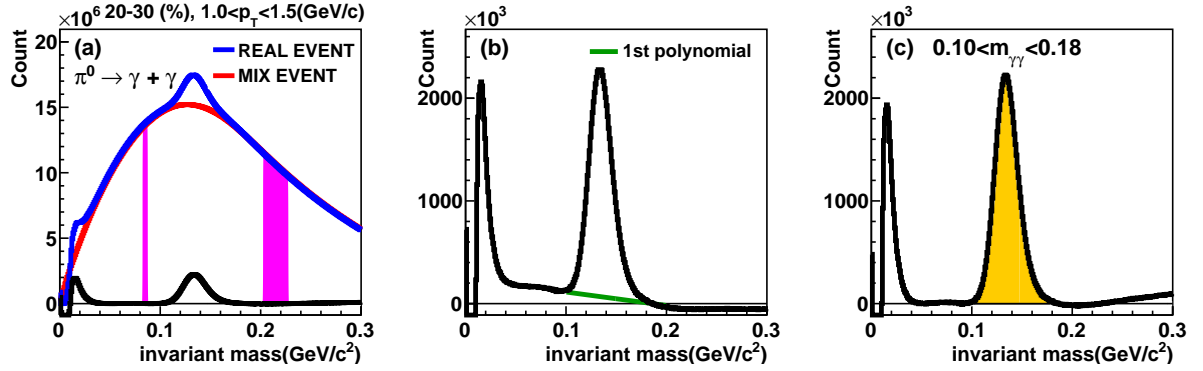


Figure 3.13: (a): π^0 invariant mass distribution which is combined two photons in same event (blue histogram) and mixed event (red histogram). (b): π^0 invariant mass distribution after subtracting mixed event. Green histogram shows the linear function to estimate residual background. (c): π^0 invariant mass distribution after subtracting residual background.

3.5.2 π^0 v_n measurement

The π^0 yield is calculated by integrating the invariant mass in $0.1 < m_{\gamma\gamma} < 0.18$ GeV/c^2 for each $\Delta\phi$ bin. The $\Delta\phi$ distribution of π^0 is then fitted by the Fourier function Eq. (3.41) and (3.42). Example figures of π^0 distribution as a function of $|\Delta\phi| (= |\phi - \Psi_n|)$ fitted by Fourier equation with 4 p_T selections are shown in Figure 3.14.

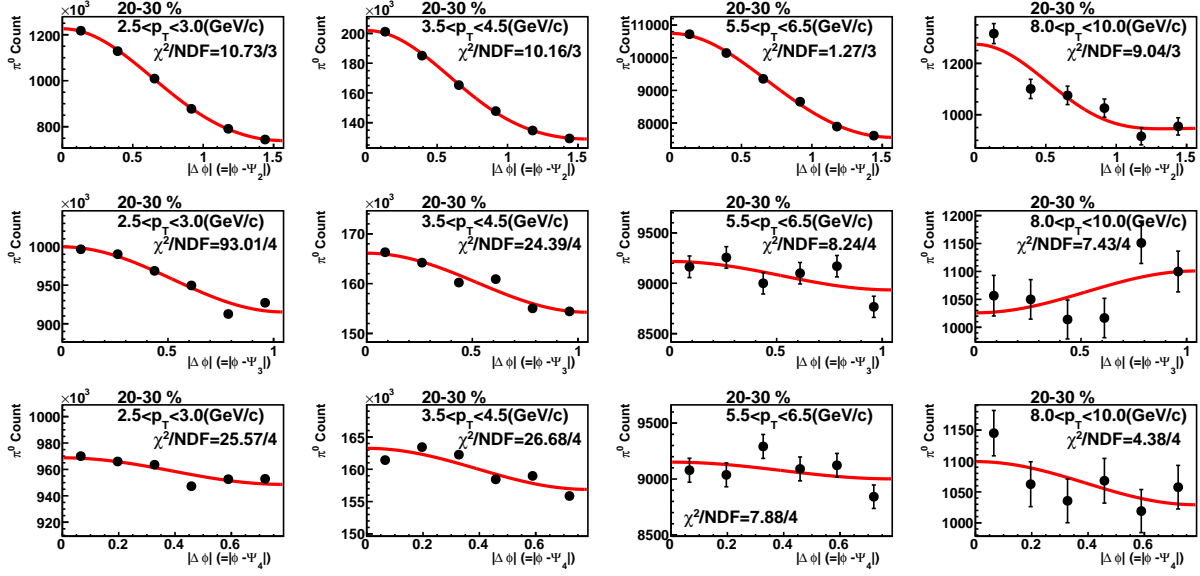


Figure 3.14: π^0 yield distribution as a function of $|\Delta\phi| = |\phi - \Psi_n|$ with 4 p_T selections. The solid lines show the fitting results of a Fourier function.

3.5.3 Systematic uncertainties

The method of estimating systematic uncertainty for $\pi^0 v_n$ is shown. Three sources are considered.

- Photon selection dependence
- π^0 extraction dependence
- Event Plane determination

Systematic uncertainty from event plane determination is shown in Section 3.4.2. Total systematic uncertainties are evaluated by adding up each source in quadrature by assuming that they are no correlations between systematic uncertainties.

Photon selection dependence

To estimate systematic uncertainty, $\pi^0 v_n$ is measured with several photon selections. The deviations between v_n with each selection and v_n with nominal selection are calculated, and it is defined as systematic uncertainty that the average of these deviations within four p_T range without any weight. The divided p_T ranges are $1 < p_T < 1.5$, $1.5 < p_T < 2.5$, $2.5 < p_T < 5.5$, and $5.5 < p_T < 15$ GeV/c. The 6 different selection patterns are tested, and they are listed in Table 3.6. Figure 3.15 shows the difference of $\pi^0 v_n$ with several photon selection, and systematic uncertainties are shown in bottom.

π^0 extraction dependence

Two parts of systematic uncertainty is estimated for extracting π^0 signal in this analysis. They are “Normalization of (mixed event) background distribution” and “Counting π^0 signal range

The table of tested photon selection for $\pi^0 v_n$			
Cluster energy threshold : E(GeV)	0.2 < E	0.5 < E	
Shower shape cut : χ^2	$\chi^2 < 2.5$	$\chi^2 < \mathbf{3.0}$	$\chi^2 < 3.5$
Asymmetry selection : α	$\alpha < 0.7$	$\alpha < \mathbf{0.8}$	$\alpha < 0.9$
PC3 charged particle rejection	with	without	

Table 3.6: This is the table of tested photon selections. Boldface is the nominal selection. The 6 pattern selections are tested to estimate systematic uncertainty of $\pi^0 v_n$ from “Photon selection dependence”.

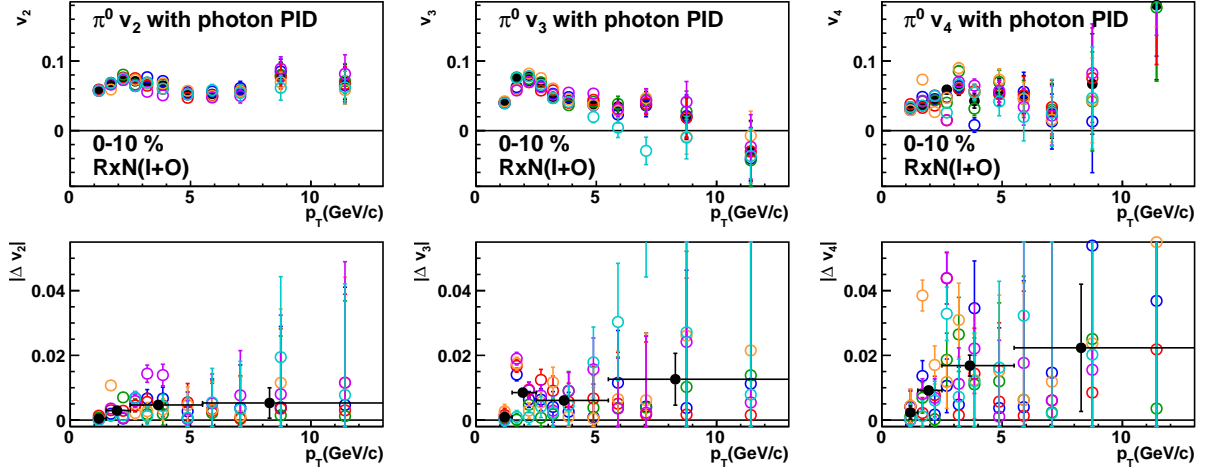


Figure 3.15: Systematic uncertainty of neutral pion v_n estimated from photon selections. (Top) : (open) $\pi^0 v_2, v_3, v_4$ with several photon selections. (solid) v_n with nominal photon selection. (Bottom) : Δv_n as a function of p_T and systematic uncertainty are shown. Systematic uncertainty of photon selection is defined as the average of these deviations within 4 p_T region, $1 < p_T < 1.5$, $1.5 < p_T < 2.5$, $2.5 < p_T < 5.5$, and $5.5 < p_T < 15$ GeV/c.

Systematic uncertainty of neutral pion $v_n(\text{RxN(I+O)})$ from photon selection					
	centrality(%)	p_T (GeV/c)			
		1 - 1.5	1.5 - 2.5	2.5 - 5.5	5.5 - 15
v_2	0 - 10	0.0005	0.0029	0.0047	0.00529
	10 - 20	0.0007	0.0018	0.0024	0.00470
	20 - 30	0.0011	0.0019	0.0018	0.00508
	30 - 40	0.0008	0.0014	0.0014	0.00365
	40 - 50	0.0005	0.0011	0.0020	0.00622
	50 - 60	0.0011	0.0006	0.0014	0.00780
v_3	0 - 10	0.0009	0.0085	0.0061	0.01262
	10 - 20	0.0012	0.0029	0.0086	0.00816
	20 - 30	0.0011	0.0028	0.0057	0.00911
	30 - 40	0.0007	0.0026	0.0091	0.01126
	40 - 50	0.0026	0.0035	0.0083	0.01832
	50 - 60	0.0016	0.0048	0.0078	0.02118
v_4	0 - 10	0.0023	0.0092	0.0168	0.02233
	10 - 20	0.0057	0.0072	0.0127	0.02511
	20 - 30	0.0020	0.0145	0.0140	0.03877
	30 - 40	0.0029	0.0087	0.0143	0.03124
	40 - 50	0.0046	0.0113	0.0206	0.06825
$v_4(\Psi_2)$	0 - 10	0.0015	0.0046	0.0065	0.01330
	10 - 20	0.0010	0.0024	0.0052	0.00587
	20 - 30	0.0002	0.0016	0.0044	0.00748
	30 - 40	0.0003	0.0016	0.0025	0.00680
	40 - 50	0.0004	0.0012	0.0038	0.01464
	50 - 60	0.0010	0.0017	0.0035	0.01711

Table 3.7: The summary of systematic uncertainty for neutral pion $v_n(\text{RxN(I+O)})$ from photon selection. They are absolute value (Δv_n).

dependence". The combination of them are defined as the systematic uncertainty of π^0 extraction dependence. Systematic uncertainty is estimated within four p_T ranges, which are $1 < p_T < 1.5$, $1.5 < p_T < 2.5$, $2.5 < p_T < 5.5$ and $5.5 < p_T < 15$ GeV/c. Each uncertainties are discussed below.

Normalization of (mixed event) background distribution In order to subtract combinatorial background, mixed event background distribution needs to be normalized to foreground distribution. Normalization should be determined by the invariant mass away from the π^0 signal. Default normalization is calculated $0.08 < m_{\gamma\gamma} < 0.09$ GeV/ c^2 and $0.2 < m_{\gamma\gamma} < 0.23$ GeV/ c^2 , which is shown in filled magenta area in Figure 3.13 (a). Systematic uncertainties are evaluated by varying the invariant mass range for normalization as listed in Table 3.8, and the deviations of v_n are used as systematic uncertainties. Figure 3.16 shows the π^0 v_n with several normalized range and nominal normalization range. Systematic uncertainty is defined as the average of these difference within 4 p_T ranges.

The table of π^0 normalized range	
Normal normalized range is 0.08-0.09+0.20-0.23 (GeV/c ²)	
0.07-0.09+0.20-0.23	0.08-0.10+0.20-0.23
0.08-0.09+0.19-0.23	0.08-0.09+0.20-0.24

Table 3.8: Invariant mass range to calculate normalization of mixed event background to foreground distribution. The 4 patterns of normalized range are considered to estimate systematic uncertainty of π^0 v_n .

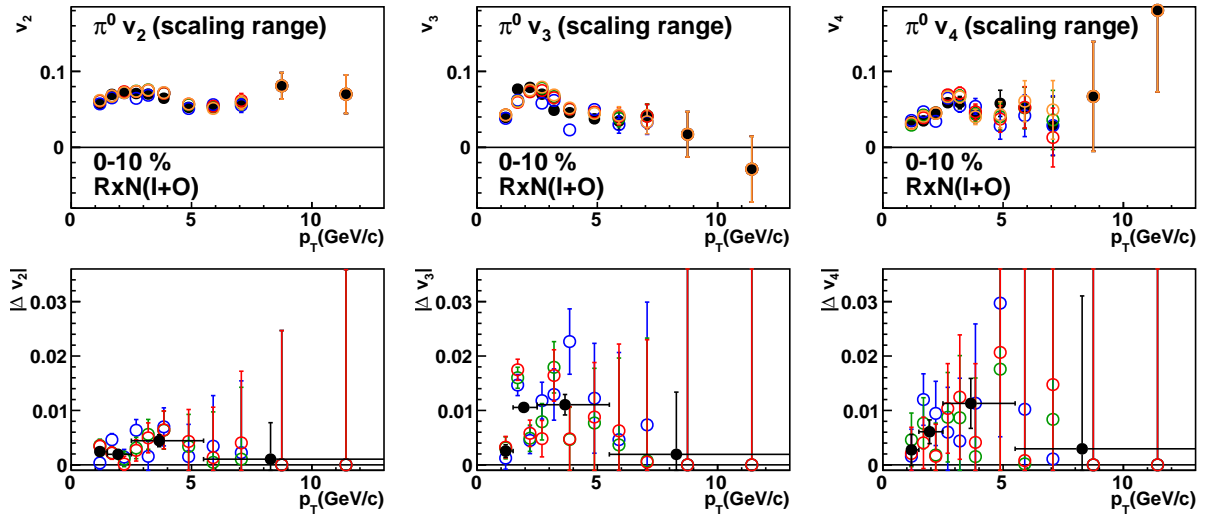


Figure 3.16: Systematic uncertainty of neutral pion v_n estimated from normalization of background distribution. (Top) : (open) π^0 v_2 , v_3 , and v_4 with several normalized range of background distribution. (solid) v_n with nominal normalization of background distribution. (Bottom) : Δv_n as a function of p_T . Systematic uncertainty of normalization of background distribution is defined as the average of these deviations within 4 p_T region, $1 < p_T < 1.5$, $1.5 < p_T < 2.5$, $2.5 < p_T < 5.5$, and $5.5 < p_T < 15$ GeV/c.

Counting π^0 signal range dependence The number of π^0 signal is counted within $0.1 < m_{\gamma\gamma} < 0.18 \text{ GeV}/c^2$, which is the range filled by orange in Figure 3.13(a). This range is changed and the deviation of v_n is defined as a systematic uncertainty. Table 3.9 summarizes the variation of invariant mass range to evaluate the systematic uncertainty on the v_n . Figure 3.17 shows the $\pi^0 v_n$ with several π^0 counting range and nominal counting range. Systematic uncertainty is defined as the average of these differences within 4 p_T ranges.

The table of π^0 counting range	
Nominal counting range is $0.10 < m_{\gamma\gamma} < 0.18 (\text{GeV}/c^2)$	
$0.09 < m_{\gamma\gamma} < 0.18$	$0.11 < m_{\gamma\gamma} < 0.18$
$0.10 < m_{\gamma\gamma} < 0.17$	$0.10 < m_{\gamma\gamma} < 0.19$

Table 3.9: The 4 pattern of π^0 counting range are performed to evaluate systematic uncertainty of $\pi^0 v_n$.

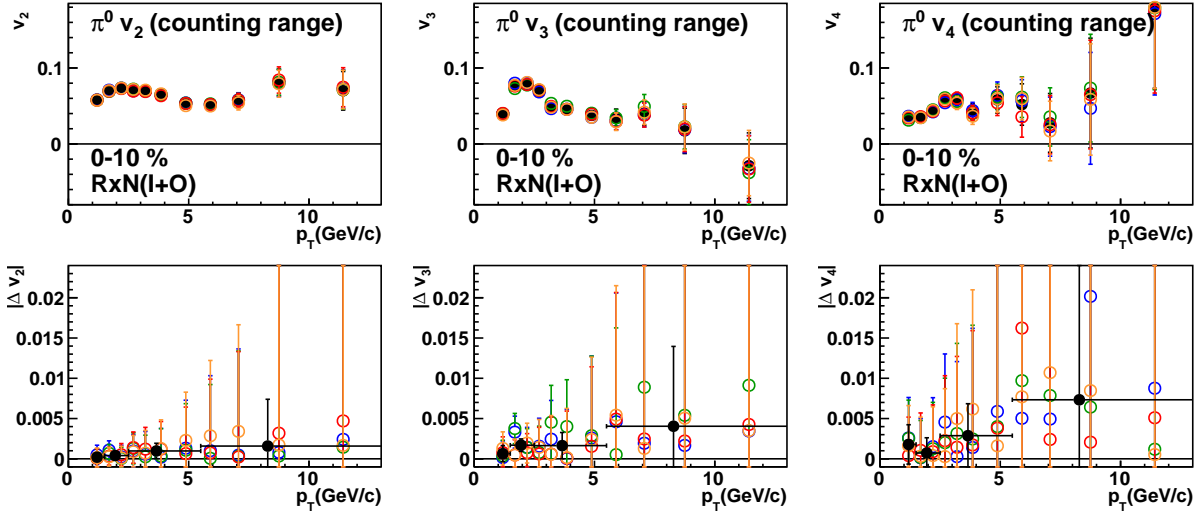


Figure 3.17: (Top) : π^0 signal range dependence of $\pi^0 v_2$, v_3 , and v_4 . (Bottom) : Δv_n as a function of p_T . Black solid points are estimated systematic uncertainties.

3.6 Decay photon v_n

Decay photon contaminations should be removed from inclusive photon in order to extract direct photon signal. Since we cannot identify decay photons experimentally, they are simulated by Monte-Carlo simulation. The hadron decay kinematics are summarized in Table 3.11. In this Section, we describe the assumptions for p_T spectra in Section 3.6.1, v_n in Section 3.6.2. In Section 3.6.3, we present systematic uncertainties on decay photon v_n .

Systematic uncertainty of neutral pion $v_n(\text{RxN(I+O)})$ from π^0 PID					
	centrality(%)	p_T (GeV/c)			
		1 - 1.5	1.5 - 2.5	2.5 - 5.5	5.5 - 15
v_2	0 - 10	0.002	0.002	0.005	0.002
	10 - 20	0.004	0.002	0.005	0.001
	20 - 30	0.005	0.003	0.003	0.001
	30 - 40	0.004	0.003	0.004	0.001
	40 - 50	0.003	0.002	0.002	0.002
	50 - 60	0.003	0.003	0.002	0.002
v_3	0 - 10	0.003	0.011	0.011	0.004
	10 - 20	0.003	0.002	0.008	0.004
	20 - 30	0.001	0.003	0.005	0.003
	30 - 40	0.000	0.002	0.008	0.005
	40 - 50	0.003	0.003	0.006	0.007
	50 - 60	0.004	0.009	0.008	0.013
v_4	0 - 10	0.003	0.006	0.012	0.008
	10 - 20	0.002	0.015	0.009	0.008
	20 - 30	0.002	0.012	0.012	0.009
	30 - 40	0.003	0.006	0.017	0.013
	40 - 50	0.005	0.008	0.014	0.014
$v_4(\Psi_2)$	0 - 10	0.001	0.008	0.005	0.004
	10 - 20	0.001	0.002	0.006	0.002
	20 - 30	0.001	0.001	0.005	0.002
	30 - 40	0.001	0.002	0.002	0.002
	40 - 50	0.001	0.001	0.002	0.004
	50 - 60	0.002	0.007	0.003	0.004

Table 3.10: The summary of systematic uncertainty for neutral pion $v_n(\text{RxN(I+O)})$ from π^0 extraction dependence. They are absolute value (Δv_n).

3.6.1 The p_T spectra of meson and decay photon

Since the meson such as η , ω , ρ , and η' are difficult to measure, they are assumed from experimental results of pion. The shape of p_T spectra is known to be estimated by m_T scaling as seen in Section 1.3.3. Meson p_T spectra (p'_T) is estimated by $p'_T = \sqrt{p_{T,\pi}^2 + M_{meson}^2 - M_\pi^2}$, where $p_{T,\pi}$, M_π and M_{meson} are pion p_T , mass and each meson mass, respectively.

The following functional forms are used for obtaining meson p_T spectra,

$$\frac{d\sigma}{p_T dp_T} = T(p_T)F_0 + (1 - T(p_T))F_1, \quad (3.44)$$

$$T(p_T) = \frac{1}{1 + \exp\{(p_T - t)/w\}}, \quad (3.45)$$

$$F_0 = \frac{c}{\{\exp(-ap_T - bp_T^2) + p_T/p_0\}^n}, \quad (3.46)$$

$$F_1 = \frac{A}{p_T^m}, \quad (3.47)$$

meson	invariant mass(MeV/c ²)	decay mode	branching ratio
π^0	134.98	2γ	(98.823 \pm 0.034) %
		$e^+e^-\gamma$	(1.174 \pm 0.035) %
η	547.86	2γ	(39.41 \pm 0.20) %
		$\pi^+\pi^-\gamma$	(4.22 \pm 0.08) %
		$e^+e^-\gamma$	(6.9 \pm 0.4) $\times 10^{-3}$
		$\pi^0 2\gamma$	(2.7 \pm 0.5) $\times 10^{-4}$
ω	782.65	$\pi^0\gamma$	(8.28 \pm 0.28) %
ρ	775.26	$\pi^+\pi^-\gamma$	(9.9 \pm 1.6) $\times 10^{-3}$
		$\pi^0\gamma$	(6.0 \pm 0.8) $\times 10^{-4}$
η'	957.78	$\rho\gamma$	(29.1 \pm 0.5) %
		$\omega\gamma$	(2.75 \pm 0.23) %
		2γ	(2.20 \pm 0.08) %
		$\mu^+\mu^-\gamma$	(1.08 \pm 0.27) $\times 10^{-4}$

Table 3.11: Summary of meson properties, such as invariant mass, branching ratio to photons, from PDG [1].

where t, w, c, a, b, p_0, n, A and m are free parameters, F_0 is modified Hagedorn function, and F_1 is power law function. Free parameters are determined by the π^\pm [6] and π^0 [26]. Parameters of F_0 are determined by fitting to the p_T spectra of π^\pm in $0.25 < p_T < 2$ GeV/c, and π^0 in $2 < p_T < 10$ GeV/c. Parameters of F_1 are defined by fitting to p_T spectra of π^0 in $6 < p_T < 20$ GeV/c. The fraction $T(p_T)$ is determined by the whole π^\pm and π^0 p_T spectra by fixing parameters in the function F_0 and F_1 .

The ratio of meson p_T spectra to pion p_T spectra is known to be constant in high p_T region. The absolute value of meson p_T spectra is scaled by this ratio at 5.0 GeV/c in this analysis. These ratios are summarized in Table 3.12. Figure 3.18 shows the pion p_T spectra fitted by Eq. (3.44) in top, estimated p_T spectra is compared with experimental measurement [27, 28] in middle, and the ratio of them in bottom. It is confirmed that the ratio of p_T spectra is consistent with unity.

The table of each meson spectra ratio to π^0	
η/π^0	0.45 \pm 0.060 [37]
ω/π^0	0.83 \pm 0.120 [28]
ρ/π^0	1.00 \pm 0.300 [38]
η'/π^0	0.25 \pm 0.075 [38]

Table 3.12: The table for the spectra ratio of each meson to π^0 [37, 28, 38].

The simulated hadronic decay photon p_T spectra and the decay photon contribution ratio which is the ratio of decay photon from each meson to the sum of decay photons are shown in Figure 3.19. Figure 3.19 shows that the simulated decay photon p_T spectra as well as the decay photon contribution ratio which is the ratio of decay photon from each meson to the sum of

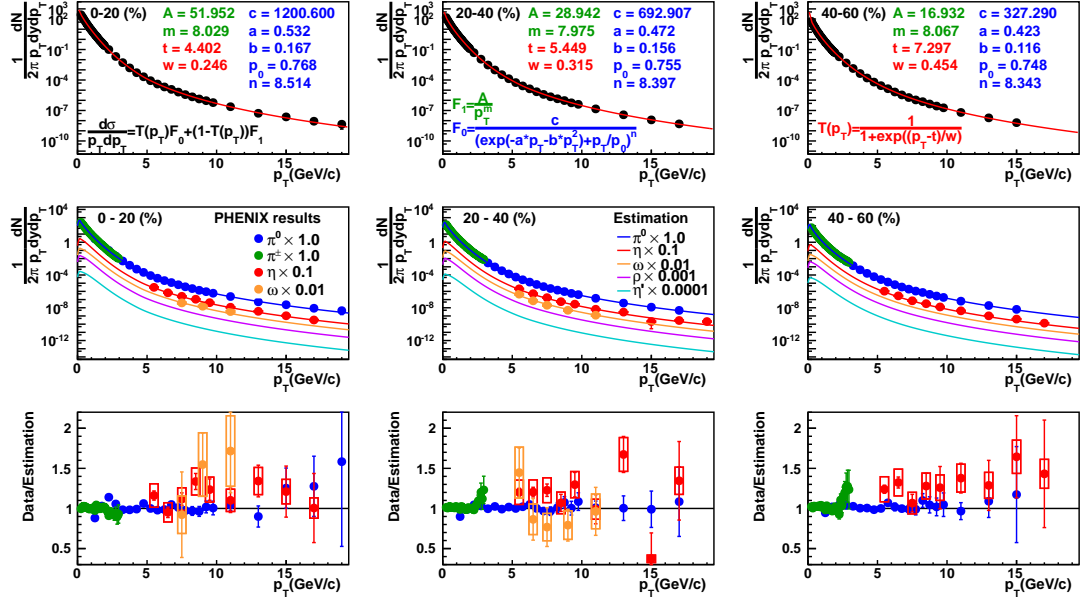


Figure 3.18: (Top) Pion p_T spectra fitted by the Eq. (3.44), and obtained parameters. (Middle) The comparison of meson p_T spectra between experimental results [6, 26, 27, 28] and meson p_T spectra estimated with m_T scaling. (Bottom) The ratio of meson p_T spectra of experimental results to estimated p_T spectra.

decay photons.

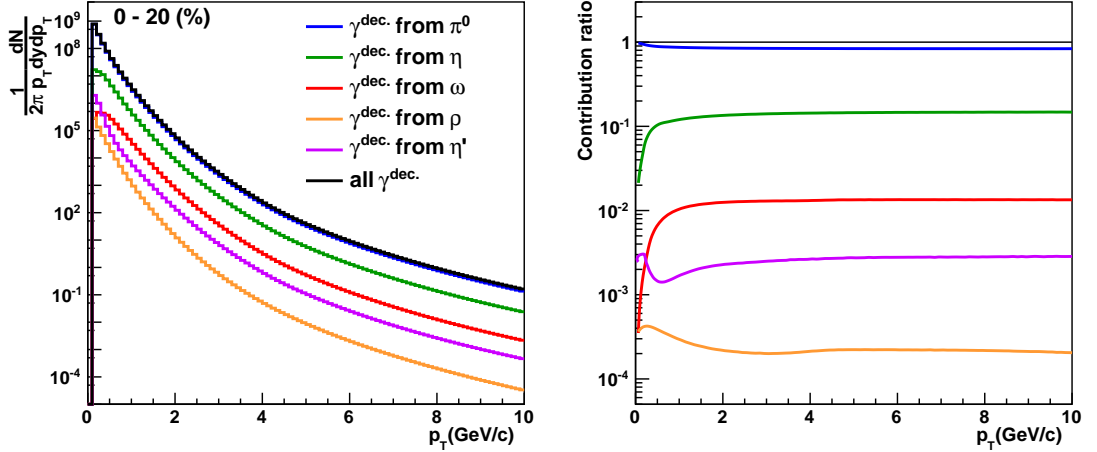


Figure 3.19: (Left): Simulated decay photon p_T spectra. (Right): Contribution ratio of decay photon from each hadron to all decay photon.

3.6.2 The v_n of meson and decay photon

Charged pion are combined with neutral pion in low p_T region and used for an input for simulation, because charged pion v_n has good statistics and small systematic uncertainty. Combined

pion v_n ($v_{n,pion}$) is given as following

$$v_{n,pion} = v_{n,\pi^\pm} F(p_T) + v_{n,\pi^0} (1 - F(p_T)), \quad (3.48)$$

$$F(p_T) = 1 - \frac{1}{1 + \exp\{(p_T - a)/b\}}, \quad (3.49)$$

where v_{n,π^\pm} , v_{n,π^0} are v_n of charged pion and neutral pion. Charged pion v_n are taken from [8]. Mean value of combined pion v_n is obtained with $a=2$ and $b=0.4$. Figure 3.20 shows the v_n of charged pion, neutral pion, and combination, as well as the $F(p_T)$ is shown in right.

It has been found that hadron v_n as a function of transverse kinetic energy KE_T is scaled by the number of constituent quarks, as shown in Section 1.3.4. Under this assumption, the v_n of η , ω , ρ and η' are estimated from that of pion v_n . Meson's $p_{T,meson}$ is given by

$$p_{T,meson} = \sqrt{\left(\sqrt{p_{T,\pi}^2 + M_\pi^2} - M_\pi + M_{meson}\right)^2 - M_{meson}^2}, \quad (3.50)$$

where $p_{T,\pi}$, M_π and M_{meson} are pion p_T , mass and each meson mass, respectively. Figure 3.21 shows the pion v_n and estimated meson v_n .

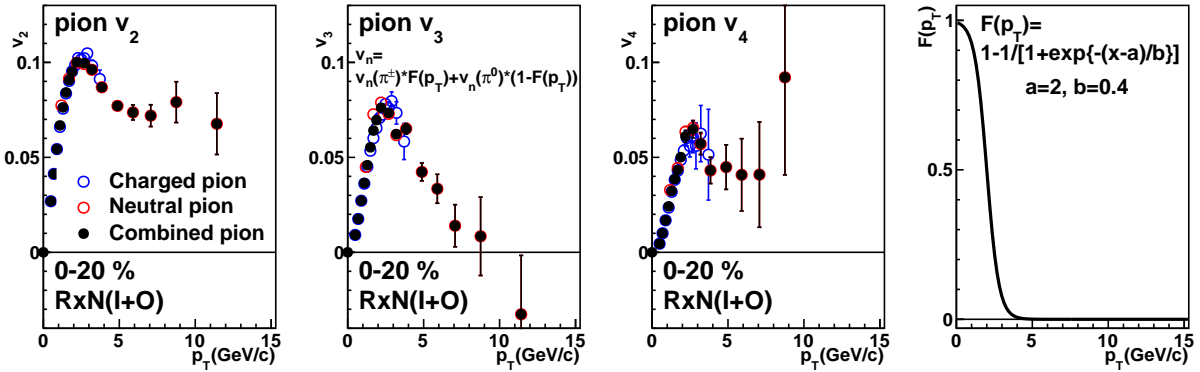


Figure 3.20: Charged pion and neutral pion v_2 , v_3 , and v_4 are combined with the $F(p_T)$ equation, and $F(p_T)$ equation is shown in right. Charged pion v_n are taken from [8].

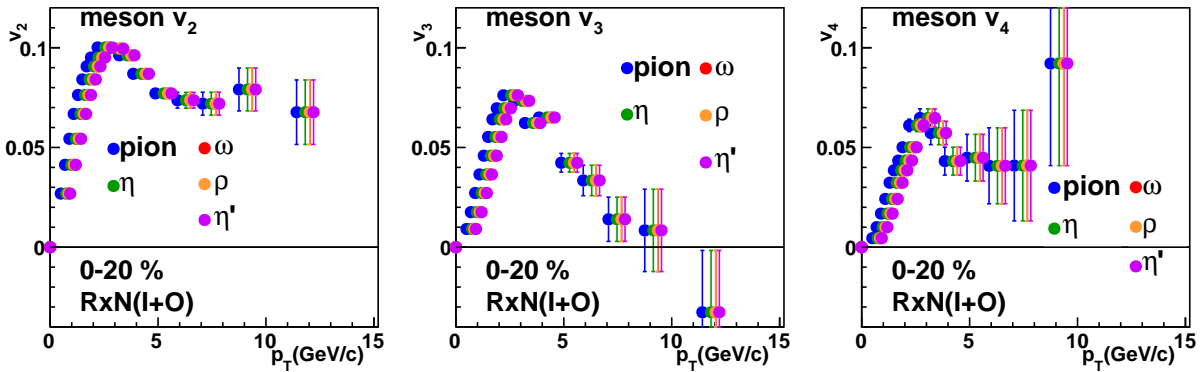


Figure 3.21: v_2 , v_3 , and v_4 of η , ω , ρ , and η' estimated from pion v_n by KE_T scaling.

Decay photon v_n originated from each meson are simulated and combined decay photon v_n are calculated by the following formula based on the relative fraction of different decay contributions

$$N^{dec.} v_n^{dec.} = \sum_i N_i^{dec.} v_{n,i}^{dec.}, \quad (3.51)$$

$$N^{dec.} = \sum_i N_i^{dec.}, \quad (3.52)$$

$$R_i = N_i^{dec.} / N^{dec.}, \quad (3.53)$$

$$v_n^{dec.} = \sum_i R_i v_{n,i}^{dec.}, \quad (3.54)$$

where $N^{dec.}$, $N_i^{dec.}$ are the sum of the number of decay photons and decay photons from each hadron i , $v_n^{dec.}$, $v_{n,i}^{dec.}$ are v_n of all decay photons and v_n of decay photons from hadron i , and R_i is the relative fractions shown in Figure 3.19. Decay photon v_n is calculated by Eq. (3.54), and they are shown in Figure 3.22.

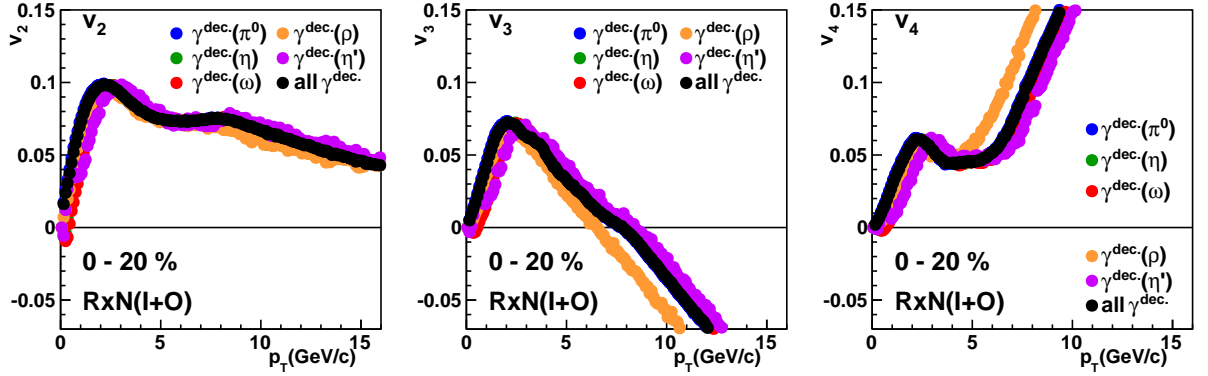


Figure 3.22: v_2 , v_3 , and v_4 of all combined decay photon and each hadronic decay photon.

The statistical error of decay photon v_n is estimated from that of pion v_n . The shape of pion v_n is varied from mean value to lower limit or upper limit by the amount of statistical error and they are used as an input of simulation in order to determine the statistical error of decay photon v_n according to the statistical error from the measured π^0 v_n .

3.6.3 Systematic uncertainties

Four sources of systematic uncertainties are estimated and they are added by quadratic-sum. Systematic uncertainty from event plane determination is the same as the value estimated for inclusive photons in Section 3.4.2.

- p_T spectra dependence
- Propagated from systematic uncertainty of pion v_n
- Propagated from input v_n
- Event plane determination

p_T spectra dependence

The systematic uncertainty from decay photon p_T spectra are discussed in this section. Two sources of systematic uncertainties are studied, which are the followings.

- Input meson p_T spectra
- Meson to pion ratio

The shape of input meson p_T spectra is obtained by fitting to pion p_T spectra, as shown in Section 3.6.1. The p_T spectra of various mesons are varied within the measured systematic uncertainty as discussed in the followings, then the variation of decay photon v_n is defined as a systematic uncertainty. The shape of p_T spectra is obtained by fitting to the pion p_T spectra connected with charged pion and neutral pion at 2.0 GeV/c. At first, connection point is changed to 3.0 GeV/c. Second, the pion p_T spectra is varied to upper and to lower limit of systematic uncertainty.

To estimate decay photon p_T spectra, the ratio of each meson to pion p_T spectra is utilized as listed in Table 3.12. The statistical and systematic errors of the ratio of meson to pion are propagated to decay photon v_n .

Systematic uncertainties from two sources above are evaluated separately, and summed as a quadratic sum. The example plots are shown in Figure 3.23.

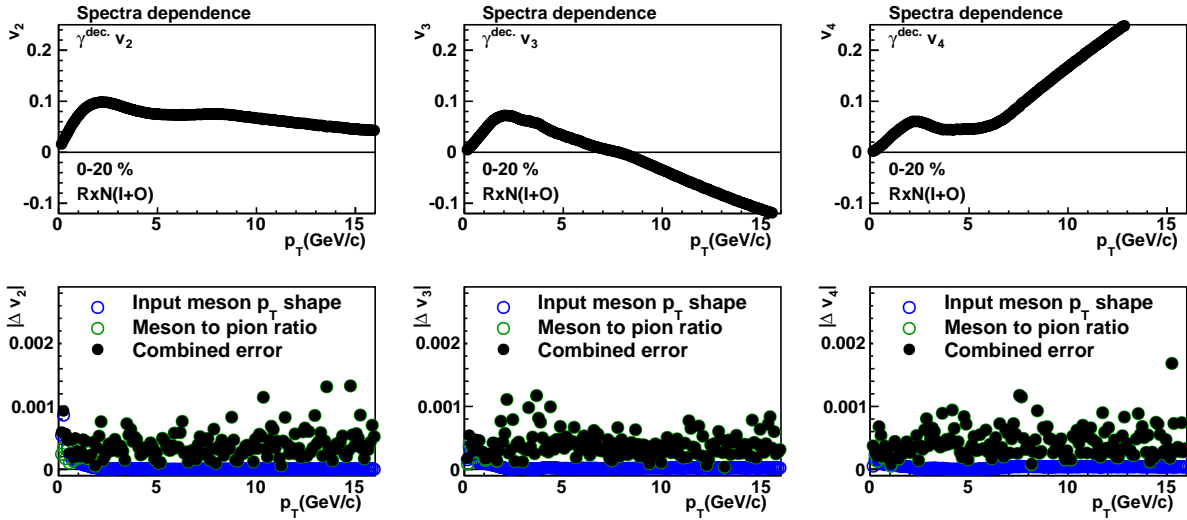


Figure 3.23: (Top) Decay photon v_2 (left), v_3 (middle), and v_4 (right) with event plane measured by RxN(I+O) in 0-20% centrality bin. (Bottom) The systematic uncertainty estimated from decay photon spectra.

Propagated from systematic uncertainty of pion v_n

Systematic uncertainty of pion v_n is propagated into decay photon v_n . Systematic uncertainty of event plane determination is excluded when they are propagated before the subtraction in order to get direct photon v_n , this is needed not to double count the same systematic uncertainty twice in both inclusive photon v_n and decay photon v_n estimations. The shape of pion v_n is

changed from mean value to lower and upper limit with systematic uncertainty. The variation of the decay photon v_n are defined as a systematic uncertainty. Figure 3.24 shows the example of systematic uncertainty propagated from systematic uncertainty of pion v_n .

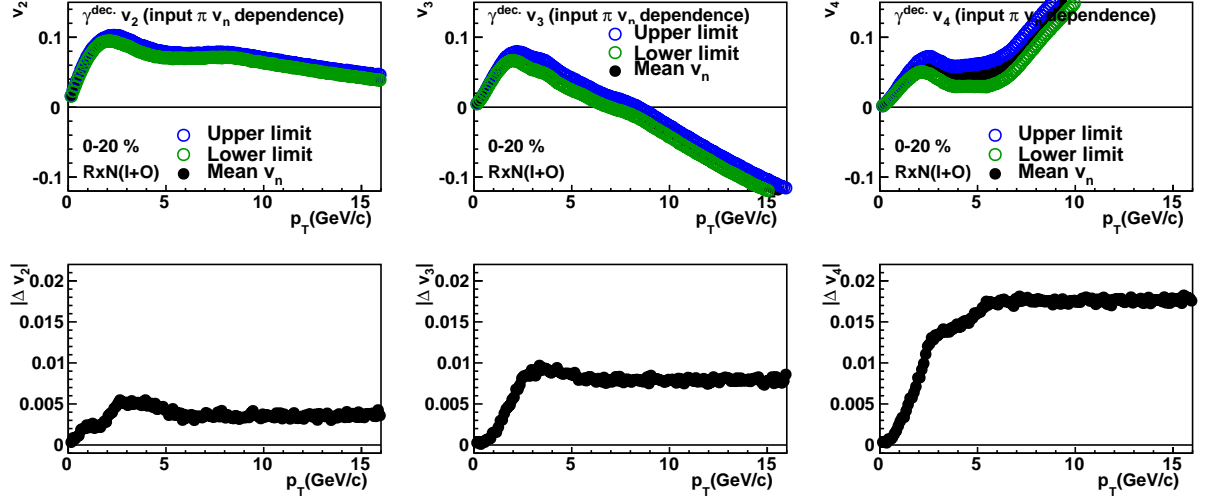


Figure 3.24: (Top) Decay photon v_2 (left), v_3 (middle), and v_4 (right) with event plane measured by RxN(I+O) in 0-20% centrality bin. (Bottom) The systematic uncertainty propagated from systematic uncertainty of neutral pion v_n .

Propagated from input v_n

As it is introduced in Section 3.6.2, decay photon v_n is simulated from combined charged and neutral pion v_n . The Eq. (3.49) is utilized to connect pion with two parameters and the variations of input pion v_n for the decay simulation by changing two parameters for the connection equation $F(p_T)$ are shown in Figure 3.25. The parameters are varied within the range shown in the Figure 3.25 and the average of difference is defined as systematic uncertainty.

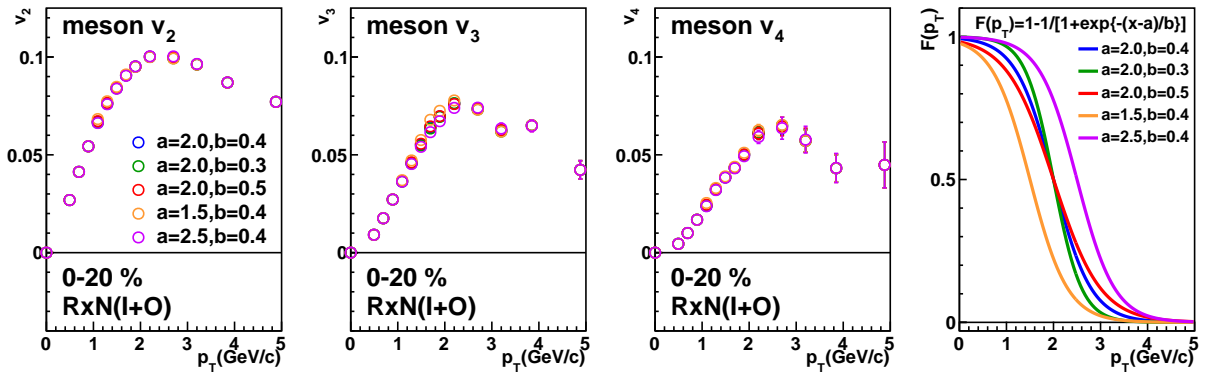


Figure 3.25: The difference of input pion v_n between the parameters in connection equation.

Because the shape of input pion v_n is connected by straight line between the nearest two data points, the shape is not smooth. The equation obtained by fitting to pion v_n is utilized as

input and the variation of decay photon v_n is defined as systematic uncertainty.

$$G_0 = A_0 p_T + A_1 p_T^2 + A_2 p_T^3 + A_3 p_T^4 + A_4 p_T^5 + A_5 p_T, \quad (3.55)$$

$$G_1 = C_0 p_T + \exp(C_1 + C_2 p_T), \quad (3.56)$$

$$T(p_T) = \frac{1}{1 + \exp\{(p_T - t)/0.4\}}, \quad (3.57)$$

$$G = T(p_T)G_0 + (1 - T(p_T))G_1, \quad (3.58)$$

where $A_0, A_1, A_2, A_3, A_4, A_5, C_0, C_1, C_2$, and t are free parameters. G_0 and G_1 are fitted to pion v_n in 0-8 GeV/c and 5-20 GeV/c, respectively. Their parameters are fixed, G is fitted in 0-20 GeV/c again. Figure 3.26 shows the example of pion v_n with Eq. (3.58). Figure 3.27 shows the estimated systematic uncertainty propagated from input v_n .

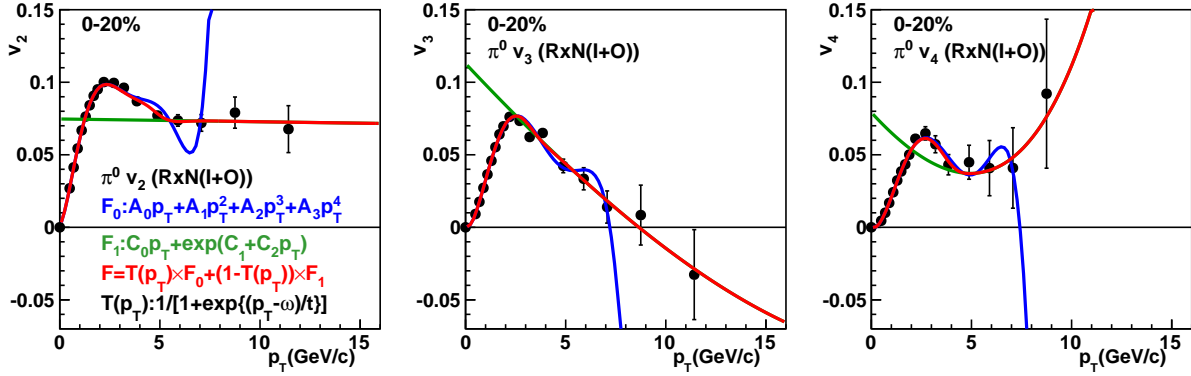


Figure 3.26: The neutral pion v_2, v_3 , and v_4 are fitted by the equations. Red lines are utilized as an input for decay photon v_n simulation.

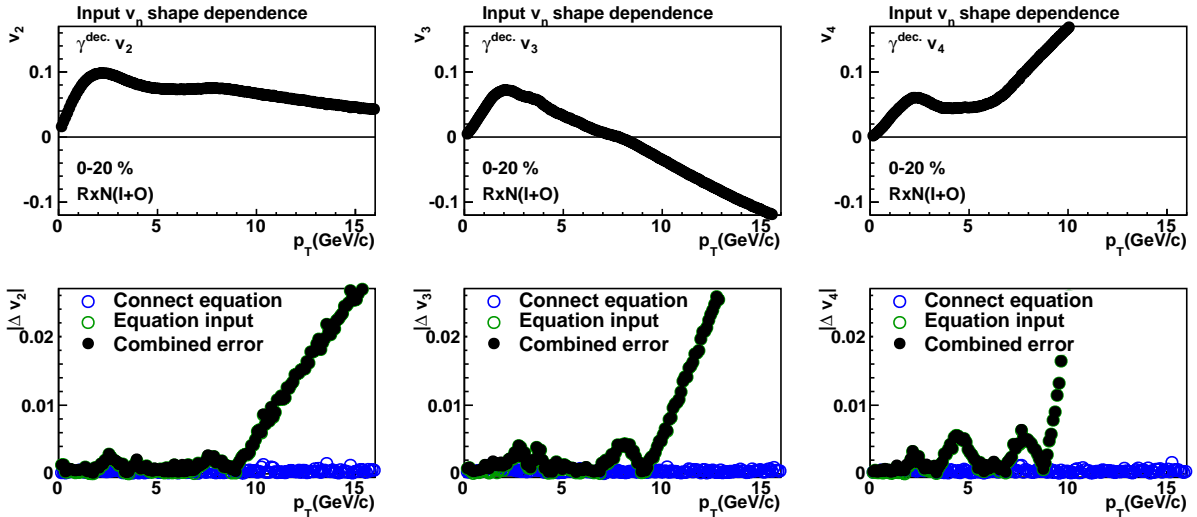


Figure 3.27: (Top) Decay photon v_2 (left), v_3 (middle), and v_4 (right) with event plane measured by RxN(I+O) in 0-20% centrality bin. (Bottom) The systematic uncertainty estimated from the shape of input of pion v_n dependence.

Systematic uncertainty

Systematic uncertainty from event plane determination is discussed in Section 3.4.2. All components of systematic uncertainty of decay photon v_n are combined by a quadratic sum as

$$v_n^{dec.} = \sqrt{\sigma_{spectra}^2 + \sigma_{pionv_n}^2 + \sigma_{shape}^2 + \sigma_{E.P.}^2}, \quad (3.59)$$

where σ_{spec} , σ_{pionv_n} , σ_{shape} , and $\sigma_{E.P.}$ are the systematic uncertainties estimated by p_T spectra dependence, propagated from systematic uncertainty of pion v_n , from input v_n , and event plane determination, respectively. Figure 3.28 shows the simulated decay photon v_n with the range of statistical error in top figures, and systematic uncertainties of each components. It is found that the systematic uncertainty propagated from that of pion v_n is dominant less than 10 GeV/c, and that of input v_n is dominant larger than 10 GeV/c in case of v_2 and v_3 . In case of v_4 , it is observed that systematic uncertainty of event plane determination is significantly dominant.

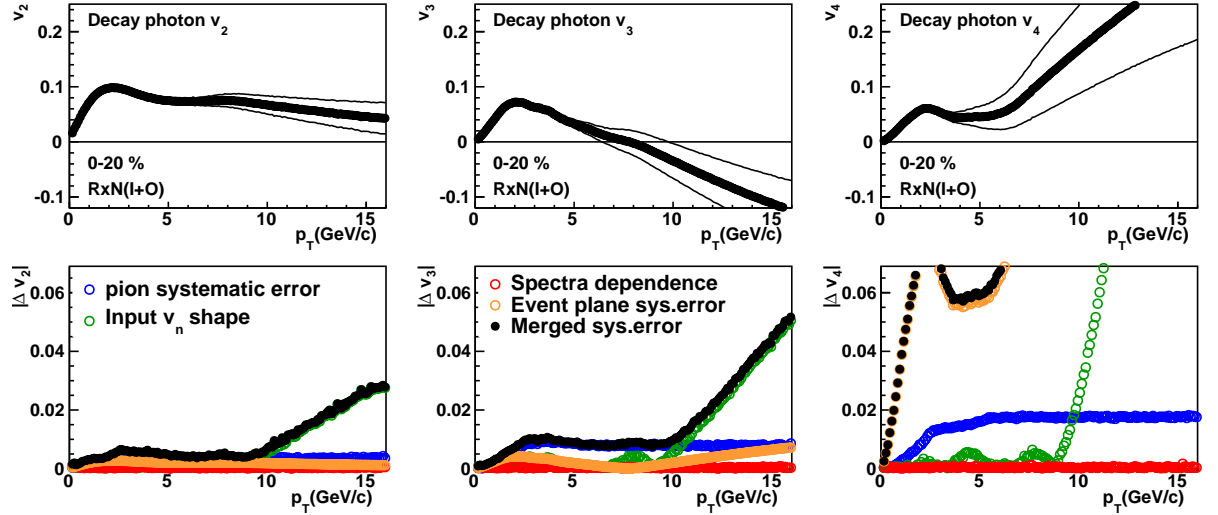


Figure 3.28: (Top) Decay photon v_2 , v_3 , and v_4 with statistical error. (Bottom) Systematic uncertainty from each components (blue, green, red, orange) and summed systematic uncertainty (black).

3.7 Direct Photon v_n Measurement

Direct photon v_n ($v_n^{dir.}$) is extracted from decay photon v_n ($v_n^{dec.}$) and inclusive photon v_n ($v_n^{inc.}$) by the equation

$$v_n^{dir.} = \frac{R_\gamma v_n^{inc.} - v_n^{dec.}}{R_\gamma - 1}, \quad (3.60)$$

where R_γ is the ratio of the number of the inclusive photon to that of decay photon. R_γ less than 4.0 GeV/c is taken from [30], which is calculated by the photons measured by external photon conversion method, and R_γ larger than 4.0 GeV/c is taken from [29], which is measured by using calorimeter. Figure 3.29 shows R_γ measured by calorimeter method, virtual photon method, and external conversion photon method.

Statistical error and systematic uncertainty are propagated by

$$\Delta v_n^{dir.} = \sqrt{\left(\frac{\partial v_n^{dir.}}{\partial v_n^{inc.}} \Delta v_n^{inc.}\right)^2 + \left(\frac{\partial v_n^{dir.}}{\partial v_n^{dec.}} \Delta v_n^{dec.}\right)^2 + \left(\frac{\partial v_n^{dir.}}{\partial R_\gamma} \Delta R_\gamma\right)^2 + \Delta \sigma_{E.P.}^2}, \quad (3.61)$$

where $\Delta v_n^{inc.}$ and $\Delta v_n^{dec.}$ do not include systematic uncertainty for event plane determination ($\Delta \sigma_{E.P.}$) in order to avoid double count. Because it is expected that $\Delta \sigma_{E.P.}$ is common for every particles, it is estimated separately.

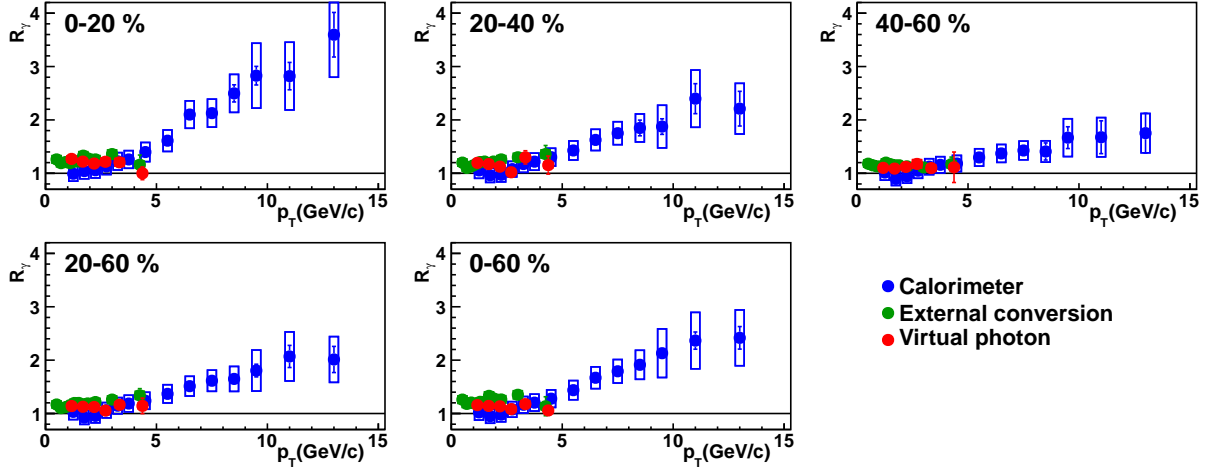


Figure 3.29: The R_γ as a function of p_T , where green points show that measured by calorimeter [29], and green points show that measured by external conversion photon method [30], red points show that measured via virtual photon [11].

Chapter 4

Results

In this section, the results of v_2 , v_3 , and v_4 with RxN(I+O) event plane of inclusive photon, neutral pion, and direct photon are shown. Because the resolution of event plane measured by RxN(I+O) is the best in all detectors as shown in Figure 3.3, the results of v_n with RxN(I+O) event plane are shown here. The others are listed in Appendix A, B, and C. Figure 4.1, 4.2, and 4.3 show the results of inclusive photon v_n , Figure 4.5, 4.6, and 4.7 show the results of neutral pion v_n , and Figure 4.8, 4.9, and 4.10 show the results of direct photon v_n .

4.1 The results of inclusive photon v_n with RxN(I+O) event plane

In $p_T < 4$ GeV/ c , it is found that there are peaks at around 2 GeV/ c for all harmonics. It is also observed that the strong centrality dependence for v_2 while v_3 and v_4 do not show strong centrality dependence. This trend is similar to that seen in charged hadron v_n in [7]. In $p_T > 4$ GeV/ c , it is found the clear difference between even harmonics and odd harmonics. The v_2 and v_4 show the positive in all centrality bin, while v_3 is close to zero in central and goes negative in peripheral. Similar behavior can be seen in neutral pion v_n and it will be discussed in Section 5.1.

4.1.1 Comparison with conversion photon method

The real photon spectra and azimuthal anisotropies has been studied via conversion into e^+e^- pairs at the material such as one of the specific detector plane at Hadron Blind Detector (HBD) outer plane. It is called as “external conversion photon method” [30]. The strength of this method is that we can detect photons in low p_T region with high purity which is higher than 90 %. We have achieved to extend the limit of lowest p_T for photon analysis to 0.2 GeV/ c from 1 GeV/ c . The v_2 and v_3 of inclusive photon have been measured with external conversion photon method in PHENIX experiment. The comparison of inclusive photon v_2 and v_3 with external conversion photon method and this analysis are shown in Figure 4.4. It is observed that two methods are consistent within systematic uncertainties for both v_2 and v_3 . The comparison of two independent methods provides the robustness of the inclusive photon v_n results.

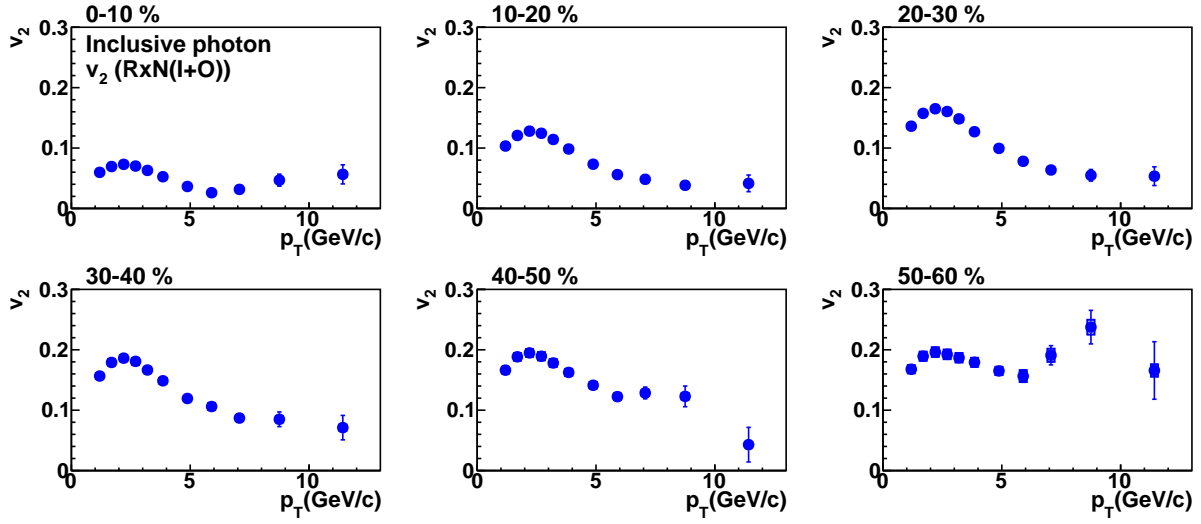


Figure 4.1: The results of inclusive photon v_2 (RxN(I+O)) with 10% centrality interval.

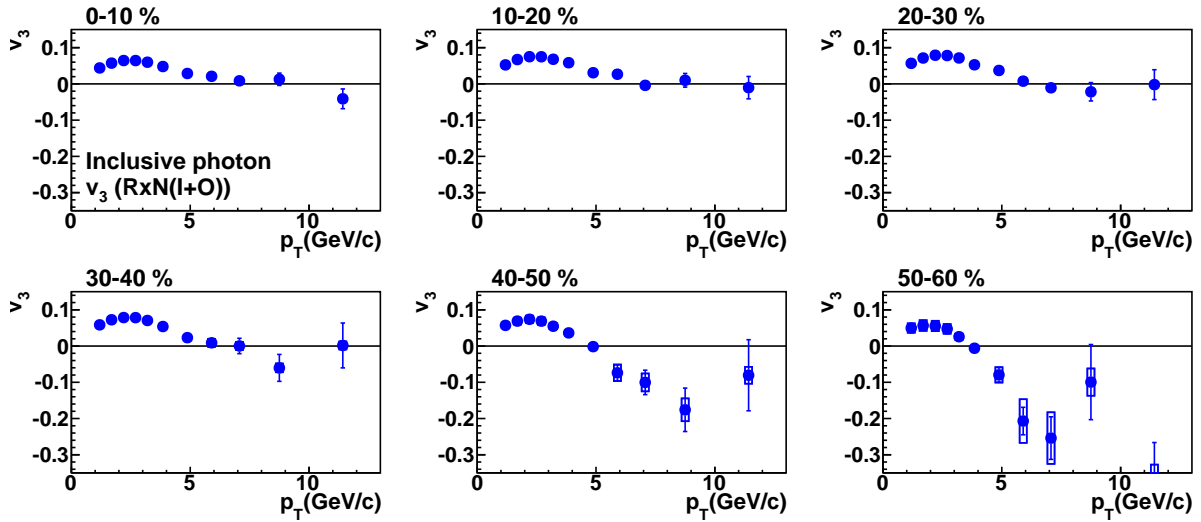


Figure 4.2: The results of inclusive photon v_3 (RxN(I+O)) with 10% centrality interval.

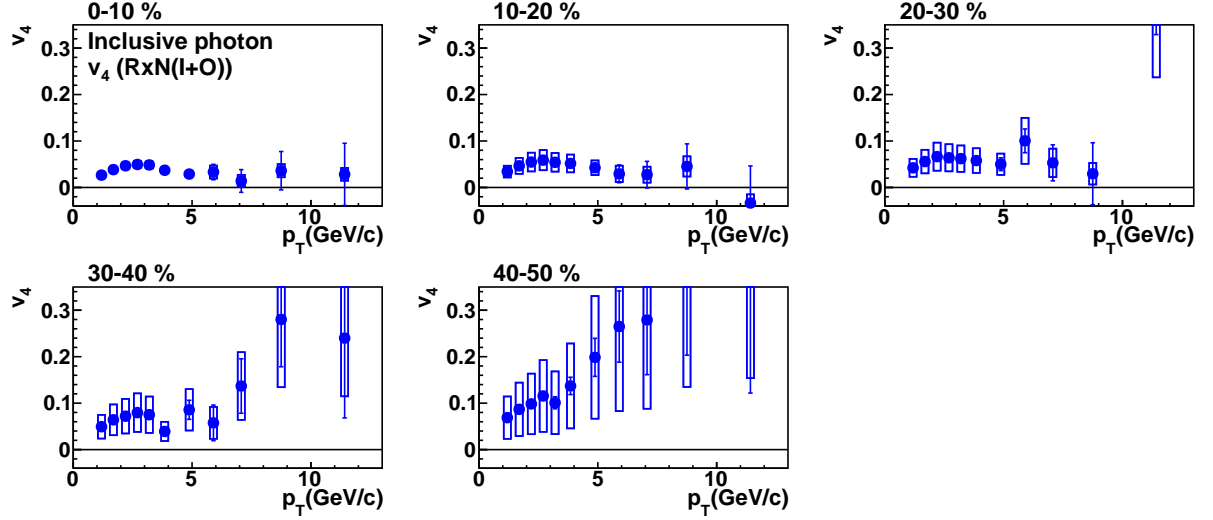


Figure 4.3: The results of inclusive photon v_4 (RxN(I+O)) with 10% centrality interval.

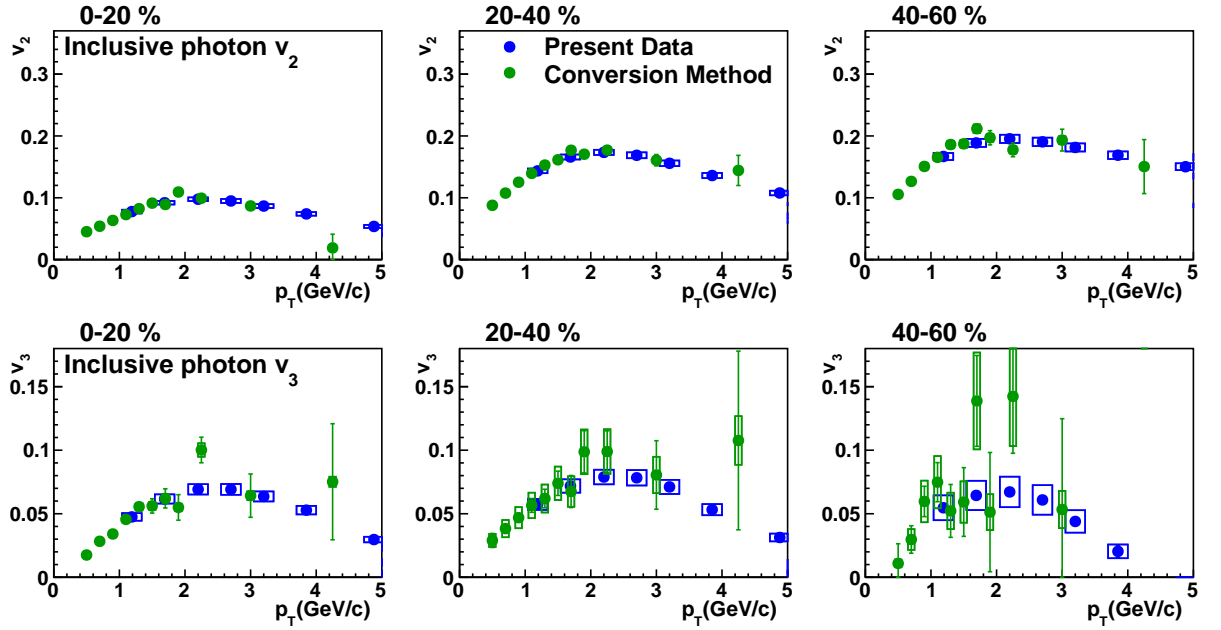


Figure 4.4: Inclusive photon v_2 (top) and v_3 (bottom) measured by calorimeter (blue) and conversion photon method (green), respectively. The results of conversion photon method are preliminary on PHENIX.

4.2 The results of neutral pion v_n with RxN(I+O) event plane

The trend of neutral pion v_n is similar to that seen in inclusive photon v_n in Section 4.1. In order to understand the p_T dependence of v_n in high p_T , the bias from jet fragmentation on v_n will be discussed in Section 5.1.

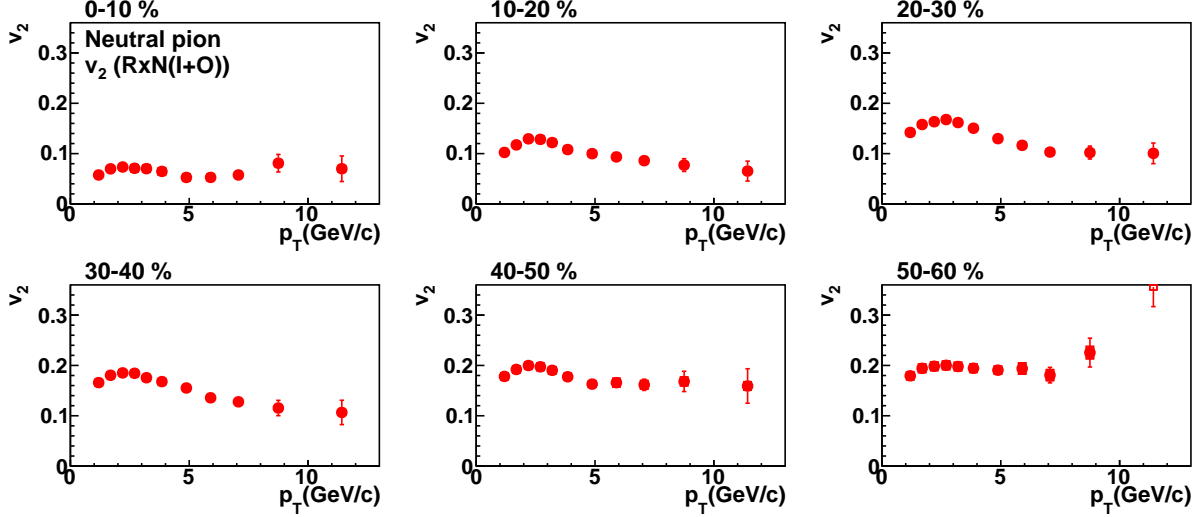


Figure 4.5: The results of neutral pion v_2 (RxN(I+O)) with 10% centrality interval.

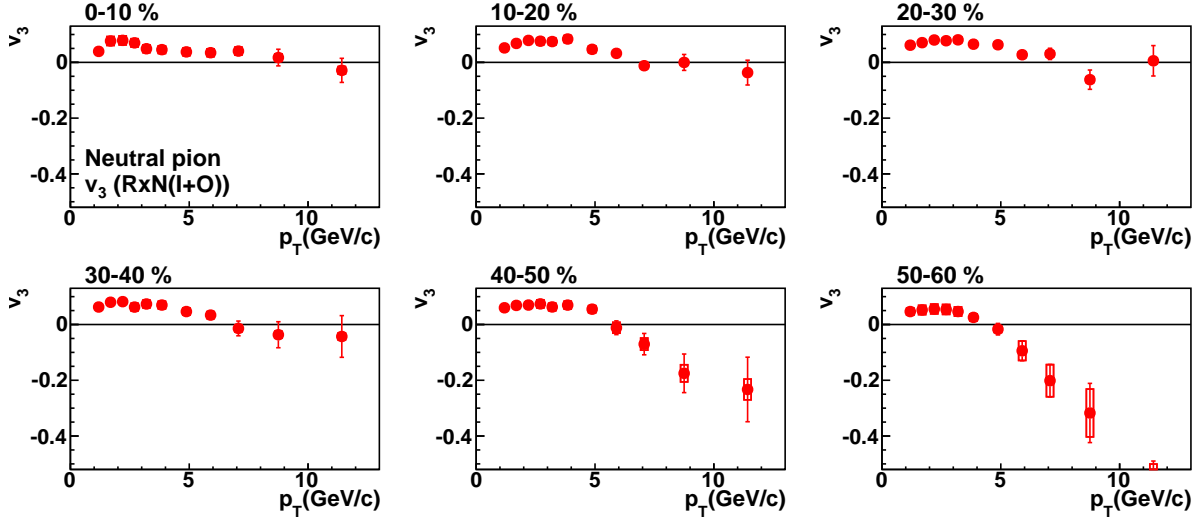


Figure 4.6: The results of neutral pion v_3 (RxN(I+O)) with 10% centrality interval.

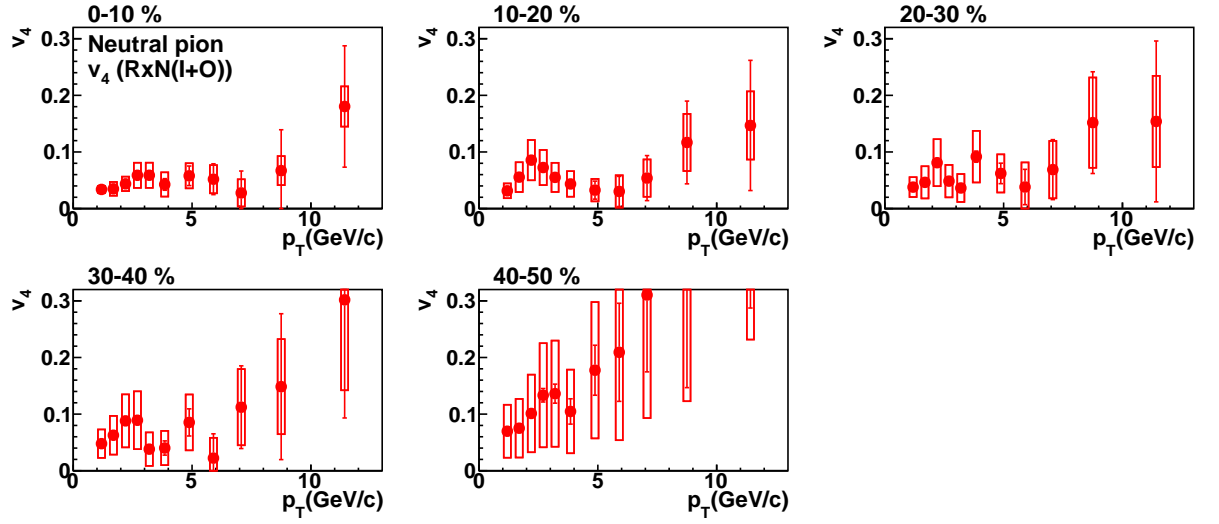


Figure 4.7: The results of neutral pion v_4 (RxN(I+O)) with 10% centrality interval.

4.3 The results of direct photon v_n with RxN(I+O) event plane

In $p_T > 4$ GeV/c, it is found that direct photon v_n is close to zero. In $p_T < 4$ GeV/c, it is observed that direct photon show non-zero and positive v_2 and v_3 . Direct photon v_4 is consistent with 0 within large systematic uncertainties in the measured p_T and centrality ranges. They will be discussed in Section 5.2.

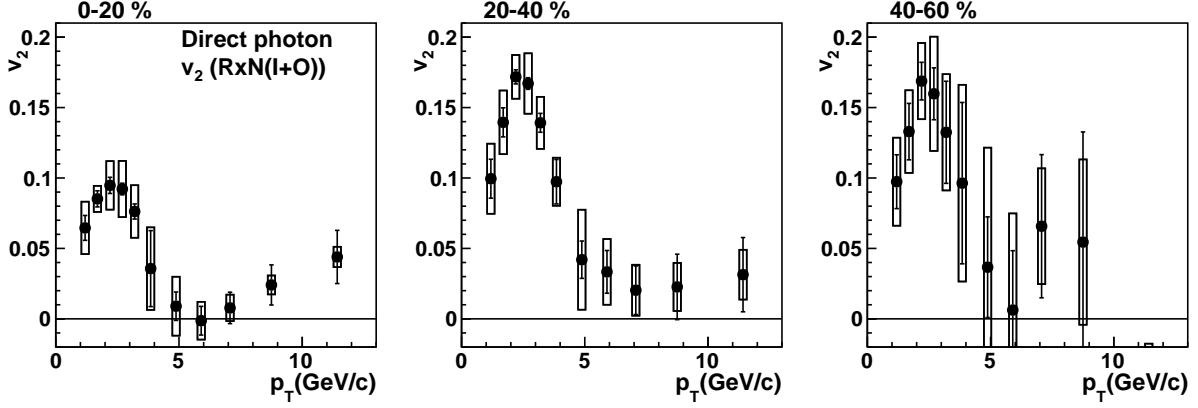


Figure 4.8: The results of direct photon v_2 (RxN(I+O)) with 20% centrality interval.

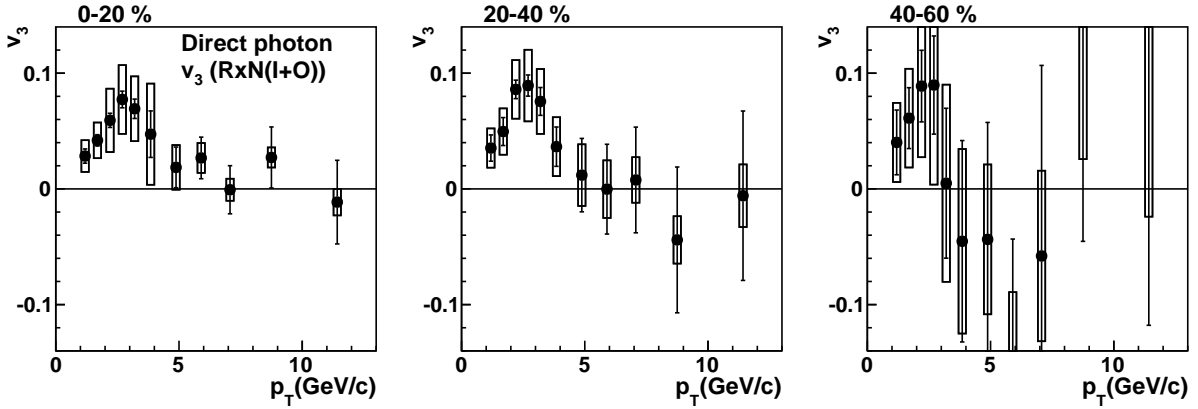


Figure 4.9: The results of direct photon v_3 (RxN(I+O)) with 20% centrality interval.

4.3.1 Comparison with conversion photon method

The direct photon v_n is extracted from inclusive photon v_n with conversion photon method by the manner used in this analysis. Statistical and systematic uncertainties are estimated as

$$\Delta v_n^{dir.} = \sqrt{\left(\frac{\partial v_n^{dir.}}{\partial v_n^{inc.}} \Delta v_n^{inc.}\right)^2 + \left(\frac{\partial v_n^{dir.}}{\partial v_n^{dec.}} \Delta v_n^{dec.}\right)^2 + \left(\frac{\partial v_n^{dir.}}{\partial R_\gamma} \Delta R_\gamma\right)^2}. \quad (4.1)$$

Because inclusive photon v_n with conversion photon method and decay photon v_n are measured in different data set, systematic uncertainty of event plane determination could be different. In order to estimate uncertainty conservatively, the systematic uncertainties of inclusive photon v_n

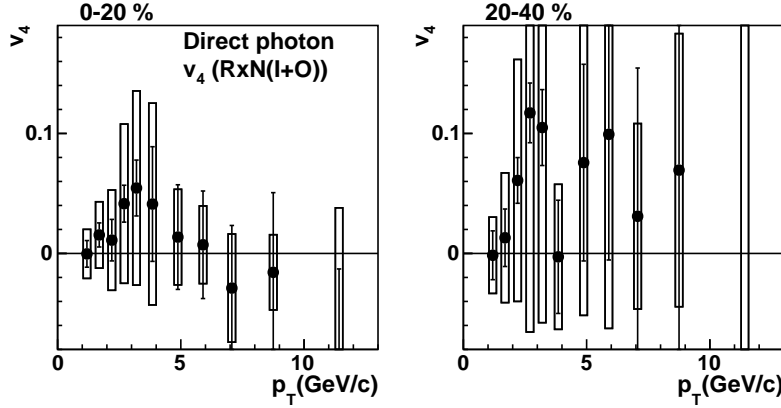


Figure 4.10: The results of direct photon v_4 (RxN(I+O)) with 20% centrality interval.

and decay photon v_n including that from event plane determination ($\Delta v_n^{inc.}$, $\Delta v_n^{dec.}$) are used. Because systematic uncertainty estimated from event plane determination is double counted, uncertainties of direct photon v_n with conversion photon method is overestimated. Figure 4.11 shows the comparison of direct photon v_n between the methods. It is observed that they agree well in the region of $1 < p_T < 2$ GeV/c.

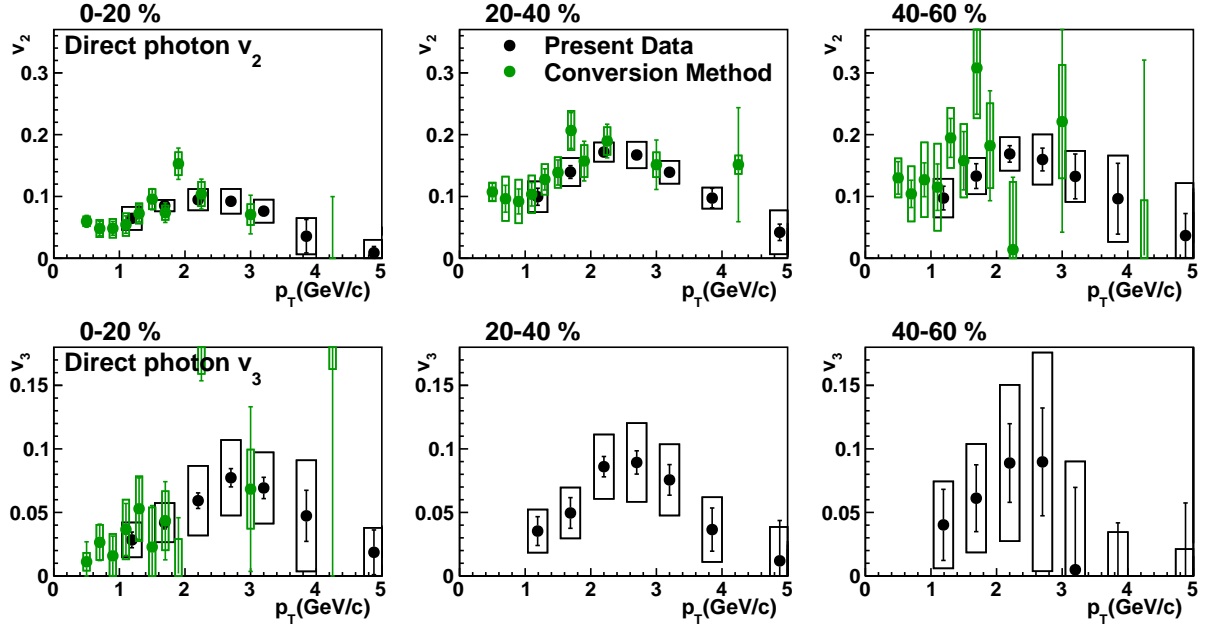


Figure 4.11: Direct photon v_2 (top) and v_3 (bottom) measured by calorimeter (black) and conversion photon method (green), respectively. The direct photon v_n with external conversion method is extracted decay photon v_n (Section 3.6) from inclusive photon v_n (Figure 4.1.1).

Chapter 5

Discussion

The neutral pion and direct photon v_2 , v_3 , and v_4 are measured with several event plane detectors in Au+Au collisions at $\sqrt{s_{NN}}=200$ GeV. The high p_T neutral pion v_n and direct photon v_n are discussed in Section 5.1 and 5.2, respectively.

5.1 Neutral pion azimuthal anisotropy

In this section, results of neutral pion azimuthal anisotropy are discussed. The jet effect on neutral pion v_n in high p_T is discussed in Section 5.1.1 and the jet effect on high p_T v_n with AMPT simulation is studied in Section 5.1.2.

5.1.1 Comparison of neutral pion v_n in high p_T with different event planes

Neutral pion v_2 , v_3 and v_4 with event plane defined by RxN(In)+MPC ($1.5 < |\eta| < 3.8$) and RxN(Out) ($1 < |\eta| < 1.5$) are shown in Figure 5.1. It is found that there is no event plane dependence in low p_T region. In high p_T region, it is observed that there is a clear event plane difference of v_2 , which increases with increasing p_T and with small rapidity gap between central arm and event plane. While there is no clear event plane dependence for v_3 in high p_T region. It is found that the v_3 is largely negative in peripheral event. In the case of v_4 , the uncertainties are too large to distinguish the difference.

Because hadron production in high p_T region is dominated by jet fragmentation, the measurement of high p_T hadron azimuthal anisotropy is probe to study jet properties within QGP. The following jet properties are expected to affect the measured v_n .

- Di-jet production
- Path length dependence of jet energy loss
- Jet bias effect on event plane determination

First, these jet effects are studied with v_2 , then v_3 and v_4 . Figure 5.2 shows the integrated v_2 , v_3 and v_4 within $6 < p_T < 15$ GeV/ c with RxN(In)+MPC ($1.5 < |\eta| < 3.8$) and RxN(Out) ($1 < |\eta| < 1.5$). It is found that the v_2 is positive in all centralities, increases with going to peripheral event and v_2 with RxN(Out) is larger than v_2 with RxN(In)+MPC. The trends

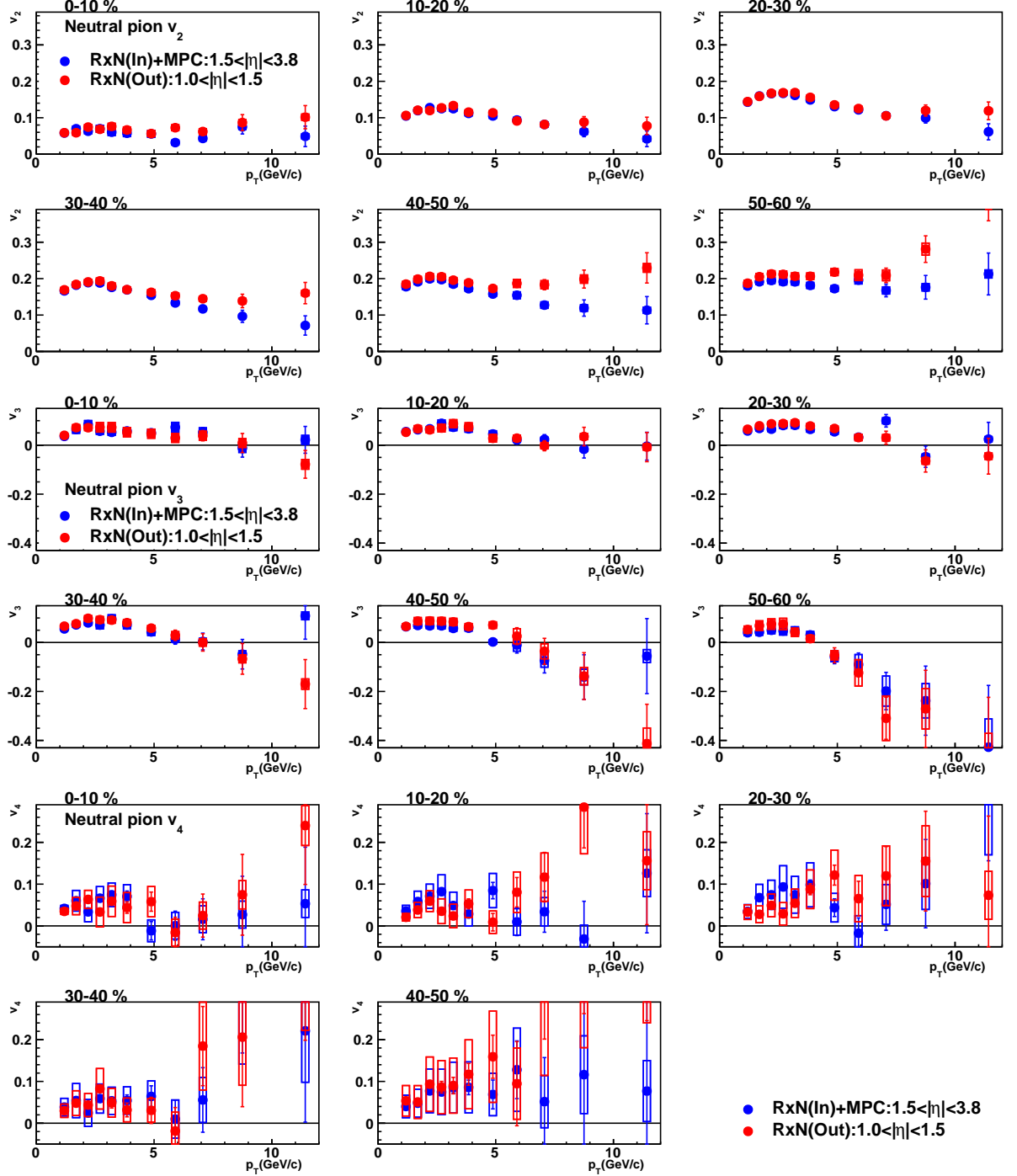


Figure 5.1: Neutral pion v_2 , v_3 , and v_4 with event plane measured by RxN(In)+MPC (blue) and RxN(Out) (red) with 10% centrality steps from 0 to 60%.

could be understood as followings. Two jets are emitted in back-to-back azimuthal direction in order to conserve transverse momentum which is called as di-jet. Di-jet event always makes v_2 large since back-to-back particle emission could resemble elliptic particle emission, even if the production does not have any correlation with reaction plane. If there is partonic energy loss in QGP followed by consequent high p_T particle suppression which would depend on path length determined by the elliptic almond shape, non-zero positive v_2 is naturally expected at high p_T . Because the central arm ($|\eta| < 0.35$) is closer to RxN(Out) than RxN(In)+MPC, v_n with event plane determined by RxN(Out) should be more affected by jet bias [51]. Especially the effect would be relatively strong for peripheral events due to small multiplicity. If the angle of event plane is affected by the particles from jet, the measured v_2 is increased due to narrow jet cone and back-to-back di-jet production, and a large eta swing of the di-jet kinematics. Because the detector which is closed to central arm is more strongly affected by the jet particles, v_2 could be strong. Therefore, high p_T hadron v_2 could be understood by the superimposition of path length dependence of jet energy loss ($v_2 > 0$) and jet bias on determination of event plane ($v_2 > 0$).

In the case of v_3 , it is expected that non-suppressed back-to-back di-jet would give smaller v_3 due to the triangular shape of participant. The energy deposit of hard parton in QGP could make v_3 positive. However there would be both positive and negative effects on v_3 when the event plane is affected by jet. It is found that the integrated v_3 is positive in central and varies to negative with going to peripheral collision. It could be understood that the effect of jet energy deposit in QGP is dominant in central collisions, and the jet bias on determining event plane gets dominant with going to peripheral events. It is observed that the trend of v_4 could be similar to that of v_2 and it agrees with the expectation because the forth order of initial geometry is quadrangular and symmetric shape. However it is difficult to distinguish the difference of v_4 between RxN(Out) and RxN(In)+MPC due to large uncertainties.

It is observed that single particles have positive v_2 and v_3 up to 60 GeV/c and 20 GeV/c, respectively, in CMS experiment [52] and jet has positive v_2 in ATLAS experiment [53] at LHC energy. They could be understood that the energy deposit of hard parton during passing through the medium has path length dependence. The v_3 and v_4 measurements could also help to study path length dependence of jet energy loss in the medium in addition to the v_2 measurement.

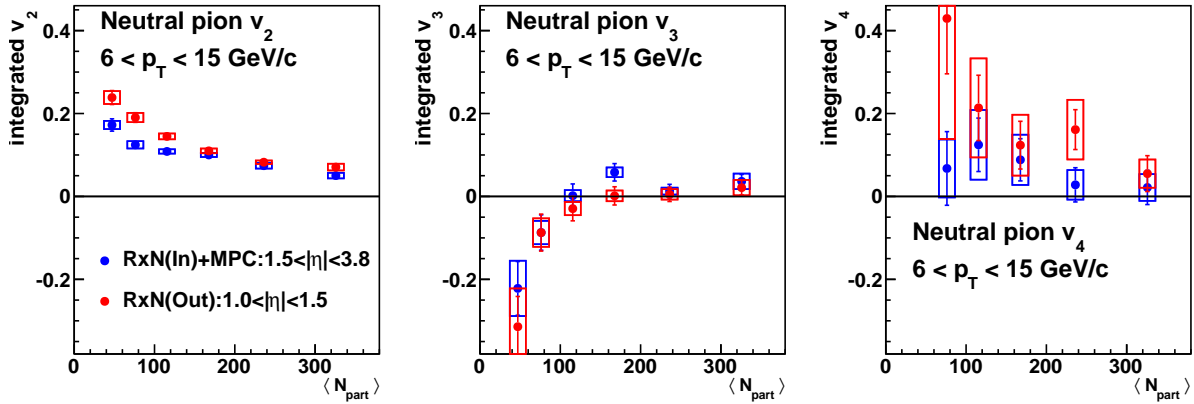


Figure 5.2: Integrated v_2 (left), v_3 (middle), and v_4 (right) of neutral pions within $6 < p_T < 15$ GeV/c as a function of $\langle N_{part} \rangle$ with respect to the RxN(In)+MPC (blue) and RxN(Out) (red).

5.1.2 AMPT model calculation of pion v_n in high p_T region

In order to understand the behavior of neutral pion v_n in high p_T region, a multiphase transport (AMPT) simulation is utilized [54]. AMPT consists of the heavy ion jet interaction generator (HIJING) for generating the initial conditions, Zhang's parton cascade (ZPC) for modeling partonic scatterings, the Lund string fragmentation model or a quark coalescence model for hadronization, and a relativistic transport (ART) model for treating hadronic scatterings. Events are generated by AMPT and azimuthal anisotropy is calculated with the same detector acceptance and analysis method as done in the experimental measurement. The events including jet with larger than 20 GeV/ c are generated and 10 million events are analyzed.

Figure 5.3 shows the comparison of v_n as a function of p_T between the experimental measurement and the AMPT simulation. It is found that v_2 and v_3 of AMPT simulations are similar to that of experimental measurement less than 10 and 5 GeV/ c , respectively. In the case of v_2 , it is observed that the v_2 with RxN(In)+MPC is smaller than that with RxN(Out) in $p_T > 2$ GeV/ c . In the case of v_3 , there seems to be some decreasing trend with increasing p_T in high p_T region as also seen in the experimental data, however it is difficult to conclude the trend because of large statistical error.

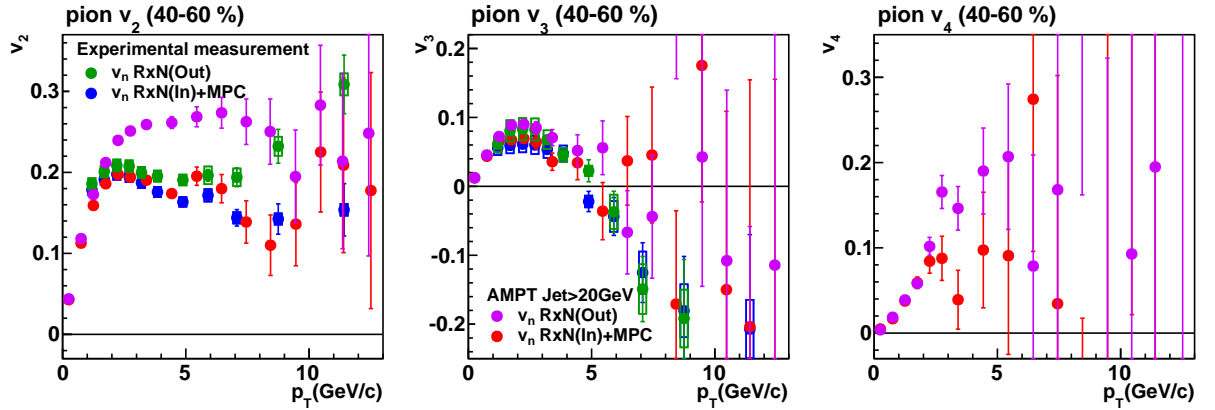


Figure 5.3: Comparison of experimental π^0 v_2 , v_3 with RxN(In)+MPC (blue) and RxN(Out) (green), and simulated pion v_2 , v_3 with RxN(In)+MPC (red) and RxN(Out) (violet). Comparison of π^0 v_2 , (left) v_3 (middle), and v_4 (right) as a function of p_T in 40-60% centrality.

In order to study jet bias on determining event plane, the particles in $p_T < 2$ GeV/ c and in $p_T > 2$ GeV/ c are used for determining event plane. It is expected that particles originated from hydrodynamical expanded medium are dominant in $p_T < 2$ GeV/ c and we would be able to increase the fraction of particles from jets by selecting $p_T > 2$ GeV/ c . Panel (a) in Figure 5.4 shows the p_T distribution within $1 < |\eta| < 2.8$ corresponding to the acceptance of RxN(I+O) detector in PHENIX. Panel (b), (c), and (d) show the event plane resolutions for second, third, and fourth order with p_T selections, respectively. It is found that the resolution with the particles in $p_T < 2$ GeV/ c agrees well with that with all particles. On the other hand, resolutions with particles in $p_T > 2$ GeV/ c increases with going to peripheral event. It could be because the jets tend to emit from the short direction of initial shape and the initial shape anisotropy is strong in peripheral. Therefore the directions of jets are well correlated with respect to initial shape of

participants and resolution is very large.

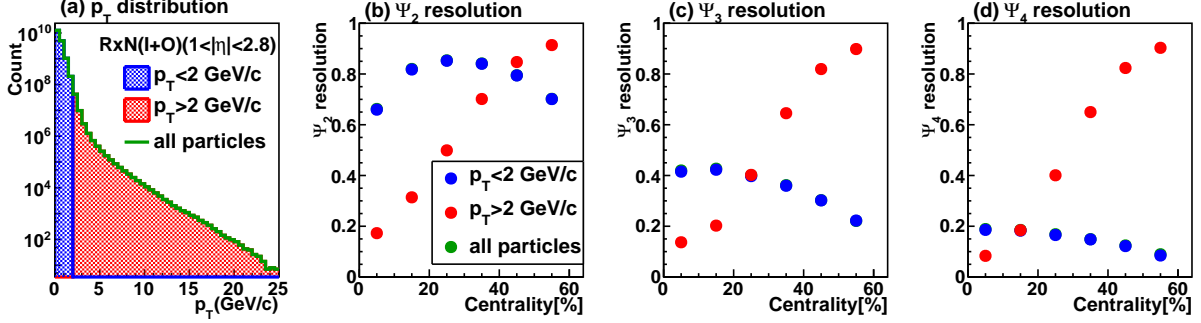


Figure 5.4: (a) The p_T distribution in the region of $1 < |\eta| < 2.8$ corresponding to the acceptance of RxN(I+O) detector. Panel (b), (c), and (d) show the second, third, and fourth order event plane resolution. Event plane is estimated by the particles in the region of $p_T < 2$ GeV/c (blue), $2 < p_T$ GeV/c (red), and all particles (green).

Figure 5.5 shows the results of pion v_n with p_T selected event plane. It is found that there are the deviations between the differences of determined event plane. In peripheral collisions, it is observed that the high p_T v_2 (v_3) with event plane determined in $p_T > 2$ GeV/c is larger (smaller) than that with event plane with $p_T < 2$ GeV/c. It is confirmed that the jet bias on determining event plane makes v_2 large and v_3 negative. Although statistical error of v_4 is too large to distinguish the difference in high p_T region. In $p_T < 4$ GeV/c, v_n with event plane biased jet is smaller than v_n with event plane not affected in 20-40 and 40-60% centralities.

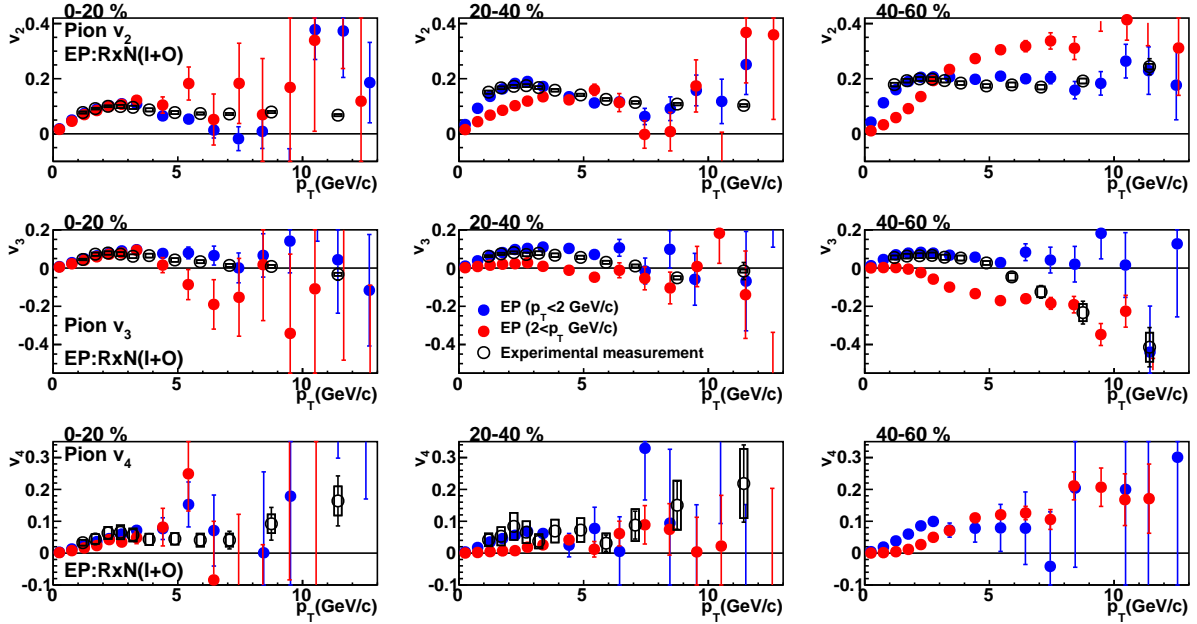


Figure 5.5: The pion v_2 (top), v_3 (middle), and v_4 with p_T selected event plane. Black points are experimental measurement, blue points are v_n with event plane defined by particles less than 2 GeV/c, and red points are v_n with event plane estimated from particles larger than 2 GeV/c.

In order to study the difference of v_n between the event planes, the integrate v_2 , v_3 , and v_4 as a function of $\Delta\eta$ are measured. The event planes are determined by 0.5 steps from 0 to 3 (-3 to 0) in pseudorapidity, and the angles of pion are measured within -3 to 0 (0 to 3) in pseudorapidity. Figure 5.6 shows the v_n with event plane determined in $p_T < 2$ GeV/c. It is found that v_n shows positive and weak $\Delta\eta$ dependence in all centrality bins. While in peripheral event, v_n within $2 < p_T < 5$ and $5 < p_T < 10$ GeV/c decreases with increasing the $\Delta\eta$, especially it is found in peripheral event. It indicates that event plane determination is biased by the particles originating from jet though particles in $p_T < 2$ GeV/c are selected due to low multiplicity. It is found that v_3 within $5 < p_T < 10$ GeV/c changes positive to negative while v_2 and v_4 are positive in all $\Delta\eta$. It could due to particles from jet bias on determining event plane and particles fragmented from away side jet. It is discussed below.

Figure 5.7 shows the v_n with event plane determined in $p_T > 2$ GeV/c. It is found that v_n within $5 < p_T < 10$ GeV/c at $\Delta\eta < 0.5$ is larger than v_n at $\Delta\eta > 0.5$. It indicates that the particles from a jet biasing for event plane angle are also detected in the region of measuring v_n . Because the azimuthal angles of particles from one jet should be correlated, v_n should be large. The v_2 and v_4 decrease with $\Delta\eta$ increasing while v_3 drops at $\Delta\eta = 0.5$ and increases. It could be understood that the particles from away side jet makes v_2 and v_4 positive while v_3 negative due to the initial geometry when one jet bias event plane. Figure 5.8 shows the image of jet bias on determining event plane. Near side jet ($\Delta\phi \approx 0$, red) makes v_n large while away side jet ($\Delta\phi \approx \pi$, blue) makes v_2 and v_4 positive but v_3 negative.

Therefore, it is confirmed that there are two types of jet bias on determining event plane when high p_T hadron v_n is measured. One is that the particles from one jet (near side jet) are produced into the both region of determining event plane and measuring v_n . Another is that the particles from away side jet are detected in the region of measuring v_n when one jet biases on the direction of event plane. This result suggests that jet bias on determining event plane should be taken into account for high p_T v_n measurement via event plane method.

The behavior of neutral pion v_2 , v_3 , and v_4 are discussed with the AMPT simulations. High p_T hadron v_n measurement is good probes to study jet properties in QGP. Path length dependence of jet energy loss in QGP has been measured actively in order to study the interaction between partons. It is found that high p_T hadron v_n is strongly affected by the jet bias on determining event plane. It provides that we should take care of it when high p_T hadron v_n is measured, especially in peripheral event. It is expected that high p_T hadron v_n measurement is very helpful to study jet properties in high energy heavy ion collisions.

5.2 Direct photon azimuthal anisotropy

In this section, direct photon v_n will be discussed. The direct photon v_2 , v_3 , and v_4 are compared with neutral pion in Section 5.2.1, the ratio of v_2 to v_3 of direct photon and charged pion are compared with model calculations in Section 5.2.2, the comparisons of direct photon v_2 and v_3 with model calculations are shown in Section 5.2.3, and the possibility of understanding photon puzzle is discussed in Section 5.2.4.

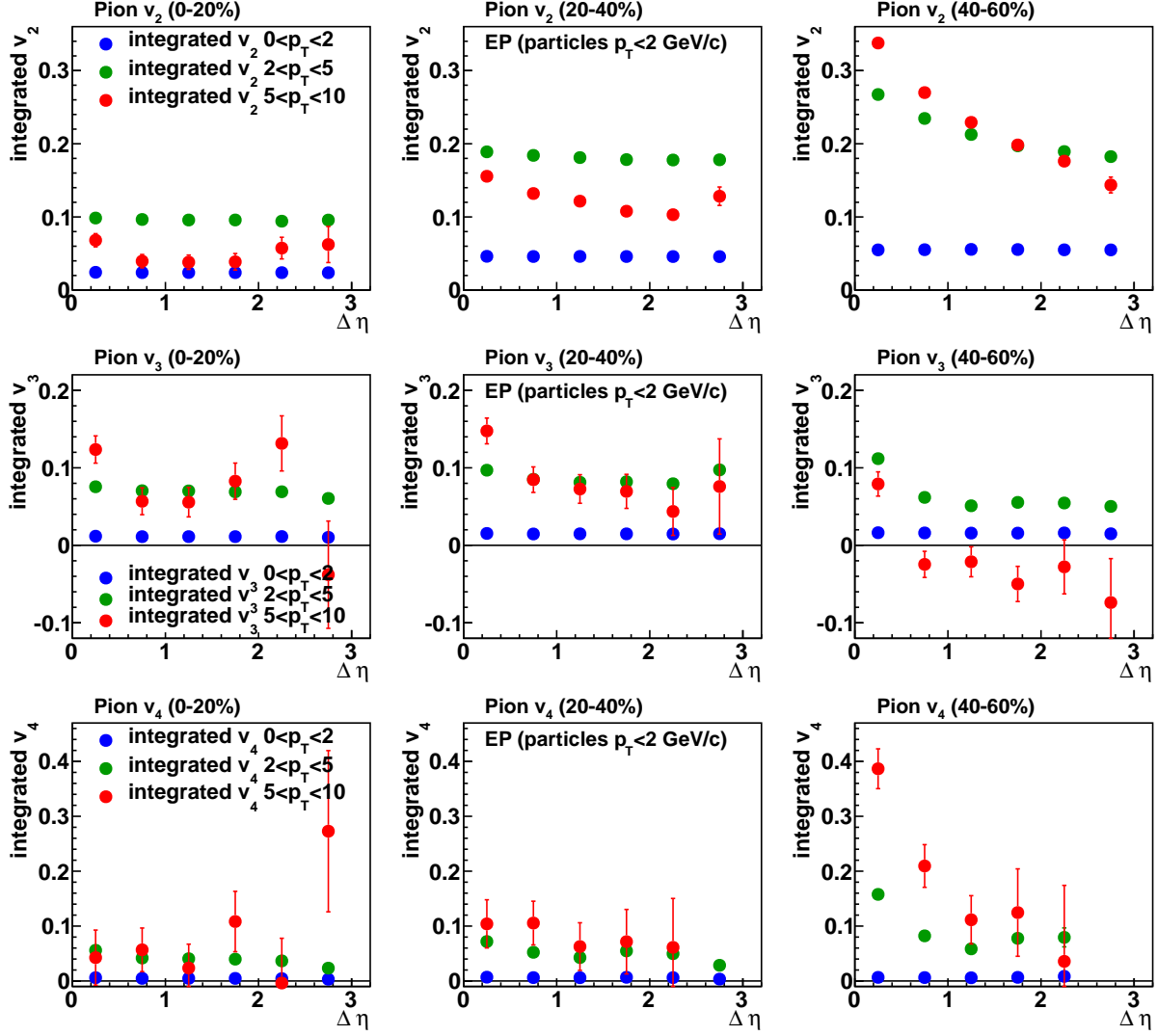


Figure 5.6: The integrated v_2 (top) and v_3 (bottom) as a function of $\Delta\eta$. Event plane is estimated by the particles in the region of $p_T < 2$ GeV/c. $\Delta\eta$ is the difference between the event plane and the region of measuring the pion angle. The v_n within $0 < p_T < 2$ (blue), $2 < p_T < 5$ (green), and $5 < p_T < 10$ GeV/c (red).

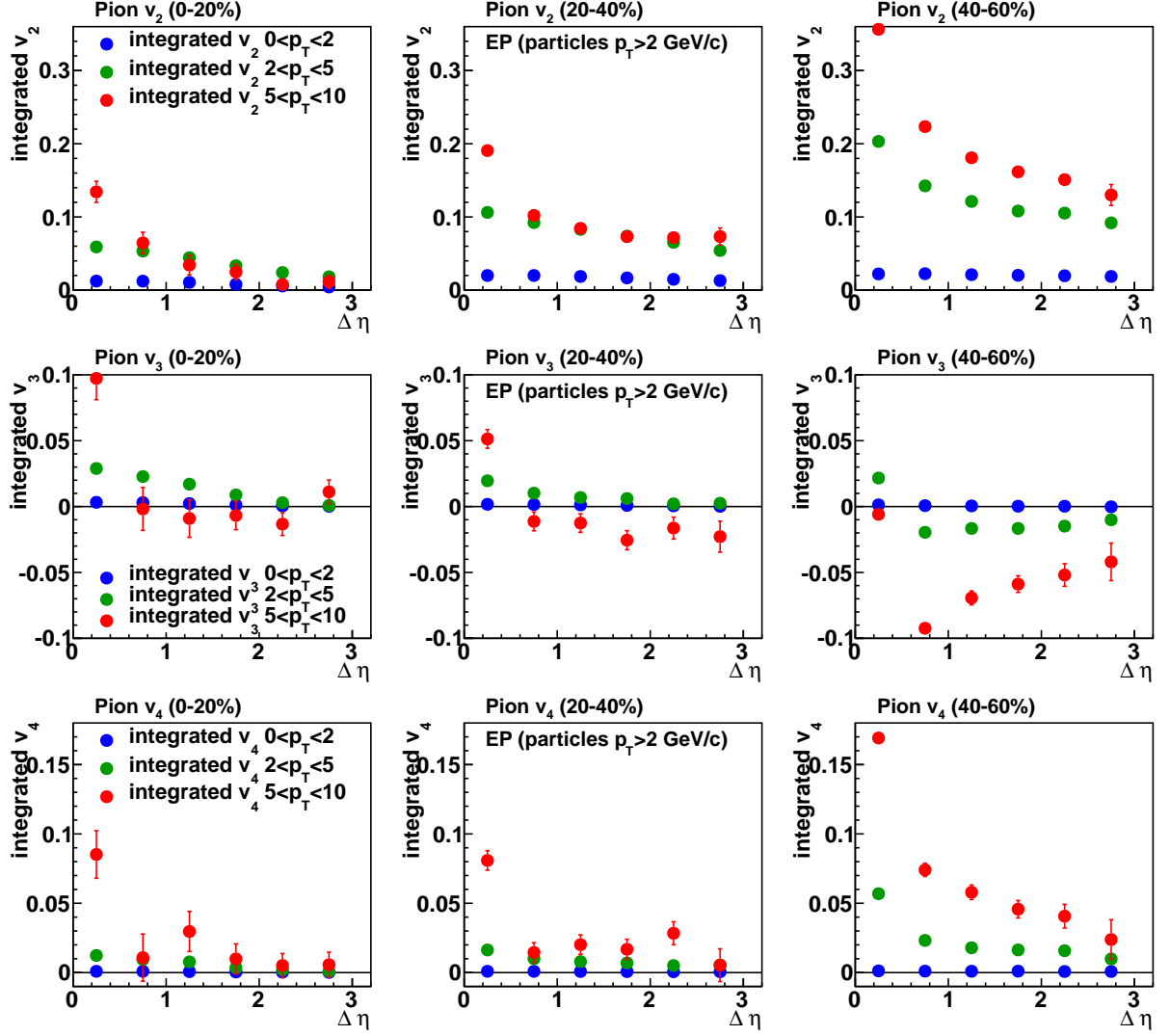


Figure 5.7: The integrated v_2 (top) and v_3 (bottom) as a function of $\Delta\eta$. Event plane is estimated by the particles in the region of $p_T > 2$ GeV/c. $\Delta\eta$ is the difference between the event plane and the region of measuring the pion angle. The v_n within $0 < p_T < 2$ (blue), $2 < p_T < 5$ (green), and $5 < p_T < 10$ GeV/c (red).

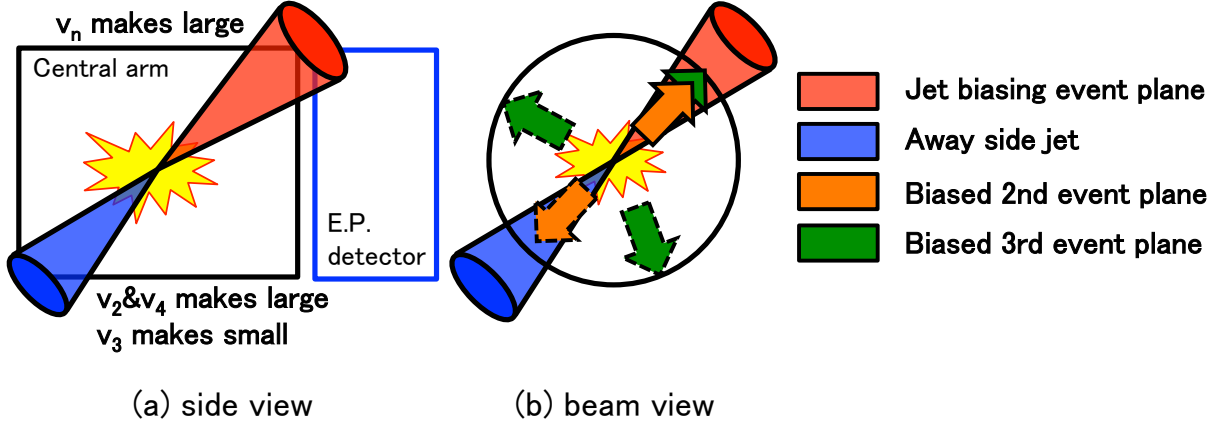


Figure 5.8: The image of the v_n with affected by particles fragmented from jet from side view (a) and beam view (b). Jet biasing on determining event plane (red) and away side jet (blue). Biased 2nd order event plane (orange) and 3rd order event plane (green).

5.2.1 Comparison of direct photon and neutral pion v_n

Figure 5.9 shows the comparison of v_2 , v_3 , and v_4 between direct photon and neutral pion measured via RxN(I+O) event plane. It is found that the strength of photon v_2 and v_3 at around 2 GeV/c is comparable to that of neutral pion and the centrality dependences of them are similar to those of neutral pion. These results suggest that the strength of direct photon v_n correlates with the initial geometry anisotropy and photons are emitted from late stages of the collisions where radial expansion is strong. The photon v_n in low p_T region will be discussed in followings. In $p_T > 4$ GeV/c, it is observed that photon v_2 is much smaller than neutral pion v_2 in all centrality bins, and there is difference for v_3 and v_4 in 40-60% and 0-20 % centrality bin, respectively.

In order to study the centrality dependence of direct photon v_n in high p_T region, the integrated v_2 , v_3 , and v_4 of direct photon and neutral pion within $6 < p_T < 10$ GeV/c are shown in Figure 5.10. It is found that there is clear difference between neutral pion and direct photon in v_2 . As discussed in Section 5.1, since neutral pion would be mostly originated from jet fragmentation after the strong energy loss in the medium, there should be difference between in-plane and out-of-plane directions due to their path length. On the other hand, direct photon would be given by the summation of jet fragmentation photon ($v_n^{dir.} \approx v_n^\pi$) and dominating prompt photon production ($v_n \approx 0$), therefore it is expected to have small v_2 . The trend of v_4 could be similar to the case of v_2 , but the uncertainties are too large to distinguish the difference. In the case of v_3 , neutral pion shows small value in central collisions, while it becomes negative in peripheral collisions which could be understood by the jet bias on event plane determination. However the photon v_3 is consistent with zero in all centrality bins, which could also be consistent with no-suppression given by small interaction of direct photon within QGP.

In the region of $6 < p_T < 10$ GeV/c, photons are dominantly originated from jet fragmentation and initial hard scattering. From comparison of photon v_n and neutral pion v_n , it is found that photons from initial hard scattering are relatively dominant.

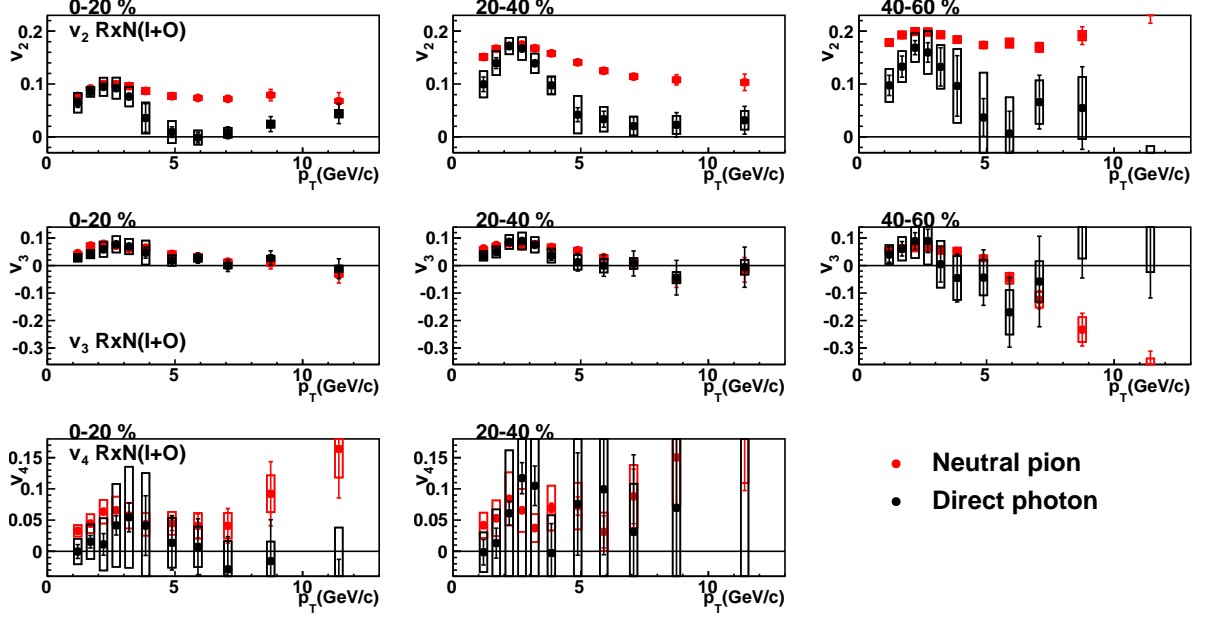


Figure 5.9: Direct photon and neutral pion v_2 (top), v_3 (middle), and v_4 (bottom) with RxN(I+O) event plane.

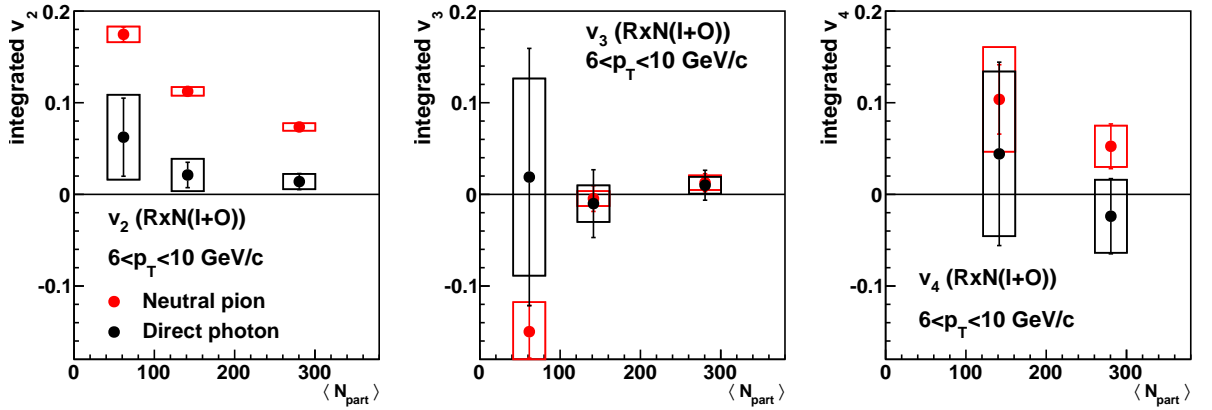


Figure 5.10: Integrated v_2 (left), v_3 (middle), and v_4 (right) within $6 < p_T < 10$ GeV/c of direct photon and neutral pion with RxN(I+O) event plane.

5.2.2 The ratio of v_2 to v_3

It is predicted that the photon v_n is more sensitive to η/s of QGP than the hadron v_n [16]. It is because the η/s affects for the both of the expansion and photon emission rate in hydrodynamic model. The models calculations are taken from one of the hydrodynamic model [31]. The photon v_2 and v_3 are calculated with the boost-invariant viscous hydrodynamical model VISH2+1. The η/s is defined as 0.08 and 0.20 for initial conditions generated from the Monte-Carlo Glauber (MCGlb) and Monte-Carlo KLN (MCKLN), respectively, in order to describe soft hadron observables at RHIC and LHC energies.

Figure 5.11 shows the comparison of the ratio of v_2 to v_3 for photon and charged pion [8] with model calculations, and the χ^2 is summarized in Table 5.1. It is observed that the ratio of photons show weak centrality dependence in $p_T=2-3$ GeV/ c region, while charged pion shows clear centrality dependence. Although uncertainties of direct photon v_2/v_3 ratios are large, MCGlb+ $\eta/s(0.08)$ describes experimental data better. On the other hand, the ratio of charged particle is described by MCKLN+ $\eta/s(0.20)$ better.

It is found that the ratio of v_2 to v_3 shows the different centrality dependence while the strength of direct photon v_n is comparable to that of pion v_n at around $p_T = 2-3$ GeV/ c . It could be because photons are emitted from all stages of the collisions while hadrons are created at the freeze-out temperature. It is expected that this result provide additional constrain on η/s of QGP and/or initial conditions (MCGlb/MCKLN) as well as the knowledges about the time dependence of photon production mechanisms.

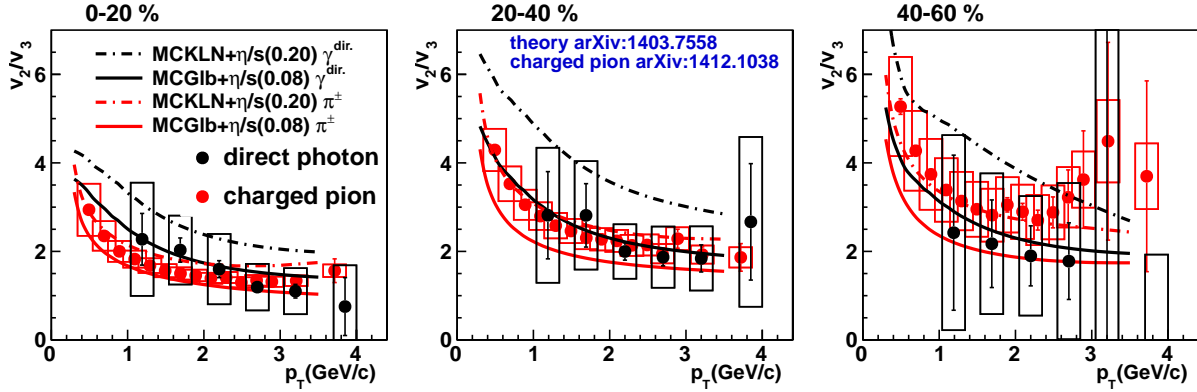


Figure 5.11: The ratio of v_2 to v_3 of direct photon (black) and charged pion [8] (red). Theoretical curves are calculated with hydrodynamic model [16, 31].

The summary of χ^2 taken from Figure 5.11				
Centrality	direct photon		charged pion	
	MCGlb+ $\eta/s(0.08)$	MCKLN+ $\eta/s(0.20)$	MCGlb+ $\eta/s(0.08)$	MCKLN+ $\eta/s(0.20)$
0-20(%)	0.09	0.91	0.30	0.57
20-40(%)	0.05	1.87	1.20	0.21
40-60(%)	0.26	1.67	2.03	0.30

Table 5.1: The summary of χ^2 taken from Figure 5.11.

5.2.3 Comparison to model calculations

There are several model calculations to describe photon v_2 and v_3 .

Figure 5.12 shows the comparison of direct photon v_2 with 20 % centrality steps from 0 to 60 %. The blue and red lines are calculated from the both of thermal and non-thermal photons in [10]. Thermal photons from not only partonic phase but also hadron phase are included such as $\pi + \rho \rightarrow \pi + \gamma$, $\pi + K^* \rightarrow K + \gamma$. Elliptic and radial flow are constructed by expanding elliptic fireball based on [55]. The difference of these lines is a inclusion of non-thermal photon yields. In this model, non-thermal photon yields are estimated from photon yield in p+p collisions. Non-thermal photon is estimated by pQCD parameterization (blue) and the fitting to experimental data in PHENIX experiment (red) [9]. Orange line is calculated by the parton-hadron-string dynamics (PHSD) model which is transport calculation [32]. The photon production mechanisms in QGP are $q + \bar{q} \rightarrow g + \gamma$, and $q(\bar{q}) + g \rightarrow q(\bar{q}) + \gamma$ as well as the photon production in the initial hard collision (pQCD) which is given by the hard photon yield in p+p collisions scaled with the number of binary collisions. In hadronic sources, meson-meson and meson-baryon Bremsstrahlung as meson+meson \rightarrow meson+meson+ γ , meson+baryon \rightarrow meson+baryon+ γ , as well as hadronic interactions are included as $\pi + \pi \rightarrow \rho + \gamma$, $\rho + \pi \rightarrow \pi + \gamma$. Cyan and pink lines are calculated by hydrodynamical model VISH2+1 [16]. This calculation includes a viscous correction to photon emission rate. Cyan is calculated using initial condition with Monte Carlo Glauber followed by a hydrodynamic evolution with $\eta/s=0.08$. Pink is calculated using initial condition with Monte Carlo KLN and then hydrodynamic evolution with $\eta/s=0.20$. Initial condition and the η/s are selected in order to successfully describe soft hadron observables at RHIC and LHC energy. Violet line is calculated by another hydrodynamical model [33]. It is calculated by initial condition with optical Glauber model tuned to hadronic observables, and 3+1D hydrodynamical simulations.

Figure 5.13 shows comparison of direct photon v_2 and v_3 in 20-40% centrality interval with model calculations. An additional dark violet line is a result of calculation of photon v_2 in a strongly coupled plasma with constant and strong magnetic field in non-central heavy ion collision given by two large charged objects passing during the collision [34]. This calculation is one of the simplified setup with a constraint and strong B-field, therefore upper bound for photon v_2 is shown.

It is found that the calculations of fireball calculations and transport model relatively describe experimental measurement in $p_T < 1$ GeV/c while they still underestimate in $p_T = 2-3$ GeV/c. It could suggest that photons from the other sources such as the interaction between hard parton and the medium should be considered at $p_T = 2-3$ GeV/c and it will be discussed in Section 5.2.4. It is observed that hydrodynamical calculations are much lower than experimental measurement while hadronic observables are well described with the same conditions. Investigation of the viscous correction to photon emission rate and including photons from hadron gas could be helpful.

5.2.4 Possible solution of photon puzzle

As introduced in Section 1.4.3, it is found that the photon p_T spectra in Au+Au collision is enhanced compared with that in p+p collision scaled by the number of binary collisions in $p_T < 4$ GeV/c. It could suggest that very hot medium exists and thermal radiated photons

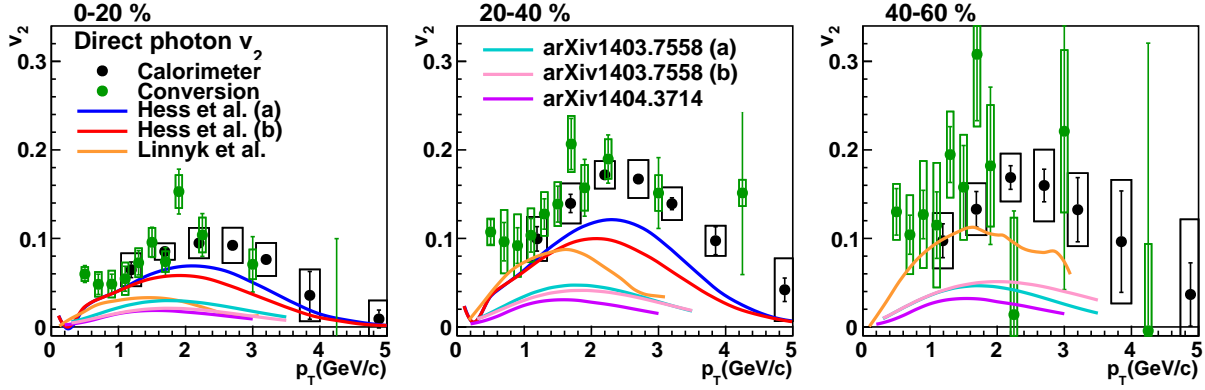


Figure 5.12: Comparison of direct photon v_2 with model calculations. Blue (red) lines are photon v_2 calculating with expanding elliptic fireball from thermal and non-thermal photons, and non-thermal photon is estimated by pQCD calculations (fit to the experimental data in PHENIX experiment) [10]. Orange line are calculated by PHSD transport model [32]. Cyan (pink) lines are calculated with initial condition calculated by Monte Carlo Glauber (KLN), and hydrodynamical simulation is started from $\tau_0 = 0.6$ fm/c to $T = 120$ MeV with $\eta/s=0.08$ (0.20) [16]. Violet line is calculated with initial condition calculated with optical Glauber model and evolved 3+1D hydrodynamical simulations [33].

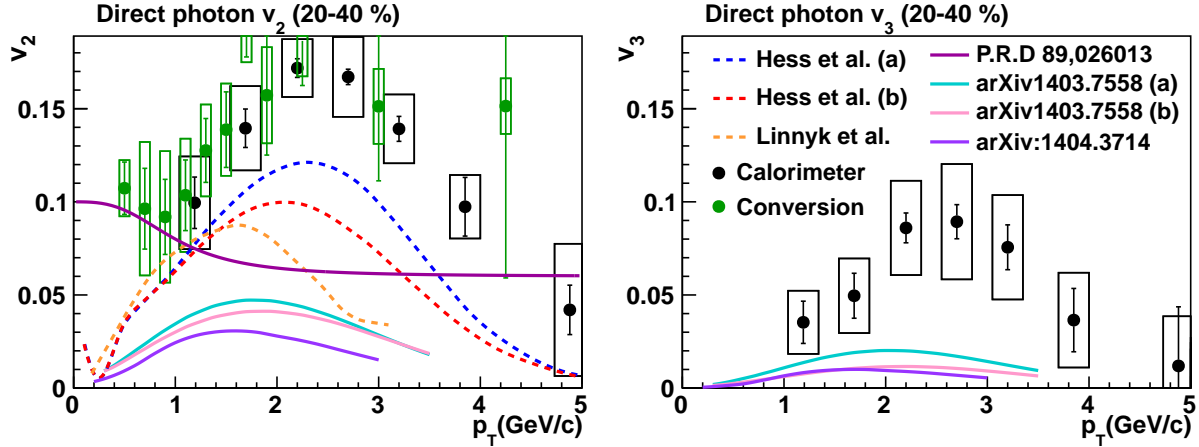


Figure 5.13: Comparison of direct photon v_2 and v_3 in 20-40% centrality bin with model calculations. Blue (red) lines are photon v_2 calculating with expanding elliptic fireball from thermal and non-thermal photons, and non-thermal photon is estimated by pQCD calculations (fit to the experimental data in PHENIX experiment) [10]. Orange line are calculated by PHSD transport model [32]. Cyan (pink) lines are calculated with initial condition calculated by Monte Carlo Glauber (KLN), and hydrodynamical simulation is started from $\tau_0 = 0.6$ fm/c to $T = 120$ MeV with $\eta/s=0.08$ (0.20) [16]. Violet line is calculated with initial condition calculated with optical Glauber model and evolved 3+1D hydrodynamical simulations [33]. Dark violet line is calculated photon v_2 in a magnetic field, and it shows upper bound for photon v_2 [34].

are dominant in this region. Therefore, thermal photons should be important to study photon puzzle. In this section, we discuss the possible keys to understand photon puzzle. The discussion with the blast wave model prediction for photon p_T spectra and v_n is shown in Section 5.2.4 and a toy model calculation with blue shift effect is discussed in Section 5.2.4.

Photon observables prediction with Blast Wave Model

Blast wave model is based on a hydrodynamical model to parameterize the expanding medium at kinetic freeze-out temperature [8, 56]. It has been known that it describes well hadronic observables such as p_T spectra and v_n less than $KE_T = 1$ GeV. The blast wave model assumes that the hadrons are emitted from an expanding source at kinetic freeze-out temperature. Photon p_T spectra and azimuthal anisotropies are parameterized with blast wave model as massless particle.

Blast wave equations used in this analysis are written as

$$\frac{dN}{p_T dp_T} \propto \int r dr \int d\phi I_0(\alpha_T) K_1(\beta_T), \quad (5.1)$$

$$v_n(p_T) = \frac{\int r dr \int d\phi \cos(n\phi) I_n(\alpha_T) K_1(\beta_T) \{1 + 2s_n \cos(n\phi)\}}{\int r dr \int d\phi I_0(\alpha_T) K_1(\beta_T) \{1 + 2s_n \cos(n\phi)\}}, \quad (5.2)$$

$$\alpha_T(\phi) = (p_T/T_f) \sinh(\rho(\phi)), \quad (5.3)$$

$$\beta_T(\phi) = (m_T/T_f) \cosh(\rho(\phi)), \quad (5.4)$$

$$\rho(\phi) = \rho_0 \{1 + 2\rho_n \cos(n\phi)\}, \quad (5.5)$$

$$\langle \rho \rangle = \frac{\int r (\rho_0 \times r/R_{\max}) dr}{\int r dr}, \quad (5.6)$$

$$\rho = \tanh^{-1}(\beta), \quad (5.7)$$

where T_f and ρ_0 are the kinetic freeze-out temperature and average transverse rapidity for azimuthal angle of medium surface, I_n and K_n are the n^{th} order of modified Bessel functions of the first and second kind, ρ_n and s_n are the transverse rapidity anisotropy and spatial density anisotropy, respectively.

In this section, since blast wave model is applied for p_T spectra, v_2 , and v_3 , there are six free parameters. They are defined by fitting to p_T spectra and v_n of π^\pm (0.14 GeV/ c^2), K^\pm (0.49 GeV/ c^2), $p\bar{p}$ (0.94 GeV/ c^2) in 0-20% centrality bin [8, 6] as shown in top of Figure 5.14. The obtained parameters are summarized in Table 5.2. Then the photon p_T spectra and v_n are predicted as massless particle. The predicted line is shown as black in bottom Figure 5.14. It is found that the both of p_T spectra and v_n are well described in $p_T < 2$ GeV/ c , while the freeze-out temperature is much less than the effective temperature, about 240 MeV [30]. It is because radial flow makes the effective temperature higher than true temperature as introduced in Section 1.4.5.

Several different lines without radial expansion $\langle \rho \rangle = 0$ are calculated. The orange, red, and magenta lines are predicted with freeze-out temperature $T_f = 104, 240$, and 300 MeV, respectively. It is observed that red line is similar to the black line while green and orange lines do not describe photon p_T spectra. It is confirmed that radial flow makes the apparent temperature higher than true temperature. Additionally, it is found that the azimuthal anisotropy $v_n = 0$ if the radial expansion $\langle \rho \rangle = 0$, as it is naively expected.

Blast wave model is used to predict photon observables though it could be not adequate model since photons are emitted from all stages of the collisions. Predicted p_T spectra, v_2 , and v_3 agree well with experimental measurement. It suggests that radial flow makes apparent temperature higher than true temperature and v_n existence. It is found that predicted v_n is a slightly higher than experimental measurements, and it could be because photons emitted from the medium which is not enough expended are included. Radial flow effect could provide us the keys to understand photon puzzle..

The parameters defined by blast wave 0-20%					
T_f [MeV]	$\langle\rho\rangle$	ρ_2	s_2	ρ_3	s_3
104.5 ± 0.6	0.661 ± 0.004	0.021 ± 0.002	0.032 ± 0.004	0.016 ± 0.001	0.006 ± 0.001

Table 5.2: Parameters of blast wave function obtained by fitting to p_T spectra and v_n of identified charged particle [8, 6]. T_f is kinetic freeze-out temperature, $\langle\rho\rangle$ is the average transverse rapidity, ρ_n and s_n are the transverse rapidity and spacial density anisotropy.

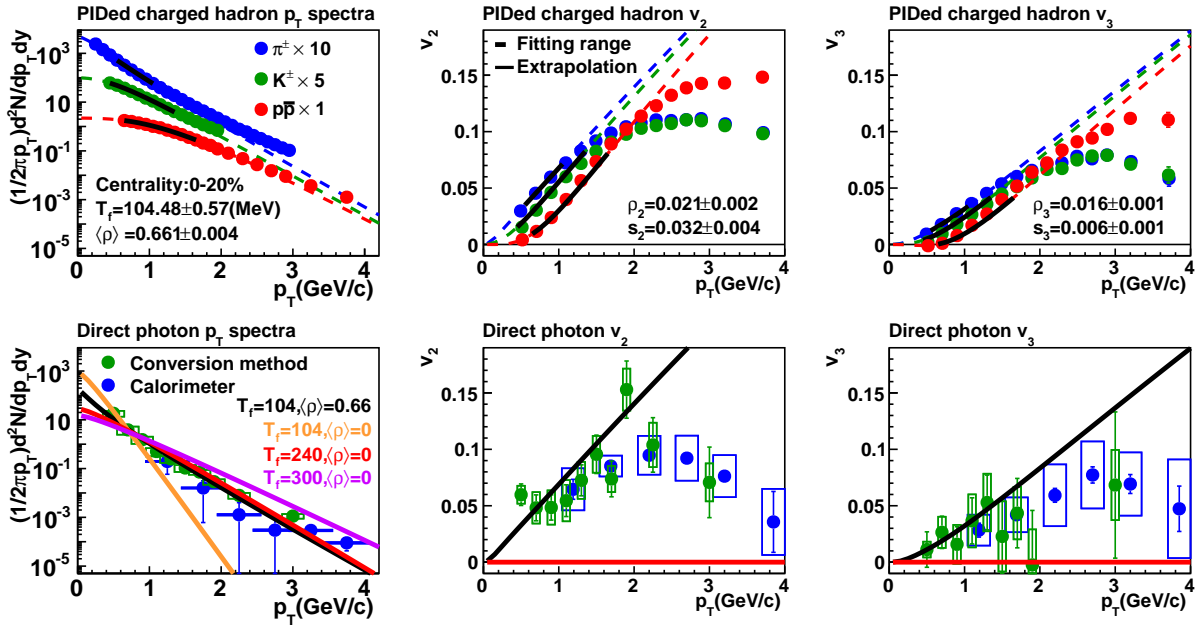


Figure 5.14: (Top) The p_T spectra (left), v_2 (middle), and v_3 (right) of identified charged particle ($\pi^\pm, K^\pm, p\bar{p}$) [8, 6]. The thick lines are the blast wave functions obtained by fitting, and thin lines are extrapolations. (Bottom) The p_T spectra [30] (left), v_2 (middle), and v_3 (right) of direct photon. Black lines are predicted photon observables. Orange, red, and violet lines are predicted lines with freeze-out temperature $T_f = 104, 240$, and 300 (MeV) with zero radial expansion $\langle\rho\rangle = 0$.

A toy model calculation for thermal photon p_T spectra and v_n with blue shift effect

In Section 5.2.4, blast wave model suggests that radial flow effect should be taken into account so that photons have high effective temperature and large v_n . However blast wave model is not appropriate for photon observables because photons are emitted from all stages of the collision. It is needed to consider the superposition of all photons from high temperature to low temperature. In this section, the photon p_T spectra and v_n are calculated with the radial flow effect (blue shift correction).

The temperature is assumed to be the highest at $t=0$ and monotonically decreases with time. In this calculation, the evolution time t is defined by the temperature from the beginning of the QGP expansion ($t=0$) to the freeze-out ($t=1$). The apparent temperature $T'(t)$ affected by blue shift effect is calculated with the velocity $\beta(t)$ as

$$T'(t) = T(t) \cdot \sqrt{\frac{1 + \beta(t)}{1 - \beta(t)}}. \quad (5.8)$$

The amount of emitted photon from the medium could be described with transverse momentum p_T and temperature $T(t)$ as

$$n(p_T, T(t)) = \frac{1}{\exp(p_T/T(t)) - 1}. \quad (5.9)$$

The assumptions in this toy model calculation are summarized below.

- acceleration of expanding medium monotonically decreases with time (and become zero at $t=1$) : $a(t)$
- azimuthal anisotropy of medium in momentum space monotonically increases with time : $v_n(p_T, t)$
- the photon p_T spectra is described with $T(t)$ as Eq. (5.9)

Because photon p_T spectra and azimuthal anisotropy v_n are superposition of different contributions from initial to final stages, they are calculated as

$$n^{\text{final}}(p_T) = \int dt n(p_T, T(t)), \quad (5.10)$$

$$v_n^{\text{final}}(p_T) = \frac{\int dt v_n(p_T, t) \cdot n(p_T, T(t))}{\int dt n(p_T, T(t))}. \quad (5.11)$$

In order to constrain the assumptions, the temperature $T(t)$, velocity $\beta(t)$ at final stage ($t=1$) are fixed to be consistent the parameters obtained from blast wave model fitting to hadron observables summarized in Table 5.2. It is assumed that the final value of azimuthal anisotropy $v_n(p_T, t)$ of direct (thermal) photon is assumed to be same as pion v_n . The time is defined by temperature from initial stage ($t=0$) to the freeze-out stage at $T_f=104$ MeV ($t=1$).

The time dependence of temperature $T(t)$, acceleration $a(t)$, velocity $\beta(t)$, and azimuthal anisotropy $v_n(p_T, t)$ of the medium are defined as

$$T(t) = T_0 - D \cdot t, \quad (5.12)$$

$$a(t) = A(1 - t), \quad (5.13)$$

$$\beta(t) = \int_0^t a(t') dt', \quad (5.14)$$

$$v_n(p_T, t) = V \cdot t, \quad (5.15)$$

where T_0 is initial temperature, and D is defined so that $T(1)=104$ MeV. Because it is expected that the medium becomes free-streaming at $t=1$, it is assumed $a(1)=0$. The constant A in Eq. (5.13) is determined from the conditions of velocity $\beta(0)=0$ and $\beta(1)=0.57$ ($=\tanh(\langle\rho\rangle)$). The V in anisotropy component is parameterized with $v_n(p_T, t=1) = v_n^{pion}(p_T)$. As a first basic assumption, Figure 5.15 shows the time dependence of temperature, the normalized yield (probability density) $N(T(t)) = N_0 \int dp_T n(p_T, T(t))$, acceleration, velocity, and azimuthal anisotropy ($p_T=2.135$ GeV/ c). The time dependence of apparent temperature corrected for blue shift effect is also shown as blue line.

Photon p_T spectra and v_2 and v_3 with basic assumptions Figure 5.16 shows the calculations of photon p_T spectra and v_n with initial temperature $T_0=300$ MeV. The calculations of p_T spectra are scaled to be consistent with experimental measurement [30] at 1 GeV/ c . To extract the effective temperature, the exponential equation is fitted in the range of $0.6 < p_T < 2$ GeV/ c . It is confirmed that the temperature of the calculation with blue shift correction is higher than that without correction. It is shown that the calculations for v_2 and v_3 with blue shift correction are larger than that without correction. In high p_T region, photons from high temperature are dominant if radial flow are not taken into account. However, if blue shift correction is considered, photons from the medium at low temperature having strong radial flow are relatively increased in high p_T region. Therefore, it could be understood that radial flow makes effective temperature high and azimuthal anisotropy large.

There are the differences of effective temperature and v_n between calculations and experimental measurement. In order to study the difference quantitatively, the relative difference σ is defined as

$$\sigma = \frac{V_{obs.} - V_{cal.}}{\sqrt{E_{sys.}^2 + E_{stat.}^2}}, \quad (5.16)$$

where $V_{obs.}$ ($V_{cal.}$) is the variable (T_{eff} , v_2 , or v_3) of experimental measurement (this calculation) and $E_{stat.}$ ($E_{sys.}$) is the statistical error (systematic uncertainty) of experimental measurement. In the case of p_T spectra, effective temperature from the fitted exponential equation at $p_T = 0.6-2$ GeV/ c is compared. In the case of v_n , the averaged values within $1 < p_T < 3$ GeV/ c are used.

While it is assumed that temperature decreases linearly with time, because the medium expands, the time dependence of acceleration, yield, and azimuthal anisotropy do not have to be linear. In the following section, the various different time dependences will be studied with the time dependence of acceleration, yield, and azimuthal anisotropy.

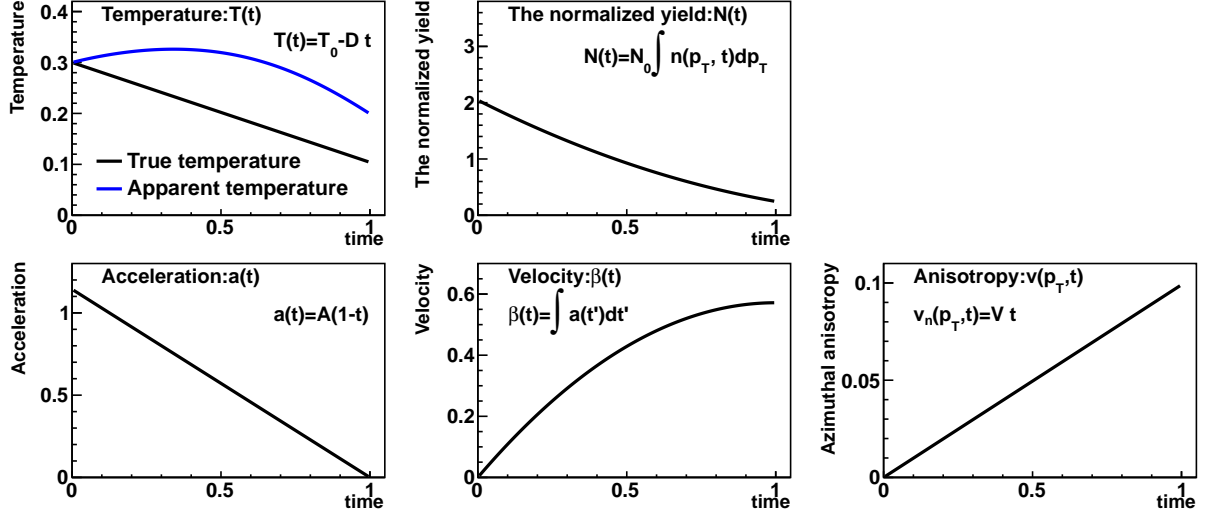


Figure 5.15: The time dependence of temperature (top left), normalized yield (top middle), acceleration (bottom left) velocity (bottom middle), and azimuthal anisotropy (0-20%, $p_T=2.135$ GeV/c) (bottom right) of the photon sources. Blue line is the time dependence of the apparent temperature.

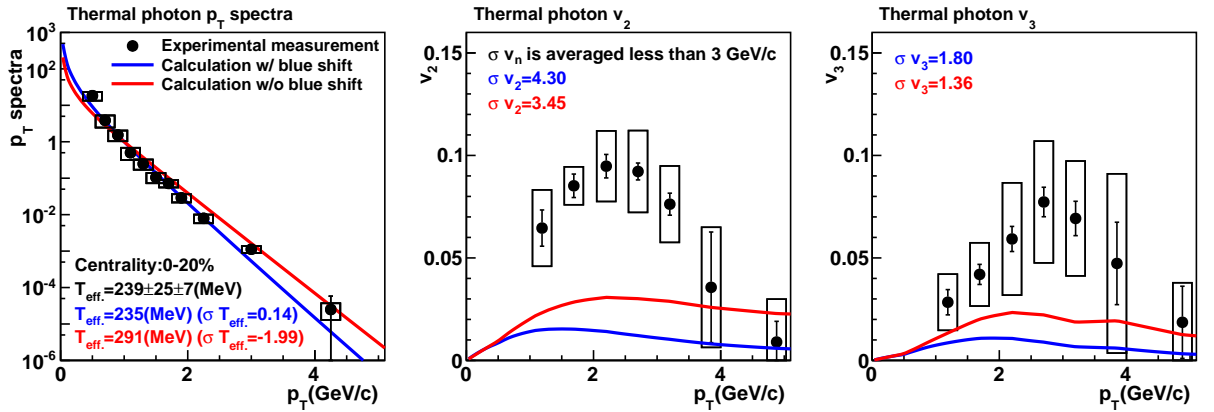


Figure 5.16: The photon p_T spectra (left), v_2 (middle), and v_3 (right) in 0-20 % centrality bin. The experimental measurement of p_T spectra is taken from [30]. The calculations of p_T spectra are scaled so that they are consistent with the experimental measurement at 1 GeV/c. The red (blue) lines are the calculations with (without) blue shift correction. The effective temperature is obtained by exponential equation fitting in the range of $0.6 < p_T < 2$ GeV/c.

The acceleration dependence The behavior of effective temperature and v_n is studied by varying the time dependence of acceleration. The time dependence of acceleration is modified as

$$a(t) = A(1 - t^\alpha) \quad (\alpha > 0). \quad (5.17)$$

The time dependence of parameters are shown in Figure 5.17. When the time dependence of acceleration is varied, the time dependence of velocity and apparent temperature are also modified accordingly with fixed initial ($\beta=0$) and final expansion velocities ($\beta=0.57$). In this assumptions, α is varied from 1/10 to 10.

Figure 5.18 shows the calculations of p_T spectra, v_2 , v_3 , and the relative difference with experimental measurements. It is found that effective temperature decreases largely with increasing α parameter, while there is only a weak change for v_n .

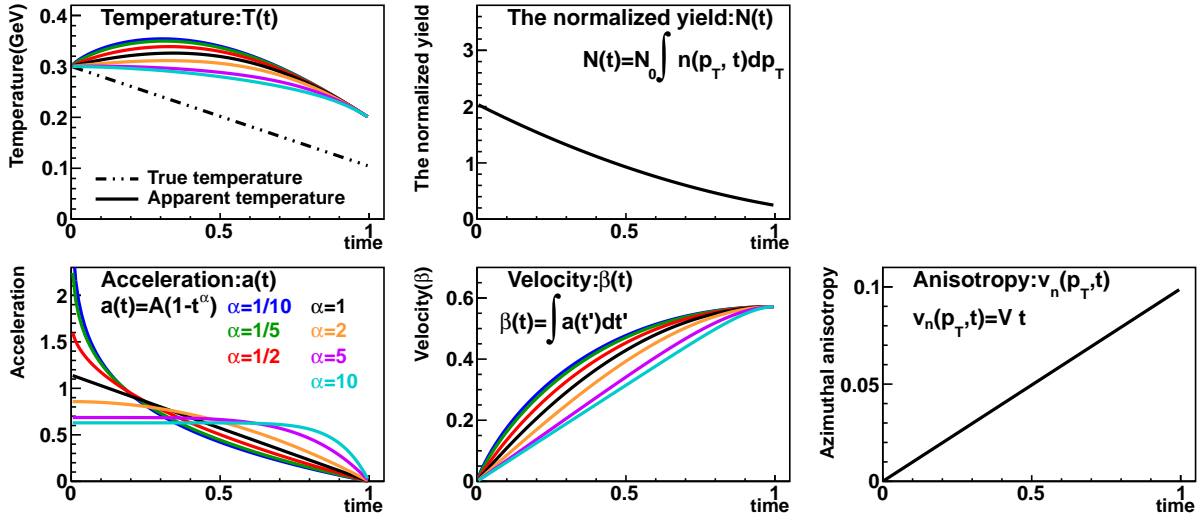


Figure 5.17: The time dependence of temperature (top left), yield (top middle), probability (top right), acceleration (bottom left) velocity (bottom middle), and azimuthal anisotropy (0-20%, $p_T=2.135$ GeV/c) (bottom right) of the photon sources. The color shows the difference of α in Eq. (5.17).

The yield dependence Because the area of photon emission source expands with time, it is expected that the amount of thermal photons would also increase with time. In order to take this effect into account, the p_T spectra is modified as

$$n(p_T, t) = t^b \frac{1}{\exp(p_T/T(t)) - 1} \quad (0 \leq b). \quad (5.18)$$

The time dependence of parameters are shown in Figure 5.19. It can be seen that the photons from late stage increase with increasing the parameter b . In this assumptions, b is varied from 0 to 10.

Figure 5.20 shows the calculations of p_T spectra and v_n . As it is expected, the effective temperature decreases and v_n increases with increasing the amounts of photons from late stage. It is found that the behavior of time dependence of yield is very sensitive to the both of effective temperature and v_n .

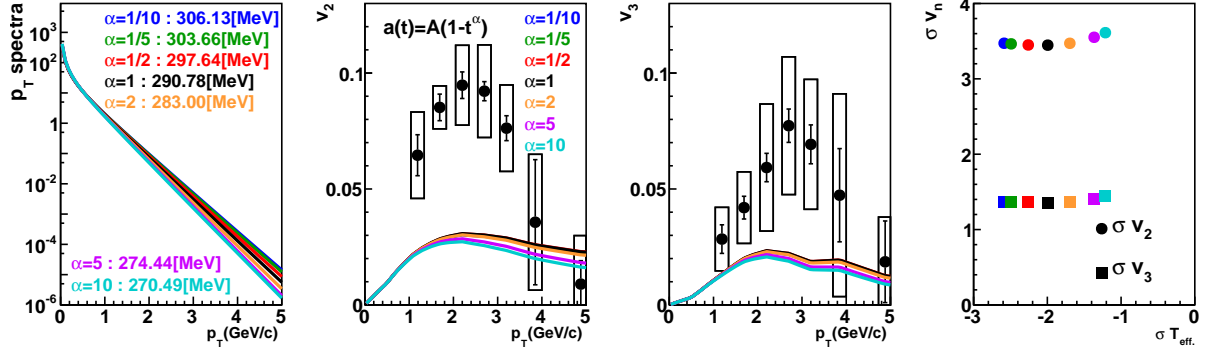


Figure 5.18: The thermal photon p_T spectra (left), the v_2 (middle), and v_3 (right) depending on acceleration development. The color shows the difference of α in Eq. (5.17). Effective temperature is obtained via fitting by exponential equation in the region of $0.6 < p_T < 2$ GeV/c.

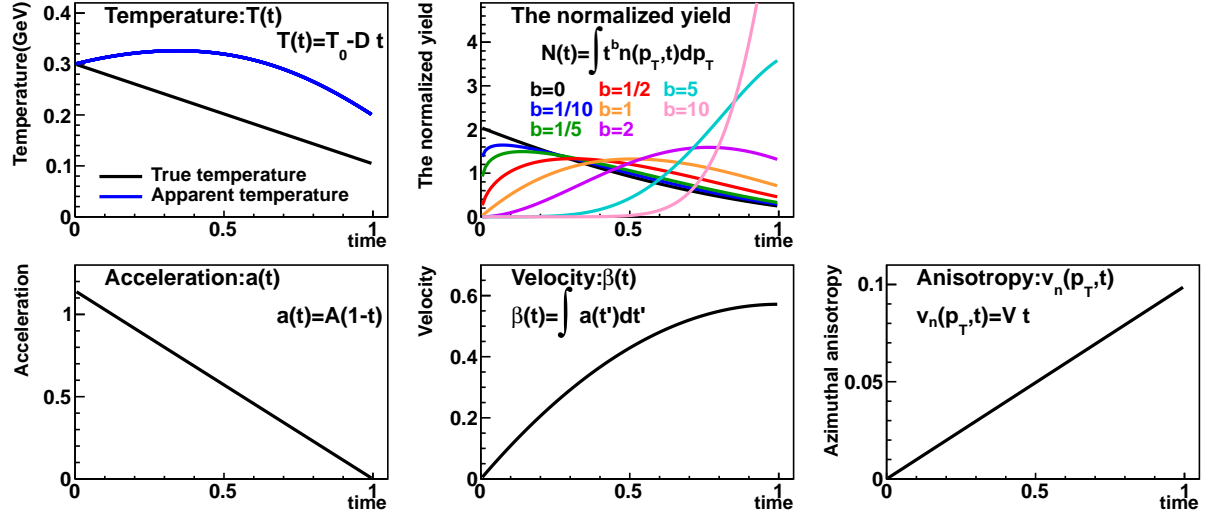


Figure 5.19: The time dependence of the yield of photon and the probability density. The color shows the difference of b in Eq. (5.18).

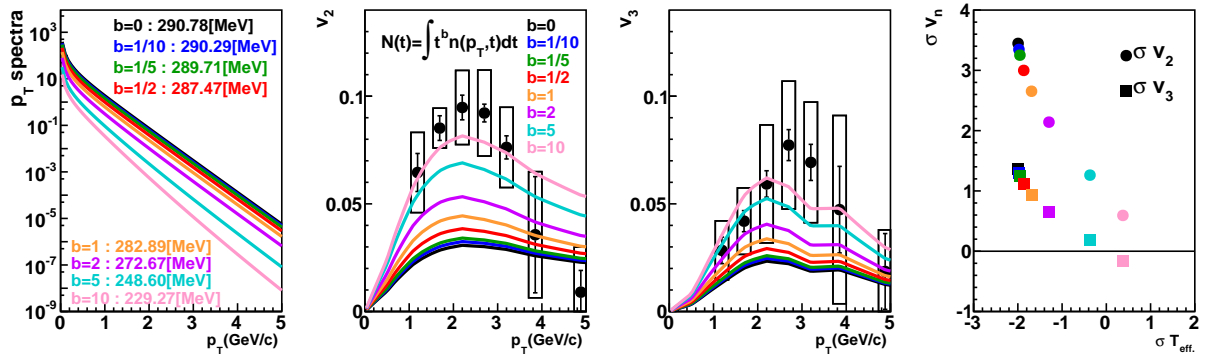


Figure 5.20: The thermal photon p_T spectra (left), v_2 (middle), and v_3 (right) depending on the photon yield. The color shows the difference of b in Eq (5.18). Effective temperature is obtained via fitting by exponential equation in the region of $0.6 < p_T < 2$ GeV/c.

The azimuthal anisotropy dependence The time dependence of anisotropy in momentum space is modified as

$$v_n(p_T, t) = V \cdot t^c \quad (0 < c). \quad (5.19)$$

Figure 5.21 shows the time dependence of parameters. In this assumptions, c is varied from $1/10$ to 10 .

Figure 5.22 shows the calculations of p_T spectra and v_n . Since the p_T spectra is not affected by the medium azimuthal anisotropy, the effective temperature is not varied. If the azimuthal anisotropy is saturated in early stage where c is small, the v_n gets larger and becomes close to the experimental measurement.

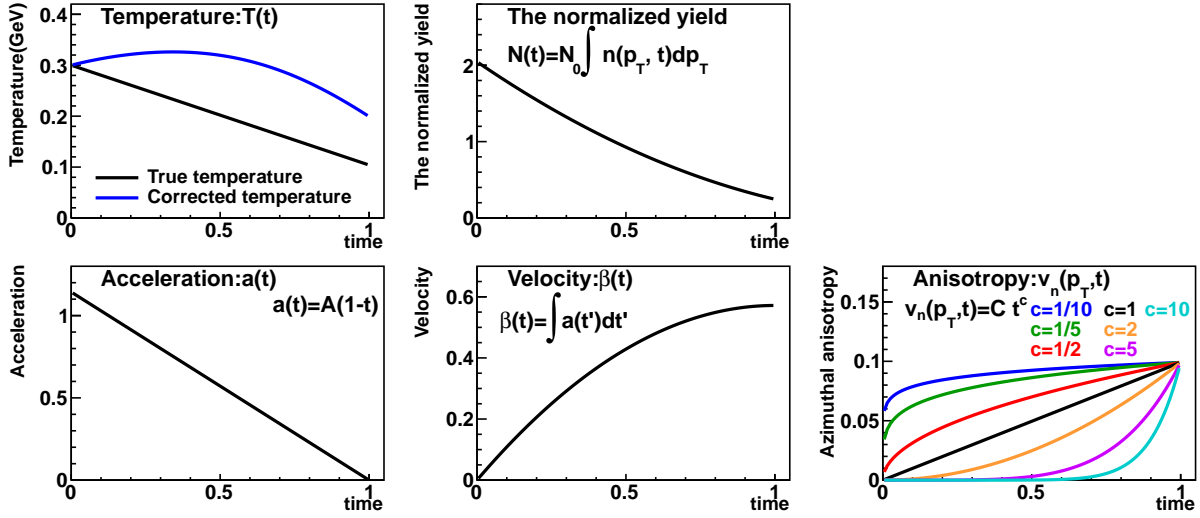


Figure 5.21: The time dependence of temperature (left), velocity (middle), and azimuthal anisotropy (0-20%, $p_T = 2.135$ GeV/c) (right) of the photon sources. The color shows the difference of c in Eq. (5.19).

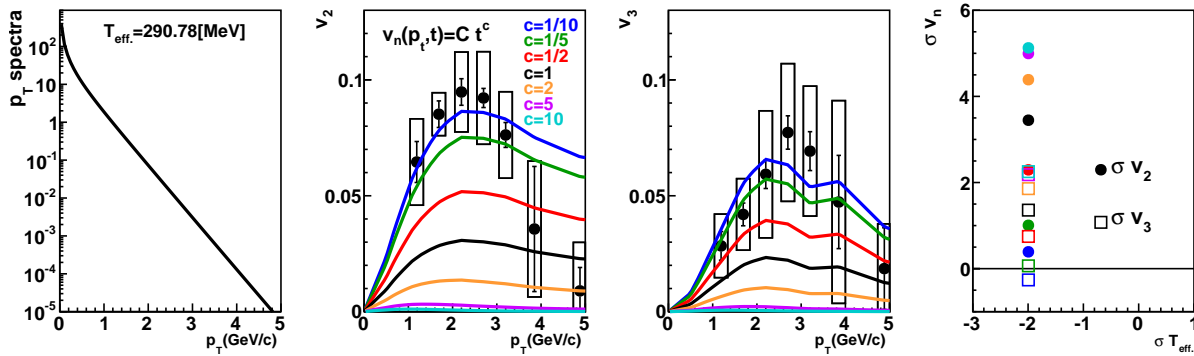


Figure 5.22: The thermal photon p_T spectra (left), the v_2 (middle), and v_3 (right) depending on azimuthal anisotropy development. The color shows the difference of c in Eq. (5.19). Effective temperature is obtained via fitting by exponential equation in the region of $0.6 < p_T < 2$ GeV/c.

The summary for the varying time dependence The difference of effective temperature and v_2 with the time dependence of parameters is shown in Figure 5.23. Black point is the difference with the first basic assumption, and solid lines show results by varying the power of t for acceleration (blue), photon yield (green) and v_n (re). It is confirmed that the effective temperature depends on the evolution of acceleration and yield, and v_n depends on all components. In order to constrain this calculations, the parameters α in Eq. (5.17) and b in Eq. (5.18) are optimized so that effective temperature is comparable to the experimental measurement ($\sigma T_{eff.}=0$). Then, the parameter c in Eq. (5.19) is determined to be consistent with experimental measurement ($\sigma v_n=0$).

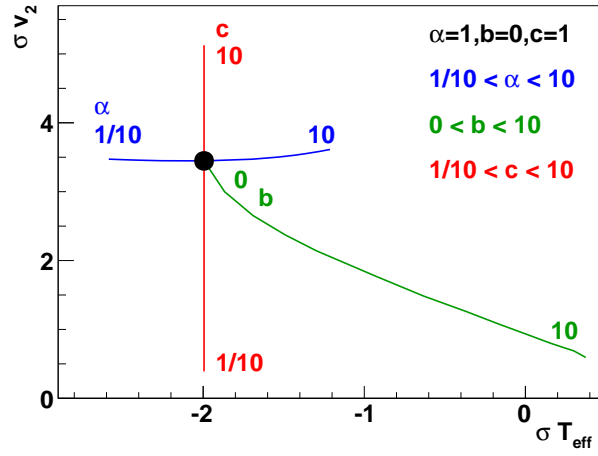


Figure 5.23: The difference of effective temperature ($\sigma T_{eff.}$) and v_2 (σv_2) between calculations and experimental measurement. (Black) The difference obtained from the basic assumption. (Blue) The α controls the time dependence of acceleration. (Green) The b controls the time dependence of yield. (Red) The c controls the time dependence of v_n .

The constraint on parameters The time dependence of acceleration $a(t)$ and velocity $\beta(t)$ can be rewritten with maximum velocity $B = \beta(1)$ from Eq. (5.17) as

$$a(t) = \frac{\alpha + 1}{\alpha} B(1 - t^\alpha), \quad (5.20)$$

$$\beta(t) = \frac{\alpha + 1}{\alpha} B \left(t - \frac{1}{\alpha + 1} t^{\alpha+1} \right). \quad (5.21)$$

If the α is taken limit, they can be calculated as

$$\lim_{\alpha \rightarrow 0} a(t) = -B \log t, \quad (5.22)$$

$$\lim_{\alpha \rightarrow 0} \beta(t) = Bt(1 - \log t), \quad (5.23)$$

$$\lim_{\alpha \rightarrow \infty} a(t) = B, \quad (5.24)$$

$$\lim_{\alpha \rightarrow \infty} \beta(t) = Bt. \quad (5.25)$$

These two limit of acceleration is used to constrain the b in the time dependence of yield. The b dependence on difference of effective temperature with the limit of acceleration in left of Figure 5.24. Then the b is defined 7.65 (2.53) when α is limit of 0 (∞).

The α and b are fixed, the c in the time dependence of anisotropy is limited. The c dependence on difference of v_2 and v_3 with the limit of acceleration and defined b in middle and right of Figure 5.24

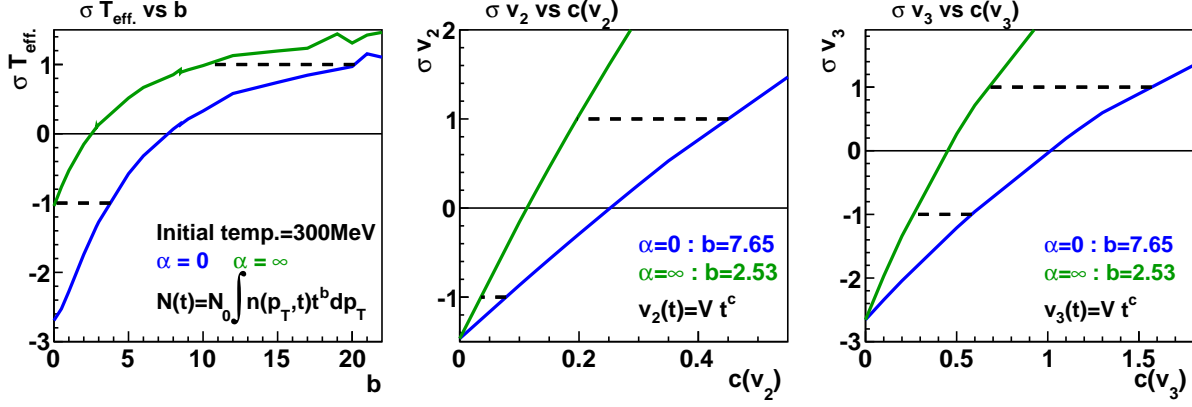


Figure 5.24: (Left) The b dependence in yield component on the difference of effective temperature between calculations and experiment measurement. (Middle) The c dependence in azimuthal anisotropy component for v_2 on the difference between calculations and experiment measurement. (Right)) The c dependence in azimuthal anisotropy component for v_3 on the difference between calculations and experiment measurement. Blue (green) line is calculated with the limitation of $\alpha \rightarrow 0$ (∞). Solid black line indicates σT_{eff} , $\sigma v_n=0$ and dotted lines indicate the limitation within 1σ .

Because the parameters, α , b , and c are defined, we can get the time dependence of the components. Figure 5.25 shows the results of p_T spectra, v_2 , and v_3 of thermal photons. Figure 5.26 shows the time dependences of temperature, normalized yield, acceleration, velocity, and anisotropy for v_2 . Initial temperature is varied from 300 MeV to 400, 500, 600 MeV, and b , c are defined with the same method. The obtained apparent temperature, true temperature, and average emission time are summarized in Table 5.3. It is confirmed that true temperature is lower than apparent (effective) temperature. It is found that true temperature is within 125 to 160 MeV regardless of initial temperature while the range of true temperature slightly increases with decreases initial temperature. This result indicate that photons are emitted in late stage under the assumptions of time dependent temperature Eq. (5.12, acceleration Eq. (5.17, yield Eq. (5.18), and azimuthal anisotropy Eq. (5.19).

The adiabatic expansion assumption

The photon observables are calculated with a simple adiabatic expansion model. This model includes the longitudinal expansion with the velocity of light and radial expansion with velocity $\beta(t)$. With thermodynamic relations, we obtain the relation of the entropy density s as

$$s \propto T^3, \quad (5.26)$$

$$s(t_0)V(t_0) = s(t)V(t), \quad (5.27)$$

$$(5.28)$$

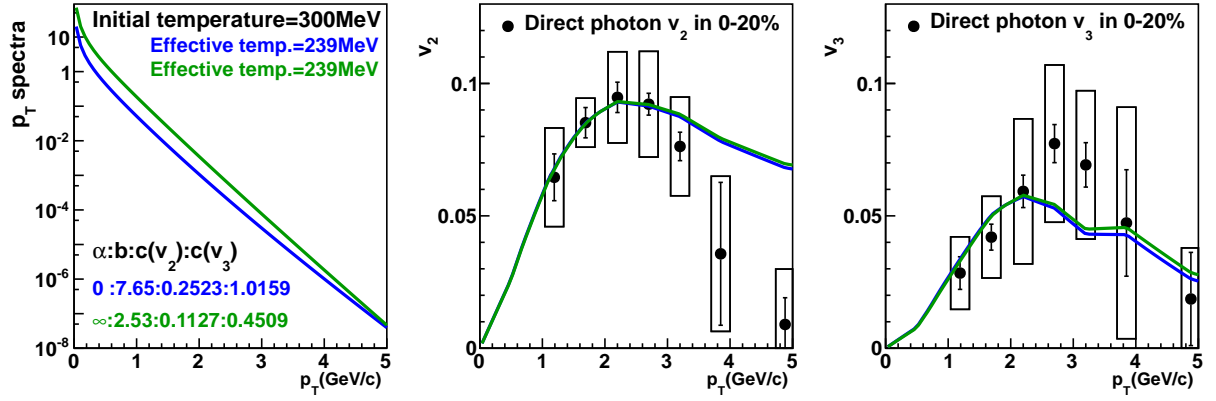


Figure 5.25: The calculation results of p_T spectra, v_2 , and v_3 . Black points are the results of direct photon v_n in 0-20 % centrality interval.

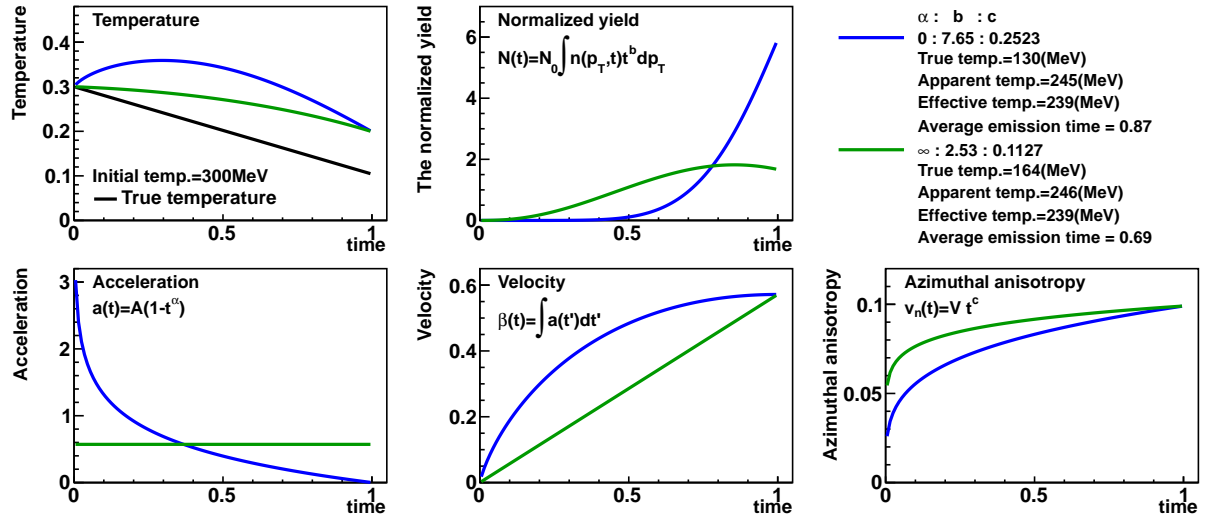


Figure 5.26: The time dependence of temperature, normalized yield, acceleration, velocity, and anisotropy. Black line in temperature is the time dependence of true temperature.

The summary of calculations			
Initial temperature	Apparent temperature	True temperature	Average emission time
300 (MeV)	245.5 (MeV)	130 - 164 (MeV)	0.69 - 0.87
400 (MeV)	246.0 (MeV)	128 - 146 (MeV)	0.86 - 0.92
500 (MeV)	245.0 (MeV)	128 - 138 (MeV)	0.91 - 0.94
600 (MeV)	244.5 (MeV)	128 - 135 (MeV)	0.94 - 0.95

Table 5.3: The summary of true temperature and average emission time. Lower (upper) limit of true temperature is determined by $\alpha = 0$ (∞). Lower (upper) limit of average emission time is determined by $\alpha = \infty$ (0). The time of freeze-out is defined as 1.

where t_0 is a given initial time, T and $V(t)$ are the temperature and volume of the photon source, respectively. The radius $R(t)$, volume $V(t)$, and temperature $T(t)$ are written as

$$R(t) = R_0 + \int_0^t \beta(t') dt', \quad (5.29)$$

$$V(t) = t\pi R(t)^2, \quad (5.30)$$

$$T(t) = T_0 \left(\frac{t_0 R(t_0)^2}{t R(t)^2} \right)^{1/3}, \quad (5.31)$$

where R_0 is the initial radius and 3 fm defined by RMS radius is utilized. In this study, the freeze-out temperature is fixed at the radius of 10 fm/ c after the expansion. The temperature and velocity at freeze-out temperature are defined at 104 (MeV) and 0.57 obtained by blast wave model. It is assumed that the time dependence of the evolution of velocity and azimuthal anisotropy in momentum are same as

$$\beta(t) = BB \times t^b, \quad (5.32)$$

$$v_n(p_T, t) = V \times t^b, \quad (5.33)$$

where BB is defined with $\beta(10)=0.57$ and V is determined with $v_n(p_T, 10)=v_n(p_T)$ of pion. Figure 5.27 shows the parameters as a function of time. Because it is natural that pressure gradient decreases with time, the b is selected at least smaller than 1. The amount of photons at temperature $T(t)$ is defined as

$$n(p_T, T(t)) = \frac{V(t)}{\exp(p_T/T(t)) - 1}. \quad (5.34)$$

The final p_T spectra and v_n are calculated with Eq. (5.10) and (5.11).

Figure 5.28 shows the calculations of photon p_T spectra and v_n . The effective temperature is obtained by fitting in the region of $0.6 < p_T < 2$ GeV/ c . It is found that the effective temperature decrease and v_n increases with decreasing the b parameter.

The calculations for photon observables with a simple adiabatic expansion is performed. It is found that the effective temperature is much higher than experimental measurement in the region of $b < 1$. This might be indicating that the energy conservation due to the photon emission should be taken into account. The azimuthal anisotropy is calculated with the same assumption of the time dependence of the evolution which is also applied for the radial expansion velocity. It is observed that the estimated v_2 and v_3 values are much smaller than experimental measurement. It might indicate that we would have to consider the v_n source which is not only given by the radial expansion velocity but also the spacial density anisotropy profile included as in the Blast Wave model such as s_n parameter.

Photon v_n calculations with pQCD calculations

As explained above, photons are created from several sources. In [30], photons are classified as thermal photon and the photons based on $p + p$ collisions. Panel (a) in Figure 5.29 shows the photon p_T spectra in Au+Au collisions. Panel (b) shows the p_T spectra estimated from $p + p$ collisions with pQCD based equation $F_1 = A \left(1 + \frac{p_T^2}{B} \right)^2$ which is scaled by the number of the

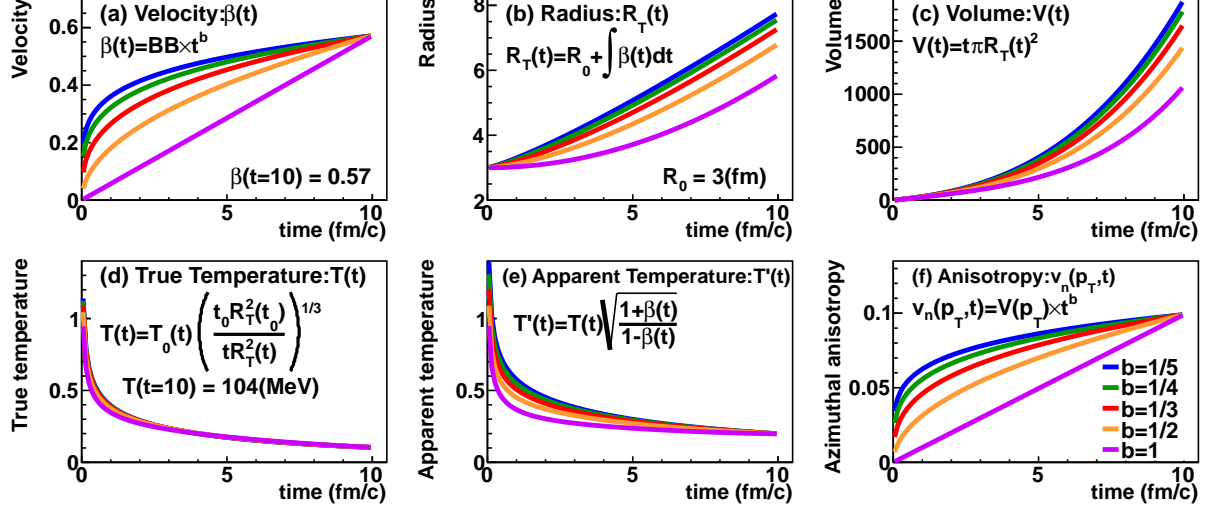


Figure 5.27: The time dependence of velocity (a), radius (b), volume (c), true temperature (d), temperature corrected by blue shift effect (e), and azimuthal anisotropy (f). The difference of line color is defined by b in Eq. (5.32) and (5.33).

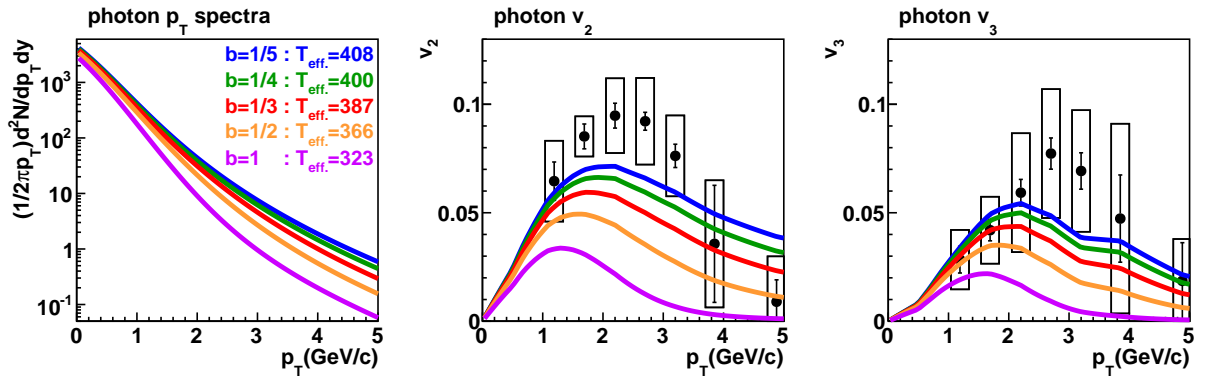


Figure 5.28: The photon p_T spectra (left), v_2 (middle), and v_3 (right). The difference of line color is defined by b in Eq. (5.32) and (5.33). The effective temperature is obtained by fitting via exponential equation in the region of $0.6 < p_T < 2$ GeV/ c .

binary collision. Panel (c) shows the p_T spectra after subtracting F_1 shown in panel (b) from p_T spectra in Au+Au collisions shown in panel (a). We assume that subtracted p_T spectra is determined as thermal photons. It is fitted with $F_2 = C \exp(-p_T/T)$ in the region of $0.6 < p_T < 2$ GeV/c. The obtained equations are combined as

$$F_3 = A \left(1 + \frac{p_T^2}{B} \right)^2 + C \exp(-p_T/T), \quad (5.35)$$

which is shown in the panel (a) as black line. The ratio of the number of thermal photon to that of all photons is shown in panel (d). It is found that thermal photons are dominant in $p_T < 2$ GeV/c and decreases $\sim 70\%$ at $p_T = 2$ GeV/c.

Photons including thermal and pQCD photons v_n (v_n^γ) can be written with thermal photon v_n (v_n^{thermal}) and pQCD based photon v_n (v_n^{pQCD}) as

$$v_n^\gamma = \frac{N^{\text{thermal}} v_n^{\text{thermal}} + N^{\text{pQCD}} v_n^{\text{pQCD}}}{N^{\text{thermal}} + N^{\text{pQCD}}}, \quad (5.36)$$

$$= \frac{N^{\text{thermal}} v_n^{\text{thermal}}}{N^{\text{thermal}} + N^{\text{pQCD}}}, \quad (5.37)$$

where N^{thermal} and N^{pQCD} are the number of thermal photon and pQCD based photon, respectively. Because it is expected that pQCD based photon do not have anisotropy, v_n^{pQCD} is zero. Thermal photon v_n is assumed to be the results in Figure 5.14 and 5.25.

Figure 5.30 shows the calculation result of photon v_2 and v_3 with Eq. (5.37). It is observed that (Thermal + pQCD) photon v_n is smaller than experimental measurement in the region of $3 < p_T < 5$ GeV/c. It may indicate that the photons originated from the other additional sources such as modification of jet fragmentations and redistribution of the lost energy coming from the energy loss inside QGP could be existing in $3 < p_T < 5$ GeV/c.

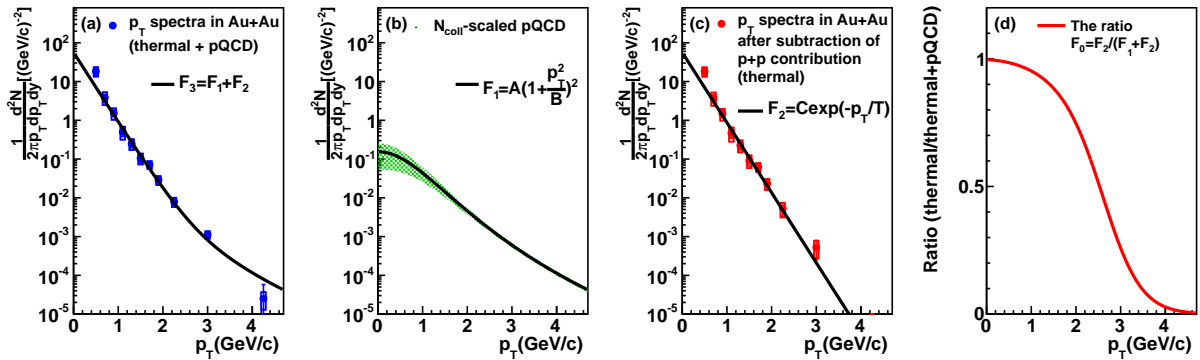


Figure 5.29: Direct photon p_T spectra in 0-20% centrality taken from [30]. (a) Direct photon p_T spectra in Au+Au collisions. (b) Photon p_T spectra estimated from $p + p$ collisions by the number of binary collisions (pQCD photon). (c) The p_T spectra after subtraction of scaled $p + p$ collisions (Thermal photon). (d) The ratio of the number of thermal photon to that of thermal and pQCD photons.

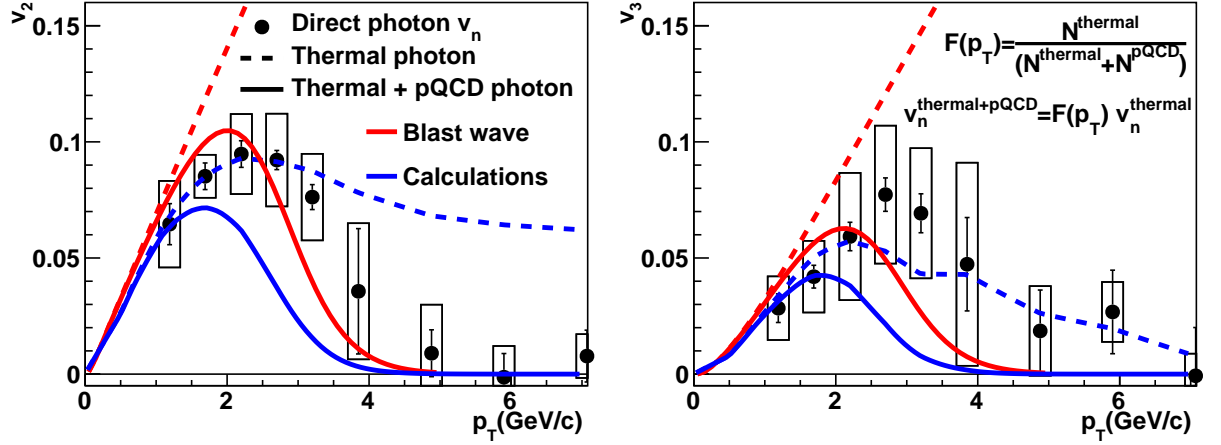


Figure 5.30: The direct photon v_2 (left) and v_3 (right). Dotted lines are predicted thermal photon v_n shown in Figure 5.14 (red) and 5.25 (blue). Solid lines are all photons v_n calculated with Eq. (5.37).

Summary for calculations

In Section 5.2.4, photon p_T spectra and v_n are discussed to understand photon puzzle. Blast wave model suggests that radial flow should be taken into account so that photon have high effective temperature and large v_n . The photon p_T spectra and v_n are calculated with blue shift effect. It is achieved to obtain the both of high effective temperature and large v_2 , v_3 simultaneously with radial flow effect. It is found that true temperature is within 125 to 160 MeV regardless of initial temperature, and photons from late stage are dominant. Photon v_n is evaluated from thermal photons and pQCD based photons. It may indicate that the photons originated from the other additional sources such as modification of jet fragmentations and redistribution of the lost energy coming from the energy loss inside QGP could be dominantly existing in the region of $3 < p_T < 5$ GeV/ c .

Chapter 6

Conclusion

The measurement of direct photon is a powerful probe to study quark-gluon plasma (QGP) in high energy heavy ion collisions. That is because photons do not strongly interact with the medium due to charge-less and color-less properties and they are emitted during all stages of the collision. It has been observed that the large excess of p_T spectra and large elliptic flow v_2 in low p_T region. It has not yet well understood, and it is called as “photon puzzle”.

The higher order azimuthal anisotropy of direct photon is measured in order to understand photon puzzle. The measurement of v_2 , v_3 , and v_4 of neutral pion and direct photon in Au+Au $\sqrt{s_{NN}} = 200$ GeV collisions at RHIC-PHENIX experiment has been carried out since year 2000.

The v_2 , v_3 , and v_4 of neutral pion are measured up to $p_T = 15$ GeV/ c with event plane determined by several forward detectors. In high p_T region, it is found that neutral pion v_2 and v_4 are positive in all centrality while v_3 varies from positive to negative especially in peripheral event. Since hadrons in high p_T region are mainly originated from jet fragmentation, high p_T single particles v_n are useful to study jet properties in heavy ion collisions. It is studied that the jet contribution to measured v_n by AMPT simulation. The jet path length dependence of energy deposit has been studied by measuring v_2 of high p_T hadron. Because di-jet makes v_3 small and third order of initial geometrical anisotropy is smaller than second order, v_3 of high p_T hadron needs to be investigated more precisely in order to understand their detailed dependencies. The behavior of v_3 of high p_T hadron could be understood qualitatively by superposition of path length dependence of jet energy-loss, di-jet effect, and jet-bias effect in determination of event plane. The v_4 of high p_T particles is similar to the behavior of v_2 , and it could be understood that it is given by the geometrical asymmetry of the QGP and energy loss of parton inside the QGP.

The v_2 , v_3 , and v_4 of direct photon are measured up to 15 GeV/ c . It is observed that the strength of photon v_3 at $p_T \sim 2$ GeV/ c is comparable to that of hadron, which is similar to the case of v_2 . These results prefer the scenario of that the photon in low p_T region are mostly emitted from late stage after the sizable azimuthally anisotropic and collective expansion. In high p_T region, it is found that v_2 , v_3 , and v_4 of direct photon are close to zero and it could be consistent with the expectation that the dominant fraction of photons is originated from the prompt photons in high p_T regions.

The ratio of v_2 to v_3 is compared with hydrodynamical model calculations. It is found that the model calculation with MCGlb+ $\eta/s(0.08)$ describes the ratio of photon well while that of

charged pion is better described by another set of parameters with MCKLM+ $\eta/s(0.20)$.

Photon p_T spectra and v_n are predicted as massless particle by the parameters determined by blast wave model fitting to hadron observables, if those photons are really emitted during the freeze-out stage. It is found that p_T spectra is well described with the combination of low temperature and large radial flow as well as that of high temperature and no radial flow. It is naturally expected in the collective expansion scenario that there would be no azimuthal anisotropy (zero v_n) if radial flow does not exist. Blast wave model suggests that radial flow is needed to be taken into account in order to understand photon puzzle.

The thermal photon p_T spectra and v_n are calculated with blue shift correction. It is assumed that the temperature, acceleration, and azimuthal anisotropy of medium vary with expansion time. The photon observables are calculated by integrating over the expansion time. The time dependence of these variables are constrained so that the effective temperature and v_n are well described. This calculation indicates that the high effective temperature and large v_n are reproduced with the blue shift correction given by the large expansion velocity during the freeze-out. It is obtained that the true temperature during the photon emission is within 120 - 160 MeV and photons from close to the end of hadronic freeze-out are dominant. Additionally, photon v_n is calculated from thermal photons and pQCD based photons. Although it is observed that there is large difference between experimental measurement and this calculation in $2 < p_T < 5$ GeV/ c . It could suggest that the photons originated from the other sources coming from jet energy loss inside of QGP and/or possible modification of jet fragmentation are dominant in $2 < p_T < 5$ GeV/ c .

In this thesis, neutral pion and direct photon v_2 , v_3 , and v_4 are measured in Au+Au $\sqrt{s_{NN}} = 200$ GeV collisions at RHIC-PHENIX experiment. In the case of neutral pion v_n , it is found that the behavior of v_n in high p_T could be understood by the jet effect; path length dependence of energy loss and jet bias on event plane determination. It is found that the direct photon v_n is close to zero in high p_T region, and it is consistent with the expectation that the prompt photons are dominant and they have small interaction in QGP as also observed as $R_{AA} \sim 1$ for direct photon. In low p_T region, it is observed that photons have non zero and positive v_3 which is similar to the case of v_2 . Blast wave model suggests that a possible explanation of photon puzzle could be the radial flow effect. The high effective temperature and large v_n could be achieved as a consequence of Doppler (blue) shift caused by a large radial flow. The extracted temperature of photon emission source is as low as 120 - 160 MeV and photons at close to the end of hadronic freeze-out are dominant. It also indicates that the photons originated from the other additional sources such as modification of jet fragmentations and redistribution of the lost energy coming from the energy loss inside QGP could be existing around 2 to 5 GeV/ c .

Appendix A

The results of inclusive photon v_n

- The results of inclusive photon v_n with RxN(In)
- The results of inclusive photon v_n with RxN(Out)
- The results of inclusive photon v_n with MPC
- The results of inclusive photon v_n with BBC
- The results of inclusive photon v_n with RxN(In)+MPC

Figure A.1: The results of inclusive photon v_2 , v_3 , and v_4 (R_xN(In)) with 10% centrality interval.

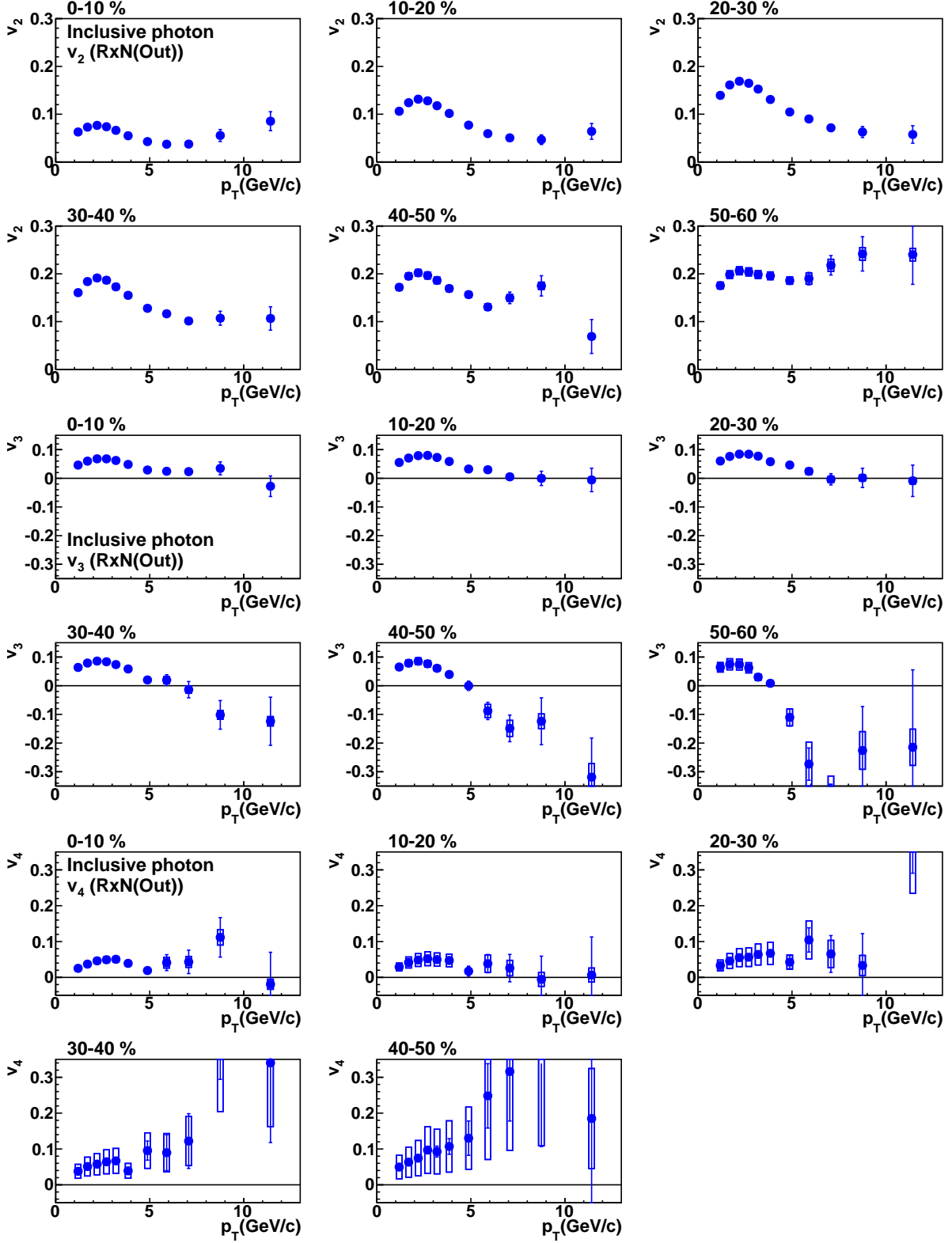


Figure A.2: The results of inclusive photon v_2 , v_3 , and v_4 (RxN(Out)) with 10% centrality interval.

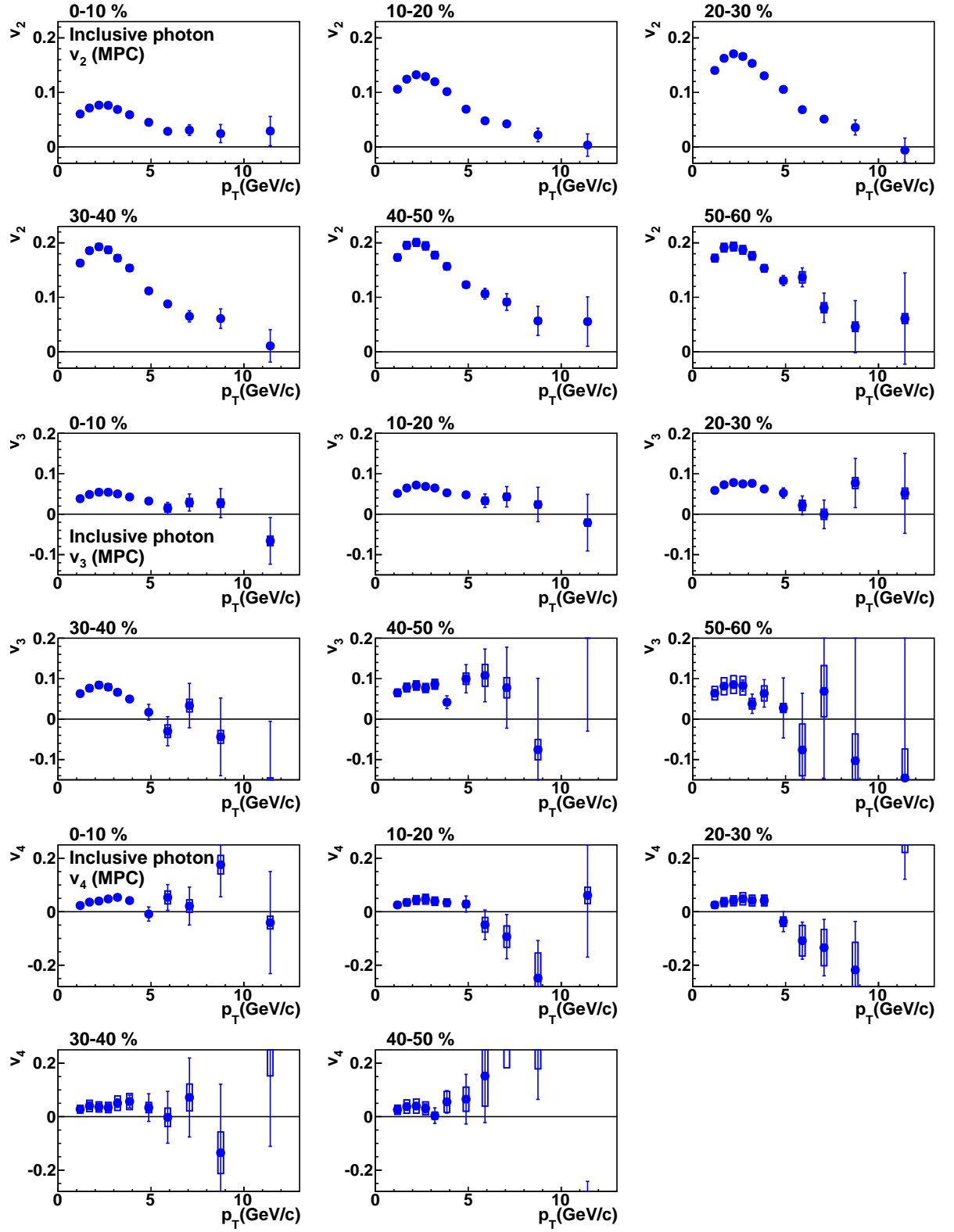
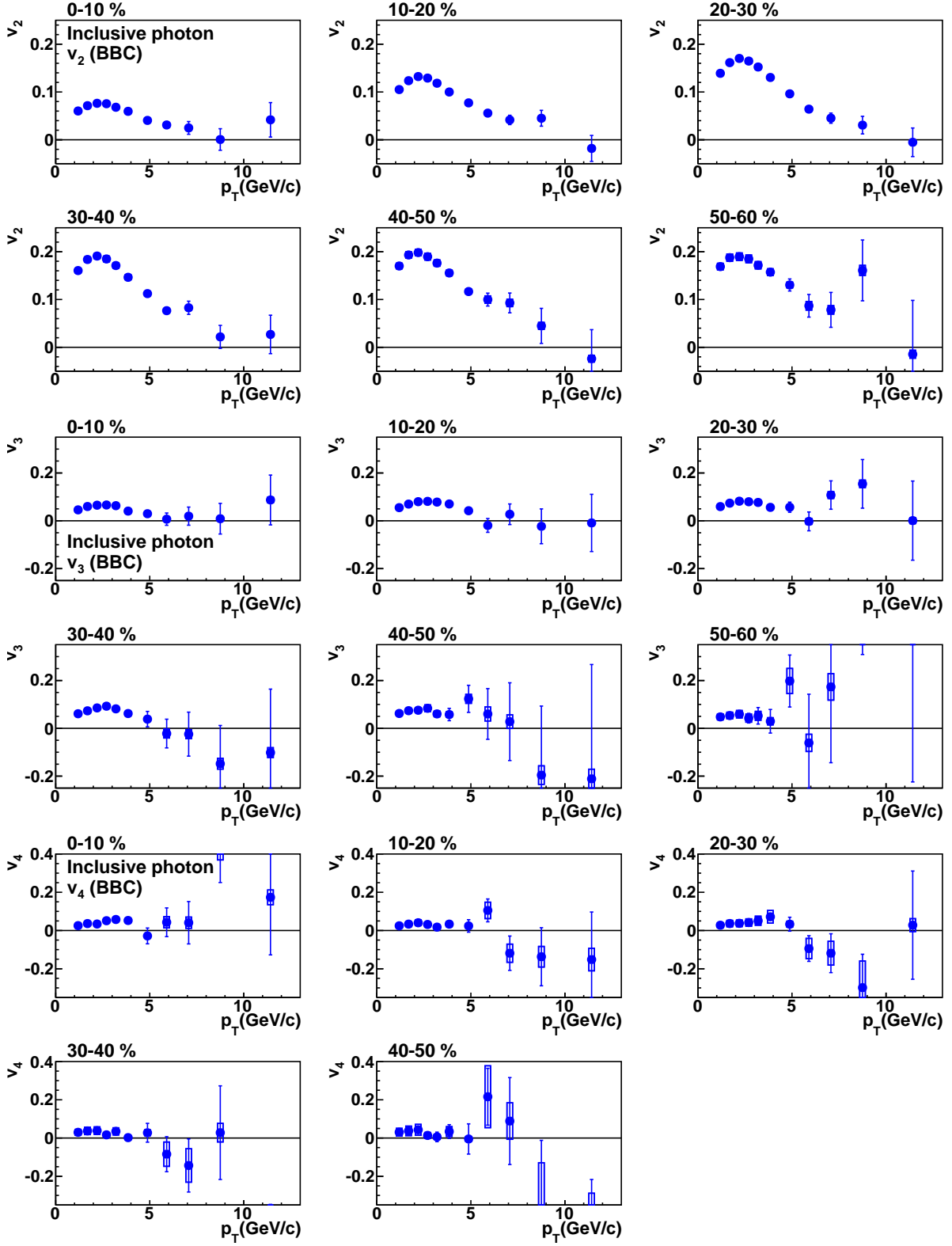


Figure A.3: The results of inclusive photon v_2 , v_3 , and v_4 MPC with 10% centrality interval.

Figure A.4: The results of inclusive photon v_2 , v_3 , and v_4 BBC with 10% centrality interval.

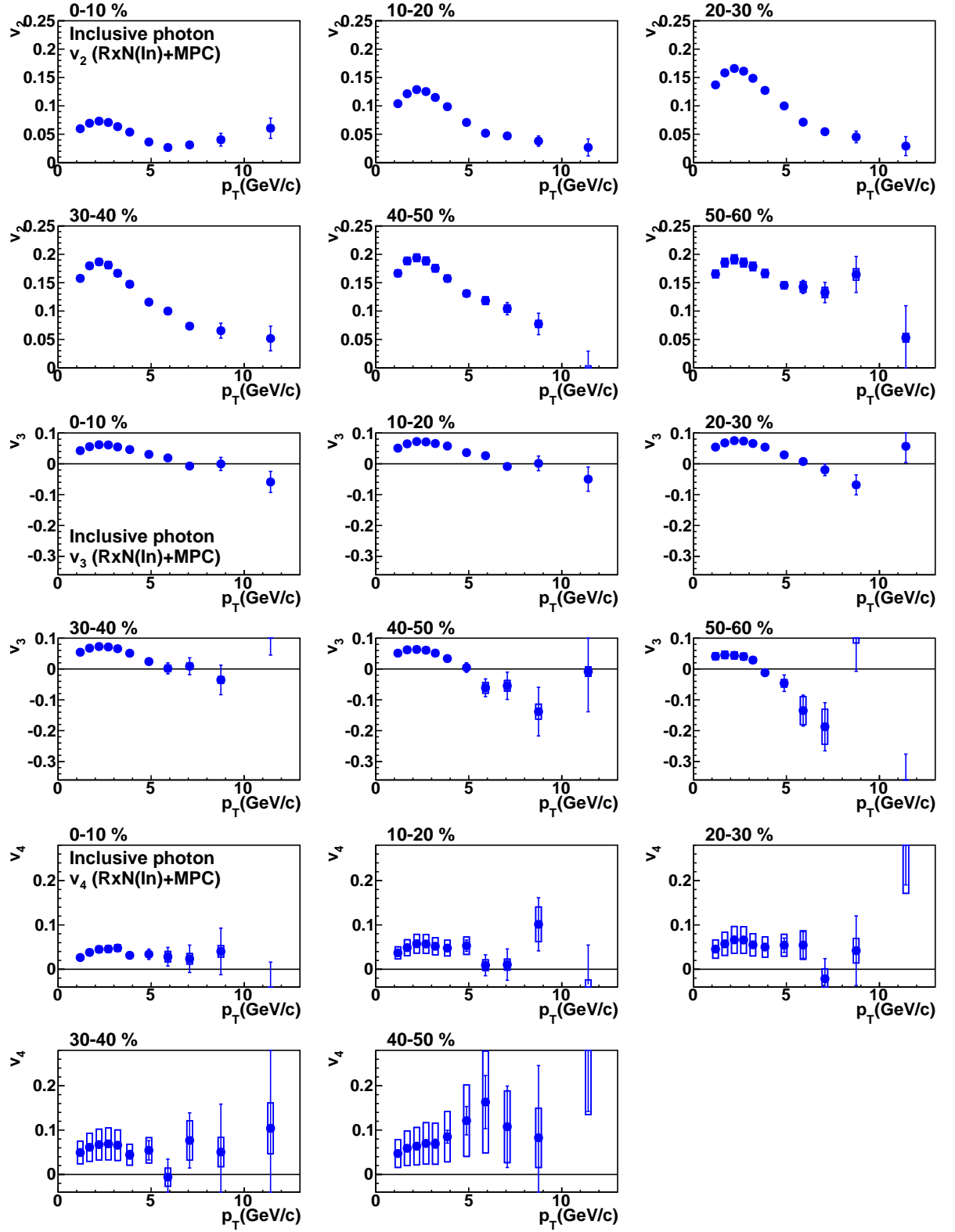


Figure A.5: The results of inclusive photon v_2 , v_3 , and v_4 RxN(In)+MPC with 10% centrality interval.

Appendix B

The results of neutral pion v_n

- The results of neutral pion v_n with RxN(In)
- The results of neutral pion v_n with RxN(Out)
- The results of neutral pion v_n with MPC
- The results of neutral pion v_n with BBC
- The results of neutral pion v_n with RxN(In)+MPC

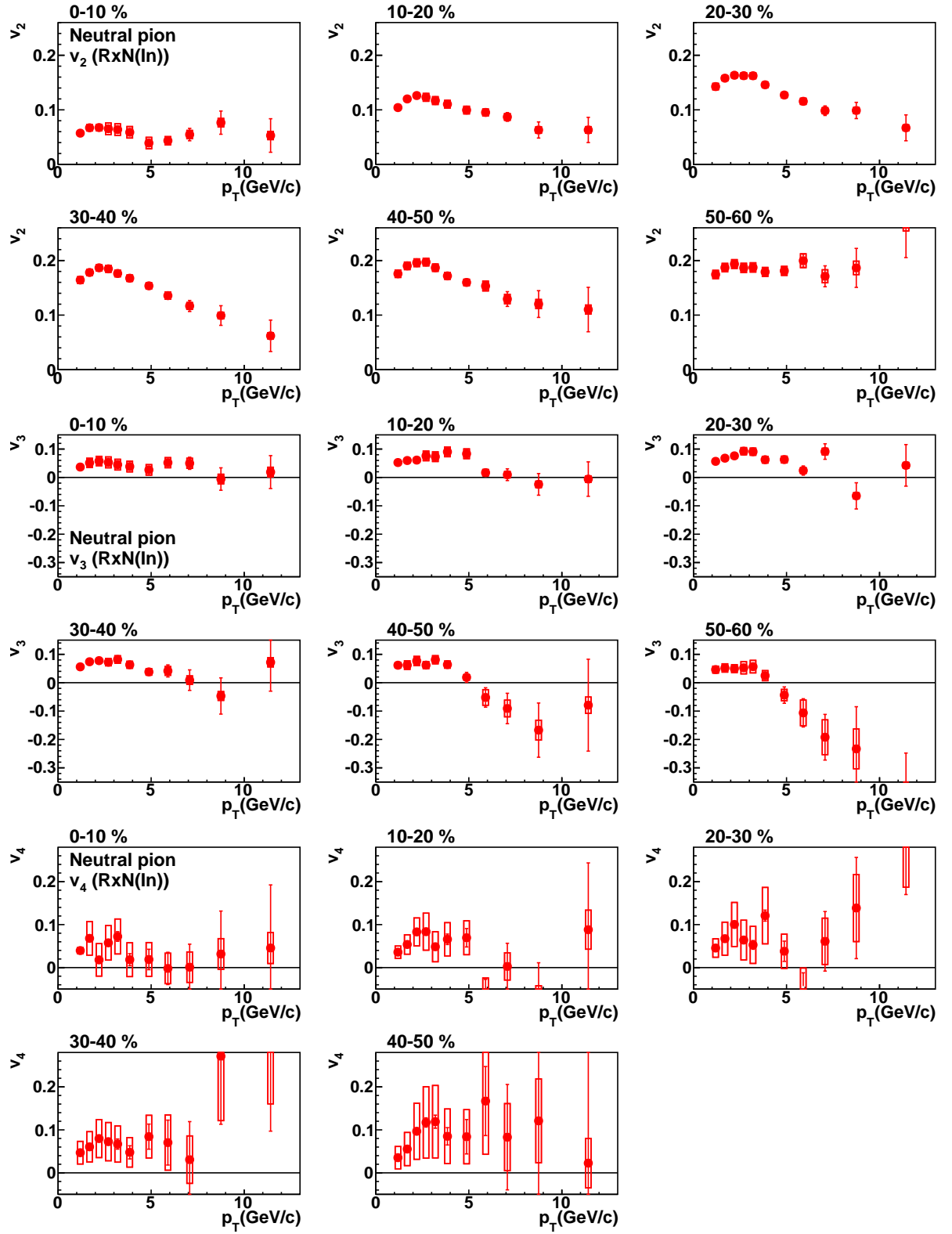
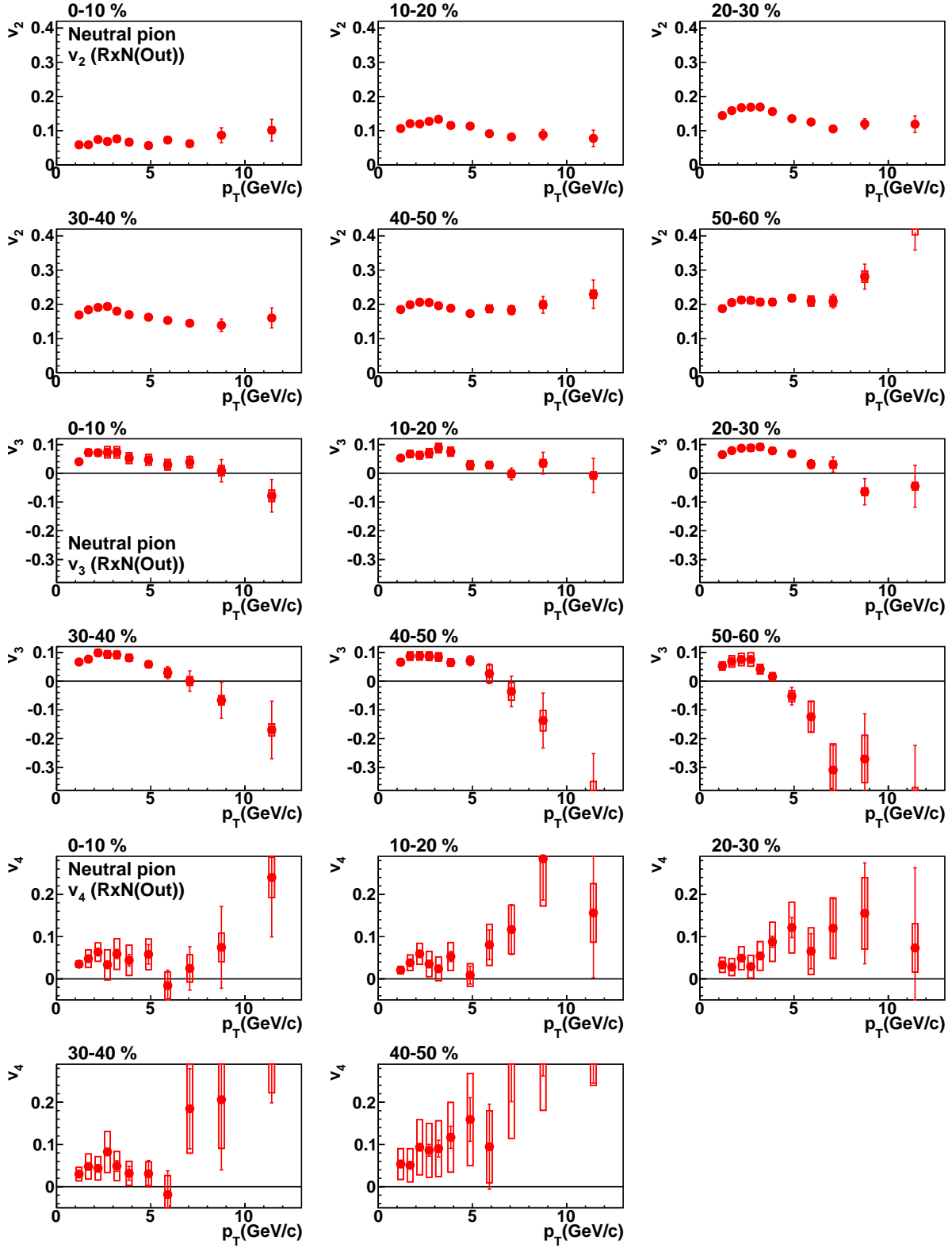


Figure B.1: The results of neutral pion v_2 , v_3 , and v_4 (Rxn(In)) with 10% centrality interval.

Figure B.2: The results of neutral pion v_2 , v_3 , and v_4 (RxN(Out)) with 10% centrality interval.

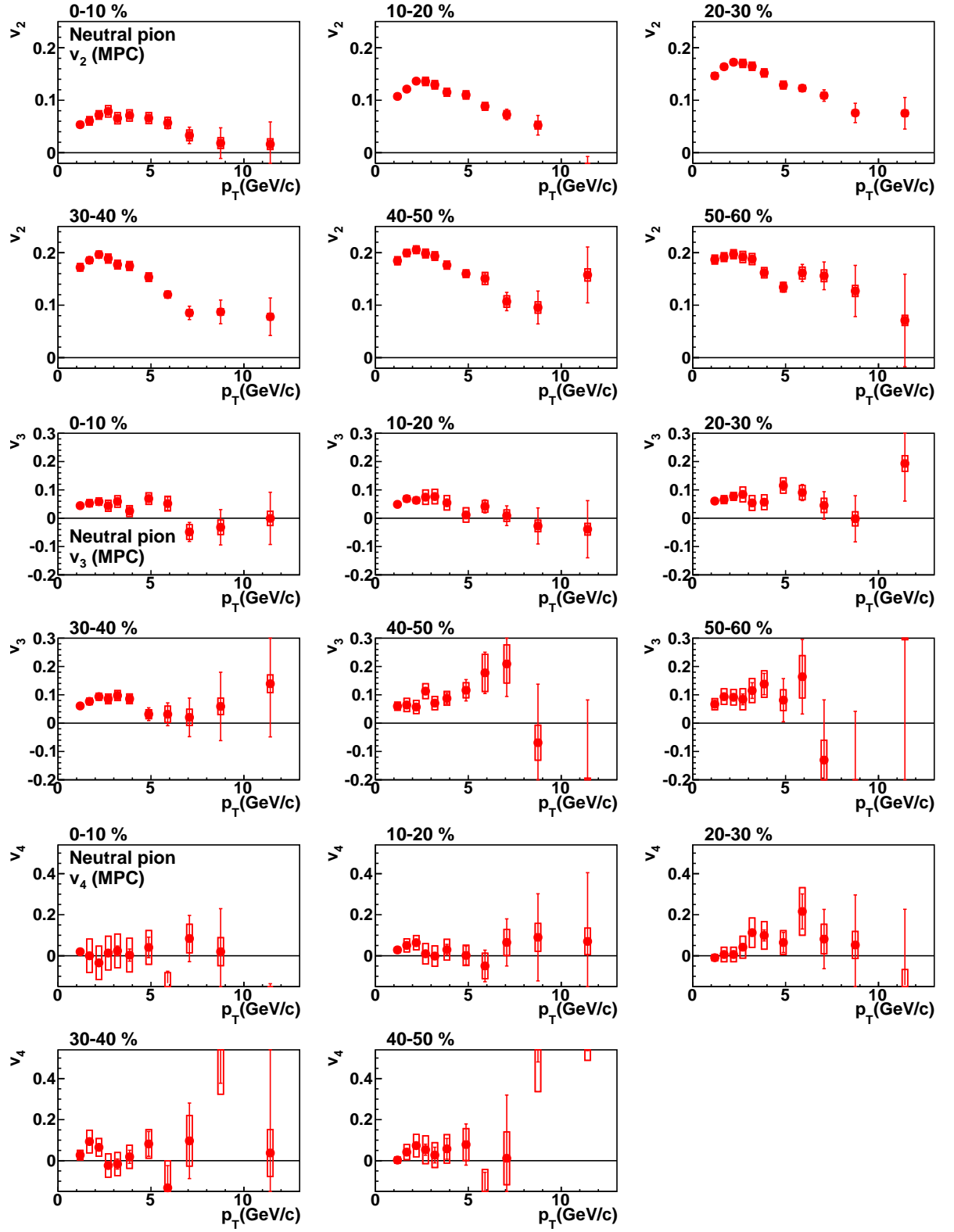
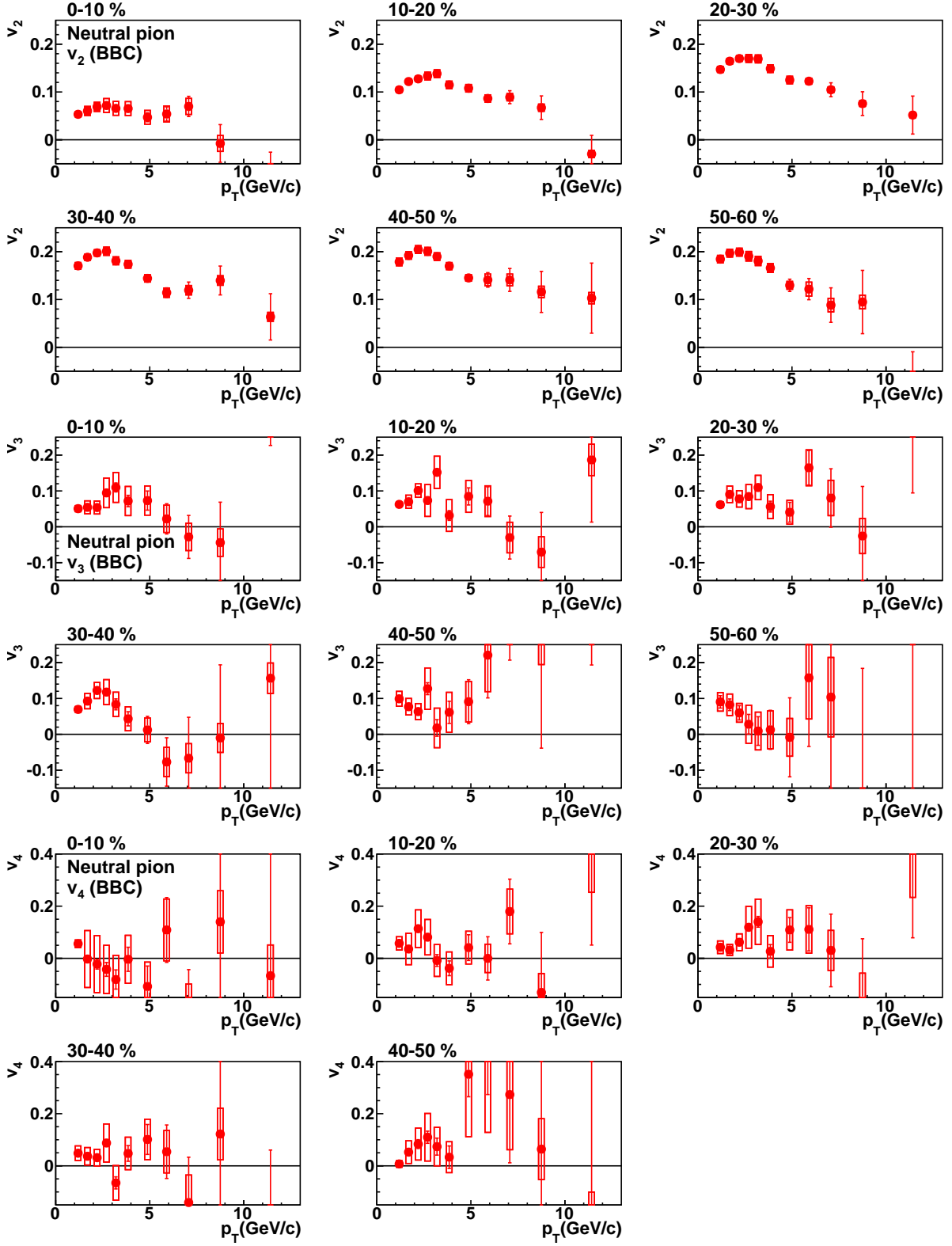


Figure B.3: The results of neutral pion v_2 , v_3 , and v_4 MPC with 10% centrality interval.

Figure B.4: The results of neutral pion v_2 , v_3 , and v_4 BBC with 10% centrality interval.

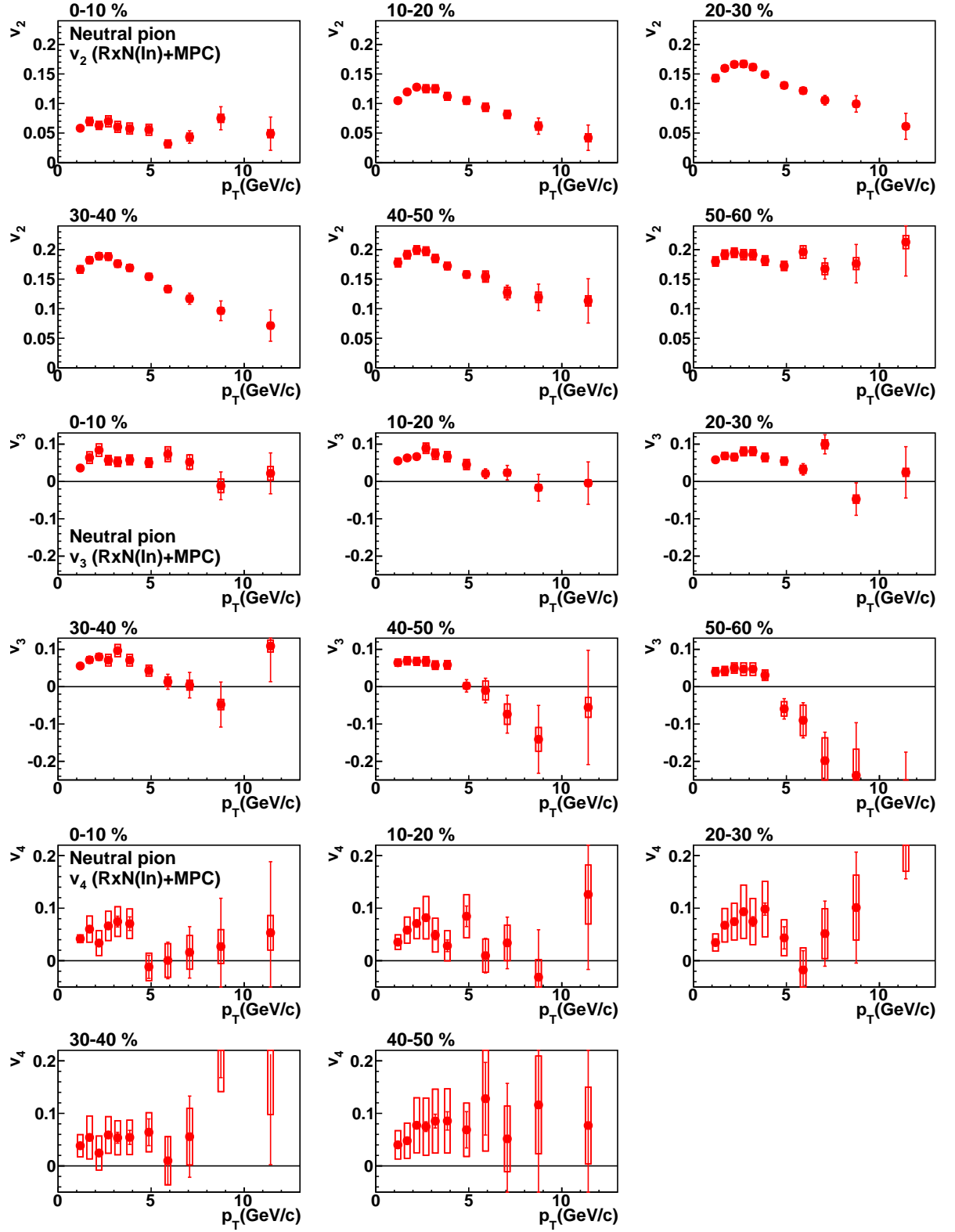


Figure B.5: The results of neutral pion v_2 , v_3 , and v_4 RxN(In)+MPC with 10% centrality interval.

Appendix C

The results of direct photon v_n

- The results of direct photon v_n with RxN(In)
- The results of direct photon v_n with RxN(Out)
- The results of direct photon v_n with MPC
- The results of direct photon v_n with BBC
- The results of direct photon v_n with RxN(In)+MPC

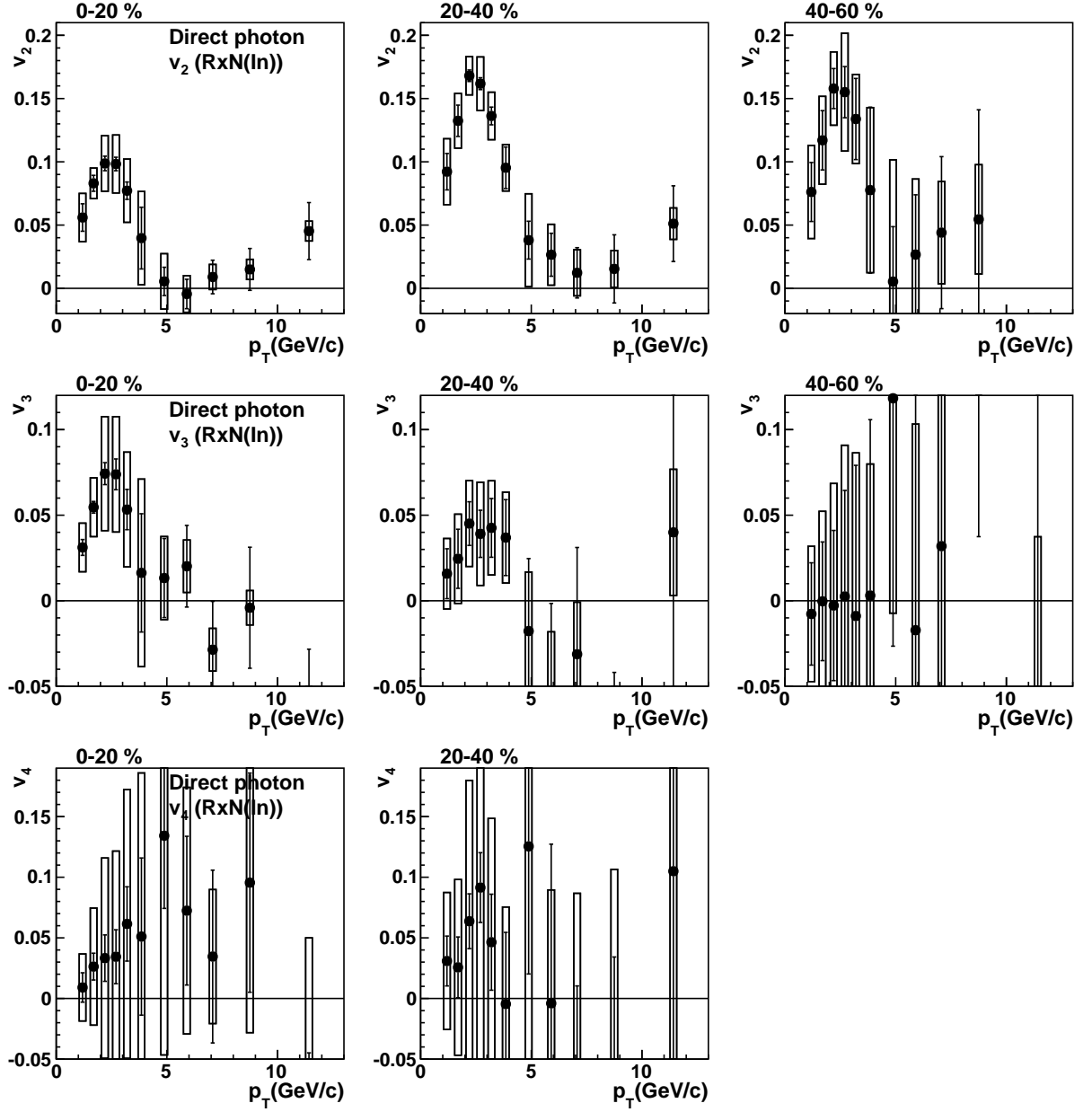


Figure C.1: The results of direct photon v_2 , v_3 , and v_4 (RxN(In)) with 20% centrality interval.

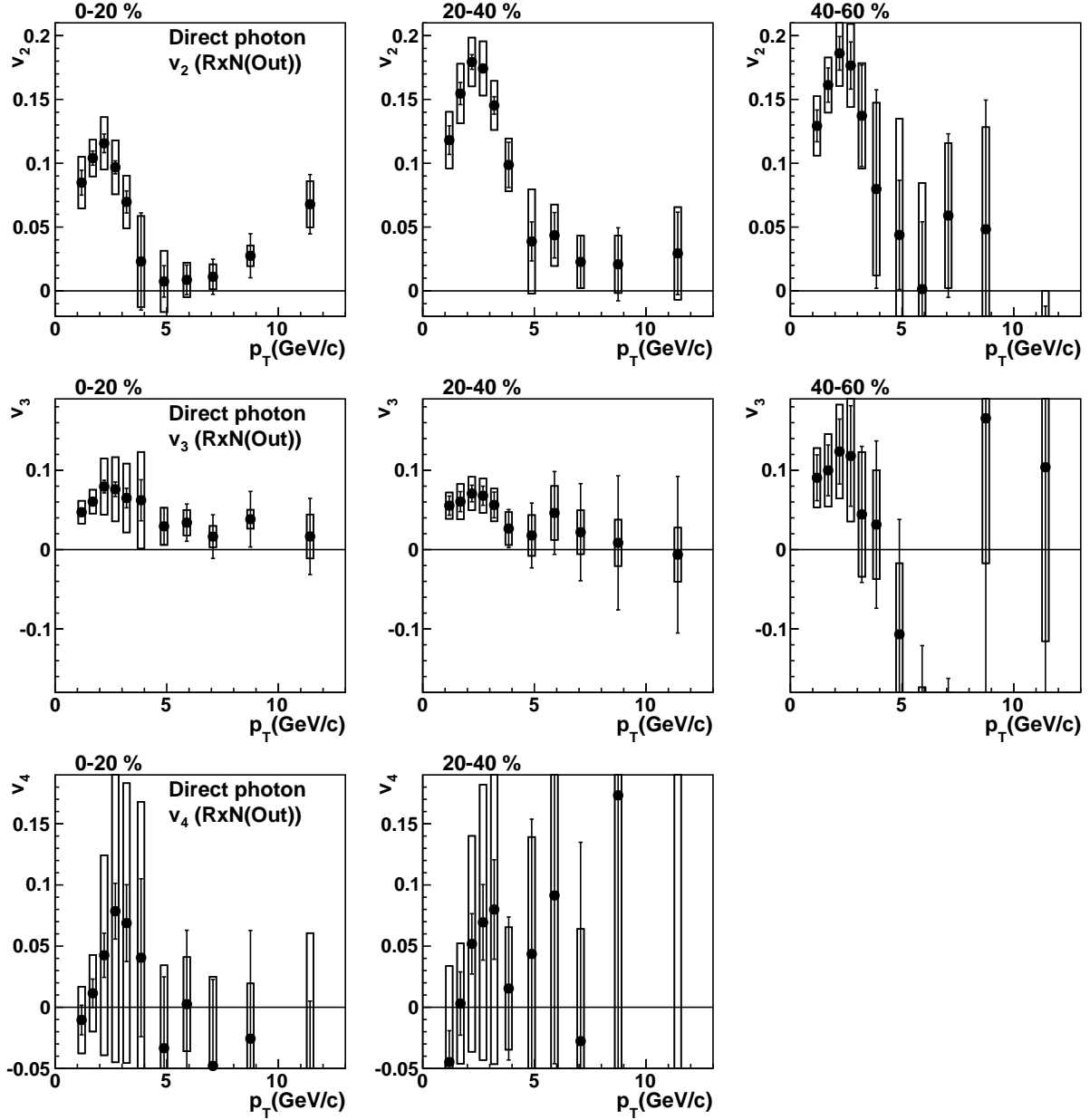


Figure C.2: The results of direct photon v_2 , v_3 , and v_4 (RxN(Out)) with 20% centrality interval.

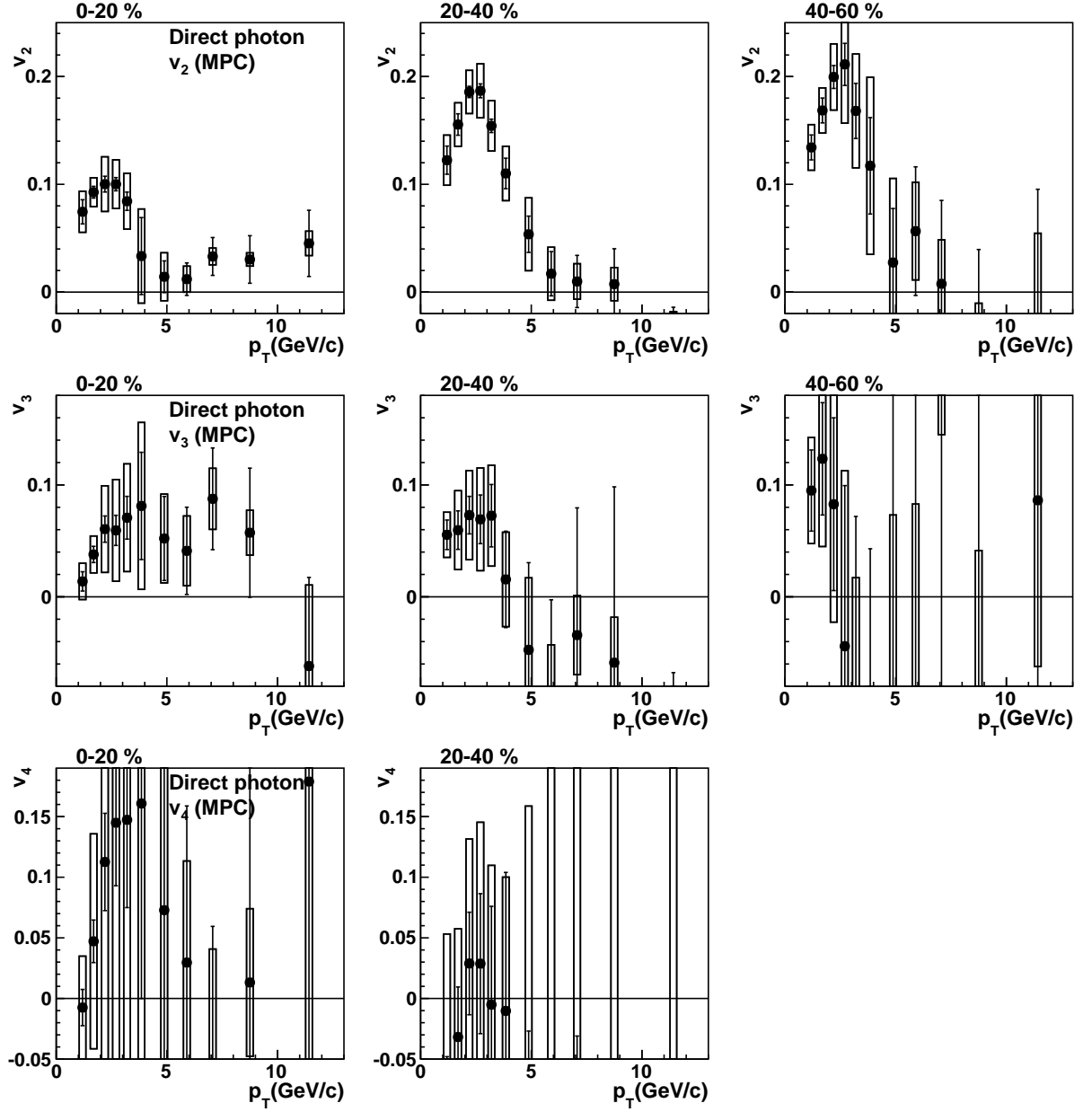


Figure C.3: The results of direct photon v_2 , v_3 , and v_4 (MPC) with 20% centrality interval.

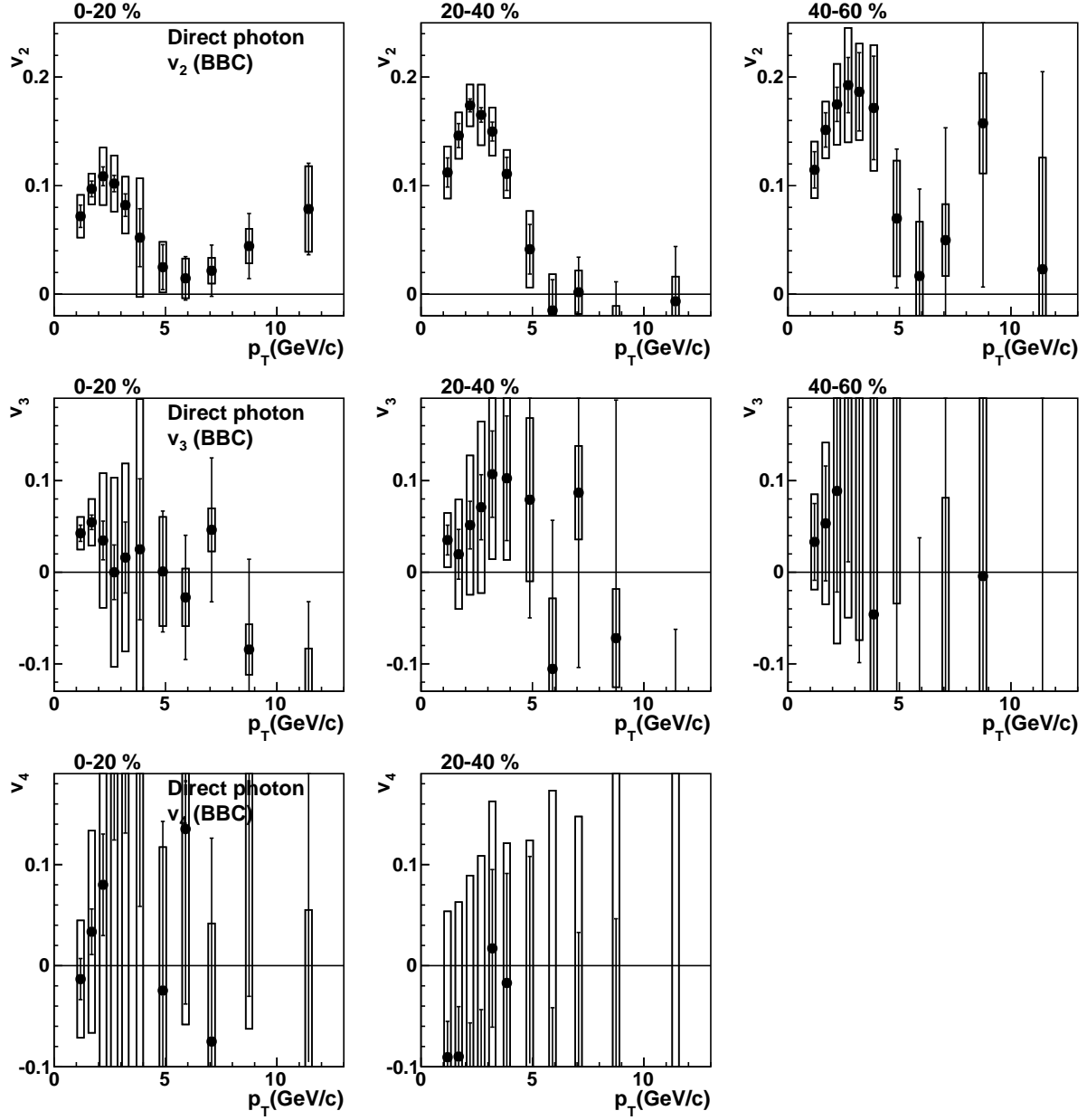


Figure C.4: The results of direct photon v_2 , v_3 , and v_4 (BBC) with 20% centrality interval.

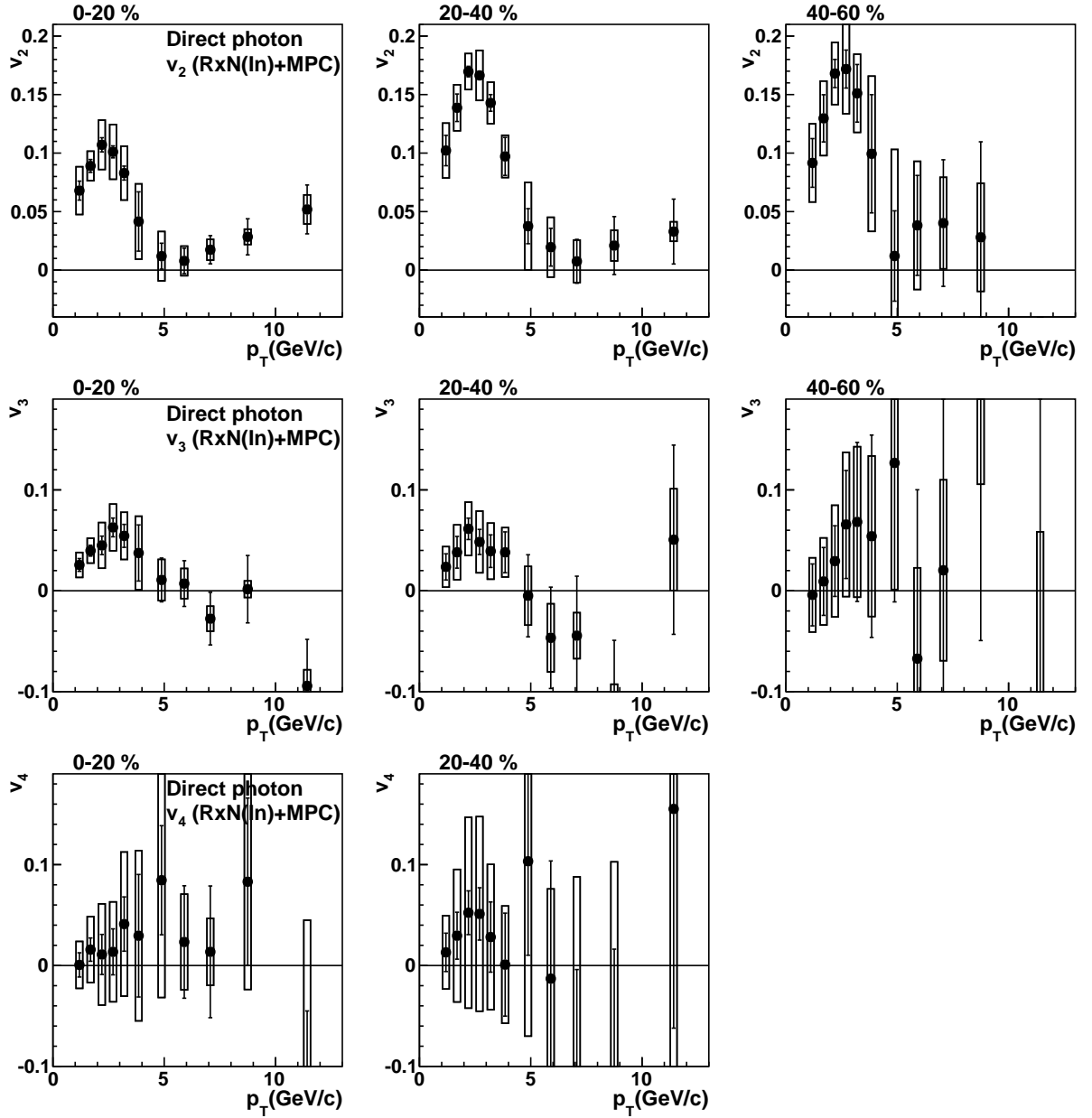


Figure C.5: The results of direct photon v_2 , v_3 , and v_4 (RxN(In)+MPC) with 20% centrality interval.

Bibliography

- [1] “Particle Data Group (<http://pdg.lbl.gov>)”, 2014.
- [2] A.Bazavov et al. “Equation of state and QCD transition at finite temperature”. *P.R.D* 80, 014504, 2009.
- [3] J.D.Bjorken. “Highly relativistic nucleus-nucleus collisions: The central rapidity region”. *P.R.D* 27, 140, 1983.
- [4] S.S.Adler et al. “Systematic studies of the centrality and $\sqrt{s_{NN}}$ dependence of the $dE_T/d\eta$ and $dN_{ch}/d\eta$ in heavy ion collisions at midrapidity”. *P.R.C* 71, 034908, 2005.
- [5] Masashi Kaneta and Nu Xu. “Centrality Dependence of Chemical Freeze-out in Au+Au Collisions at RHIC”. *arXiv:0405068v1 [nucl-th]*, 2004.
- [6] S.S.Adler et al. “Identified charged particle spectra and yields in Au+Au collisions at $\sqrt{s_{NN}}=200\text{GeV}$ ”. *P.R.C* 69, 034909, 2004.
- [7] A.Adare et al. “Measurements of Higher Order Flow Harmonics in Au+Au Collisions at $\sqrt{s_{NN}}=200\text{GeV}$ ”. *P.R.L.* 107, 252301, 2011.
- [8] T.Todoroki et al. “Measurement of the higher-order anisotropic flow coefficients for identified hadrons in Au+Au collisions at $\sqrt{s_{NN}}=200\text{GeV}$ ”. *arXiv:1412.1038v1 [nucl-ex]*, 2014.
- [9] S.S.Adler et al. “Measurement of Direct Photon Production in p+p Collisions at $\sqrt{s} = 200\text{GeV}$ ”. *P.R.L.* 98, 012002, 2007.
- [10] Hendrik van Hees. “Thermal photons and collective flow at energies available at the BNL Relativistic Heavy-Ion Collider”. *P.R.C* 84, 054906, 2011.
- [11] A.Adare et al. “Enhanced Production of Direct Photons in Au+Au Collisions at $\sqrt{s_{NN}}=200\text{GeV}$ and Implications for the Initial Temperature”. *P.R.L.* 104, 132301, 2010.
- [12] Daniel Lohner et al. “Measurement of Direct Photon Elliptic Flow in Pb-Pb Collisions at $\sqrt{s_{NN}}=2.76\text{TeV}$ ”. *arXiv:1212.3995v2 [nucl-ex]*, 2013.
- [13] A.Adare et al. “Observation of Direct-Photon Collective Flow in Au+Au Collisions at $\sqrt{s_{NN}}=200\text{GeV}$ ”. *P.R.L.* 109, 122302, 2012.
- [14] Chun Shen et al. “Thermal photons as a quark-gluon plasma thermometer reexamined”. *P.R.C* 89, 044910, 2014.

- [15] Martin Wilde et al. “Measurement of Direct Photons in pp and Pb-Pb Collisions with ALICE”. *arXiv:1210.5958*, 2012.
- [16] Chun Shen et al. “Thermal photon anisotropic flow serves as a quark-gluon plasma viscometer”. *Xiv:1403.7558v1 [nucl-th]*, 2014.
- [17] S.H.Aronson et al. “PHENIX magnet system”. *NIM A499 480-488*, 2003.
- [18] C.Adler et al. “The RHIC zero-degree calorimeters”. *NIM A499 433-436*, 2003.
- [19] M.Allen et al. “PHENIX inner detectors”. *NIM A499 549-559*, 2003.
- [20] Mickey Chiu. “Single Spin Transverse Asymmetries of Neutral Pions at Forward Rapidities in $\sqrt{s}=62.4$ GeV Polarized Proton Collisions in PHENIX”. *arXiv:0701031v1 [nucle-ex]*, 2007.
- [21] E.Richardson et al. “A reaction plane detector for PHENIX at RHIC”. *NIM A636 99-107*, 2011.
- [22] L.Aphecetche et al. “PHENIX calorimeter”. *NIM A499 521-536*, 2003.
- [23] S.S.Adler et al. “PHENIX on-line systems”. *NIM A499 560-592*, 2003.
- [24] Kentaro Miki and Sasha Milov. “PHENIX Internal Analysis Note 645”, 2007.
- [25] K.Miki. “Azimuthal Anisotropy Measurement of Neutral Pion and Direct Photon in $\sqrt{s_{NN}}=200$ GeV Au+Au Collisions at RHIC-PHENIX”. *Ph.D Thesis at the University of Tokyo*, 2009.
- [26] A.Adare et al. “Suppression Pattern of Neutral Pions at High Transverse Momentum in Au+Au Collisions at $\sqrt{s_{NN}}=200$ GeV and Constraints on Medium Transport Coefficients”. *P.R.L. 101, 232301*, 2008.
- [27] A.Adare et al. “Transverse momentum dependence of η meson suppression in Au+Au collisions at $\sqrt{s_{NN}}=200$ GeV”. *P.R.C 82, 011902*, 2010.
- [28] A.Adare et al. “Production of ω mesons in p+p, d+Au, Cu+Cu, and Au+Au collisions at $\sqrt{s_{NN}}=200$ GeV”. *P.R.C 84, 044902*, 2011.
- [29] S.S.Adler et al. “Centrality Dependence of Direct Photon Production in $\sqrt{s_{NN}}=200$ GeV Au+Au Collisions”. *P.R.L. 94, 232301*, 2005.
- [30] A.Adare et al. “Centrality dependence of low-momentum direct-photon production in Au+Au collisions at $\sqrt{s_{NN}}=200$ GeV”. *arXiv:1405.3940 [nucl-ex]*, 2014.
- [31] Chun Shen (Private Communication).
- [32] O.Linnyk et al. “Centrality dependence of the direct photon yield and elliptic flow in heavy-ion collisions at $\sqrt{s_{NN}}=200$ GeV”. *P.R.C 89, 034908*, 2014.
- [33] Gojko Vujanovic et al. “Probing the early-time dynamics of relativistic heavy-ion collisions with electromagnetic radiation”. *arXiv:1404.3714v1 [hep-th]*, 2014.

- [34] Berndt Müller et al. “Elliptic flow from thermal photons with magnetic field in holography”. *P.R.D* 89, 026013, 2014.
- [35] K.Adcox et al. “PHENIX detector overview”. *NIM A499* 469-479, 2003.
- [36] Maya Shimomura et al. “PHENIX Internal Analysis Note 768”, 2009.
- [37] A.Adare et al. “Neutral pion production with respect to centrality and reaction plane in Au+Au collisions at $\sqrt{s_{NN}}=200\text{GeV}$ ”. *P.R.C* 87, 034911, 2013.
- [38] Ralf Averbeck et al. “PHENIX Internal Analysis Note 349”, 2005.
- [39] Simon Turbide, Ralf Rapp, and Charles Gale. “Hadronic production of thermal photons”. *P.R.C* 69, 014903, 2004.
- [40] Rainer J.Fries et al. “High-Energy Photons from Passage of Jets through Quark-Gluon Plasma”. *P.R.L.* 90, 132301, 2003.
- [41] A.Adare et al. “Measurement of Direct Photons in Au+Au Collisions at $\sqrt{s_{NN}}=200\text{GeV}$ ”. *P.R.L.* 109, 152302, 2012.
- [42] S.Turbide et al. “Azimuthal Asymmetry of Direct Photons in High Energy Nuclear Collisions”. *P.R.L.* 96, 032303, 2006.
- [43] Kirill Tuchin. “Photon decay in a strong magnetic field in heavy-ion collisions”. *P.R.C* 83, 017901, 2011.
- [44] Gökçe Başar et al. “Conformal anomaly as a source of soft photons in heavy ion collisions”. *arXiv:1206.1334v2 [hep-ph]*, 2012.
- [45] “Quark-Gluon Plasma”, 2006.
- [46] T.Ludlam. “Overview of experiments and detectors at RHIC”. *NIM A499* 428-432, 2003.
- [47] K.Adcox et al. “PHENIX central arm tracking detectors”. *NIM A499* 489-507, 2003.
- [48] J.Barrete et al. “Proton and pion production relative to the reaction plane in Au+Au collisions at 11A GeV/c”. *P.R.C* 56, 3254, 1997.
- [49] A.M.Poskanzer and S.A.Voloshin. “Methods for analyzing anisotropic flow in relativistic nuclear collisions”. *P.R.C* 58, 1671, 1998.
- [50] K.Oyama. “ π^0 Production in Au+Au Collisions at $\sqrt{s_{NN}}=130\text{ GeV}$ ”. *Ph.D Thesis at the University of Tokyo*, 2002.
- [51] A.Adare et al. “Azimuthal anisotropy of π^0 and η mesons in Au+Au collisions at $\sqrt{s_{NN}}=200\text{GeV}$ ”. *P.R.C* 88, 064910, 2013.
- [52] The CMS Collaboration. “Very high- p_T dihadron correlations in PbPb collisions at $\sqrt{s_{NN}}=2.76\text{ TeV}$ ”. *CMS PAS HIN-12-010*, 2012.

- [53] G.Aad et al. “Measurement of the Azimuthal Angle Dependence of Inclusive Jet Yields in Pb+Pb Collisions at $\sqrt{s_{NN}}=2.76\text{TeV}$ with the ATLAS Detector”. *P.R.L.* 111, 152301, 2013.
- [54] Zi-Wei Lin et al. “Multiphase transport model for relativistic heavy ion collisions”. *P.R.C* 72, 064901, 2005.
- [55] Hendrik van Hees et al. “Heavy-quark probes of the quark-gluon plasma and interpretation of recent data taken at the BNL Relativistic Heavy Ion Collider”. *P.R.C* 73, 034913, 2006.
- [56] P.Huovinen et al. “Radial and elliptic flow at RHIC: further predictions”. *P.R.B* 503, 58-64, 2001.